Novel Dopants in TCOs for Improved Infra-Red Transparency

By

THOMAS FEATHERSTONE

Department of Physics
UNIVERSITY OF LIVERPOOL

Thesis submitted in accordance with the requirements of the University of Liverool for the degree of DOCTOR OF PHILOSOPHY.

MARCH 2021

Word count:56630

Abstract

Transparent conductive oxides (TCOs) are a class of material used in a wide range of applications due to them presenting both transparency and conductivity, two properties which are usually mutually exclusive. TCOs are primarily based on three materials, In_2O_3, SnO_2 and ZnO, doped n-type with the p-block elements. The most common dopants were chosen due to their proximity to the host elements in the periodic table. The close proximity means they are expected to the similar in size to the element they are replacing, minimising lattice strain. This led to the assumption that these dopants would provide the highest electron mobilities. However recent experimental work has shown that transition metal (d-block) or lanthanide (f-block) doping of these materials may lead to improved mobilities compared to the traditional dopants.

In this thesis, two novel dopants which provide higher electron mobilities than their traditional counterparts are identified. These are Ce in In_2O_3 and Ta in SnO_2. The mechanism behind the improved mobility was also identified as the donating electron orbitals sitting 'resonantly' within the conduction band of the host material. This means that the donating orbital sits well above the conduction band minimum, minimising mixing of the host and donor states. As such, the shape of the host conduction band is maintained and the band edge electron effective mass remains low. These conclusions were drawn from observations made from experimental photo-emission and theoretical DFT results. These experiments and calculations were performed for the resonantly doped systems, Ce doped In_2O_3 and Ta doped SnO_2 and also their traditional analogues, Sn doped In_2O_3 and Sb doped SnO_2. Modelling of the relationship between the Fermi level and carrier concentration was fitted to the Fermi level extracted from the HAXPES which showed that the resonant dopants resulted in lower band edge effective masses. The DFT band structure calculations showed that the dopant levels sat well above the the CBM and partial charge density calculations showed that the charge density around the dopant atoms was much lower in the resonantly doped systems.

While this results in improved mobility, these dopants tend to result in lower carrier concentrations than their traditional counterparts. This means that any resulting improvement in conductivity is minimal. However, is was found that the reduced carrier concentration results in improved transparency in the near infra-red region. Modelling of the optical response of photovoltaic devices showed that utilising the improved optical properties provided by these resonant dopants could lead to improved efficiencies. A selection rule is suggested, saying that a transparent electrode with a plasma frequency less than the band gap of the absorber material should be used in photovoltaic devices as modelling shows that having a greater plasma frequency leads to parasitic absorption.

Finally, a new quantity dubbed 'optical suitability' is defined. This quantifies the suitability of the optical properties of a transparent conductor for a photovoltaic absorber with a specific band gap. Unlike previous 'Figures of Merit' this quantity accounts for losses due nature of the

absorber and weights optical losses dependent on wavelength accordingly. The optical suitability shows requirements for transparent conductors for photovoltaic devices, especially those that utilise a narrow band gap absorber, are different than those captured in older figures of merit.

Dedication and acknowledgements

Completion of this thesis would not have been possible without the help and support of many people. Here I would like to thank and acknowledge both those who assisted in the work presented here and friends and family who supported me throughout my time at the University.

Firstly, I wish to express my gratitude to my supervisor, Prof. Tim Veal. When I applied for my PhD position, Tim was supposed to be my secondary supervisor, but due to changes in circumstances out of either of our control, he took over as my primary. While in many cases of situations like this, I believe it could be all too easy for a student to slip through the cracks, forgotten and left without direction. However, I got unbelievably lucky, landing with one of the most supportive and knowledgeable academics I have ever encountered. The work within this thesis would have been impossible without his guidance and support. I also wish to extend my thanks to Prof. Ken Durose and Dr Jon Major for providing access to their lab and equipment as well as sharing their knowledge in the field of photovoltaics.

There are many others who I worked along side in the Stephenson Institute for Renewable Energy who deserve acknowledgement for both sharing their knowledge and making the SIRE a wonderful place to work. Firstly there are the other members of the research group, past and present: Jack Swallow, Huw Shiel, Leanne Jones, Matthew Smiles and Max Birkett. Thank you for the support through day to day research as well as the long nights at Diamond and constantly keeping group meetings both interesting and entertaining. There are also all those who I did not work with regularly but have become some of the closest friends I have ever had the fortune of having. So many people made the SIRE a joy to spend time at but in particular I must thank Tom Shalvey, Nicole Fleck, Theo Hobson, Jack Bean, Joe Horne and Jacob Leaver. Each has helped keep me sane and social over the past few years, particularly in the last year where it could have been so easy to fall out of touch.

I would also like to extend my thanks to other members of CDT cohort, C3, (Making Tom Shalvey the only person to be acknowledged twice in this thesis) who make every time we reunite a joy and in particular made the first year of my PhD an adventure I will never forget.

I have also been incredibly lucky to collaborate with a wide range of wonderful people outside of the University of Liverpool in my work. The work I present here would have never been as strong without the DFT calculation performed by collaborators at UCL, Prof. David Scanlon, Ben Williamson and Joe Willis. Also the time spent at Diamond lightsource at the I09 beamline was paramount to the success of this project and for that I must thank Tien-Lin Lee for allowing us to use what is probably the most expensive piece of equipment I have ever touched. I would also like to thank Pardeep Thakur and David Duncan, the beamline scientists who provided much assistance during the experiments at diamond. I am grateful to Anna Regoutz who was present on many of my trips to diamond and imparted much knowledge about photoemmision during those times.

There are also people outside of my academic life that deserve as much appreciation. Without my parents support (emotional and financial) I would never be where I am today. They supported me as a three year degree became four years and as that became eight when I decided to pursue a PhD. Being able to follow this path without financial worries and a caring home I always had the ability to return to is one of the greatest gifts I could ask for.

Finally, and probably most importantly, I want to thank Summer. Thank you for sharing the good times with me and supporting me through the bad. It would be a lie to say that it has all been easy, but with you by my side and your willingness work through the difficult, you have certainly made it easier. I can never express my gratitude for that enough but I can hope to repay you in kind and support you in future endeavours as much as you have already supported me in mine, but for now all I can say is thank you.

Once again I would like to express my gratitude to all those mentioned above as well as everyone else who I have had the pleasure of meeting over the past four years. Its been an adventure I never forget and if I meet as many wonderful people over the next four years I will be very lucky.

Author's declaration

I declare that the work in this dissertation was carried out in accordance with the requirements of the University's Regulations and Code of Practice for Research Degree Programmes and that it was performed at the University of Liverpool under the supervision of Prof. T. D. Veal.

Ta doped SnO_2 samples were prepared by S. S. Sathasivam (University College London). Ce doped In_2O_3 samples were prepared by T. Koida (National Institute of Advanced Industrial Science and Technology) who also performed ICP-MS on those samples. DFT calculations were performed by J. Willis (University College London) for Ce doped In_2O_3 and B. A. D. Williamson (Norwegian University of Science and Technology) for Ta doped SnO_2. J. E. N Swallow (University of Oxford), L. A. H. Jones, H. Shiel, M. J. Smiles (University of Liverpool) and A. Regoutz (University College London) assisted in taking of HAXPES data. L. E. H. Jones also took XPS data at the national XPS labratory. All of the remaining data collection and calculations were performed by the author. The data analysis, simulation and interpretation was all performed by the author.

Several articles based on work in this thesis have been published or submitted for publication:

B. A. D. Williamson, T. J. Featherstone, S. S. Sathasivam, J. E. N. Swallow, H. Shiel, L. A. H. Jones, M. J. Smiles, A. Regoutz, T. Lee, X. Xia, C. Blackman, P. K. Thakur, C. J. Carmalt, I. P. Parkin, T. D. Veal, and D. O. Scanlon.

Resonant Ta doping for enhanced mobility in transparent conducting SnO_2.

Chemistry of Materials, 32(5):1964–1973, 2020

T. J. Featherstone, J. Willis, J. E. N. Swallow, B. A. D. Williams, L. A. H. Jones, T. Lee, P. K. Thakur, G. W. Watson, T. Koida, D. O. Scanlon, and T. D. Veal.

Resonant Ce doping for high-mobility In_2O_3-based conductors with enhanced near-infrared transparency.

Submitted to Advanced Functional Materials

T. J. Featherstone, J. E. N. Swallow, and T. D. Veal.

Mechanism of enhanced infra-red transparency in resonantly doped TCOs.

In Preparation

SIGNED: .... DATE: ....

Table of Contents

Page

List of Tables xiii

List of Figures xv

1 Introduction 1

1.1 Overview . . . 1

1.2 Conductivity in TCOs . . . 2

1.2.1 Basics of Semiconductors . . . 2

1.2.2 Doping . . . 3

1.2.3 Optimising Conductivity . . . 4

1.2.4 Sheet Resistance . . . 6

1.3 Transparency in TCOs . . . 6

1.3.1 High Energy Cut Off . . . 6

1.3.2 Optical bandgap and the Moss-Burstein Effect . . . 8

1.3.3 Bandgap Shrinkage . . . 9

1.3.4 Low Energy Cut Off . . . 9

1.4 The Importance of Band Structure to TCOs . . . 10

1.4.1 Relation Between Band Dispersion and Conductivity . . . 10

1.4.2 Atomic Orbitals and Band Dispersion . . . 10

1.5 TCOs for Photovoltaics . . . 11

1.5.1 Basics of Photovoltaics . . . 11

1.5.2 The AM 1.5 Spectrum . . . 13

1.5.3 The Shockley-Queisser Limit . . . 14

1.5.4 Resistive Losses in Solar Cells . . . 15

1.5.5 Transparent Electrodes and Busbars . . . 16

1.5.6 Power Loss in the TCO Layer . . . 16

2 Transparent Conductors Literature Review 19

2.1 Introduction . . . 19

2.2 Common TCOs . . . 19

2.2.1 Host materials 19
2.2.2 Dopant Selection 20
2.2.3 Multi-electron Donors 21
2.2.4 In_2O_3-based TCOs 22
2.2.5 SnO_2-based TCOs 23
2.2.6 ZnO-based TCOs 24
2.2.7 Indium Gallium Zinc Oxide 25
2.3 Doping Mechanisms In TCOs 25
2.3.1 Work Function, Ionisation Energy and Electron Affinity 26
2.3.2 Charge Neutrality Level and Fermi Level Stabilisation 26
2.3.3 Resonant Doping 27
2.4 Non-Metal Oxide Transparent Conductors 28
2.4.1 Ultra Thin Metal Films 28
2.4.2 Graphene 30
2.4.3 Carbon Nanotubes 31
2.4.4 Strongly Correlated Metals 32
2.5 P-type Transparent Conductors 33
2.5.1 P-type TCOs 33
2.5.2 Non-oxide p-type Transparent Conductors 33

3 Theoretical Background and Computational Methods 35
3.1 Introduction 35
3.2 Relative Permittivity and Refractive Index 35
3.3 Modelling the Dielectric Function 36
3.3.1 The Classical Drude Oscillator 37
3.3.2 The Two Oscillator Model 37
3.3.3 The Three Oscillator Model 37
3.4 The Transfer Matrix Method 38
3.4.1 Coherence of Light 38
3.4.2 Coherent Systems 39
3.4.3 Incoherent Systems 41
3.4.4 Partial Coherence 41
3.5 Modelling of Electronic Band Structure 42
3.5.1 The Carrier Effective Mass 42
3.5.2 Effective Mass and Bandgap Relationship 44
3.5.3 Parabolic Band Approximation 45
3.5.4 $\mathbf{k}\cdot\mathbf{p}$ Perturbation Theory 46
3.5.5 Calculating Density of States 48
3.5.6 Fermi Statistics and Carrier Concentration 48

3.5.7 Inter-band Absorption 51
3.6 Electrostatic Screening 56
3.6.1 Debye Screening Length 57
3.6.2 Thomas-Fermi approximation 57
3.7 Scattering Mechanisms 57
3.7.1 Ionised Impurity Scattering 58
3.7.2 Grain Boundary Scattering 58
3.7.3 Phonon Scattering 59
3.7.4 Dislocation Scattering 60
3.8 Density Functional Theory 61

4 Experimental Methods **63**
4.1 Introduction 63
4.2 Hall Effect Measurements 63
4.2.1 Van der Pauw Geometry 64
4.3 Optical Measurements 66
4.3.1 UV-Vis Spectroscopy 66
4.3.2 Extracting Film Thickness 68
4.3.3 FTIR 68
4.3.4 Extracting Plasma Frequency 69
4.4 X-ray Diffraction 70
4.4.1 Measurement Geometry 71
4.5 X-ray Photo-electron Spectroscopy 72
4.5.1 Basic Working Principles 72
4.5.2 X-ray Generation and Monochromators 74
4.5.3 Peak Broadening 74
4.5.4 Binding Energy Shifts 75
4.5.5 HAXPES 76
4.5.6 Spin Orbit Splitting 77
4.5.7 Valence Band and Conduction Band Emission 78
4.5.8 Interaction Cross-sections 78
4.5.9 Probing Depth and Photon Energy 79
4.5.10 Auger Electrons 81

5 Ce doping of In_2O_3 **85**
5.1 Introduction 85
5.2 f-Block elements 85
5.2.1 Abundance 85
5.2.2 Oxidation States 87

5.2.3 Ionic Radii . . . 88
5.3 Novel Dopants in In_2O_3 . . . 88
5.3.1 Mo Doping of In_2O_3 . . . 89
5.3.2 Other Transition Metal dopants . . . 90
5.3.3 Ce Doping of In_2O_3 . . . 91
5.4 In_2O_3:Ce Thin Films . . . 91
5.4.1 Fabrication . . . 91
5.4.2 Electrical Properties . . . 92
5.4.3 Optical Properties . . . 92
5.5 Photo-emission . . . 94
5.5.1 Surveys . . . 94
5.5.2 Fermi Edge Calibration . . . 96
5.5.3 Carbon 1*s* calibration . . . 97
5.5.4 In and O Core Levels . . . 98
5.5.5 Ce Core Levels . . . 99
5.5.6 Doping Density Dependence . . . 102
5.5.7 Depth Dependence . . . 102
5.5.8 Conduction Band Emission . . . 104
5.5.9 Carrier Concentration Limit . . . 104
5.5.10 Defect Thermodynamics . . . 105
5.6 Origin of High Mobilities . . . 106
5.6.1 Fermi Level to VBM Separation . . . 107
5.6.2 Infra-Red Reflectivity . . . 107
5.6.3 Carrier Effective Mass . . . 108
5.7 Optical Gap . . . 109
5.8 Resonant Doping . . . 111
5.8.1 In_2O_3 Band Structure . . . 111
5.8.2 Partial Charge Density . . . 112
5.8.3 Impact on Carrier concentration . . . 112
5.9 Infra-Red Transparency . . . 115
5.10 Conclusion . . . 117

6 Ta doping of SnO_2 **119**
6.1 Introduction . . . 119
6.2 Potential Dopants in SnO_2 . . . 120
6.2.1 Vanadium . . . 120
6.2.2 Niobium . . . 120
6.2.3 Tantalum . . . 121
6.3 SnO_2:Ta and SnO_2:Sb thin films . . . 122

6.3.1 Fabrication 122
6.3.2 Electrical Properties 123
6.3.3 Optical Properties 124
6.4 X-ray Diffraction 125
6.4.1 Crystallinity 125
6.4.2 Orientation 126
6.5 Infra-Red Reflectivity 126
6.6 HAXPES 127
6.6.1 Surveys 128
6.6.2 Conduction Band Emission and midgap states 129
6.7 Resonant Doping 131
6.7.1 Valence Band to Fermi Level Separation 131
6.7.2 Valence Band Emission Fitted With Calculated DOS 133
6.7.3 Extracting Effective Mass 137
6.7.4 Orbital Energies 140
6.7.5 Calculated Band Structure 140
6.7.6 Partial Charge Densities 142
6.8 Defect Thermodynamics 142
6.9 Conclusion 144

7 Improved Infra-red Transparency and Impact for PV **147**
7.1 Introduction 147
7.2 Origin of Enhanced IR Transparency 148
7.2.1 Plasma Frequency, Effective Mass and Carrier Concentration 148
7.2.2 Scattering Times 149
7.2.3 Relating Scattering Limited Mobility to Plasma Frequency 152
7.3 Absorption 154
7.3.1 Free Carrier Absorption 154
7.4 Optical Modelling 156
7.4.1 Variable Dependencies 156
7.4.2 Modelling Results 158
7.5 Comparing TCOs for Photovoltaics 161
7.5.1 Figures of Merit 162
7.5.2 Defining Optical Suitability 163
7.5.3 Comparing Real Materials 164
7.5.4 Comparing Theoretical Materials 168
7.5.5 Discussion 171
7.6 Conclusion 173

8 Summary and Future Work **175**
8.1 Summary 175
8.2 Future Work 179

Bibliography **181**

List of Tables

Table **Page**

4.1 Exponent values for absorption Tauc plot 67
4.2 Area ratios for doublets for each orbital. 77

5.1 Properties of undoped and Ce doped In_2O_3 thin films studied in this work: Ce concentration determined from ICP-MS expressed as a percentage of the cation lattice sites, film thickness, t, sheet resistance, $R_{\square}$, resistivity, ρ, carrier concentration, n, and carrier mobility, μ. 92

6.1 Electrical properties of TaTO and ATO thin films 123

LIST OF FIGURES

FIGURE **Page**

1.1 Metal, semiconductor and insulator density of states. 4
1.2 Demonstration of n-type and p-type doping. 5
1.3 Example spectra for transmission (T), reflection (R) and absorption (A) of a TCO . . . 7
1.4 Demonstration of Moss-Burstein shift. 8
1.5 Spacial band diagram of a photovoltaic device 12
1.6 Solar Spectrum 13
1.7 The Shockley-Queisser Limit as a function of bandgap 15
1.8 Diagram of dimensions used for calculating power loss in the TCO layer of a solar cell 18

2.1 The band energies of common TCOs 20
2.2 Unit cells of common TCOs 22
2.3 Defect formation energy diagrams demonstrating the origins of Fermi level pinning . 27
2.4 Structure of graphene and diagram of Dirac cones 30

3.1 Schematic of the transfer matrix method 38
3.2 Different effective mass values as a function of carrier concentration 44
3.3 Fermi-Dirac distribution at $T = 0$ and $T > 0$ 49
3.4 Plots displaying the parabolic and α approximations 50
3.5 Interband absorption coefficient for a range of Fermi energies in In_2O_3 55

4.1 Schematic diagram of the Hall effect 64
4.2 Schematic diagram showing the van de Pauw geometry 65
4.3 Schematic diagram a Michelson interferometer 69
4.4 Diagram of Bragg diffraction. 70
4.5 Diagrams of standard XRD geometries. 71
4.6 Diagram of the experimental setup for XPS. 73
4.7 Comparison of Gaussian, Lorentzian and Voigt line shapes 76
4.8 Photo-ionisation cross-sections for In and O 80
4.9 Diagram showing characteristic and background electrons 80
4.10 The probing depth for XPS and the dependence on photon energy. 82

4.11 Diagram of Auger effect 83

5.1 The abundance of lanthanides in the Earth's crust 86
5.2 The sum of the first four ionisation potentials of the lanthanides 87
5.3 Review of mobility as a function of carrier concentration for a range of In_2O_3 based TCOs in the literature 89
5.4 Optical Spectra of ICO Thin Films 93
5.5 HAXPES and XPS survey of ICO sample. 95
5.6 Fermi function fitted to the Fermi edge in 3% ICO sample 96
5.7 Fitted C 1s XPS spectrum for ICO 1% sample 97
5.8 Fitted In 3d and O 1s XPS spectrum for ICO 1% sample 98
5.9 Fitted In 3d XPS spectra for ICO 2% and 3% samples 100
5.10 Fitted Ce 3d HAXPES spectra of ICO samples. 101
5.11 Percentage of HAXPES signal attribited to each Ce oxidation state for each ICO sample.102
5.12 [Fitted Ce 3d HAXPES and XPS spectra of the most heaviy doped ICO sample 103
5.13 HAXPES spectra of conduction band emission of ICO thin films 104
5.14 Ce doped In_2O_3 defect formation energy diagrams 106
5.15 Fermi level to VBM separation of the ICO samples. 108
5.16 Fermi level to VBM separation of the ICO samples. 109
5.17 Tauc plots extracting the optical gap for ICO sample 110
5.18 Diagram demonstrating resonant doping 112
5.19 Calculated band structures for Ce doped In_2O_3 113
5.20 Calculated CBM partical charge density for Ce doped In_2O_3 114
5.21 Calculated relationships between Fermi level and carrier concentration for different effective masses. 115
5.22 Comparison of transmission of ICO and ITO thin films 116

6.1 Energy level diagrams for VTO and NTO 121
6.2 Mobilities of TaTO and ATO thin films from this work and literature 124
6.3 Transmission spectra of ATO and TaTO thin films with comparable carrier concentrations 125
6.4 XRD Patterns for doped and undoped SnO_2 samples 126
6.5 Reflectivity spectra of doped SnO_2 samples 127
6.6 Reflectivity spectra of Ta and Sb doped SnO_2 samples with comparable carrier concentrations 128
6.7 HAXPES survey spectra for an Sb and an Ta doped SnO_2 samples. 129
6.8 HAXPES Spectra for conduction band emission of all SnO_2 samples 130
6.9 HAXPES Spectra for region containing Sn 3d peaks 131
6.10 HAXPES Spectra showing the Sn (II) mid-gap states present in SnO_2 132

6.11 HAXPES spectra showing the VBM to E_F separation for doped SnO_2 samples. 134
6.12 Valence band HAXPES spectra for ATO and TaTO fitted with calcualated density of states. 135
6.13 Orbitally resolved density of states for Ta and Sb doped SnO_2 136
6.14 HAXPES spectra and calculated DOS of semi-core levels in Ta doped SnO_2 137
6.15 Effective masses extracted from Fermi level to VBM separations for TaTO and ATO 138
6.16 Comparison of Fermi level effective mass and density of states averaged effective masses for TaTO and ATO 139
6.17 Orbital configuration energies of Sn, O, Ta and Sb 141
6.18 Calculated Band Structure and DOS for Ta doped SnO_2 143
6.19 The partial charge densities for TaTO, ATO and FTO at the CBM 143
6.20 Formation energies of Ta, Sb and F related species in SnO_2 as a function of Fermi level.144

7.1 Scattering limited mobilities for scattering mechanisms present in TCOs fro resonant dopants 150
7.2 Scattering limited mobilities for scattering mechanisms present in TCOs for non resonant dopants 151
7.3 Plasma frequency against carrier concentration based on scattering models. 152
7.4 Model for plasma frequency compared to experimental values 153
7.5 Free carrier absorption coefficient for a range of doped In_2O_3 155
7.6 Flow chart of property relationships in optical modelling 157
7.7 Modelled optical spectra for hypothetical In_2O_3 thin films with different effective masses159
7.8 Modelled optical gap and plasma frequency as a function of resistivity for different effective masses 160
7.9 The energy range over which modelled materials are transparent for different effective masses 161
7.10 Theoretical power density limits for a solar absrober with a band gap of 1.2 eV with ICO and ITO transparent electrodes 165
7.11 The optical suitability of ICO and ITO thin films as a function of absorber band gap . 167
7.12 Theoretical power density limits for a solar absrober with a band gap of 1.2 eV with In_2O_3 based transparent electrodes with different carrier effective masses 169
7.13 The optical suitability of modelled In_2O_3 thin films with different effective masses as a function of absorber band gap 170

Chapter 1

Introduction

1.1 Overview

In nature, the properties of transparency and conductivity rarely coexist. Transparency requires photons to pass through a material without being absorbed. This requires a gap in the energy bands of the material, a bandgap, greater than the energy that the photon possesses. Meanwhile, conductivity requires free charge carriers, electrons or holes, to carry charge throughout the material. For this to be the case, no bandgap, should be present, so that charge carriers can move freely through the unoccupied bands. Materials with very small bandgaps can be conductive if impurities or thermal excitations introduce carriers into the conduction band. A bandgap wide enough for transparency throughout the visible range, however, would be too wide for this to be the case. In addition to this, the high carrier concentration in most conductive materials makes them reflective causing further optical losses. Therefore, it is easy to see that these two properties can be expected to be mutually exclusive.

Despite this, transparent conductors are required for a wide range of modern technologies: touchscreens, light emitting diodes and solar panels all utilise them [4, 5]. There are a range of ways these properties are obtained but the most common is to use a range of materials based on wide bandgap, metal oxide, semiconductors called transparent conductive oxides (TCOs).

For transparency throughout the visible range a bandgap of at least 3 eV is required. A bandgap of this magnitude will result in an insulating material. To overcome this the material can be doped. Doping is the intentional introduction of impurities to introduce additional charge carriers into a material. With the introduction of enough carriers the Fermi level can be shifted towards, or into, the conduction or valence bands, depending on the type of carrier introduced, making the material conducting. A material in which the Fermi level has been moved into these

bands via doping is said to be 'degenerately doped'. Therefore, to create a transparent conductor a material of a suitable bandgap which is dopable to a degenerate level is required [6].

This principle was first demonstrated in 1907 by Bädeker who created the world's first TCO in the form of a CdO thin film deposited by sputtering Cd onto glass then allowing it to oxidise in air [7, 8]. While CdO based TCOs do still attract some interest among academic communities, its toxicity and the fact that it is highly hygroscopic means most interest in TCOs has since been focused else where, particularly when it comes to industrial applications [9].

Despite moving away from CdO, metal oxides proved to be the best candidates for transparent conductors due to their ideal bandgaps and being highly dopable. By 1971, the three main materials of interest had been established and their capabilities to be transparent conductors demonstrated [10]. These materials were ZnO, SnO_2 and In_2O_3. While all three of these materials have shown high conductivity while maintaining transparency as a result of decades of research, In_2O_3-based TCOs, usually doped with Sn, have displayed the lowest resistivities and as a result have dominated the commercial TCO market [11].

Reliance on In_2O_3-based TCOs presents an issue due to the scarcity of In within the Earth's crust. This scarcity, discussed in detail in section 2.2.4, means cost of In is both high and volatile. As a result a large amount of current TCO research is driven by the aim to find a cheap and Earth abundant replacement with comparable electrical properties, either through improving the conventional alternative, ZnO and SnO_2, or searching for new materials all together. This cost issue is already so significant, lower conductivity SnO_2-based alternatives are used for wide area application such as solar panels or low emissivity windows [12].

While a wide range of alternatives with competitive electrical properties have arisen over recent years, one property many have exhibited has been reduced infra-red transparency. Examples of such materials are Ag nanowire arrays [13] or transition metal oxide perovskites [14]. For many applications where only visible light it of concern this is not an issue. However, most solar panel technologies utilise light from near infra-red range. This means using a transparent conductor with reduced infra-red transparency will have a negative impact on the efficiency of the solar panel.

As wide area applications are the most in need of an alternative to In_2O_3 infra-red transparency needs to be considered in this search.As a result, replacement TCOs should meet the following three criteria: comparable conductivity to doped In_2O_3, consist of Earth abundant and cheap elements and high transparency over the visible and near infra-red ranges.

1.2 Conductivity in TCOs

1.2.1 Basics of Semiconductors

Transparent conductive oxides are a class of semiconductors. Therefore, semiconductor physics is core to understanding the physics of TCOs.

Each element has discrete energy levels, or orbitals, in which an electron can exist while bound to an atom. In a crystal the orbitals of the atoms overlap and therefore can not have the same energy due to the Pauli exclusion principle. As a result, the orbitals split into a large number of discrete orbitals, equal to the number of atoms with an orbital of that energy. These split orbitals are so close in energy to adjacent orbitals that they can be considered a continuous energy band. Some orbitals will be occupied by electrons and make up the valence band. Others are unoccupied and make up the conduction band [15].

The energy range covered by these bands is dependent on the material and the electronic structure of the elements in the lattice. In some cases the conduction bands and valence bands will overlap. Such materials are metals and their conductivity arises due to the electrons being able to freely move into the unoccupied states of the conduction band and move freely through the material.

In many cases the conduction and valence bands do not overlap. In most of these cases the material is an insulator as the electrons will be trapped in the fully occupied valence bands and unable to move. Semiconductors are an exception to this. In a semiconductor there is no overlap between the conduction and valence bands but the energetic gap between them, the bandgap, E_g, is very small. The bandgap required to class a material as a semiconductor rather than an insulator is not clear but it is generally considered to be one narrow enough for the population of the conduction bands through thermal excitations. This generally means a bandgap of a few eV.

Figure 1.1 shows a cartoon demonstration the difference in the density of states, DOS, of metal, semiconductors and insulators. The DOS of a material is the number of occupiable states as a function of energy. Figure 1.1 also shows the Fermi level, E_F. The Fermi level is the average energy of highest occupied state within the material. The Fermi levels shown is figure Figure 1.1 correspond to a temperature, T, of absolute zero, $T = 0$ K. In a metal the Fermi level will lie within the bands while in a semiconductor or insulator it will sit between the conduction and valence bands [16].

1.2.2 Doping

In an intrinsic semiconductor, a defect and impurity free periodic crystal, at T=0 K the Fermi level sits equidistant from the conduction band minimum, CBM, and the valence band maximum, VBM. However, real materials are rarely, if ever, truly intrinsic as defects will form during growth. These defects can be neutral or charged, either positively or negatively. A positively charged defect will contribute an additional electron raising the Fermi level. Such a defect is known as a donor. A negatively charged defect will remove an electron from the valence band contributing a hole. This lowers the Fermi level and such a defect is known as an acceptor [17].

The type of carriers introduced dictates whether the system is n-type of p-type. If electrons are added the system is considered n-type as the free carriers are negatively charged. If holes are added the system is p-type as the carriers are positively charged.

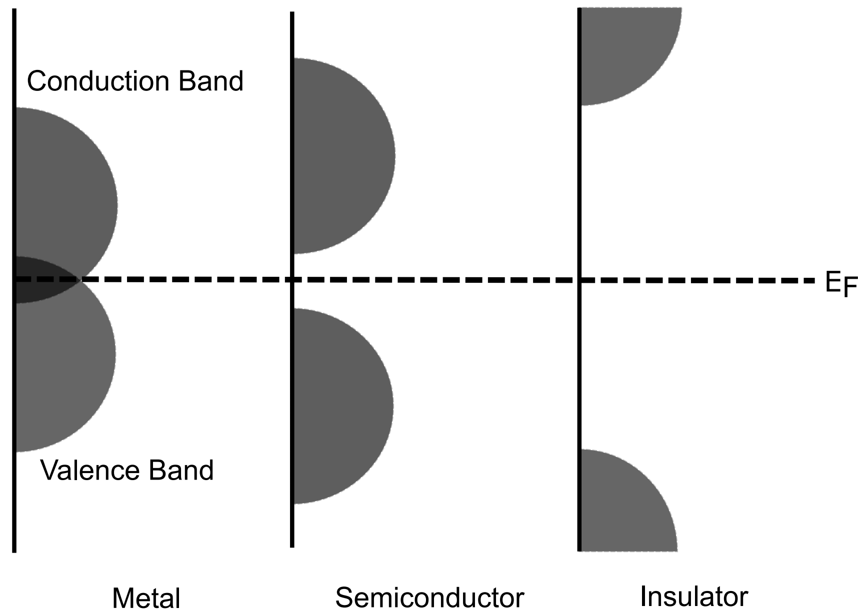

FIGURE 1.1. Cartoon of metal, semiconductor and insulator density of states. The conduction band states overlap in the metal but are separated by the bandgap in semiconductors and insulators. The Fermi level, E_F, is shown for each material.

Shifting the Fermi level of a material in this way is desirable for a wide range of applications including the creation of TCOs as addition of free carriers to the bands make the material more conductive [10]. To achieve this, donor or acceptor defects can be intentionally added to make the material n-type or p-type respectively. This is most commonly done by the addition of substitutional impurities which are atoms of a different element of a different oxidation state replacing an atom within the lattice. If the element has a higher oxidation state than the atom it is replacing it will have excess electrons that are not used in bonding and act as a donor. If it has an oxidation state lower than the atom it is replacing it will have to few electrons to use in bonding and will act as an acceptor. The addition of these substitutional impurities is doping. Figure 1.2 shows a diagram of a crystal lattice for an intrinsic, n-type and p-type doped semiconductors as well as DOS for the three cases. In a TCO the level of doping is at such that the Fermi level is within one of the bands, generally the conduction bands as most TCOs are n-type [17].

As charge carriers are removed from the dopant atoms, a charged ion is left at the lattice site. These ionised impurities will act as a scattering centre and will have a negative impact on carrier mobility and therefore conductivity [18].

1.2.3 Optimising Conductivity

The conductivity, σ, of a material is dependent on two properties of the material, the density of free charge carriers, n or p, and the free carrier mobility, μ. The expression for conductivity is

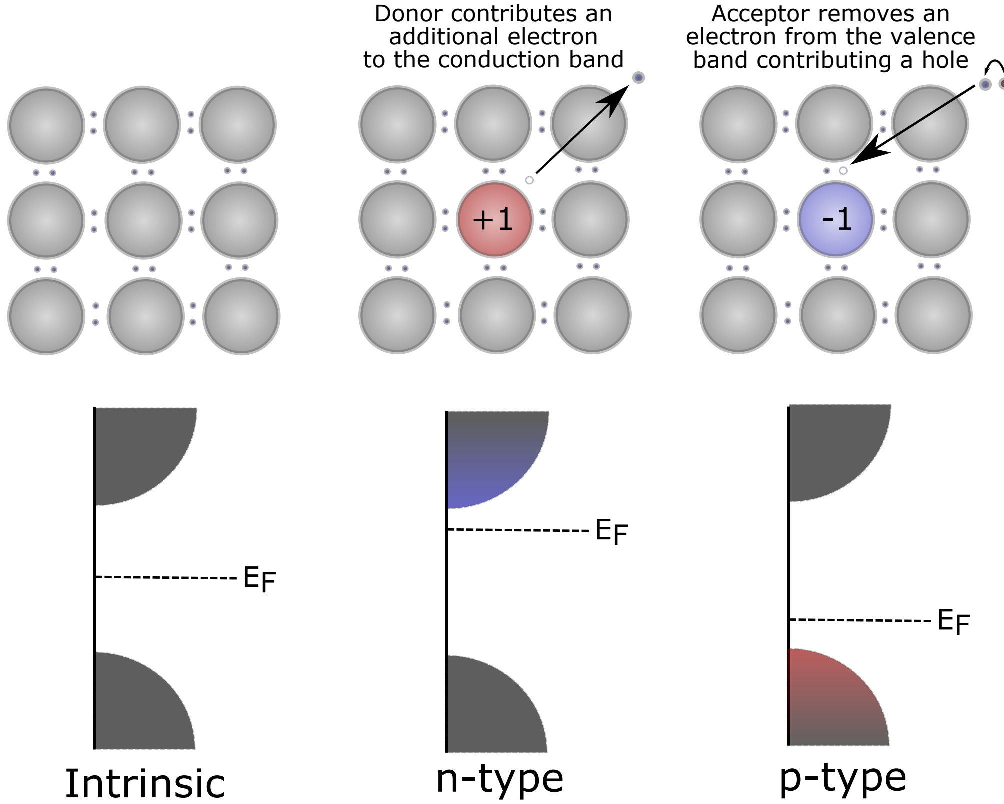

FIGURE 1.2. Cartoon of a simple crystal lattice showing that of an intrinsic semiconductor and demonstrating n-type and p-type doping. Below shows the density of states and the change in the position of the Fermi level for each case.

$$\sigma = (n\mu_e + p\mu_h)e \tag{1.1}$$

in which e is the charge on an electron, n and p are the concentration of electrons and holes respectively and μ_n and μ_h are the electron and hole mobilities. In most cases either n or p is orders of magnitude larger than the other meaning the smaller value can be ignored. As TCOs are primarily n-type, n will be much larger and p can be ignored [17].

As donor dopants are added they contribute additional electrons, therefore, increasing n. Equation 1.1 shows that higher n means higher σ. Therefore, it follows that the material should be as highly doped as possible to maximise σ. However, the carrier mobility is described by

$$\mu = \frac{e\tau}{m^*} \tag{1.2}$$

where τ is the carrier scattering time and m^* is the carrier effective mass. The scattering time is the average time a carrier travels for between two scattering events. As each donor is an ionised impurity and a scattering centre, τ will decrease with an increased donor density, N_D [19].

This results in a balancing act, the additional carriers introduced by aa dopant increases conductivity but scattering from the ionised impurities that are introduced decreases it. At low carrier concentrations the benefit of additional carriers significantly outweighs the negative impact of the ionised impurity scattering. At higher carrier concentrations this dichotomy shifts and the negative impact outweighs the positive. Finding the optimal doping density, the value of N_D at which this change occurs, for a material has always been at the forefront of TCO research.

When discussing TCOs it more common to report electrical properties in terms resistivity,ρ, rather than conductivity. ρ is simply equal to $1/\sigma$.

1.2.4 Sheet Resistance

When reporting the electrical properties of TCOs, it is common to report sheet resistance, $R_\square$, rather than conductivity or resistivity. The sheet resistance treats the thin film as a 2-dimensional sheet and describes the resistance felt by charges moving along the plane of the sheet. $R_\square$ is mathematically linked to the bulk resistivity by

$$R_\square = \frac{\rho}{t} \tag{1.3}$$

where t is the film thickness. From equation 1.3 the units of $R_\square$ can be extracted to be Ω. However a unit of $\Omega/\square$ is commonly used for reporting sheet resistance as a way to distinguish the quantity from bulk resistance [20].

1.3 Transparency in TCOs

When a photon enters a medium there are four possible ways that photon could interact with that medium: transmission, reflection , absorption and scattering. For a TCO transmission of as many photons as possible is desirable. Which of these interaction occurs varies over wavelength and energy. In a TCO there is a range of transparency with a high-energy cut off, usually in the ultra violet (UV) range, and a low energy cut off, usually in the near infra-red (IR) range.

Figure 1.3 shows an example of transmission, reflection and absorption spectra in a typical TCO. The region in which it is transparent is labelled as well as the dominating phenomena outside this region. These phenomena are explained in detail in the following sections.

1.3.1 High Energy Cut Off

The high energy cut off for transparency is due to absorption of photons and is at an energy equal to the bandgap of the material. If a photon entering the material has an energy greater than or equal to the bandgap of the material it can excite an electron from the valence band to the conduction band. These photons are absorbed. In this region interband absorption dominates

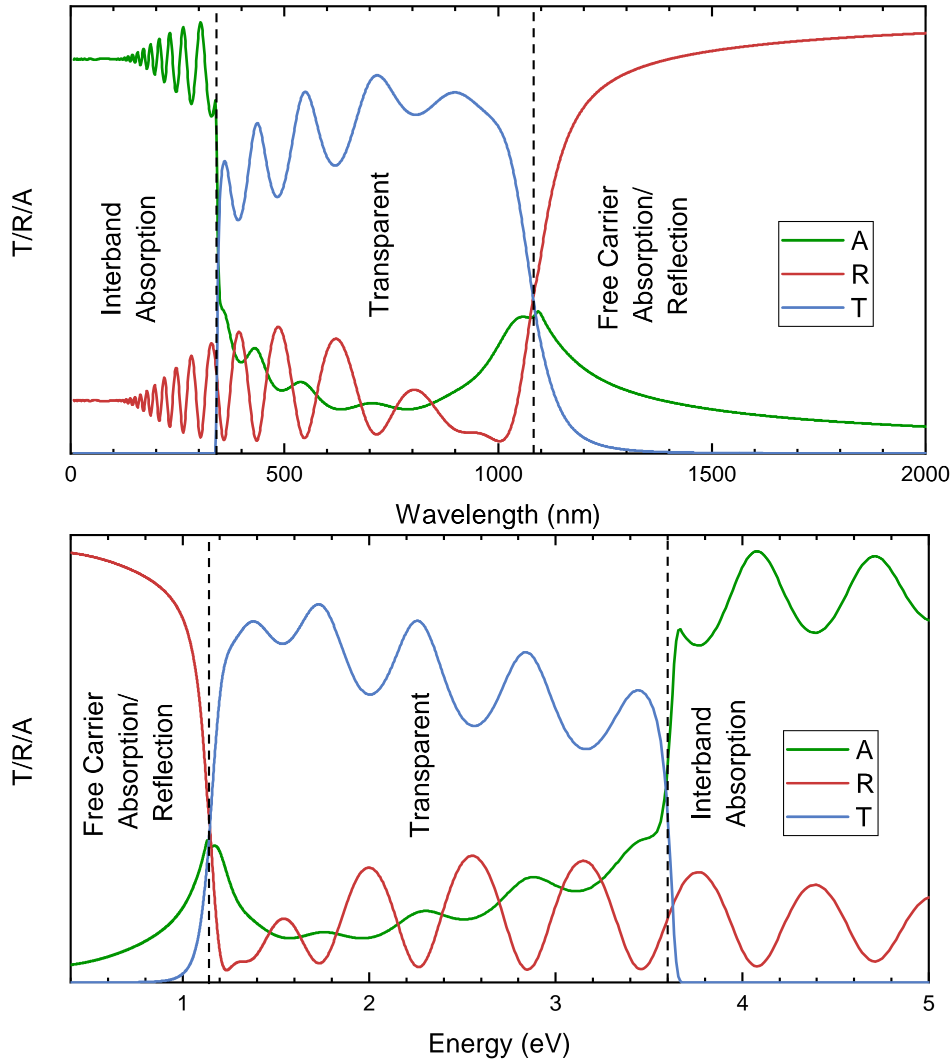

FIGURE 1.3. Example spectra for transmission (T), reflection (R) and absorption (A) of a typical TCO shown on both a wavelength and an energy scale. The spectrum is split into three regions, one where interband absorption dominates, one where the material is considered transparent and one where free carrier absorption and reflection dominate.

shown in figure 1.3. If a photon has an energy less than the bandgap of the material it will pass through without being absorbed and be transmitted. The material is transparent in this range.

Visible light has a wavelength range of 380-740 nm which is equivalent to an energy range of 3.0-1.6 eV. This mean a high energy cut off, and therefore bandgap, of greater than 3.0 eV is required for full transparency in the visible range [5].

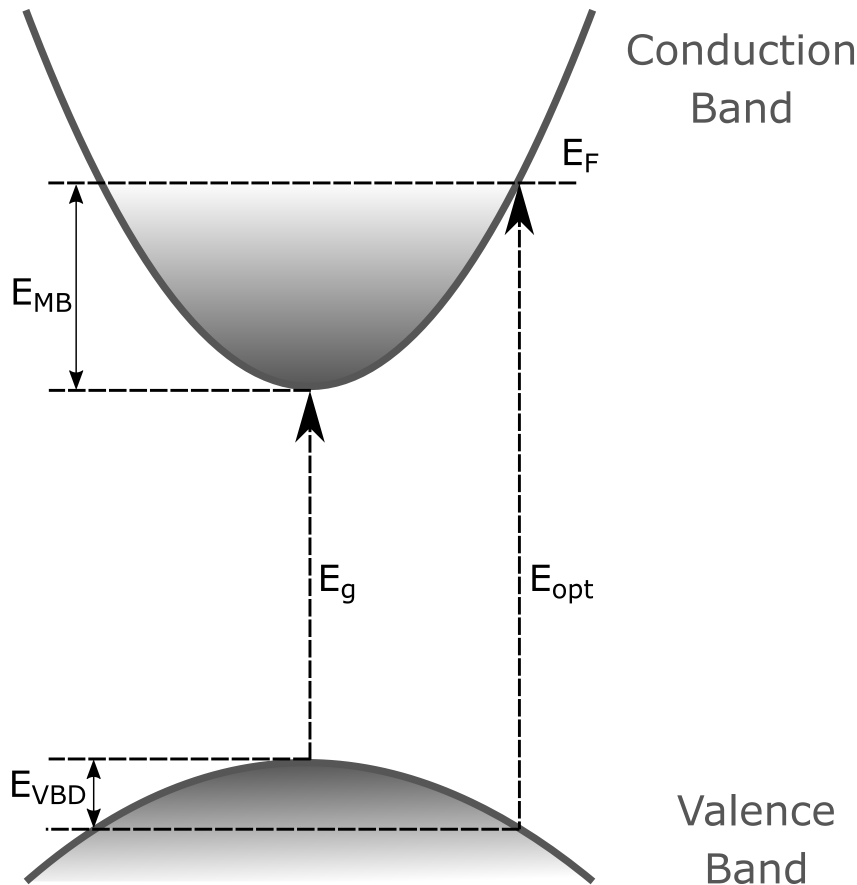

FIGURE 1.4. E vs k diagram demonstrating the difference between the electronic bandgap, E_g, and the optical bandgap, E_{opt}, of a material. The change due to Moss-Burstein shift, E_{MB}, and the change due to valence band dispersion, E_{VBD}, are also depicted.

1.3.2 Optical bandgap and the Moss-Burstein Effect

As a material is doped and extra electrons are introduced the Fermi level of the material increases. TCOs are degenerately doped meaning that enough electrons have been introduced that the Fermi level sits in the conduction band. In this case the states at the CBM and just above are occupied. This means that excitations can not occur from the valence band to the CBM and must instead occur to the Fermi level. This results in a change in the perceived bandgap as measured optically, referred to as the optical bandgap, E_{opt}. This change is called Moss-Burstein shift, named for those who originally observed it in InSb in 1954, and is equal to the difference between the CBM and the Fermi level [21, 22].

Band structures are usually displayed as Energy, E, versus the momentum vector, k. The optical bandgap also changes dependent on valence band dispersion. This because at the Fermi level in degenerately doped semiconductors there are no available states in the conduction band

at k=0. This means that excitations can only occur from states in the valence band at a k values at which conduction band states exist at the Fermi level. As this is away from the VBM, the state that the excitation occurs from will be at a lower energy and this will further increase the optical bandgap [23].

The optical bandgap can be describes as

$$E_{opt} = E_g + E_{MB} + E_{VBD} \tag{1.4}$$

in which E_{MB} is the the change in energy due to the Moss-Burstein effect and E_{VBD} is the change in energy due to valence band dispersion. The quantities are depicted on an E versus k diagram in Figure 1.4.

As a result of these effects E_{opt} is generally 0.3-0.6 eV higher that E_g dependent on the material and the level of doping. As a result, materials with bandgaps slightly smaller than 3.0 eV can be used as transparent conductors and still maintain transparency across the full visible range.

1.3.3 Bandgap Shrinkage

Beyond the factors presented in equation 1.4, another effect that has an impact on the optical gap in degenerately doped semiconductors is bandgap shrinkage. Due to interactions between the free electrons, or between the electrons and impurities within the system, the bandgap, E_g, is slightly reduced within degenerately doped regimes. As doping density increases the magnitude of bandgap shrinkage also increases. As such the increase in the optical gap due to Moss-Burstein shift

1.3.4 Low Energy Cut Off

At lower energies, loss of transparency occurs due to reflectivity and absorption. In a conductive material the free electrons oscillate collectively relative to the stationary atoms within the lattice. These oscillations have a set frequency called the plasma frequency, ω_p. If an photon incident on the material has an energy less than plasma frequency is will be reflected due to the electrons screening the electric field of the light. As a result the plasma frequency is the low energy cut off for transmission.

The plasma frequency is described by the expression

$$\omega_p = \sqrt{\frac{ne}{m^* \epsilon_\infty \epsilon_0}} \tag{1.5}$$

in which n is the electron density, e is the fundamental charge, m^* is the electron effective mass, ϵ_∞ is the high frequency dielectric constant and ϵ_0 is the permittivity of free space [24].

Note that ω_p is proportional to the $\sqrt{n}$; this means that the plasma frequency increases as the material is more heavily doped. As result the low energy cut off for transmission moves to higher energies as the material is doped. Generally for TCOs, the plasma frequency fall in the infra-red range, close to the red end of the visible range. This means that transmission at the low energy end of the visible range is maintained.

1.4 The Importance of Band Structure to TCOs

So far we have established that for a material to be suitable for use as a transparent conductor it needs a bandgap of at least 3.0 eV (or slightly below due to the Moss-Burstein effect). However this is not the only criteria, the band structure of the undoped material is also of importance.

1.4.1 Relation Between Band Dispersion and Conductivity

The shape of the CBM is of particular importance as it has an impact on electron mobility. Near the CBM the conduction band of a material can be approximated to be a parabola described by

$$E(k) = \frac{\hbar^2 k^2}{2m^*} \tag{1.6}$$

$\hbar$ is the reduced Planck's constant meaning the only variable to have an impact on the shape of the parabola is the electron effective mass. This means that a broader conduction band near the CBM means a higher electron effective mass [16].

The electron effective mass is linked to the to the electron mobility by

$$\mu = \frac{\tau e}{m^*} \tag{1.7}$$

where τ is the scattering time, the average time between electron scattering events. This expression means that a higher effective mass will reduce mobility. Therefore, a broader conduction band means lower mobility. Based on the relationship between mobility and conductivity shown in equation 1.1, this means that to maximise conductivity a material with as narrow conduction band as possible should be utilised. A narrow conduction band means a low density of states at the CBM.

1.4.2 Atomic Orbitals and Band Dispersion

An atomic orbital is a mathematical function that describes the wave like nature of the electrons it contains. It contains information on the region in which an electron can be found and the probability of finding an electron at any position. Orbitals are classified by their angular momentum quantum number, ℓ. For values of ℓ=0, 1, 2 and 3 the orbitals are referred to as s, p, d and f

orbitals respectively. For values of ℓ greater than 3 the labelling continues alphabetically from g but omitting j; however, these orbitals are rarely of importance.

Electron orbitals have a different shape and size dependent on their value of ℓ. As discussed in section 1.2.1 bands form due to overlapping orbitals from atoms within the crystal lattice. Dependent on this the degree to which orbitals within a lattice overlap will vary. Less overlap means a lower number of states and therefore a narrower band. Overlap generally increases with increasing ℓ. Therefore s orbitals will have the narrowest bands with the width increasing for p, d and f. A conduction band is generally made up of a mixture of many orbitals but generally one will dominate at the CBM.

As previously stated, to maximise electron mobility and therefore conductivity, a material with an as narrow as possible conduction band should be used and therefore a CBM dominated by an s orbital is preferable. This now gives the criteria for a transparent conductor as a material with a bandgap close to 3.0 eV and with dominant s orbital character at the CBM.

1.5 TCOs for Photovoltaics

Photovoltaics is one of the most common uses of TCOs and they can causes losses in a photovoltaic device, both optically and electrically. This section discusses the basics of photovoltaic devices and the impact the properties of a TCO can have upon the efficiency of a device.

1.5.1 Basics of Photovoltaics

The photovoltaic effect is the excitation of an electron to a higher energy state within a material through interaction with a photon. This varies from the photoelectric effect as in that case the charge carrier is excited to a higher energy state outside of the material, usually the vacuum level. Utilising this effect to capture the energy of photons is the basic principle of photovoltaic devices, however this effect alone is not enough to create a current as the excited carrier will just relax back into the valence band if no force is present to cause it to flow.

To generate a current, the excited charges need to be extracted from the material. To do this, a built in bias is introduced by creating a p-n junction. A p-n junction forms when a p-type and an n-type semiconductor are placed in contact with each other. When two semiconductors are in contact with one another their Fermi levels align. For this realignment to occur electrons diffuse across the junction from the n-type semiconductor to the p-type semiconductor. This diffusion does not carry on until the two semiconductors are in equilibrium, however, as a build up of charge either side of the junction prevents this. This build up of charges creates an electric field, the region covered by this field is known as the depletion region as it is almost fully free of mobile charge carriers. Any excited charge carriers generated within or near this region will feel the electric field causing them to flow. The current generated by this flow of charge is known as the drift current.

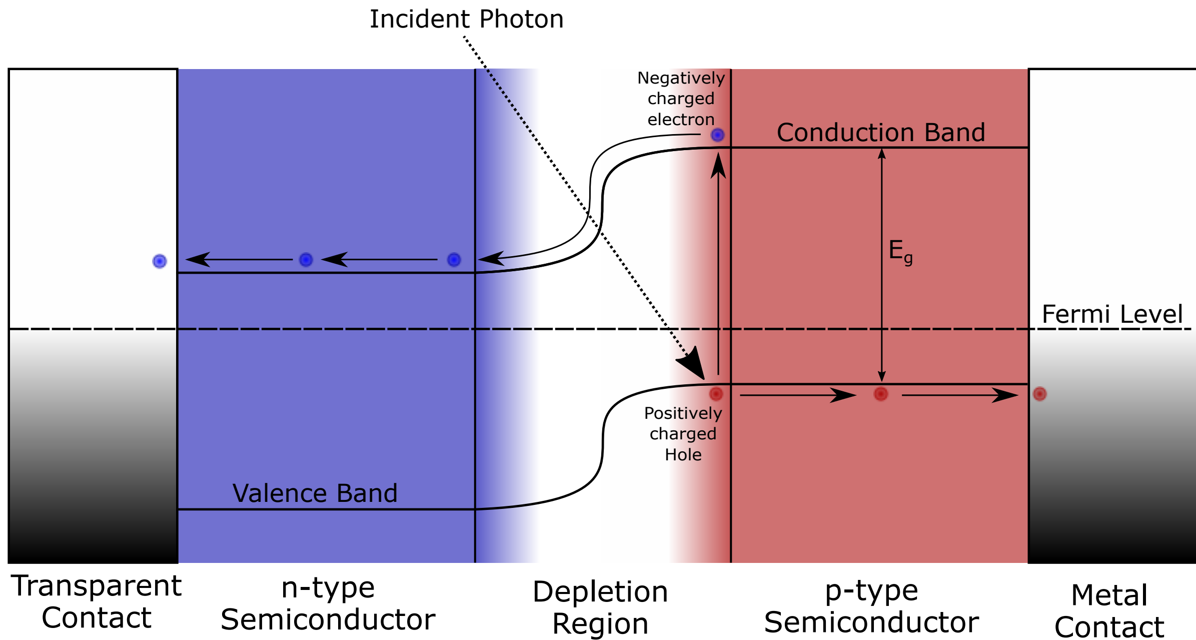

FIGURE 1.5. A spacial band diagram of a basic photovoltaic device in which the absorber is p-type. The movement of photo-generated charge carriers though the device is shown with electrons in blue and holes in red. The y-axis in the diagram is energy.

In a complete photovoltaic device, a photon enters the depletion region and interacts with an electron within the valence band of the device, exciting it into the conduction band. In the valence band a hole is generated where the electron is excited from. The electric field, or built in bias, causes the hole and electron to drift in opposite directions due to their opposite charges. Conductive contacts are placed on the exposed side of the two semiconductors to extract the charges to an external circuit, one of which needs to be transparent to allow photons to enter the device, this is where a TCO is utilised in many device structures. The semiconductor in contact with the transparent contact also needs to be very thin to allow the photons to reach the depletion region. This thinner layer is referred to as the window layer while the other thicker layer is called the absorber layer as most photons are absorbed within that layer.

Figure 1.5 shows a spacial band diagram for a basic photovoltaic device displaying the movement of photo-generated charge carriers through the structure. In the diagram the window layer is n-type and the absorber is p-type. While this is often the case the opposite is also possible. Most real devices also include additional layers beyond the four in shown Figure 1.5. These layers act to remove barriers at junction between the layers in the device [25].

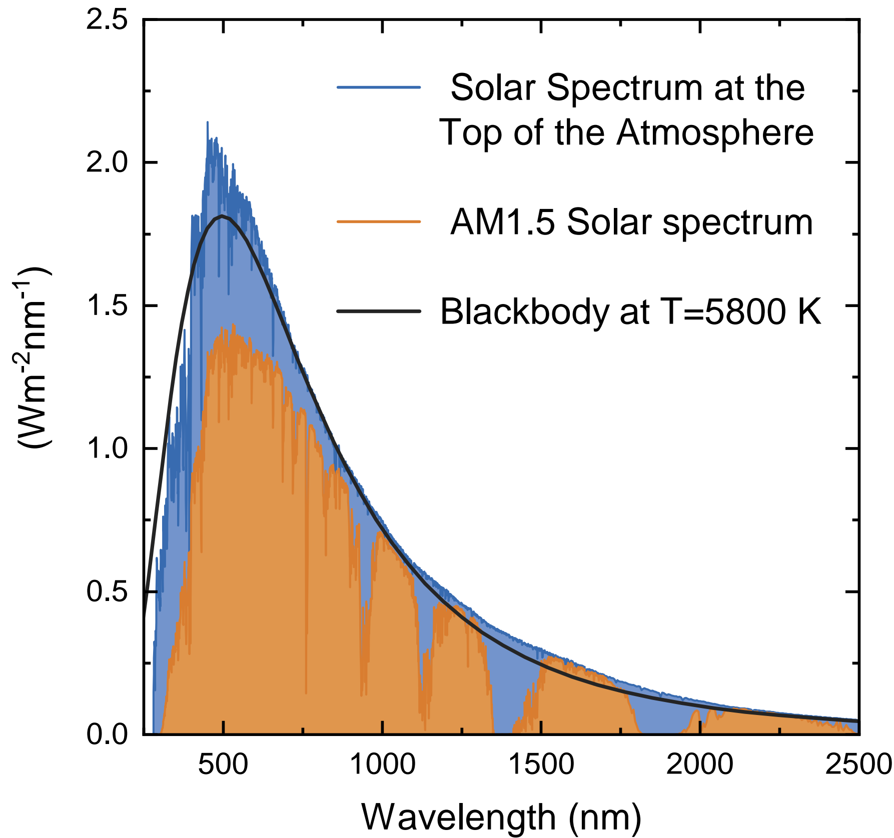

Figure 1.6: The irradiance of the solar spectrum at the top of the atmosphere (AM0) and after passing through an an air mass of 1.5 (AM1.5), representative of the solar irradiance at the majority of the Earth's population centres. The black line shows the spectral irradiance of a black body at a temperature of 5800 K which is often used as an approximation for the Sun's spectrum.[26, 27]

1.5.2 The AM 1.5 Spectrum

The efficiency of a photovoltaic device is measured with respect to its response to the solar spectrum as it reaches the surface of the Earth. Upon emission the solar spectrum closely matches that of a black body at a temperature of about 5800 K. However, once it has reached the Earth's surface some of the emitted light will be attenuated due to absorption and scattering by the chemicals making up the atmosphere.

Dependent on the latitude, the light will enter at different angles and will have a further or a shorter distance to travel through the atmosphere. The distance travelled is described by the air mass coefficient, AM. An AM of one is the distance travelled through atmosphere for light entering perpendicular to the Earth's surface at the zenith. To standardise measurements of photovoltaic efficiency, the spectrum for an AM of 1.5 was chosen. The AM1.5 spectrum was chosen as it is the AM coefficient for for an angle of entry of 48.2° which is representative of the

average angle of entry for light travelling to the majority of the Earth's Major population centres.

Figure 1.6 shows the spectra for AM1.5 as well as the solar spectrum at the top of the atmosphere and a black body at a temperature of 5800 K. The peak irradiance for all of these spectra is at a wavelength of around 550 nm. This wavelength is also the peak for sensitivity of the human eye, an evolutionary response to the solar spectrum. As a result, the transmission of materials is often quoted at 550 nm. While such a measurement is suitable for applications where the response of the human eye is important, such as touch screens or windows, it is not suitable for photovoltaic applications as a much wider range of the spectrum is utilised.

1.5.3 The Shockley-Queisser Limit

The efficiency of a photovoltaic device utilising a single p-n junction is inherently limited. This limit is known as the Shockley-Queisser limit named for those who initially proposed it. For the AM1.5 spectrum this limit is 33.7% [28, 29].

While several factors contribute to the limit, the one with the biggest impact is spectral losses due to the bandgap of the absorber material. Photons can be split into two regimes, those with energy less than the absorber's bandgap, E_g and those with energy greater than E_g. When a photon has an energy less than E_g it will be unable to excite an electron from the valence band to the conduction band. Therefore, no photons with energies within this regime are absorbed and no power is generated.

In the case where a photon has energy greater than or equal to E_g the photon will be absorbed and an electron will be excited into the conduction band. However, not all of that photon's energy can be extracted. Any energy the photon has above E_g will be lost as the electron will thermalise into the conduction band and the energy will be lost as heat. The fraction of energy absorbed for a photon of frequency, ν, is described mathematically for the two regimes in equations 1.8 and 1.9.

$$h\nu < E_g, \quad \alpha = 0 \tag{1.8}$$

$$h\nu \geq E_g, \quad \alpha = \frac{E_g}{h\nu} \tag{1.9}$$

This phenomena alone limits the maximum efficiency of a single junction solar cell to around 48%. When other factors such as impedance matching and recombination are accounted for this number falls to the previously mentioned 33.7%.

Due to the bandgap dependence of the regimes described in equations 1.8 and 1.9, this limit is also bandgap dependent. 33.7% is only the limit for the optimal bandgap of 1.34 eV, bandgaps greater or less than this have a lower limit. Figure 1.7 shows the maximum conversion efficiency of a single junction solar cell as a function of E_g. The range of bandgaps where the highest efficiencies can be achieved is between ~1.1 - 1.6 eV [30–33]. The entirety of this range falls

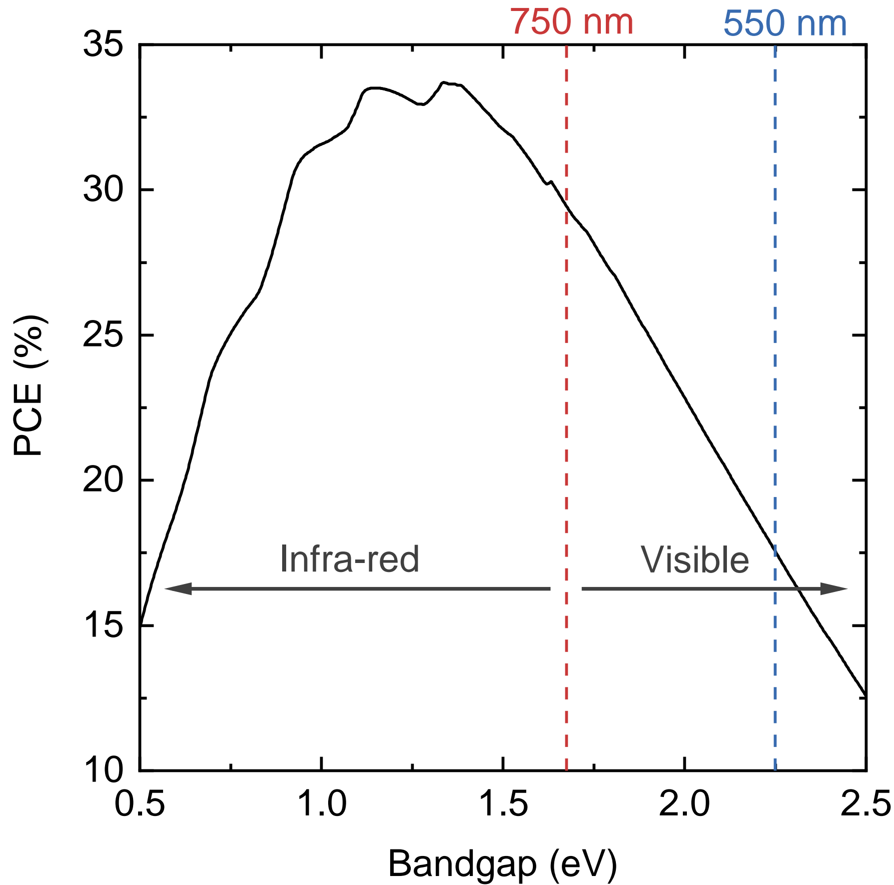

Figure 1.7: The maximum photovoltaic conversion efficiency as a function of bandgap for a single junction solar cell. Dashed lines are shown for wavelengths of 750 nm, the onset of infra-red light, and 550 nm, the peak of the solar spectrum.

within the infra-red range for light meaning for a solar absorber to reach the maximum potential efficiency infra-red light must be utilised.

Thus, for photovoltaic applications, ideally a TCO should be as transparent as possible at all energies above the band gap of absorber as any photon absorbed or reflected by the TCO will not be absorbed by the photovoltaic absorber and the efficiency of the device will be reduced. As for ideal absorbers E_g falls within the infra-red range, transparency in that range is required in that range from a TCO to maximise efficiency. Even for the largest bandgaps in this range, some of the infra-red region is utilised.

1.5.4 Resistive Losses in Solar Cells

The Shockley-Queisser limits relies on a range of assumptions. Main among them is that all photo-generated charges are extracted from the device. In real devices this is not the case as there are resistive losses throughout the device. Losses are attributed to two resistances in a

device, the shunt resistance, R_{SH}, and the series resistance, R_S.

Ideally the shunt resistance should be as high as possible as it describes the resistance of alternative current paths for the photo-generated current. If a low resistance path is available a proportion of the electrons will take it instead of travelling across the p-n junction reducing current in the device. This generally occurs in devices with poor coverage of a layer as the layers either side touch, providing an alternative path.

Series resistance is the resistance of the interfaces and individual layers making up the device. The series resistance is the sum of the resistance of each individual layer. Electrical losses within a TCO contribute to the series resistance [25].

1.5.5 Transparent Electrodes and Busbars

In silicon based solar cells, the most developed photovoltaic technology, TCOs are not generally used. Instead, charges are extracted from the device by a series of metal strips called 'fingers' on the surface of the silicon. These strips carry the charge to larger metal strips called 'busbars'. This works for silicon because the resistivity of silicon is relatively low so that the metallic strips can be placed at such a distance that the loss due to shading is less than optical losses in a TCO [34].

Newer generations of photovoltaic devices utilise compound semiconductors such as copper indium gallium sulphide, CIGS, or cadmium telluride, CdTe. These layers, and the window layers they are paired with, are much more resistive. This means that the fingers would have to be much closer together and shade much more of the device to effectively collect the photo-generated charges. In these cases a TCO is used. As in this case the transparent electrode covers the entire surface of the device, charges only need to travel perpendicular to the plane of the surface to reach it.

The resistivity of most TCOs is still much higher than that of most metals. Busbars are therefore still used for these technologies but their spacing is much greater than would be possible without the TCO. The purpose of the TCO is therefore to transport the charge carriers in the plane of the surface to the busbars. As it is the movement of charge in the plane of the surface that matters, the sheet resistance is the value of importance. The lower the sheet resistance of the TCO, the further apart the busbars can be spaced, meaning shading can be further reduced.

Optimisation of the spacing of busbars and fingers is a complex balancing act of resistive losses in the TCO or window layer, resistive losses in the fingers as narrow fingers mean not insignificant losses and shading from the fingers and busbars [35].

1.5.6 Power Loss in the TCO Layer

Reduction in efficiency of a solar cell due to the TCO comes in two forms, optical and electrical. Optical losses occur as incident photons are not transmitted through the TCO and therefore not reaching the absorber. Electrical losses are due to the resistance of the TCO.

Figure 1.8 shows a diagram of the top surface of a solar cell utilising a TCO and metal front contacts displaying each of the parameters used in calculating P_{loss}. Photo-generated current will be generated at a distance, y, from a metallic contact. The current will travel this distance through the TCO in the plane parallel to the surface. In a 2-dimensional plane the incremental power loss over a section of width dy can be described

$$dP_{Loss} = I^2 dR \tag{1.10}$$

where I is the current and dR is the differential resistance across the region. dR is dependent on the width of the section decreases with the length, l, of the section. It is described by

$$dR = \frac{R_{\square}}{l} dy \tag{1.11}$$

The current is also dependent on the distance from the metal contact and is given by

$$I(y) = Jly \tag{1.12}$$

where J is the current density, the current generated per unit area.

The total power loss across a section of width dy and length l is given by

$$P_{loss} = \int I(y)^2 dR \tag{1.13}$$

The maximum distance between a contact and the point where photo generatated can be generated if half the contact separation, $S/2$. As a result the limits on y should be 0 and $S/2$. Using these limits and inserting equations 1.11 and 1.12 into equation 1.13 gives

$$P_{loss} = \int_0^{S/2} \frac{J^2 l^2 y^2 R_{\square}}{l} dy = \frac{J^2 l R_{\square} S^3}{24} \tag{1.14}$$

For simplicity the length of a the metallic finger contacts can be used as l making equation 1.14 the equation for the power loss over an area of $A = Sl/2$. The surface power loss density, Pd_{loss} is therefore P_{loss}/A which gives

$$Pd_{loss} = \frac{J R_{\square} S^2}{12} \tag{1.15}$$

It is of note that for a solar cell generating the same photo-generated current and utilising the same spacing for metallic contacts and busbars the power loss in the TCO is purely dependent on the sheet resistance.

This derivation focuses on a basic grid lay out of finger contacts. Other contact geometries can more efficiently balance contact separation and shading but actual solar panels tend to utilise the geometry used in this derivation for simplicity.

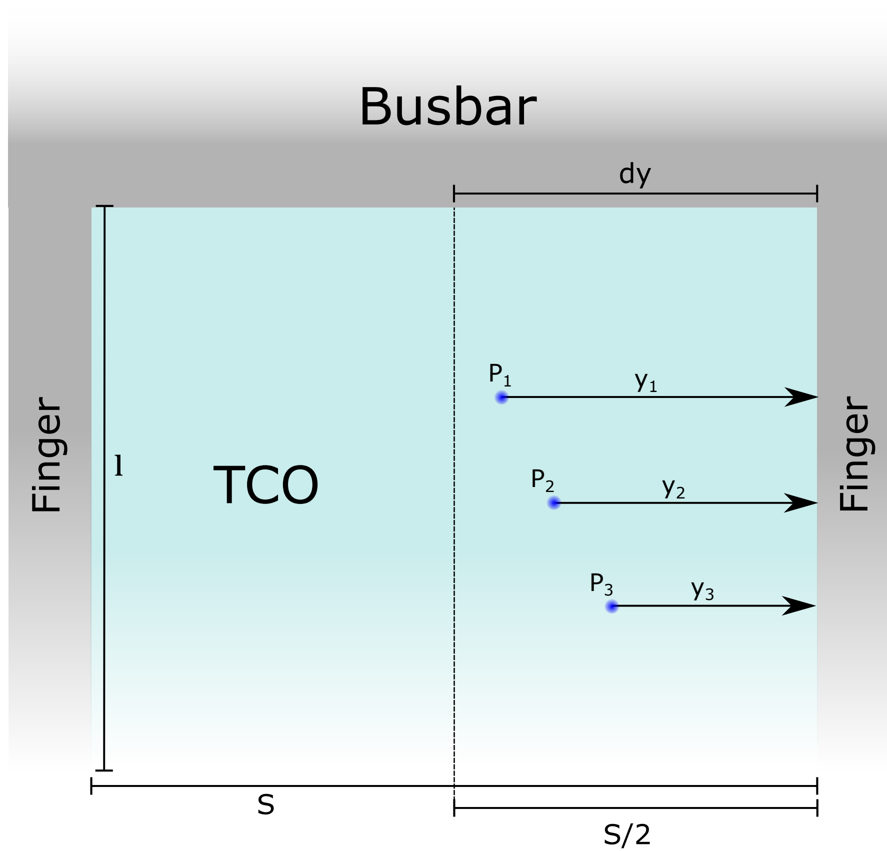

FIGURE 1.8. A diagram showing the dimensions required for calculating the power loss in the front contact of a solar cell. P_x show demonstration of positions at which photo-generated charge could generate at y_x show the corresponding y. In reality all possible y values within the width dy must be integrated over.

CHAPTER 2

TRANSPARENT CONDUCTORS LITERATURE REVIEW

2.1 Introduction

In the slightly more than a century since the principles of TCOs were first demonstrated thousand of research papers on their optimisation and underlying physics have been published. The majority of these papers focus on a small handful of materials which are well established to display transparent and conductive properties. These most heavily researched materials appear to have already reached their maximum potential so much recent research has been focused on finding alternatives which can surpass them or new ways to break through this perceived barrier. Meanwhile much research is performed into finding a p-type transparent conductor with properties comparable to those seen in n-types. While potential candidates have been identified their properties still fall short.

2.2 Common TCOs

2.2.1 Host materials

Throughout chapter 1 criteria for an ideal host material for an n-type TCO were identified and presented. These criteria were a band gap close to 3 eV to allow for transparency and a narrow conduction band at the CBM so that the free carriers would have a low effective mass allowing for high carrier mobilities.

A wide range of material fit the first criteria of a band gap wide enough for transparency but most lack the low electron effective mass. Three materials which closely meet both criteria are the post-transition metal oxides, ZnO, SnO_2 and In_2O_3. Each of these have CBMs dominated by the metal *s* states which means a low density of states and a low electron effective mass while

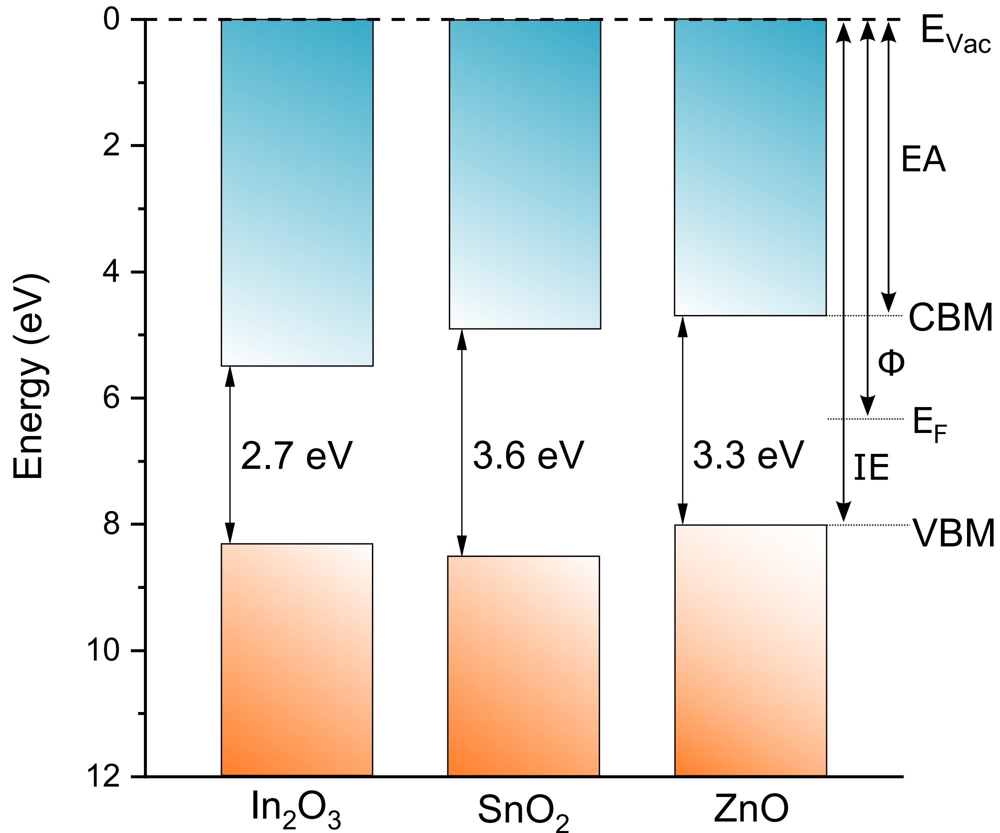

Figure 2.1: Energies of the VBM and CBM of In_2O_3, SnO_2 and ZnO relative to the vacuum level with the band gaps labelled [36–38]. The definitions of Ionisation energy, IE, work function, ϕ, and Electron Affinity, EA, are also shown.

having a band gap around 3 eV. The band energies of each of these materials and their band gaps are shown in Figure 2.1

2.2.2 Dopant Selection

For n-type doping the most important property of a dopant is that it incorporates into the host in an oxidation state greater than that of the element it is replacing. Second to this an element of similar atomic size to the host element is desirable as it will minimise lattice strain which can impact mobility [39].

The combination of these two requirements gives an obvious choice of dopant of the element directly to the right of the host element in the periodic table. Such elements should be readily available in an oxidation state one greater than the host element and be similar in atomic size. As ZnO, SnO_2 and In_2O_3 are all oxides the anion in all three materials is oxygen. Therefore the obvious dopant for anion doping of all of these materials is fluorine. Following the same rules for cation doping the dopant of choice is gallium in ZnO (Although aluminium is also often used as

discussed in more detail in section 2.2.6), antimony in SnO_2 and tin in In_2O_3.

Based on this assumption the majority of work on TCOs focuses on these dopants.

2.2.3 Multi-electron Donors

The difference between the oxidation states of a dopant and the host atom it is replacing will be number of electrons each dopant atom donates. Therefore, by choosing a dopant with a greater difference in oxidation state a higher carrier concentration can be achieved for the same doping density. This means a higher carrier concentration with a reduced number of ionised impurities acting as scattering centres which should mean higher conductivities. However, this is not the case as the ionised impurities will have a greater charge, Z, and increase scattering as the charge on the impurity is equal to the number of electrons removed which is the ratio of the carrier concentration, n and impurity density, N_i.

$$Z = \frac{n}{N_i} \tag{2.1}$$

For a single electron donor, with an oxidation state one greater than the element it is replacing, Z would therefore be 1 as the ratio of electrons to impurities is one to one. Z would increase with greater difference in the oxidation state as more electrons are donated and that ratio increases. Assuming that all of the dopant atoms donate the same number of electrons Z will be an integer equal to the number of electrons each dopant donates.

The mobility of charge carriers in a system is dictated by scattering mechanisms. Scattering mechanisms in TCOs are discussed in detail in section 3.7.In that section it is shown that the mobility of a carrier in a system where ionised impurity scattering dominates, such as TCOs, is related to carrier concentration, n, the average charge of an impurity, Z, and impurity density N_i by

$$\mu \propto \frac{n}{Z^2 N_i} \tag{2.2}$$

Combining equations 2.1 and 2.2 shows that mobility is proportional to $1/Z$ which is equal to the the inverse of the number of electrons donated per donor atom.

$$\mu \propto \frac{1}{Z} \tag{2.3}$$

Equation 1.1 states that conductivity is proportional to the product of the mobility and carrier concentration. As n is proportional to Z and μ is inversely proportional to Z, any impact from the increases carrier concentration will be cancelled out by a proportional decrease in mobility. As such no net impact on conductivity can be expected. Multi-electron dopants are also likely to have a greater difference in atomic size to the host element and are therefore will likely be detrimental compared to their single-electron donor counterparts.

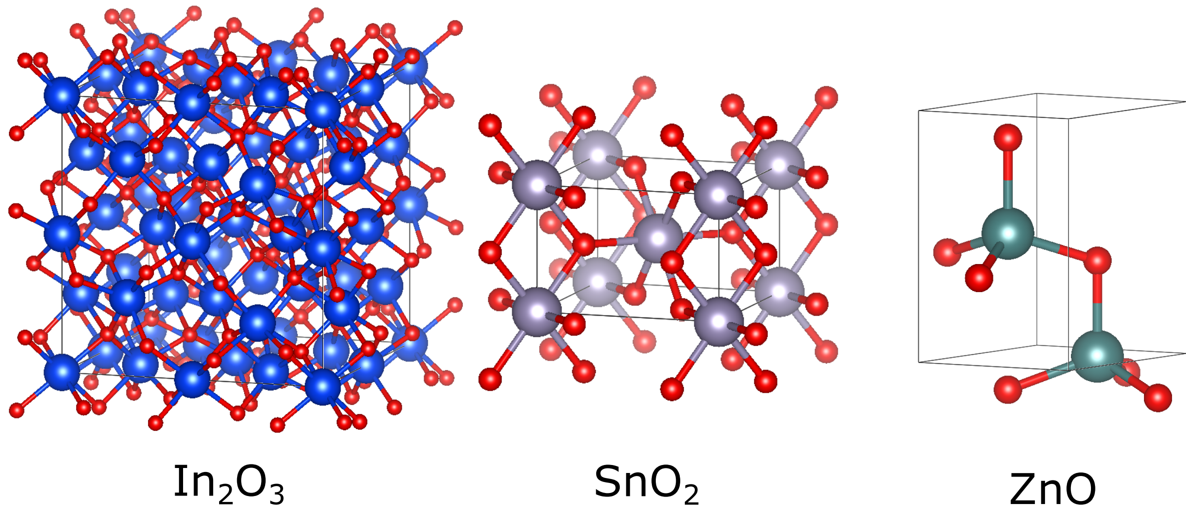

Figure 2.2: The unit cells of In_2O_3 [40], SnO_2 [41] and ZnO [42]. In each case the O sites are shown smaller and in red. The unit cells shown for In_2O_3 and ZnO are the bixbyite and wurtzite crytsal structures respectively, the most commonly utilised forms of each material.

2.2.4 In_2O_3-based TCOs

Of the common TCOs, In_2O_3 has been the most successful, from experimental and commercial standpoints. Of the two obvious candidates for dopants, Sn and F, Sn doping of In_2O_3 has displayed the best electrical properties, not just for In_2O_3 based TCOs but TCOs generally.

In_2O_3 exists in two crystalline phases, cubic bixbyite [43] and rhomboidal corundum [44]. Of these phases, bixbyite is the most stable and is the structure commonly seen in In_2O_3 thin films used for transparent conductors [45–47]. The unit cell of the cubic phase of In_2O_3 is shown in Figure 2.2. The large unit cell of the bixbyite crystal structure is a result of it having two different cation sites. In In_2O_3, In sits on these sites, the Wyckoff sites 8b and 24d. Both have a coordination number of 6. Dopants will have a preference on which site they incorporate, but in most cases it can be expected to have little impact due to their identical coordination numbers.

The electronic band gap on In_2O_3 is recently been revised to be around 2.7–2.9 eV [48, 49]. Older literature reports the band gap to be closer to 3.7 eV, even some more recent work occasionally reports this value. This discrepancy is due to the transition from the VBM to CBM being forbidden by parity [48]. An allowed transition exists from a state around 0.8 eV below the VBM. As a result, optical measurements observe this transition rather than the electronic band gap resulting in the overestimation in older publications. This also means that photons require energy equal to the larger transition to be absorbed and therefore In_2O_3 is transparent up to an energy of 3.7 eV. Figure 2.1 shows the energy bands of In_2O_3 along side those for SnO_2 and ZnO.

Sn doped In_2O_3 (ITO) has regularly been shown to display resistivities as low as 8×10^{-5} Ωcm as a result of carrier concentrations of up to 1.2×10^{21} cm^{-3} while maintaining mobilities of around 50 cm^{2}V^{-1}s^{-1} [11]. Such carrier concentrations are not regularly seen in any none In_2O_3

based TCOs and mobilities as high are only seen at significantly lower carrier concentrations.

F doping of In_2O_3 (IFO) has also been investigated but with less success. Record resistivities of around 3×10^{-4} Ωcm have been achieved while maintaining high transparency [50, 51]. The higher resistivity seen in IFO compared to ITO appears to be due to the carrier concentrations obtained being lower rather than lower mobilities. Measured F concentrations has been measured to be three times higher than carrier concentrations in IFO films and it has thus been inferred that over certain concentrations fluorine incorporates as an acceptor defect in In_2O_3 [52]. A similar phenomena has been observed in F-doped SnO_2 which is better understood and discussed in greater detail in section 2.2.5.

Issues arise from the elemental composition of In_2O_3 as In is relatively rare within the earth's crust. The abundance of In in the Earth's crust is estimated to be roughly 0.1 ppm. For comparison, the alternatives Sn and Zn have abundances of 2.2 and 75 ppm respectively [53].The annual production of In is also orders of magnitude lower than that of the alternative materials. The result is an expensive and highly price volatile material.

For small area applications, such as touch screens, this is not a major issue as the price per unit area for the rest of the device will significantly outweigh that of the ITO. This is not the case for photovoltaic applications, as the cost of the other layers in PV devices has drastically fallen over recent years utilising ITO would be relatively costly and prohibitive to wide spread technological implementation. As such, ITO is often used in devices fabricated in labs with the aim of achieving as high efficiency as possible but in commercial panels cheaper alternatives are utilised [54].

2.2.5 SnO_2-based TCOs

For wide area applications, SnO_2-based TCOs have often been the material of choice. SnO_2 is often easily deposited by chemical vapour deposition in-line during glass manufacturing making SnO_2 coated glass incredibly cost effective. F is easily added in this process as a dopant to create transparent conducting FTO. As a result, SnO_2 based TCOs are of particular interest to industrial researchers focused on commercialisation. FTO is already widely used in large are solar installations as a transparent contact.

SnO_2 has the largest bandgap of the three materials at 3.6 eV, as shown in Figure 2.1 [38]. Figure 2.2 shows the rutile unit cell of SnO_2, its only stable crystal structure [55]. Its unit cell is much smaller and much simpler than In_2O_3 with Sn sitting on only one Wyckoff site. In theory, this simpler structure should make understanding of dopant behaviour in SnO_2 simpler than in In_2O_3.

Of the two standard n-type dopants in SnO_2, F has been the most successful. However, while fluorine doped SnO_2 (FTO) regularly displays resistivities below 5×10^{-4} Ωcm, it still falls significantly short of ITO in terms of electrical properties [56]. The higher resistivity is due to FTOs inability to surpass mobilities of 35 $cm^2V^{-1}s^{-1}$ at carrier concentrations of $> 3\times10^{20}$ cm^{-3}.

Even with lower mobilities, carrier concentrations higher than around 4×10^{20} cm^{-3} have been rarely reported in FTO [57].

Understanding of what limits the electrical properties of FTO was of debate until recently when the presence of interstitial fluorine was identified as the cause. The presence of interstitial fluorine in FTO at high doping densities has been know for a some time [58–60] but recent studies have confirmed it as the limiting factor [56]. Density functional theory (DFT) calculations paired with experimental results from Hall effect measurements and x-ray photo-electron spectroscopy (XPS) confirmed that for Fermi energies 0.5 eV or more above the CBM it is energetically favourable for F to incorporate as interstitial defects. In this form, F acts as an acceptor rather than a donor. This effectively pins the Fermi level, preventing the addition of further carriers while still introducing more ionised impurities which, acting as scattering centres, reduce carrier mobility. This means that it is unlikely that any further improvements to the electrical FTO will be made and an alternative dopant will be required if SnO_2 is to ever compete with In_2O_3.

SnO_2 doped with the other obvious choice of dopant, Sb, generally displays higher resistivities than FTO. While Sb-doped SnO_2 (ATO) has been shown to achieve slightly higher carrier concentrations of up to 6×10^{20} cm^{-3}, it suffers from lower mobilities. ATO generally displayes mobilities of 20 $cm^2V^{-1}s^{-1}$ or below for carrier concentrations of greater than 1×10^{20} cm^{-3}. As a result, the lowest resitivities achieved in ITO are around 5×10^{-4} Ωcm. The limitation on ATO has been identified to be the multi-valency of Sb which incorporates as both Sb (III) and Sb (V) as both oxidation states have been observed is Mössbauer spectroscopy and in XPS studies [61–64]. Sb (V) is the desirable oxidation state as is acts as an donor when substitutional on a Sn site while Sb (III) will act as acceptor reducing the carrier concentration.

With these limitations it seems unlikely that FTO or ATO will achieve electrical properties comparable to those seen in ITO and if SnO_2 is to replace In_2O_3 a different approach will be required.

2.2.6 ZnO-based TCOs

As shown in Figure 2.1, ZnO has a band gap of around 3.3 eV, ideal for TCO applications. As with In_2O_3, ZnO is stable in two crystalline structures, in this case hexagonal wurtzite and cubic zincblende. Of the two, it displays a preference to crystallise in the wurtzite structure for which the unit cell is shown in Figure 2.2.

The majority of work looking into ZnO-based TCOs has focused on cation doping on the Zn site. Investigations into F doped ZnO (FZO) have only yielded resitivities greater than 2×10^{-3} Ωcm, an order of magnitude greater than those seen in SnO_2 and In_2O_3-based TCOs [65, 66].

Following the rule of choosing the element to the right of the host on the periodic table, Ga is obvious choice for doping on the Zn site. However, as much work has been invested in Al-doped ZnO (AZO) as Ga-doped ZnO (GZO). The lowest resistivities reported for both AZO and GZO are around 1.5×10^{-4} Ωcm, a slight improvement compared to those those achieved in FTO but

still higher than ITO [67, 68]. This arises due to high carrier concentrations of $>1\times10^{21}$ but with comparable mobilities to those seen in FTO, generally <40 cm^{2}V^{-1}s^{-1}.

One property of ZnO based TCOs that limit their potential applications is their low thermal stability. When heated above around 200–300 °C (dependant on doping density), increases in resistivity of several orders of magnitude have been observed in AZO and GZO [69]. As a result incorporation into any stacks where later layers require high temperature depositions is not possible.

Zn is significantly more abundant in the Earth's crust than either In or Sn at around 75 ppm [53]. As a result, for applications where its low thermal stability is not an issue, utilising ZnO based TCOs would be the most sustainable and lowest cost option of the three.

2.2.7 Indium Gallium Zinc Oxide

One commonly used metal oxide based transparent conductor is indium gallium zinc oxide (IGZO). This differs from the previously discussed materials as it is amorphous, has no long range, recurring crystalline structure. In recent years IGZO has been commonly used for touch screen devices such as tablets or phones. The use of an amorphous material such as IGZO provides the benefit that it can be used in applications where flexibility is required and they can generally be deposited at low temperatures.

Generally it is expected that amorphous material will display lower carrier mobilities than their crystalline counterparts due to the lack of long range order. This is not the case for IGZO which displays mobilities between 10 and 75 cm^{2}V^{-1}s^{-1} dependent on the ratio of its constituent elements, generally displaying higher mobilities with higher concentrations of In [70]. These high mobilities are attributed to significant overlap of metal *s* orbitals providing a conduction path for electrons[71].

Generally, high quality IGZO films have been reported as being deposited by pulsed laser deposition (PLD). As the films can be deposited at room temperature, this technique remains low cost but is still challenging over a large area.

Within the visible range, high mobility IGZO films display transmission of up to 90% and maintaining up to 80% transmission for wavelengths up to 1100 nm. As such high quality IGZO films display better optical properties than many of its polycrystalline alternatives.

2.3 Doping Mechanisms In TCOs

The basic principles of doping were discussed in section 1.2.2, this section seeks to expand upon this, exploring aspects of doping which are of importance to TCOs. This section aims to aid in understanding why the different systems discussed above display different properties such as upper limits on carrier concentration or mobility.

2.3.1 Work Function, Ionisation Energy and Electron Affinity

Three quantities important in understanding the electronic behaviour of semiconductors and the behaviour of dopants within them are the work function, Φ, the ionisation energy, IE, and electron affinity, EA. Each of these quantities are defined by the relative position of specific energy levels to the vacuum level, E_{vac}. The vacuum level is defined as the energy of en electron removed from the materials surface. The work function is the separation of the Fermi level and E_{vac}, the ionisation energy is the separation of the VBM and E_{vac} and the electron affinity is the separation of the CBM and E_{vac}. Each of these quantities can be considered the energy required to liberate an electron sat in their corresponding energy level from the material [72]. Each of these values is shown and labelled in figure **??** which was previously used to show the energy levels of In_2O_3, SnO_2 and ZnO.

2.3.2 Charge Neutrality Level and Fermi Level Stabilisation

The charge neutrality level (CNL) is an important quantity in understanding the behaviour of doping within semiconductors. The CNL is a level within the complex band structure within a material where surface defects, dubbed virtual gap states (ViGS), display equal donor and acceptor like properties. Also known as the branch-point energy, E_{bp}, this energy marks a natural limit for the Fermi level within a material as further doping will be compensated by a change in the behaviour of surface states. This means that the Fermi level will be pinned at the CNL.

The branch-point energy is universal an absolute energy scale for all materials. However, this level sits in the middle of the band gap averaged over the entire Brillouin zone. This means that materials with low lying, narrow conduction bands will have CBMs that fall below the CNL. In rare cases, when a material has a less dispersive valence band, the VBM can sit above the CNL. If the CBM sits closer to or below the CNL a material will be easily doped n-type as the Fermi level move towards the CNL and if the VBM sits closer or above the CNL the material will be more easily doped p-type.

In the materials discussed in this thesis the narrow conduction bands means that the CNL sits above the CBM. This is what allows these materials to be degnerately doped and for such high conductivities be achieved. However with their differing band structures the relative position of the CBM to the CNL varies and dictates an upper limit on the carrier concentrations achievable in the material.

It is generally accepted that in semi-conductors the energy of the transition for hydrogen from donor to acceptor, H(+/-) is equal to the CNL[73]. As such calculations or measurements of the H(+/-) transition allow for a good estimation of the relative postion CNL in semiconductors. The relative positions of the CNL in In_2O_3, SnO_2 and ZnO have been calculated to be 0.65 eV, 0.5 eV and 0.45 eV above the CBM respectively [49, 74]. This signifies that higher carrier concentrations may be achievable in In_2O_3 than the other two materials and this is what is seen experimentally.

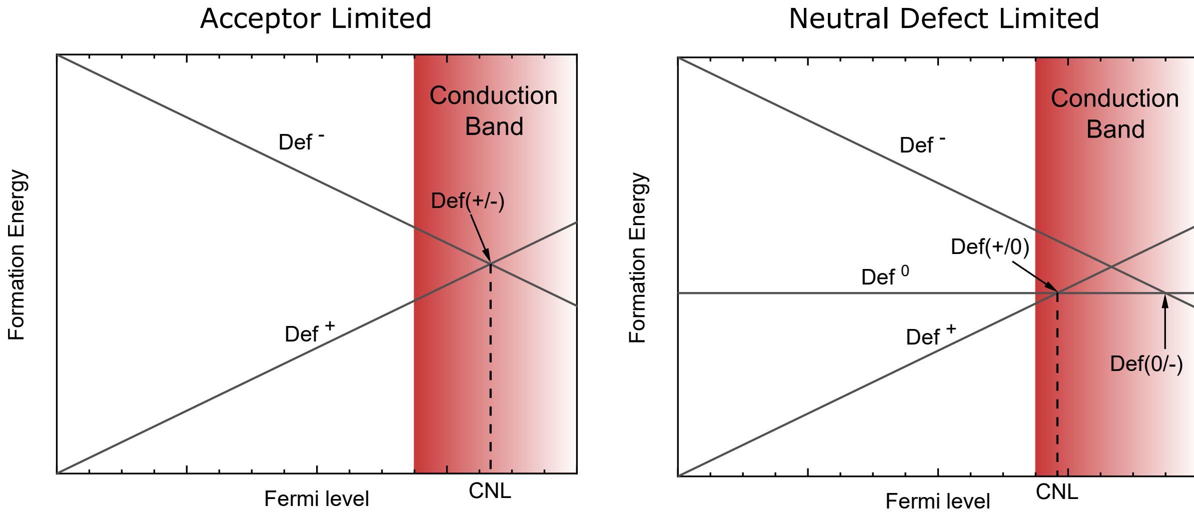

Figure 2.3: Diagrams demonstrating the position of the defect formation energy transitions where Fermi level pinning occurs for cases where carrier concentration is limited by the formation of an acceptor and the formation of a neutral defect. The neutral defect limited case only occurs when the neutral defect is due to a change in preferred charge state of the dopant as other neutral defects would no inhibit the introduction of donors to the system.

A dopant will not necessarily be able to introduce enough carriers to raise the Fermi level to the CNL. Other acceptor defects or a change in the preferred oxidation states of the dopant defects. An example of this is the limits seen in F doping of both In_2O_3 and SnO_2 where F incorporates as interstitial acceptor defects for Fermi levels above a certain energy. This transition occurs below the CNL and therefore the Fermi level is pinned at a lower energy reducing the upper limit on carrier concentration.

In most cases the limiting factor and preferred change in the the charge state of the substitutional defect introduced by doping. For n-type doping this means that the dopant incorporates as either a neutral defect or an acceptor after the Def(+/0) or the Def(+/-) transitions respectively which denote the change in preferred charge state. As such incorporation of more dopant contributes no more carriers. Figure 2.3 shows defect formation graphs for case where the carrier concentrations is limited by the formation of an acceptor and the case where it is limited by the formation of neutral substitutional defects.

2.3.3 Resonant Doping

A mechanism which is key to the work presented in this thesis is one dubbed 'resonant doping'. This refers to a phenomenon recently discovered in Mo doped In_2O_3 (IMO). Higher mobilities have been achieved in Mo doped In_2O_3 than in its traditional analogue Sn doped In_2O_3 (ITO). This higher mobility has been attributed to the fact that the donating orbital is a *d* orbital which sits at an energy well above the CBM. As the conduction band of In_2O_3 has predominantly *s* and

p character there is minimal mixing between these states. This allows the host materials band structure to be maintained giving the doped material lower band edge effective mass than its traditional analogue [75].

So far this mechanism has only been identified in IMO but is likely applicable in other cases. A large portion of the work within this thesis is focused on identifying other potential resonant dopants in In_2O_3 and applying it to the cheaper and more abundant alternative SnO_2.This mechanism is discussed in more detail in the results chapters 5 and 6 where other potential resonant dopants are explored in In_2O_3 and SnO_2.

Some confusion may arise from this use of the term 'resonant doping' as the term is also used to refer to another mechanism in semi-conductor physics outside of the study of TCOs. The term is sometimes used in reference to a phenomena that occurs when doping dilute nitrides. In this case N doping of certain semiconductor compounds, such as GaAs, cause a significant change in the hosts band structure, almost the opposite of what is observed in IMO. The donating N orbitals sit close to the CBM mix with the hosts conduction band, undergoing an effect known as band anti-crossing, increasing the carrier effective mass and the conduction band density of states[76].

While the use of the same term for two significantly different phenomena is not ideal, and future consideration should be taken with regards to this convention, in the work presented in this thesis the term 'resonant doping' is used to refer to the phenomenon observed within IMO and other TCOs explored in this work exclusively. The mechanism observed in the dilute nitrites is not discussed again within this work.

2.4 Non-Metal Oxide Transparent Conductors

While TCOs are the most commonly used and investigated transparent conductors, TCs, many non-metal oxide based TCs exist. Some have shown promise in specific industrial applications while others have been proven in concept only. While alternatives with better optical or electrical properties than even ITO have been reported they have usually have issues that prevent them from replacing it in industrial applications.

2.4.1 Ultra Thin Metal Films

The Beer-Lambert law states that the intensity of light of wavelength λ transmitted through a material, I, is related to the intensity of the incident light, I_0 by:

$$I_\lambda = I_{\lambda 0} e^{\mu_\lambda l} \tag{2.4}$$

where μ_λ is the attenuation coefficient of the material at wavelength λ and l is the optical path length. Equation 2.4 means that as $\mu_\lambda l$ approaches 0, I_λ approaches $I_{\lambda 0}$. Transmission, T_λ is the ratio of I_λ to $I_{\lambda 0}$,

$$T_\lambda = I_\lambda / I_{\lambda 0} \tag{2.5}$$

so to maximise transmission, $\mu_\lambda l$ needs to be minimised.

Metals are conductive due to overlap between the occupied valence band and unoccupied conduction band. This means that transitions of a wide range of energies are allowed meaning light of most wavelengths above the plasma frequency is absorbed. As a result, metals have a large μ_λ value for wavelengths in the visible range. Thus, to obtain high transmission l must be small. Based on this, it is possible deposit metal thin films which are transparent if they are of a thickness of around 15 nm or thinner. These are commonly referred to as ultra thin metal films, UTMFs. While UTMFs have been deposited of a large range of metals, the best optoelectrical properties have been observed using silver, Ag, and copper, Cu, primarily due to their low bulk resistivities [77, 78].

One primary issue faced in utilisation of these materials is achieving deposition of a continuous film. Islands can form from nucleation points leaving voids within the film when depositing a film as thin as required to maintain high transmission. This is particularly an issue for films with thickness <10 nm. This can be overcome through the use of seed layers where the attraction between deposited atoms and the substrate atoms is greater than the attraction between adjacent deposited atoms. However, introduction of a seed layer will have an impact on the optical properties of the stack of materials.

Another issue faced in utilising UTMFs is oxidation of the metal films when exposed to air for prolonged periods. In particular, this can cause issues with Cu UTMFs as Cu oxidises easily. This can be prevented too by encapsulating the film by coating it in a thin layer of a metal oxide but this will have an impact on both the optical and electrical properties of the stack. Ag is more resistant to oxidation that Cu but has reduced strength so being exposed to the elements can cause erosion to the film meaning some form of encapsulation is still required [77].

Bulk resistivities of UTMFs of Ag and Cu have been reported to range from 1.6-2.4$\times 10^{-6}$ Ωcm which is around two orders of magnitude lower than those regularly reported in ITO. However, due to the necessity of the films being 15 nm or thinner, sheet resistances obtained are generally around 10 Ω/□, comparable to those seen in many ITO or FTO thin films [79]. Below thicknesses of 10 nm the resistivity of UTMFs increases rapidly,

As expected based on equation 2.4 the transmission of UTMFs reduces with increased thickness. At thicknesses below 10 nm Ag UTMFs have been shown to have transmission of up to 90% at 550 nm. At greater thickness this value begins to decrease. UTMFs display much greater optical losses in the near infra-red region, at a wavelength of around 800 nm transmission falls below 50%, falling even lower at longer wavelengths. This reduced infra-red transparency is due to the high carrier concentrations in metals giving them a high plasma frequency and therefore reflecting most light in the infra-red region [79]. This makes UTMFs unsuitable for application where transparency into the infra-red region is required. An application where Ag UTMFs are

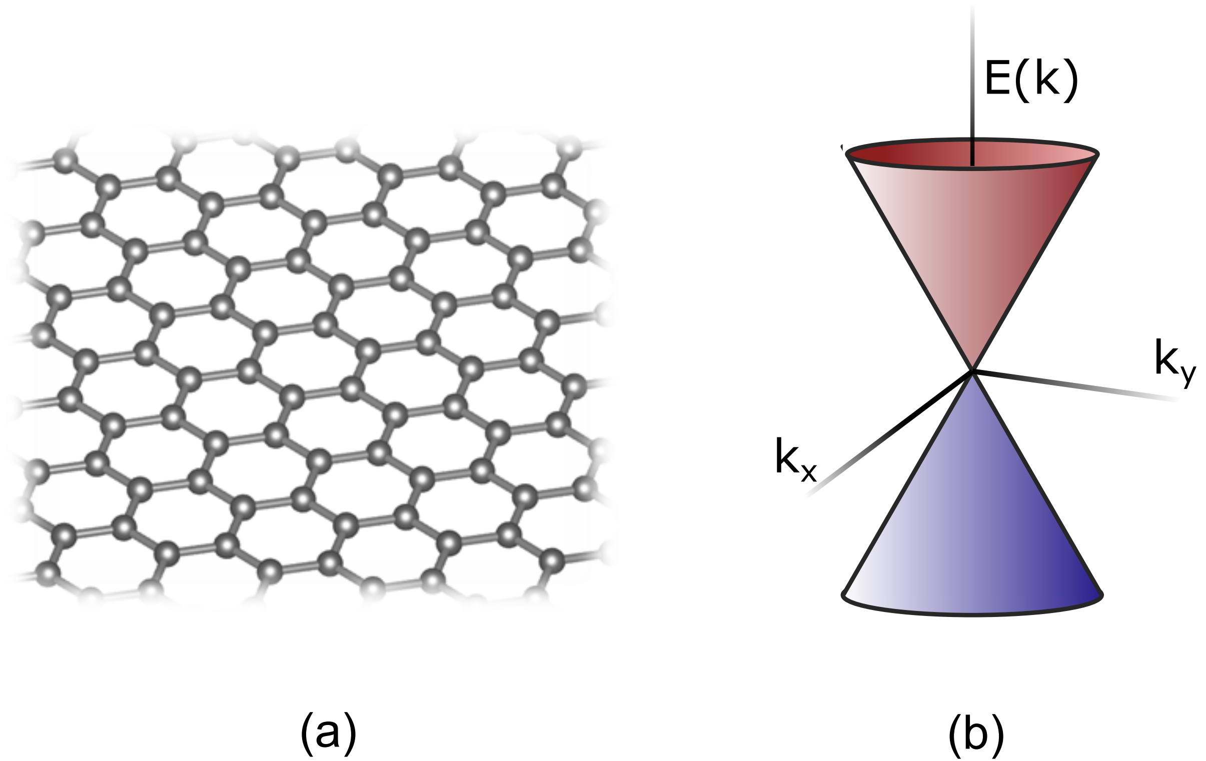

Figure 2.4: (a) The atomic structure of a graphene monolayer and (b) a diagram showing the 3-dimensional band dispersion of a Dirac cone as seen in the band structure of graphene.

used due to their high infra-red reflectivity is low emissivity windows. Low emissivity windows are designed to reflect infra-red light to reduce heat flow to prevent heat loss through the window in winter or heating of the interior during hot periods [80].

2.4.2 Graphene

Since its discovery in 2004, graphene has been proposed to be used for a massive range of applications. Among these applications, it has been suggested that graphene could be a suitable transparent electrode.

Graphene is mono-atomically thick layer of carbon atoms arranged in an hexagonal pattern. Its unique structure gives it a range of properties rarely seen in other materials, including incredible strength in proportion to its thickness, high thermal and electrical conductivity and high transmission of visible wavelengths of light. The last two of these properties are why its has garnered interest as a potential transparent electrode.

Optically, graphene displays properties superior to most TCOs, but its transmission is still lower than expected for a mono-atomic layer. In the visible range, a monolayer of graphene transmits 97-98% of light depending on wavelength [81]. The transmission decreases with increasing number of layers and further optical losses can be expected from a substrate if the

graphene is deposited on one.

Carrier mobilities in excess of 15,000 $cm^2V^{-1}s^{-1}$ have been reported for graphene for both electrons and holes [82] with electron mobilities reaching 2×10^5 $cm^2V^{-1}s^{-1}$ in certain cases [83]. The high mobility carriers are attributed to graphene's unique band structure in which the conduction and valence bands meet at a single point known as a Dirac point. This structure means that the charge carriers can be described as massless. This allows for the extremely high mobilities observed [84].

Carrier concentrations are much lower than those seen in other materials used as transparent electrodes, reported to fall between 10^{10} and 10^{12} cm^{-3}. Despite these significantly lower carrier concentrations, the high mobilities mean that bulk resistivities in graphene are comparable to, or better than, its alternatives at 10^{-4} to 10^{-6} Ωcm. The lowest resistivities within this range are only achievable in isolated graphene monolayers as scattering from phonons in adjacent layers within a stack will limit mobilities. Deposited onto a SiO_2 substrate the mobility of graphene is limited to ~40,000 $cm^2V^{-1}s^{-1}$ [83].

These reported electrical properties in combination with the thickness of graphene gives a monolayer a sheet resistance of around 100 Ω/□, significantly higher than other developed transparent conductors. This means that electron transport in the plane of the film is reduced compared to ITO or UTMFs [85].

Despite this, graphene does have some advantageous properties over its competitiors. Its flexibility allows for its use in applications where a rigid material like ITO would not suitable such a wearable electronics and flexible PV [86]. With recent reports of low resistivity, flexible ITO deposited by liquid metal printing, graphene may not even have this over its main competitor [87].

2.4.3 Carbon Nanotubes

Carbon nanotubes, CNTs, similarly to graphene, are made up of an hexagonal arrangement of carbon atom. Rather than being in a flat, one-dimensional sheet, however, CNTs are rolled into a tube with a diameter of the order of nanometers. The existence of CNTs was in fact proven in 1993 before the discovery of graphene [88].

CNTs primarily come in two varieties, single-walled nanotube, SWNTs, and multi-wall nanotubes, MWNTs. SWNTs consist of a single sheet of carbon atoms rolled into a tube while MWNTs consist of SWNTs nested within one another [89].

Continuous films of SWNTs have been shown to display both transparency and conductivity. Films of thickness around 50 nm have sheet resistances of ∼30 Ω/□ while achieving transparency of up to 90% at 550 nm [90]. While these properties are promising, they fall short of making CNTs a superior choice to conventional TCOs.

Similar to graphene, CNTs offer the benefit of flexibility allowing for their use in niche applications where rigid materials are not suitable.

2.4.4 Strongly Correlated Metals

Another category of transparent conductor that have gained significant interest in recent years are those based on highly correlated metals. These tend to not be based on elemental metals but instead compounds that display metallic properties. For transparent conductors these tend to be transition metal oxides with particular interest in, but not exclusively, vanadates and molybdates [14]. The main design principle for using these as transparent conductors is to, instead of taking a transparent material and raising the carrier concentration to make it conductive, take a material which is already conductive and shift the plasma frequency outside of the visible range to make the material transparent [91].

The main approach to achieve this is rather than changing the carrier concentration, n, the effective mass, m^*, is controlled to optimise the plasma frequency, ω_p while maintaining as high conductivity, σ, as possible. In these materials m^* is changed by renormalisation effects due to electronic correlation. The effective mass due to renormalisation is expressed as $m_r^* = m^*/Z_k$ where Z_k is the renormalisation factor. The value of Z_k is determined by the overlap of orbitals within the system [92] and, while this is primarily determined by the compound itself, it can be controlled by 'tilting' within the crystal structures changing the coordination number of certain lattice sites [14].

Highly correlated metal based transparent conductors have been shown to display promising properties experimentally. $SrVO_3$ has displayed carrier concentrations above 2.2×10^{22} cm^{-3} placing them an order of magnitude higher that the highest concentrations observed in conventional TCOs. These carrier concentrations correspond to conductivities of about σ=3.5×10^4 Scm^{-1} which corresponds to resistivities of around $\rho = 2.9\times10^{-4}$ Ωcm^{-1} [91]. This is a slight improvement on the lowest resistivity ITO but the order of magnitude difference in carrier concentration does not translate to conductivity due to the mobilities observed in $SrVO_3$ falling below 10 cm^{2}V^{-1}s^{-1}. Similar properties have been observed with other candidates for this kind of material: $CaVO_3$ and $SrMoO_3$ also display carrier concentration of the order of magnitude of 10^{22} cm^{-3} corresponding to high conductivity but are slightly limited by higher effective masses, and therefore lower mobilities, than those seen in conventional TCOs [14, 91].

In the optimisation of these materials the plasma frequency is brought as close to 1.75 eV, the transition between the near infra-red and visible range, as possible. As such, these materials are highly reflective within the infra-red up to these energies. This will limit the potential applications of these materials, in particular in the field of photovoltaics, as the band gaps of most widely used photovoltaic absorbers are smaller than 1.75 eV. As such, use of these materials as a transparent electrode in a photovoltaic device can be expected to lead to significant optical losses.

2.5 P-type Transparent Conductors

While the majority of transparent conductors are n-type extensive research has been performed into p-type transparent conductors. Despite this creating high conductivity p-type transparent conductors remains a challenge. Development of high conductivity, p-type transparent materials is desirable for multiple reasons, primarily to achieve transparent electronics[93]. In the field of photovoltaics p-type transparent conductors are desirable as they could provide an ohmic contact to p-type materials unlike their n-type counterparts allowing for whole new device architectures.

2.5.1 P-type TCOs

Initial research into p-type transparent conductors primarily focused on taking the traditional n-type TCOs (In_2O_3, SnO_2, ZnO) and attempting to dope them p-type through the intentional introduction of acceptors. Much current research still focuses on this aim [94]. Recent theoretical studies found that successful p-type doping of these metal oxides is unlikely due to a thermodynamical preference for the formation of donor defects. This means that any introduced holes would expected to be immediately compensated by intrinsic donor defects. In addition to this the hole effective masses of these oxides are significantly higher than the electron effective masses so significantly lower mobilities would be expected even if degenerate p-type doping was achieved [95]. Experimental efforts to fabricate p-type TCOs have supported these conclusions as hole carrier concentrations are generally low or mobilities reported fall to around 1 $cm^2V^{-1}s^{-1}$ or lower when higher concentrations are achieved [96].

Based on this, another approach to p-type transparent conductors is necessary. A key feature in identifying a suitable material for a p-type transparent conductor is a high hole mobility, something lacking in these metal oxides. As holes generally have higher effective masses than electrons in the majority of compounds identifying a material with this property as well as a suitable band gap and a preference towards forming acceptor defects proves difficult [97].

2.5.2 Non-oxide p-type Transparent Conductors

Some promising, non-oxide, transparent conductors have been identified but still fall short of p-type TCOs with regards to electrical properties. The two most widely researched have been copper iodide, CuI, and boron phosphide, BP [98]. Both of these materials have relatively low hole effective masses at 0.3 and 0.35 m_0 respectively, overcoming one of the main issues that prevent successful p-type doping of the metal oxides.

CuI has been deposited by a wide range of techniques but the lowest resistivity reported is 6×10^{-3} Ωcm for films fabricated by RF sputtering [99–101]. The mobility of this film was comparable to those seen in ZnO or SnO_2-based n-type TCOs at 34 $cm^2V^{-1}s^{-1}$; however the carrier concentration was relatively low at 8.5×10^{18} cm^{-3} [101]. Of any p-type transparent conductor CuI has been Incorporated into the most optoelectronic devices including photovoltaic

devices, particularly in organic solar a a p-type hole collecting layer. The highest efficiency reported for such a device is around 3.4% [102].

BP has had significantly less work focused on its BP has had significantly less work focused on its incorporation into devices into devices. Similarly to CuI, BP falls short in carrier concentration compared to n-type TCOs with the highest reported being around 10^{19} cm^{-3} corresponding to resistivities around 1.4×10^{-3} Ωcm. The bandgap of BP is also less ideal, with an indirect bandgap of around 2 eV and a direct gap of around 2.5 eV [98].

Recently, some other materials have garnered interest as p-type transparent conductors. Two are the copper sulphide based $CuAlS_2$ and $Cu_xZn_{1-x}S$. While these materials have ideal bandgaps and low hole effective masses the resistivities they display still fall short of those seen in n-type materials at 1.3×10^{-3} Ωcm and 1.8 $\times10^{-3}$ Ωcm respectively. The carrier concentrations achieved with these materials are higher than those seen in CuI or BP but the mobilities in samples with such carrier concentrations fall below 2 cm^{2}V^{-1}s^{-1} [103, 104].

While these materials have shown significant promise a lot of work has already been performed researching them and they still fall short of the conductivities seen in n-type TCOs. It is possible that further work could improve on the properties and discovery of a highly conductive and transparent p-type material would have massive impact on many fields including transparent electronics and photovoltaics.

Chapter 3

Theoretical Background and Computational Methods

3.1 Introduction

To develop better understanding of TCOs a full understanding of the underlying physics is required. Mathematical descriptions of how light interacts with different media and statistical models describing how carriers fill the conduction band within a material are useful tools in developing an understanding of the relationship between the structure of a material and its optoelectronic properties. In this chapter, the theory behind the properties of materials and statistical models used in this work are discussed in depth.

3.2 Relative Permittivity and Refractive Index

The relative permittivity, ϵ_r, of a material is a property of a material that describes the change in an electric field entering the medium. It is generally given as a ratio relative to the relative permittivity of a vacuum, commonly known as the permittivity of free space, ϵ_0.

$$\epsilon_r = \frac{\epsilon}{\epsilon_0} \tag{3.1}$$

where ϵ is absolute permittivity of the medium. This value is key in describing the optical response of a material as it will dictate the response of electromagnetic radiation entering, permeating or exiting the medium.

In any medium other than a vacuum, the permittivity varies as a function of frequency and is a complex quantity described by real and imaginary parts.

$$\tilde{\epsilon}(\omega) = \epsilon + i\tilde{\epsilon} \tag{3.2}$$

This complex function is also know as the dielectric function of the medium.

For many uses of the permittivity of a material, the high and low frequency limits are important. At high frequencies, ω approaching infinity, the relative permittivity approaches the high frequency dielectric constant, ϵ_∞. At low frequencies, ω approaching 0, the relative permittivity approaches is the static dielectric constant ϵ_s.

The relative permittivity of a material is closely related to another property of a material which in important in describing its optical response, the refractive index, n.In its most basic form, the refractive index is the ratio of the speed of light in the medium, v to the speed of light in a vacuum, c.

$$n = \frac{c}{v} \tag{3.3}$$

This describes the change to incident light at the interface between the medium and another. In a medium other than a vacuum, light will be attenuated as it travels through it. To describe this the refractive index can be described as a complex term, $\tilde{n}$.

$$\tilde{n} = n + ik \tag{3.4}$$

in which n is the real refractive index and k is the imaginary refractive index. k describes the attenuation of light within the medium. k is often referred to as the extinction coefficient of a material.

As previously stated, the relative permittivity of a medium is closely related its refractive index. Mathematically, they are related by

$$\tilde{\epsilon}_r = \tilde{n} = n + ik^2 \tag{3.5}$$

3.3 Modelling the Dielectric Function

For simulating or fitting reflectance or other optical data, models of a dielectric function can be used. In these models the medium is described as series of oscillators pertaining to free charge carriers or to phonons, collective oscillations of the crystal lattice. The most commonly utilised models are described in the subsections below. It is of note that these models tend to only be accurate for lower frequencies covering the near infra-red.

3.3.1 The Classical Drude Oscillator

The Drude oscillator model for dielectric functions is a very basic model which assumes that, while carriers are in motion, the crystal lattice is motionless. The electron oscillations are described using classical theory of free electron transport [16].

$$\tilde{\epsilon}(\omega) = \epsilon_\infty \frac{\omega_p^2}{\omega(\omega + i\gamma_p)} \tag{3.6}$$

in which ω_p and γ_p are the plasma frequency and damping respectively describing the contribution carrier oscillations. This model can be applicable in certain situations, for example, amorphous materials where no collective oscillation of a crystal lattice is possible or in metals where the high carrier concentration means the contribution from plasma oscillations will significantly outweigh those from phonon oscillations.

3.3.2 The Two Oscillator Model

This next model for the dielectric function of a material uses two oscillators, one for the phonons and one for the charge carriers. The major assumption that differentiates this model from others is that for the phonon oscillations only transverse modes contribute and not longitudinal. The carrier oscillation are still described by the classical Drude model as in the previous model. The expression for this model is given by the sum of the terms for each oscillator [105].

$$\tilde{\epsilon}(\omega) = \epsilon_\infty + \frac{(\epsilon_s - \epsilon_\infty)\omega_{TO}^2}{\omega_{TO}^2 - \omega^2 - i\omega\gamma_{TO}} - \frac{\epsilon_\infty \omega_p^2}{\omega(\omega + i\gamma_p)} \tag{3.7}$$

in which ω_{TO} and γ_{TO} are the transverse optical phonon frequency and damping respectively describing the contributions from phonon oscillations; ω_p and γ_p maintain their previous meanings.

3.3.3 The Three Oscillator Model

The next step complexity beyond the two oscillator model is the three oscillator model. This model utilises the oscillators in the first model but adds an additional one for longitudinal phonon mode oscillations [105, 106].

$$\tilde{\epsilon}(\omega) = \epsilon_\infty + \left(\frac{\omega_{LO}^2 - \omega^2 - i\omega\gamma}{\omega_{TO}^2 - \omega^2 - i\omega\gamma} - \frac{\omega_p^2}{\omega(\omega + i\gamma_p)} \right) \tag{3.8}$$

This model does, however, assume that the damping for the two phonon modes is the same and is given in the expression as γ. Also, coupling between the different phonon modes and plasmon-phonon coupling are not accounted for in any of these models. Models accounting for these phenomena exist but are generally unnecessary for the applications within this thesis.

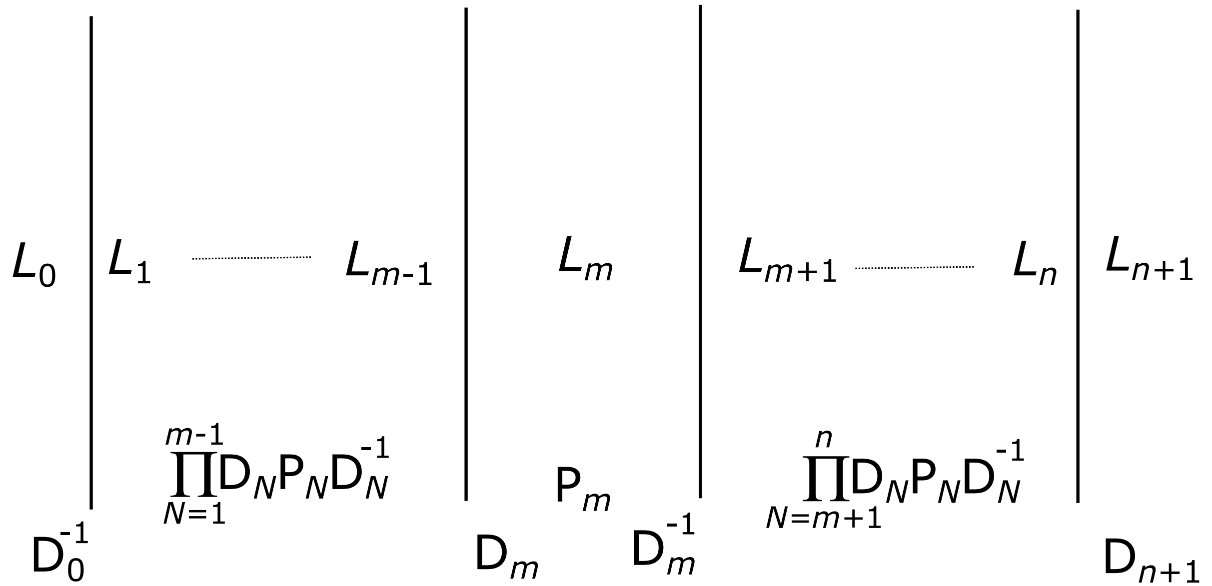

Figure 3.1: Schematic diagram of a stack of n layers. The dotted lines represent an unspecified number of layers between layer L_m and the ends of the stack. The matrices describing the movement of electromagnetic radiation through the layer are shown at the bottom where D is a dynamical matrix which describe behaviour at the interfaces and P is a propagation matrix which describe behaviour as the radiation propagates throughout the layer

3.4 The Transfer Matrix Method

The transfer matrix method is a method for calculating the transmission and reflectance of a system or stack of multiple layers of different thicknesses and refractive indexes. The method is useful for both optimisation of stacks of materials with known properties and fitting of models to optical data to extract unknown properties of a material [107].

3.4.1 Coherence of Light

The transfer matrix method allows for the calculations to be performed for stacks where the propagation of light through the interfaces is coherent, incoherent or partially coherent. In the case of coherent propagation, light is either completely in phase, resulting in purely constructive interference, or 180° out of phase, resulting in completely destructive interference and zero total transmission. Incoherent propagation occurs in all other cases when the light is constructed of many different phases.

It is possible that the propagation of light through a system is partially coherent. This occurs when interfaces within the system are not smooth. The roughness introduces partial coherence.

3.4.2 Coherent Systems

The simplest version of the transfer matrix method assumes that propagation through the entire stack is coherent. This version can be applicable for systems consisting of thin layers, the thickness of layers is of the order of nm.

The Fresnel equations are used to calculate the transmissivity and reflectivity at each interface. For the interface between a layer, m, and a neighbouring layer, $m+1$ these equations can be obtained by applying Snell's law [108].

$$\tilde{t}^{p}_{m,m+1} = \frac{2\tilde{n}_m \cos\tilde{\theta}_m}{n_{m+1}\cos\tilde{\theta}_m + n_m \cos\tilde{\theta}_{m+1}} \tag{3.9}$$

$$\tilde{r}^{p}_{m,m+1} = \frac{\tilde{n}_{m+1}\cos\tilde{\theta}_m - \tilde{n}_m \cos\tilde{\theta}_{m+1}}{n_{m+1}\cos\tilde{\theta}_m + n_m \cos\tilde{\theta}_{m+1}} \tag{3.10}$$

$$\tilde{t}^{s}_{m,m+1} = \frac{2\tilde{n}_m \cos\tilde{\theta}_m}{n_m\cos\tilde{\theta}_m + n_{m+1} \cos\tilde{\theta}_{m+1}} \tag{3.11}$$

$$\tilde{r}^{s}_{m,m+1} = \frac{\tilde{n}_m\cos\tilde{\theta}_m - \tilde{n}_{m+1} \cos\tilde{\theta}_{m+1}}{n_m\cos\tilde{\theta}_m + n_{m+1} \cos\tilde{\theta}_{m+1}} \tag{3.12}$$

t^p and r^p are the transmission reflection coefficients for p-polarised light and t^s and t^p are for s-polarised light. $\tilde{n}$ and $\tilde{\theta}$ are the complex refractive index and complex angle of propagation for each medium.

In the most simple case of an entirely coherent system the amplitude of field either side of the interface is related by the product of the dynamical matrices , $\mathbf{D}_j$, of the layers either side [107].

$$\begin{pmatrix} E^{+}_{m} \\ E^{-}_{m} \end{pmatrix} = \mathbf{D}^{-1}_{m}\mathbf{D}_{m+1} \begin{pmatrix} E^{+}_{m+1} \\ E^{-}_{m+1} \end{pmatrix} \tag{3.13}$$

The product of these two matrices is:

$$\mathbf{D}^{-1}_{m}\mathbf{D}_{m+1} = \frac{1}{\tilde{t}_{m,m+1}} \begin{bmatrix} 1 & \tilde{r}_{m,m+1} \\ \tilde{r}_{m,m+1} & 1 \end{bmatrix} \tag{3.14}$$

This resulting matrix is called the transmission matrix of the interface. This has the same form for p-polarised and s-polarised light, except incorporating the corresponding Fresnel equations.

The field amplitude before and after the bulk of each layer can similarly be related by a propagation matrix, $\mathbf{P}_j$.

$$\begin{pmatrix} E'^{+}_{m} \\ E'^{-}_{m} \end{pmatrix} = \mathbf{P}_{m} \begin{pmatrix} E^{+}_{m} \\ E^{-}_{m} \end{pmatrix} \tag{3.15}$$

which is given by:

$$\mathbf{P}_m = \begin{bmatrix} \exp(-i\tilde{\delta}_m) & 0 \\ 0 & \exp(i\tilde{\delta}_m) \end{bmatrix} \tag{3.16}$$

where $\tilde{\delta}_m$ is the phase change of light travelling through layer m and is calculated using:

$$\tilde{\delta}_m = 2\pi \bar{k} \tilde{n}_m d_m \cos\tilde{\theta}_m \tag{3.17}$$

$\bar{k}$ is the wavenumber of the incident light and d_m is the thickness of layer m.

The full system transfer matrix for a stack of N layers, $\mathbf{T}_{0,N+1}$, can be calculated from the product of $\mathbf{D}_j$ for each interface and $\mathbf{P}_j$ for the bulk of each layer. This describes the relationship between the field amplitude either side of the stack.

$$\begin{pmatrix} E_0^+ \\ E_0^- \end{pmatrix} = \mathbf{T}_{0,N+1} \begin{pmatrix} E'^+_{N+1} \\ E'^-_{N+1} \end{pmatrix} \tag{3.18}$$

where:

$$\mathbf{T}_{0,N+1} = \mathbf{D}_0^{-1} \left[\prod_{m=1}^{N} \mathbf{D}_m \mathbf{P}_m \mathbf{D}_m^{-1} \right] D_{N+1} \tag{3.19}$$

The system transfer matrix is a 2×2 matrix and for a completely coherent system can also be written in terms of the complex transmission and reflection coefficients:

$$\mathbf{T}_{0,N+1} = \frac{1}{\tilde{t}_{0,N+1}} \begin{bmatrix} 1 & -\tilde{r}_{N+1,0} \\ \tilde{r}_{0,N+1} & \tilde{t}_{0,N+1}\tilde{t}_{N+1,0} - \tilde{r}_{0,N+1}\tilde{r}_{N+1,0} \end{bmatrix} \tag{3.20}$$

Therefore, the complex transmission and reflection coefficients for light travelling both ways through the stack can be obtained:

$$\tilde{t}_{0,N+1} = \frac{1}{T_{11}} \tag{3.21}$$

$$\tilde{r}_{0,N+1} = \frac{T_{21}}{T_{11}} \tag{3.22}$$

$$\tilde{t}_{N+1,0} = \frac{\text{Det}T}{T_{11}} \tag{3.23}$$

$$\tilde{r}_{N+1,0} = -\frac{T_{12}}{T_{11}} \tag{3.24}$$

3.4.3 Incoherent Systems

If a thick layer is introduced to the stack, such as a glass substrate where d is of the order of mm rather than nm, the propagation of light will become incoherent. In this case the system can be represented by two interfaces, one representing the interfaces from layer 0 to layer m, the thick layer, and one representing layer m to layer $N+1$. These two interfaces will have intensity components $\mathbf{T}^{int}_{0,m}$ and $\mathbf{T}^{int}_{m,N+1}$.

$$\mathbf{T}^{int}_{0,m} = \frac{1}{|\tilde{t}_{0,m}|^2} \begin{bmatrix} 1 & -|\tilde{r}_{m,0}|^2 \\ |\tilde{r}_{0,m}|^2 & |\tilde{t}_{0,m}\tilde{t}_{m,0}|^2 - |\tilde{r}_{0,m}\tilde{r}_{m,0}|^2 \end{bmatrix} \tag{3.25}$$

As either side of the thick layer all layers will be thin, and therefore propagation through them will be coherent, equations 3.21 to 3.24 can be used to calculate this. The same form is taken by $\mathbf{T}^{int}_{m,N+1}$. The propagation intensity for the thick layer has the form:

$$\mathbf{P}^{int}_{m} = \begin{bmatrix} |\exp(-i\tilde{\delta}_m)|^2 & 0 \\ 0 & |\exp(i\tilde{\delta}_m)|^2 \end{bmatrix} \tag{3.26}$$

The intensity transfer matrix of an incoherent system therefore takes the form:

$$\mathbf{T}^{incoh}_{0,N+1} = \mathbf{T}^{int}_{0,m}\mathbf{P}^{int}_{m}\mathbf{T}^{int}_{m,N+1} \tag{3.27}$$

In the case of a system with multiple thick layers each layer will require its own propagation intensity matrix and an interface intensity matrix needs to be calculated between each one.

From the intensity transfer matrix the transmission reflectance can be obtained.

$$T^{incoh}_{0,N+1} = \frac{1}{T^{incoh}_{11}} \tag{3.28}$$

$$R^{incoh}_{0,N+1} = \frac{T^{incoh}_{21}}{T^{incoh}_{11}} \tag{3.29}$$

For cases where the light in unpolarised the reflectance and transmission for p- and s-polarised light can be calculated and averaged.

3.4.4 Partial Coherence

It is possible that the propagation of light through a system is partially coherent. This occurs when interfaces within the system are not smooth. The roughness introduces partial coherence.

To account this the Fresnel equations are modified. This is done with the introduction of an exponential term accounting for the effect of variations in height across interfaces. The exponential term accounts for a Gaussian distribution in height irregularities. The modified Fresnel equations in terms of the original Fresnel coefficients are [107]:

$$\tilde{r}'_{m,m+1} = \tilde{r}_{m,m+1} \exp(-2(2\pi\bar{k}\tilde{n}_m Z)^2) \tag{3.30}$$

$$\tilde{r}'_{m+1,m} = \tilde{r}_{m+1,m} \exp(-2(2\pi\bar{k}\tilde{n}_{m-1} Z)^2) \tag{3.31}$$

$$\tilde{t}'_{m,m+1} = \tilde{t}_{m,m+1} \exp(-2(2\pi\bar{k}Z)^2(\tilde{n}_{m-1} - \tilde{n}_m)^2/2) \tag{3.32}$$

$$\tilde{t}'_{m+1,m} = \tilde{t}_{m+1,m} \exp(-2(2\pi\bar{k}Z)^2(\tilde{n}_m - \tilde{n}_{m-1})^2/2) \tag{3.33}$$

In which Z is the route mean squared, rms, of the height Gaussian distribution.

This method can be used either to model theoretical systems or fitting to real transmission or reflection data to extract optical constants of layers or layer thickness.

3.5 Modelling of Electronic Band Structure

The electronic band structure of a material is key in determining the optical and electronic properties of a material. Modelling of the complete band structure of a material is complicated due to the large number of interacting potentials for each individual atom and electron. However, for the regions near the VBM or CBM, much simpler approximations can be applied. This is useful as free carriers which are utilised in conductivity sit in states near the CBM. In this section, these approximations are described and limitations to their use discussed.

3.5.1 The Carrier Effective Mass

The effective mass, m^*, of a free carrier is the mass the carrier appears to have in measurements due to its response to external forces such as the periodic potentials of the ionic cores of the atoms in the crystal lattice acting upon it. It is a quantity of great importance as it is useful in simplifying models for band structure and is required for the models discussed below. The effective mass can change dependent on where within the band the carrier sits with carriers higher in the conduction band generally having higher effective masses. The standard parabolic model of band structure does not account for this and assumes that the effective mass is constant

throughout the conduction band, this approximation, along side the non-parabolic approximation that does account for the varying effective mass, is discussed in the following sections.

For many calculations, the effective mass of carriers at the CBM is used. This is generally referred as the band edge effective mass, m^*_{BE}. The effective mass is different at k values away from the CBM, generally larger. As such effective masses other than the band edge effective mass need to be defined. One of particular importance is the Fermi edge effective mass, m^*_F and is the effective mass at the the Fermi surface. As free carriers, which contribute to conductivity in a system, move at the Fermi surface the quantity is used to calculate properties such as free carrier mobility.

The density of states averaged effective mass, m^*_{DOS} is also of importance and is the average effective mass across the occupied states within the conduction band. This is also often referred to as the optical effective mass due to its importance in fitting of optical data. In a reflectance measurement the collective free carriers, within all occupied conduction band states, are excited. As such when calculating properties such as plasma frequency which are extracted from reflectance data this effective mass is used.

The effective mass at a specific k value can be calculated from the curvature of the band at this point and therefore the effective mass is given by [16]

$$\frac{1}{m^*} = \frac{1}{\hbar^2}\frac{d^2E}{dk^2} \tag{3.34}$$

For m^*_{BE} approximating the conduction band as a parabola ($E(k) = \hbar^2 k^2/2m^*$) and calculating its curvature using 3.34 suffices. Calculating m^*_F and m^*_{DOS} prove more complicated. For m^*_F the can be calculated from the gradient of the conduction band at the Fermi level.

$$\frac{1}{m^*_F} = \frac{1}{\hbar^2 k_F}\left|\frac{dE}{dk}\right|_{k=k_F} \tag{3.35}$$

in which k_F is the k value at which there are states at the Fermi level. In the parabolic approximation this will give the same value as the band edge effective mass but in real systems the conduction band is not parabolic and more complex models which account for this can result in significantly different values for $m*_{BE}$ and $m*_F$. Such models are discussed in detail below in the following subsections.

Finally the density of states averaged effective mass is the most complicated to calculate. This is calculated as the average of the curvature of the conduction band for all occupied states [24]. A model following Fermi carrier statistics gives m^*_{DOS} as

$$m^*_{DOS} = \frac{\int m^*_{BE} g(E) f(E,E_F) dE}{n(E)} = \frac{\int m^*_{BE} g(E) f(E,E_F) dE}{\int g(E) f(E,E_F) dE} \tag{3.36}$$

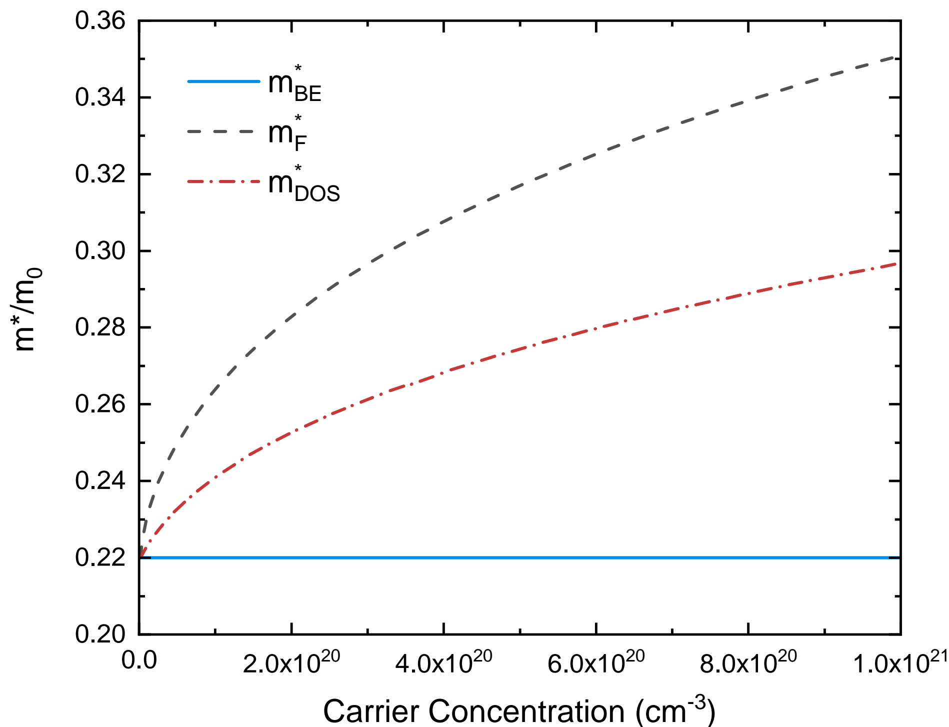

Figure 3.2: The three kinds of effective mass discussed above, band edge effective mass, Fermi surface effective mass and density of states averaged effective mass, as a function of carrier concentration for a band edge effective mass of 0.22 m_0 and a bandgap of 2.8 eV, the values reported for undoped In_2O_3

where $g(E)$ is the density of states and $f(E,E_F)$ is a Fermi function [9]. These are defined below in equations 3.55 and 3.57.

Figure 3.2 shows each of these effective masses as a function of carrier concentration showing that with increases carrier concentration the disparity between them increases. For the carrier concentration range over which most TCOs operate, the differences between the three effective masses are significant showing the importance of utilising the correct form of effective mass in each situation.

3.5.2 Effective Mass and Bandgap Relationship

A trend can be observed between the bandgap and the band edge effective mass of a semiconductor. Wider band gap semiconductors tend to have higher band edge effective masses. As a result it can be expected that wider bandgap materials will display lower carrier mobilities [109].

This had implications for TCOs, having a bandgap wider than necessary to allow it to be transparent within the visible range will be expected to have a negative impact on the materials conductivity. This further helps understand why In_2O_3 based TCOs have dominated. Due to the forbidden transition from the VBM to CBM discussed in section 2.2.4, In_2O_3 is transparent in

the desired range while having a smaller electrical bandgap of 2.7 eV. As such, it has a lower band edge effective mass than those materials that have fundamental bandgaps large enough to achieve full visible transparency and therefore higher mobilities are achievable when doping.

3.5.3 Parabolic Band Approximation

As with light sometimes exhibiting wave and some times exhibiting particle like properties, particles with mass, such as electrons, sometimes exhibit wave like properties. As a result it can be mathematically necessary to describe them as waves. The wavelength, λ, of a massive particle, known as the de Broglie wavelength, is described by

$$\lambda = h/p \tag{3.37}$$

where h is Planck constant and p is the momentum of the electron.

Equation 3.37 can be rearranged to give

$$p = \hbar k \tag{3.38}$$

where $\hbar$ is the reduced Planck constant and k is particle's wave vector.

In the absence of external forces, the energy, E, of a particle with mass m is given by

$$E = \frac{p^2}{2m} = \frac{\hbar^2 k^2}{2m} \tag{3.39}$$

The dispersion of the conduction band in k-space near the CBM, where $k = 0$, can be described using a variant of equation 3.39 where the effective mass, m^*, of the electrons is used as m.

$$E(k) = E_0 + \frac{\hbar^2 k^2}{2m^*} \tag{3.40}$$

where E_0 is the energy of the CBM. The gradient of the parabola is dictated by the value of m^* as $\hbar$ is a constant. This dispersion relationship holds true for the region close to the CBM. Further from the CBM the energy varies non-parabolically with k, hence the change in the effective mass higher in the conduction band. The degenerate nature of TCOs means that the Fermi level is at such an energy that electrons occupy states in the region where the parabolicity breaks down. Adjustments to this model are required to account for this in the case of degenerate semiconductors.

3.5.4 k·p Perturbation Theory

To account for the non parabolicity of the conduction band away from the CBM, while maintaining the simplicity of the parabolic approximation as much as possible, **k.p** perturbation theory can be utilised.

The wave function of an electron within a periodic environment, such as a crystal lattice, has a wave-function, Ψ, which follows the Bloch wave form [110].

$$\Psi(r) = e^{ik\cdot r}u(r) \tag{3.41}$$

where r is the electron's position and u is a periodic function with the periodicity of the crystal lattice [111].

Electrons are often treated as experiencing the same average potential, $V(r)$ to negate the complexity implicit in changing potentials due to them moving through the lattice. In this approximation, the mean field approximation, the Schrödinger equation to describe the motion of an electron is given by

$$\mathcal{H}_n\Psi_n(r) = \left(\frac{p^2}{2m} + V(r)\right)\Psi_n(r) = E_n\Psi_n(r) \tag{3.42}$$

Where $\mathcal{H}_n$, E_n and Ψ_n are the Hamiltonian, energy and wave function of an electron in the eigenstate n. It is of note that each eigenstate can be occupied by up to two electrons, one of each spin [19].

By inserting the Bloch wave function, equation 3.41, into the Schrödinger equation and using the relationship for momentum relationship $\mathbf{p}= -i\hbar\nabla_\mathbf{k}$ The Schrödinger equation becomes [112]

$$\left[H_0 + \frac{\hbar}{m}\mathbf{k}\cdot\mathbf{p} + V\right]u_{n\mathbf{k}}(\mathbf{r}) = E_{n\mathbf{k}}u_{n\mathbf{k}} \tag{3.43}$$

At the Γ point **k**=(0,0,0) and equation 3.43 can be simplified to

$$[H_0 + V]\,u_{n\mathbf{k}}(\mathbf{r}) = E_{n0}u_{n\mathbf{k}} \tag{3.44}$$

The solutions to this expression form an orthonormal set. As such the wave function at a value of **k** near the Γ-point and the corresponding energy values can be found by applying small perturbations to represent $\mathbf{k}\cdot\mathbf{p}$ interactions between the conduction and valence bands. These perturbations can be expressed mathematically as

$$u_{n\mathbf{k}}(\mathbf{r}) = u_{n0}(\mathbf{r}) + \frac{\hbar}{m}\sum_{n'\neq n}\frac{\langle u_{n0}\,|\,\mathbf{k}\cdot\mathbf{p}\,|\,u_{n'0}\rangle}{E_{n0} - E_{n'0}}u_{n'0} \tag{3.45}$$

and

$$E_{n\mathbf{k}}(\mathbf{r}) = E_{n0}(\mathbf{r}) + \frac{\hbar^2 k^2}{2m} + \frac{\hbar^2}{m^2} \sum_{n' \neq n} \frac{|\langle u_{n0} | \mathbf{k} \cdot \mathbf{p} | u_{n'0} |^2 \rangle}{E_{n0} - E_{n'0}} \tag{3.46}$$

Solving equation 3.43 for a given point group is non trivial due to the impact of anisotropic effects and a lack of experimental information on the band structure of many materials. However, for the simple case of isotropic cubic systems thorough investigation has been possible. Through these investigations simplified models which can be widely applied have been proposed.

Considering a four band model for the band structure for Zincblende structures Kane arrived at [113]

$$E_c(k) = \frac{1}{2}(-E_g + \sqrt{E_g^2 + 4k^2p^2}) + E_k \tag{3.47}$$

if spin orbit splitting is neglected and the system is simplified to two bands, the valence and conduction bands. In this, Kane's matirx element is given by

$$p^2 = \frac{\hbar^2}{2m^*}\left(1 - \frac{m^*}{m}\right)E_g \tag{3.48}$$

While Kane proposed this for zincblende structures specifically it has become one of the most widely applied models for band structure when non-parabolicity needs to be considered.

For a direct bandgap semiconductor the energy dispersion of a band can be approximated by a Taylor expansion around $|\mathbf{k} - \mathbf{k}_0|$

$$E(\mathbf{k} - \mathbf{k}_0) = E_0 + A|\mathbf{k} - \mathbf{k}_0|^2 + B|\mathbf{k} - \mathbf{k}_0|^4 + \ldots \tag{3.49}$$

The model above proposed by Kane gives an informed approximation of the coefficients required in the Taylor expansion. This gives

$$\frac{\hbar^2 k^2}{2m^*} \simeq E(q + \alpha E + \beta E^2) \tag{3.50}$$

where

$$\alpha = \frac{1}{E_g}\left(1 - \frac{m*}{m}\right)^2 \tag{3.51}$$

and

$$\beta = -\frac{2}{E_g^2}\frac{m^*}{m}\left(1 - \frac{m^*}{m}\right) \tag{3.52}$$

The term containing the β is often dropped to simplify the model, an approximation known as the α-approximation. This model accounts for the non-parbolicity of the conduction band and therefore can be used in analysis and modelling of degenerate semiconductors such as TCOs and as such is utilised throughout this thesis.

3.5.5 Calculating Density of States

The previous models and approximations describe the shapes of the bands in a material, describing the positions of available energy states in k-space. The next step is to describe the density of states, the number of states per unit energy.

an expression for density of states can be derived by treating the free carriers as particles in a box. The full derivation by this method is given in reference [114]. This derivation gives the total number of states with a wave vector of magnitude k as

$$g(k)dk = \left[\frac{k^2V}{\pi^2}\right]dk \tag{3.53}$$

Equation 3.53 gives the density of states as a function of wave vector, k. The density of states is generally expressed in terms of states per unit energy, E. The relationship between E and k is given by equation 3.39. Inserting equations 3.39 into equation 3.53 gives an expression for the total density of states, g, in terms of E. The volume term has also been removed from this expression to express the density of states per unit volume as is standard. [115]

$$g(E)dE = \frac{m^*[2m^*E]^{1/2}}{\pi^2\hbar^3} \tag{3.54}$$

This derivation used equation 3.39 throughout and therefore holds up for the parabolic approximation only and is applicable within the same regime. By following the same derivation but replacing equation 3.39 with equation 3.50 the density of states for the non-parabolic approximation can be derived. Doing so gives

$$g(E) = \frac{\sqrt{2E}[2m^*E(1+E/E_g)]^{3/2}}{\pi^2\hbar^3} \tag{3.55}$$

This gives a more accurate model of the density of states for away from the CBM.

3.5.6 Fermi Statistics and Carrier Concentration

The density of states gives information on the number of states available and at what energy but do not tell us whether they are occupied or not. The carrier concentration, n and density of states are related by

$$n(E) = \int_0^\infty g(E)f(E)dE \tag{3.56}$$

in which $f(E)$ is a Fermi-Dirac distribution function, commonly referred to as the Fermi distribution, which is given by

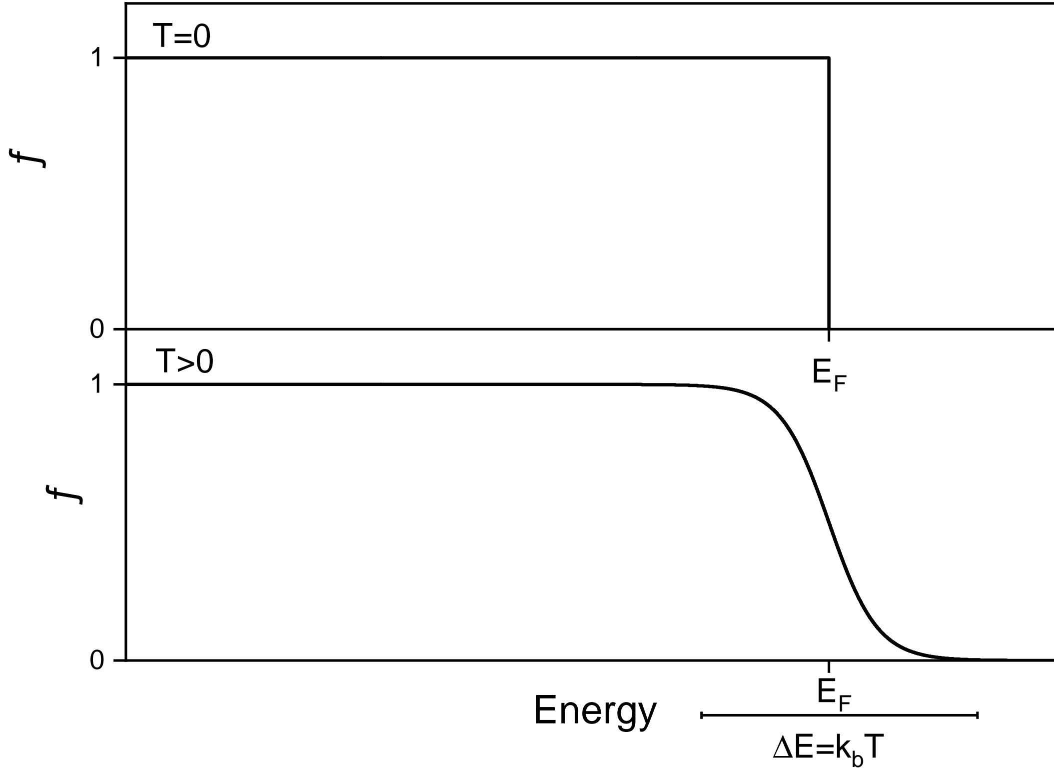

Figure 3.3: The Fermi-Dirac distribution function at temperatures of $T=0$ and $T>0$

$$f(E)=\frac{1}{1+e^{\frac{(E-E_F)}{k_bT}}} \tag{3.57}$$

where k_b is the Boltzmann constant. The Fermi function describes the probability of a state at energy E being occupied at a temperature of T. At T=0 the Fermi function is a step function with the step at the Fermi energy, E_F; the probability of a state below E_F being occupied is 1 and the probability of a state above E_F being occupied is 0. At temperatures above zero the step broadens by $\pm k_BT$ as it is possible for a carrier to be excited into a state within k_bT of the Fermi level. Figure 3.3 shows the Fermi function at T=0 and for a non zero case [115].

Inserting equation 3.57 into equation 3.56 along with either equation 3.54 or 3.55 gives the expressions for carrier concentration:

$$n(E)=\int_0^\infty \frac{m^*[2m^*E]^{1/2}}{\pi^2\hbar^3}\frac{1}{1+e^{(E-E_f)/k_BT}}dE \tag{3.58}$$

in the parabolic approximation and

$$n(E)=\int_0^\infty \frac{\sqrt{2E}[2m^*E(1+E/E_g)]^{3/2}}{\pi^2\hbar^3}\frac{1}{1+e^{(E-E_f)/k_BT}}dE \tag{3.59}$$

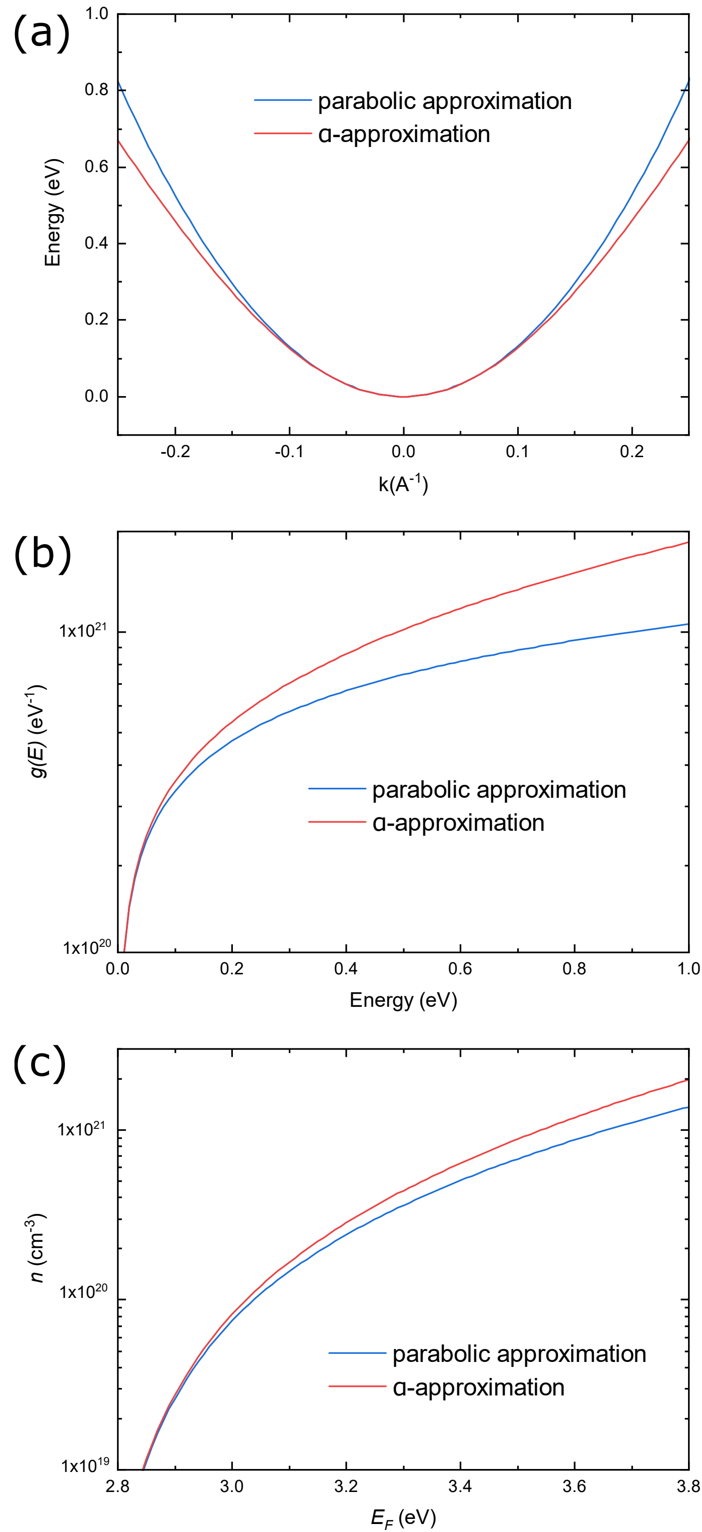

Figure 3.4: Calculations using the parabolic and non-parabolic α approximations for a material with an effective mass of $0.2m_0$, a band gap of 2.8 eV at a temperature of 300 K. (a) The energy dispersion of the conduction band as a function of wave number. (b) The density of states per unit energy. (c) The carrier concentration as a function of Fermi level.

in the non-parabolic approximation.

Figure 3.4 shows the the calculated band dispersion, density of states as and carrier concentrations for a hypothetical material with an effective mass of $0.2m_0$, a band gap of 2.8 eV at a temperature of 300 K. These values were chosen as they are representative of those observed in In_2O_3.

As seen in Figure 3.4, the main differences between the approximation is that the gradient of the dispersion of the conduction band under the α approximation is less than the parabolic approximation; the difference increases with increasing k. This means that in the α approximation there is a higher density of states for the same energy in comparison to the parabolic approximation. Similarly, the α approximation gives higher carrier concentrations at the same Fermi energy.

3.5.7 Inter-band Absorption

Another consideration when looking at the optical properties of a material is inter-band absorption, primarily between the valence band and conduction band. This is the mechanism that prevents a material from being transparent as shorter wavelengths. This is not accounted for in the oscillator models discussed in section 3.3 and as such those models are highly inaccurate at short wavelengths where this mechanism dominates. A seperate model is therefor required for modelling inter-baand absorption. The rate of transitions between an initial and final state such as in a in described by Fermi's 'golden rule' [116]

$$W = \frac{2\pi}{\hbar} \mid \langle f \mid H_I \mid i \rangle \mid^2 \delta(E_f - E_i - \hbar\omega) \tag{3.60}$$

where $|i\rangle$ and $|f\rangle$ are the initial and final states respectively. H_i is the interaction Hamiltonian between the two states and E_f and E_i and the energies of the final and initial states respectively. In the case of a direct optical transition, the final and initial states will be the energies of the conduction and valence band for a given k value ($E_c(k)$ and $E_v(k)$). To consider all possible transitions between the bands the sum of the rates at all k values should be taken. Treating k as a continuous variable, this can be done by integrating over the first Brillouin zone as k repeats beyond this. Equation 3.60 can be then be expressed as

$$W = \frac{2\pi}{\hbar} \mid \langle f \mid H_I \mid i \rangle \mid^2 \int \frac{1}{4\pi^3} \delta(E_c - E_v - \hbar\omega) \tag{3.61}$$

the $1/4\pi^3$ normalisation arises from the number of spin states per unit volume. The matrix element $\mid \langle f \mid H_I \mid i \rangle \mid^2$ can be placed outside the integral for direct transitions as there is no change in k between the initial and final states; this would not be the case in an indirect transition. The integral in equation 3.61 is the joint density of states, g_j.

$$g_j(\hbar\omega) = \int \frac{1}{4\pi^3}\delta(E_c - E_v - \hbar\omega) \tag{3.62}$$

g_j combines the density of occupied states in the valence band and unoccupied states in the conduction band. $E_c(k)$ and $E_v(k)$ can be expresses as

$$E_c(k) = E_c(0) + \frac{\hbar^2 k^2}{2m_e^*} \tag{3.63}$$

and

$$E_v(k) = E_v(0) - \frac{\hbar^2 k^2}{2m_h^*} \tag{3.64}$$

in the parabolic approximation. To account for non-parabolicity, these equations can be adjusted as discussed in section 3.5.4.

In the case of a momentum preserving transition the photon energy, $\hbar\omega$, must equal the energy difference between the initial and final states. This gives

$$\hbar\omega = E_f(k) - E_i(k) = E_c(0) - E_v(0) + \frac{\hbar^2 k^2}{2m_e^*} - \frac{\hbar^2 k^2}{2m_h^*} = E_g + \frac{\hbar^2 k^2}{2m_r^*} \tag{3.65}$$

where m_r^* is the reduced effective mass which is given by $1/(1/m*_e + 1/m*_h)$. Expressing this in terms of k gives

$$k = \sqrt{\frac{2m_r^*}{\hbar^2}}\sqrt{\hbar\omega - E_g} \tag{3.66}$$

Combining this with equation 3.62 gives

$$g_j(\hbar\omega) = \frac{1}{2\pi^2}\left(\frac{2m_r^*}{\hbar^2}\right)\sqrt{\hbar\omega - E_g} \tag{3.67}$$

Therefore the transition probability can be expressed as [117]

$$W = \frac{2\pi}{\hbar} \mid \langle f \mid H_I \mid i \rangle \mid^2 \frac{1}{2\pi^2}\left(\frac{2m_r^*}{\hbar^2}\right)\sqrt{\hbar\omega - E_g} \tag{3.68}$$

It is of note that this is where the $\sqrt{\hbar\omega - E_g}$ dependence of the absorption coefficient in direct gap semiconductors, which is used in fitting of optical data, arises from.

In equation 3.68 all quantities are known outside of the matrix element. The interaction Hamiltonian for electromagnetic interactions can be expressed as

$$\langle f|H_I|i\rangle = -\left(\frac{e}{mc}\right)\langle v|\overrightarrow{A}\cdot\overrightarrow{p}\,|c\rangle \tag{3.69}$$

in which $\overrightarrow{A}$ is the vector potential and $\overrightarrow{p}$ is the momentum.

The square of the coupling matrix element is therefore

$$|\langle f|H_I|i\rangle|^2 = \left(\frac{e}{mc}\right)^2 |A|^2 \langle v|p|c\rangle \tag{3.70}$$

Thus the rate can be expressed as

$$W = \frac{2\pi}{\hbar}\left(\frac{e}{mc}\right)^2 |A|^2 \langle v|p|c\rangle \frac{1}{2\pi^2}\left(\frac{2m_r^*}{\hbar^2}\right)\sqrt{\hbar\omega - E_g} \tag{3.71}$$

The absorption coefficient, $\alpha(\omega)$ is defined as the transition rate over the incident magnetic flux. The incident electromagnetic flux can be calculated by the Poynting vector, S. Therefore α can be expressed as

$$\alpha(\omega) = \frac{\hbar\omega \times W}{\overrightarrow{S}} \tag{3.72}$$

$\overrightarrow{S}$ can be calculated using

$$\overrightarrow{S} = \frac{c}{8\pi} Re(\overrightarrow{E}^* \times \overrightarrow{H}) \tag{3.73}$$

where $\overrightarrow{E}$ is the electric field vector and $\overrightarrow{H}$ is the magnetic field vector. These can both be expressed in terms of the vector potential $\overrightarrow{A}$.

$$\overrightarrow{E} = -1/c\frac{\delta\overrightarrow{A}}{\delta t} = \frac{i\omega}{c}\overrightarrow{A} \tag{3.74}$$

and

$$\mu\overrightarrow{H} = \overrightarrow{B} = \overrightarrow{\nabla}\times\overrightarrow{A} \tag{3.75}$$

Assuming the material in non-magnetic the permeability, μ can be assumed to be one. Assuming that $\overrightarrow{A}$ takes the form of a plane wave

$$\overrightarrow{A} = \overrightarrow{A_0} e^{i(\overrightarrow{K}\cdot\overrightarrow{r} - \omega t)} \tag{3.76}$$

where $\overrightarrow{K}$ is the wave vector. Utilising these expressions the Poyting vector can be expressed as

$$\overrightarrow{S} = \frac{c}{8\pi} Re\left[-\frac{i\omega}{c}\overrightarrow{A}^* \times (i\overrightarrow{K} \times \overrightarrow{A})\right] = \frac{\omega}{8\pi} Re\left[(\overrightarrow{A}^* \cdot \overrightarrow{A})\overrightarrow{K} - (\overrightarrow{A}^* \cdot \overrightarrow{K})\overrightarrow{A}\right] \tag{3.77}$$

For a transverse plane wave $\overrightarrow{A}^* \cdot \overrightarrow{K} = 0$ so

$$\overrightarrow{S} = \frac{n\omega^2}{8\pi c} \mid A \mid^2 \hat{K} \tag{3.78}$$

where n is the real part of the refractive index and $\hat{K}$ is a unit vector in the direction of the Poynting vector.

combing equations 3.68 and 3.78 in equation 3.72 gives

$$\alpha(\omega) = \frac{\hbar\omega \times \frac{2\pi}{\hbar}(\frac{e}{mc})^2 \mid A \mid^2 \mid \langle v \mid p \mid c \rangle \mid^2 \rho_{cv}(\hbar\omega)}{\frac{n\omega^2}{8\pi c} \mid A \mid^2} \tag{3.79}$$

which simplifies to

$$\alpha(\omega) = \frac{16\pi^2 e^2}{m^2 cn\omega} \mid \langle v \mid p \mid c \rangle \mid^2 \rho_{cv}(\hbar\omega) \tag{3.80}$$

In its current form, this expression assumes that the valence band is fully occupied and that the conduction band is fully unoccupied. To include an expression that represents the occupation of the the two bands due to thermal excitations. Fermi functions are included. $f(E_v)$ is a Fermi function describing the occupation of the valence band and $f(E_c)$ describes the occupation of the conduction band. The additional term to include in equation 3.80 is

$$f(E_v)[1 - f(E_c)] - f(E_c)[1 - f(E_v)] \tag{3.81}$$

where the first term describes the probability of states being available for the absorption process and the second term describes the probability that the states are available for the emission process. The above expression simply reduces to $f(E_v) - f(E_c)$. Adding this to equation 3.80 the expression for absorption coefficient becomes

$$\alpha(\omega) = \frac{16\pi^2 e^2}{m_e^{*2} cn\omega} \mid \langle v \mid p \mid c \rangle \mid^2 \rho_{cv}(\hbar\omega)[f(E_v) - f(E_c)] \tag{3.82}$$

In the case of TCOs the Fermi level sits well above the CBM. This means that the $f(E_v)$ will be approximately 1 for all energies as full occupation can be expected.

Finally the momentum matrix element can be approximated to

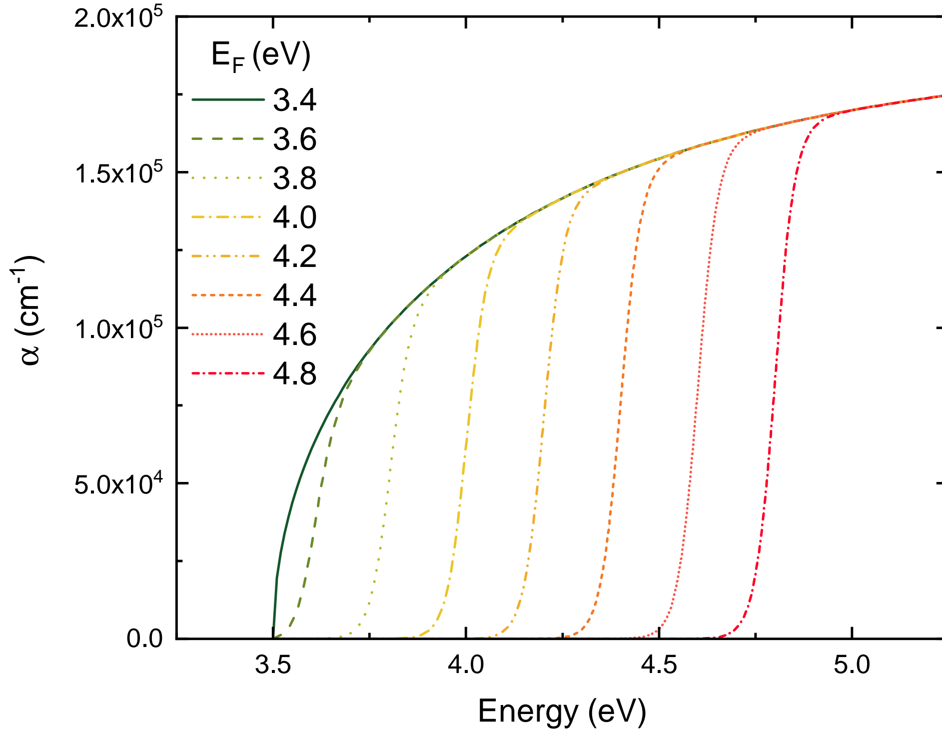

Figure 3.5: The interband absorption coefficients for Fermi energies ranging from just below the CBM to 1.3 eV above the CBM in In_2O_3. The absorption coefficients have been calculated using equation 3.82

$$|\langle v|p|c\rangle|^2 \simeq \frac{m_0 E_g}{2}\frac{m_0}{m_e^*} \tag{3.83}$$

Implementing this into equation 3.82 the absorption coefficient for interband absorption can be calculating using only knowable quantities.

Calculating the absorption coefficient for interband absorption for In_2O_3, it is important to account for the forbidden transition between the VBM and CBM. To properly represent absorption in In_2O_3, the energy gap of the first allowed transition should be used in place of E_g or the interband absorption onset will appear at a lower energy than the values observed in experiments. As such, for calculations regarding interband absorption in In_2O_3 going forward, the optical gap of 3.5 eV will be used in place of E_g. This means that on the energy scale the second valence band will be set to 0 eV.

Figure 3.5 shows the interband absorption coefficient for In_2O_3 for a range Fermi levels. The lowest Fermi energy shown, 3.4 eV, is representative of all cases where the Fermi level is below the CBM. In this case the $\sqrt{\hbar\omega - Eg}$ term from the joint density of states dominates the absorption as the conduction band is unoccupied so $f(E_c)$ will be 0 for all energies. This is what allows for the use of the Tauc plot in obtaining the optical gap in non-degenerate semi-conductors.

For the Fermi levels greater than the CBM the onset of absorption is dominated by the Fermi function describing the occupation of the conduction band, $f(E_c)$. As below E_F the conduction band is occupied absorption into theses states is not allowed, above E_F the absorption coefficient has the same value as the case where E_F is less that the CBM. As the absorption onset is not dominated by the $\sqrt{\hbar\omega - Eg}$ and instead $f(E_c)$ the Tauc plot method for obtaining the optical gap will be inaccurate. Linearly fitting a Fermi function will underestimate the Fermi level and therefore the optical gap. For example, plotting a Tauc plot for the calculated absorption coefficient for E_F = 4.0 eV gives an optical gap of 3.96 eV. This is in the case of an absorption coefficient which is entirely based on the model above, in a real system the absorption coefficient will be further affected by other factors.

Beyond the dependence on E_F the absorption coefficient has a dependence on the electron effective mass with a $1/m_e^{*2}$ term in the prefactor, $1/m_e^*$ term in the momentum matrix operator and a dependence on the reduced effective mass, m_r^* in the joint density of states. Despite this, differences in effective mass of the order of magnitude seen later within this work have little impact on the absorption coefficient. Therefore it can be expected that for comparable Fermi levels choice of dopart should have little impact on interband absorption.

The transmission (ignoring reflectance) can be calculated from the absorption coefficient using

$$A = 2 - \log(T) \tag{3.84}$$

where A is the absorbance and

$$\alpha = 2.303A/t \tag{3.85}$$

where t is the film thickness

3.6 Electrostatic Screening

In a solid the mobile charge carriers have a damping effect on electric fields within the material, this effect is commonly known as screening. In an n-type material where the mobile charge carriers are electrons the mobile charge carriers can be treated as a fluid consisting of negative charges. Each of these negative charges will repel all other negative charges. This repulsive force counteracts the force of an electric field felt by the electrons.

Charged impurities, such as dopants, have an electric field which can impact the motion of carriers throughout the solid. The distance at which these fields are felt by the carriers is dependent on the number of carriers, n, due to screening. This distance is called the 'screening length' and several approximations exist for calculating its value.

3.6.1 Debye Screening Length

The simplest approximation for the screening length in a semi-conductor is the Debye screening length. In this approximation the screening length λ_D is given by [118]

$$\lambda_D = \sqrt{\frac{\epsilon k_B T}{e^2 N}} \tag{3.86}$$

in which ϵ is the dielectric constant, k_B is the Boltzmann constant, T is the temperature, e is the fundamental charge and N is the doping density.

At high doping densities the screening length is longer than half the average separation of ionised impurities. $\lambda_D < R_0/2$ where R_0 is the average distance to the nearest neighbour for ionised impurities. When this condition is met is called the Mott transition and is when a material will start to display metalic behavior. In this case the screening length stops depending on N and a different model is required. This is generally the case in degenerate semi-conductors such as TCOs.

3.6.2 Thomas-Fermi approximation

The Thomas-Fermi approximation treats the electrons as delocalised in 'free gas'. As stated above, there is no dependence on the density of ionised impurities and the expression for the Thomas-Fermi screening length, λ_{TF} is [119]

$$\lambda_{TF} = \sqrt{\frac{2\epsilon E_F}{3e^2 n}} \tag{3.87}$$

When discussing the screening length in TCOs, this expression is more applicable than the one presented in equation 3.86

3.7 Scattering Mechanisms

The free carrier mobility in a material is described by

$$\mu = \frac{e\tau}{< m^* >} \tag{3.88}$$

where e is the elementary charge, τ is the carrier scattering time and m^* is the carrier effective mass. τ varies strongly with many of a materials properties including m^* and carrier concentration n. It is also heavily dependent on the dominant scattering mechanisms in the material.

Models describing the scattering limited mobility exist which account for this factor. The model used and the dependence of the mobility on other properties of the material is dependent

on the dominant scattering mechanism. In turn the dominant scattering mechanism will be dependent on the defect and carrier concentration of the material.

In TCOs grain boundary scattering (GBS) at dominates low carrier concentrations while ionised impurity scattering (IIS) dominates at higher carrier concentrations. Beyond these, optical phonon scattering (OPS), acoustic phonon scattering (APS), surface scattering (SS) and dislocation scattering (DS) can have impacts in certain regimes. Other scattering mechanisms exist but are negligible or non-applicable in degenerately doped systems.

Combining of mobility limits from multiple mechanisms is performed using Metthiessen's rule:

$$\frac{1}{\mu_{tot}} = \sum_i \frac{1}{\mu_i} \tag{3.89}$$

where μ_i is the mobility limit for each scattering mechanism.

Each of the previously mentioned scattering mechanisms are discussed below and a model suitable for use in degenerately doped systems are shown. Figures showing the results of these models are displayed in chapter 7 where the models are used.

3.7.1 Ionised Impurity Scattering

At high doping densities, and therefore carrier concentrations, ionised impurity scattering is the dominant scattering mechanism [120]. This occurs when an electron is scattered by the coulombic field of an ionised impurity, such as the ionic core of donor or acceptor defect, this includes dopants. In a degenerately doped system, such as a TCO, the ionised impurity scattering imposed mobility limit, μ_{IIS}, is given by [121]:

$$\mu_{IIS} = \frac{24\pi^3 \epsilon_s^2 \epsilon_0^2 \hbar^3 n}{e^5 Z^2 < m^* >^{1/2} N_i} \left[\ln(1+y) - \frac{y}{1+y} \right], \tag{3.90}$$

where

$$y = \frac{3(2n\pi^8)^{1/3} \hbar^2 \epsilon_s \epsilon_0}{e^2 < m^* >} \tag{3.91}$$

in which ϵ_s is the static dielectric constant and ϵ_0 is permittivity of free space. n is the free carrier concentration, e is the elementary charge, Z is the charge on the ionised impurity and N_i is the density of ionised impurities.

3.7.2 Grain Boundary Scattering

For lower carrier concentrations grain boundary scattering is the dominant mechanism. Grain boundary scattering occurs due to charge carrier accumulating in trap states in the grain boundaries. The accumulated carriers give rise to an electrostatic potential which other carriers

scatter off [122]. The mobility limited by grain boundary scattering is described by described by [120]:

$$\mu_{GBS} = \frac{l}{\sqrt{2\pi < m^* > k_b T}} \exp(-E_b/k_b T) \tag{3.92}$$

in which l is the grain size and E_b is the grain boundary barrier height. The expressions exist to describe the barrier height and which is applicable depends on the carrier concentration, n, the grain size, l, and the trap density within the grain boundaries, Q_t.

For the regime where $ln > Q_t$ the barrier height is described by:

$$E_b = \frac{e^2 Q_t^2}{8\epsilon_s \epsilon_0 n} \tag{3.93}$$

while for the regime where $ln < Q_t$ it is described by:

$$E_b = \frac{e^2 l^2 n}{8\epsilon_s \epsilon_0} \tag{3.94}$$

The change between these two regimes is due to a transition between the traps being partially filled in the first regime to being filled completely in the second.

The carrier concentration at which ionised impurity scattering begins to dominate over grain boundary scattering is primarily dependent on grain size and trap density. Smaller grains and higher trap densities means that grain boundary scattering dominates for higher carrier concentrations.

3.7.3 Phonon Scattering

Phonons are collective excitations of atoms within the crystal lattice. Photons can be split into two categories, optical and acoustics. Optical phonons are out of phase oscillations of atoms within the lattice. Meanwhile acoustic are collective displacement of the atoms moving through the lattice. The movement of acoustic phonons though the lattice is similar to the movement of a sound wave through air, hence the name acoustic.

Charge carriers are scattered by opitcal phonons as the vibrations cause oppositely charged, neighbouring atoms to move closer to one another. This results in dipole moment that produces a small electric field which carriers scatter off. The production of this dipole moment is called the Fröhlich interaction. [123]

At room temperature the most significant phonon scattering mechanism is longitudinal polar optical scattering due to the Fröhlich interaction. While never the dominant scattering mechanism in TCOs the scattering times it induces are low enough to be significant. The mobility limit due to this mechanism is described by [124]:

$$\mu_{LPO} = \frac{\hbar}{2e\alpha_{LO}E_{LO} < m^* >} \frac{f(\alpha_{LO})}{[1+(\alpha_{LO}/6)]^3}[\exp(E_{LO}/k_BT)-1], \tag{3.95}$$

where

$$\alpha_{LO} = \frac{1}{4\pi\epsilon_0}\frac{e^2}{\hbar}\left(\frac{< m^* >}{2E_{LO}}\right)^{1/2}\left(\frac{\epsilon_s-\epsilon_\infty}{\epsilon_s\epsilon_\infty}\right) \tag{3.96}$$

α_{LO} is referred to as the polaron coupling constant, E_{LO} is the longitudinal optical phonon energy and ϵ_∞ is the high frequency dielectric constant of the material. $f(\alpha_{LO})$ varies between ~1-1.5 dependent on the value of α_{LO} [125].

Acoustic phonons also have an impact on scattering within a material, the highest impact mechanism is acoustic deformation potential scattering. The vibrations of the lattice cause variation in the electronic band structure though out the material which creates a potential which scatters free carriers. This mechanism is described by:

$$\mu_{ADP} = \frac{2(2\pi)^2}{2}\frac{\rho v_s^2\hbar^4}{E_c^2 * < m^* >^{5/2}(k_BT)^{3/2}} \tag{3.97}$$

where ρ is the density of the material, v_s is the speed of sound in the material and E_c is the acoustic deformation potential.

Other phonon scattering mechanisms such acoustic piezoelectric (AP) and transverse polar-optical (TPO) produce scattering times of orders of magnitude that mean they have negligible impact when combined with those described using equation Metthiessen's rule as described in the main text.

3.7.4 Dislocation Scattering

Dislocation scattering can also have an impact on the total mobility limit, primarily depending on the density of dislocations. These behave similarly to grain-boundaries but in some semiconductors can be charged which also contributes to scattering. The scattering time for dislocation scattering is described by [126]:

$$\mu_{DS} = \frac{32k_BT\hbar}{3\pi E_D^2 l_s^2 < m^* > N_{dis}}\left(\frac{1-\nu}{1-2\nu}\right)^2 \tag{3.98}$$

in which E_D is the dislocation potential, l_s is the slip distance, N_{dis} is the 2D dislocation density and ν is the Poisson ratio of the material. Generally dislocation scattering has a small impact on the imposed mobility limit compared to the other mechanism unless the material has an unusually high dislocation density.

3.8 Density Functional Theory

Throughout this thesis, results from density functional theory, DFT, calculations performed by collaborators are presented. As such, in aid of understanding the technique, and its limitations, a brief explanation is given here. DFT has a broad range of applications in predicting material properties but in particular, for the work presented here, its ability to predict band structure and defect formation energies is of interest.

DFT is, in its simplest definition, a method for approximating the solution to the Schrödinger equation of a many-body system to determine the allowed energy states of the system. Solving the Schrödinger for a many-body system is impossible, hence the approximation is required. Many approximate solutions to the many body Schrödinger equation exist but most are incredibly computationally expensive. DFT overcomes this by approximating the problem to a single body problem in which an approximate wavefunction of the electron density is used rather than the individual wavefunctions of each electrons [127, 128].

In DFT, different functionals of electron density can be used for electron exchange interactions and coulomb correlation interactions. The choice of functional will have impact on the computational intensity of the calculations and the accuracy of the results. Pertaining to semiconductors, one are that DFT calculations tend to have poor agreement with experiment is a materials bandgap [129]. Three classifications of functionals are generally employed: The local density approximation which basically assumes that electron density is homogeneous [130]; the generalised gradient approximation which applies gradients of electron density [131] and hybrid functionals which utilise the exact fomalisation of these exchanges which arise from Hatree-Fock theory combined with approximations of exchange and correlation interaction calculated through DFT [132]. Of these, the hybrid functionals show the most agreement with experimental data with regards to bandgaps but they are also the most computationally demanding. The exact details the formalisation behind this is beyond the scope of this thesis, for more detailed discussion and descriptions the literature referenced throughout this section is recommended.

The focus of this thesis is doping within metal oxides. DFT calulations deal with dopants by replacing one atom per super cell with the dopant. As such the system being modelled is closer to an dilute ordered alloy than a randomly doped system. However, this is the closest approximation possible without making the calculations too computationally intensive. In the case of In_2O_3, which has an 80 atom unit cell, even theses calculations are incredibly time consuming. These limitations need to be taken into consideration when discussing the DFT results shown throughout this thesis.

CHAPTER 4

EXPERIMENTAL METHODS

4.1 Introduction

Throughout this thesis a broad range of experimental techniques have been utilised. This chapter covers the basics of the physics underlying the techniques used and the principles of analysing the data. The techniques discussed are Hall effect measurements, reflection, transmission and absorption spectroscopy, X-ray diffraction (XRD) and X-ray photo-emission spectroscopy (XPS).

4.2 Hall Effect Measurements

Hall effect measurements are of significant importance in characterisation of the electrical properties of semiconductors, including TCOs. Such measurements give information on film resistivity, carrier concentration, carrier mobility and the type, p or n, of the majority carriers.

As the name suggests, the measurements rely on the Hall effect which describes the force felt by charge carriers subjected to an external magnetic field. A schematic depicting the hall effect is shown in Figure 4.1

In a Hall effect measurement a sample is placed in a magnetic field B and a current, I, is applied across the sample normal to the magnetic field, The Lorentz force generates a transverse electric field normal to both B and I. In Figure 4.1, the magnetic field is applied in the z-direction and the current is applied along the x-axis inducing a electric field along the y-axis. The magnitude of the voltage induced across the sample, the Hall voltage, V_H, is related to the sheet carrier concentration, n_s, by

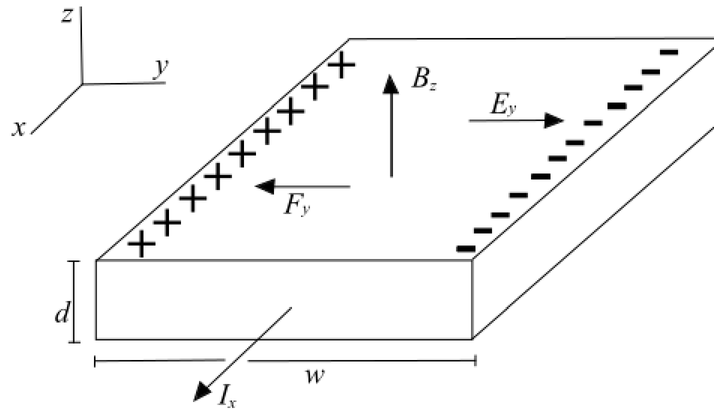

Figure 4.1: Schematic depicting the hall effect where carriers feel the Lorentz force, F, due to the external magnetic field, B.

$$n_s = \frac{IB}{e|V_H|} \tag{4.1}$$

where e is the elementary charge. From the sheet carrier concentration it is possible to determine the bulk carrier concentration using the relationship $n_s = nd$ where d is the thickness of the conducting layer. Hence is possible to establish the carrier concentration of a film of known thickness using this method [111].

4.2.1 Van der Pauw Geometry

Figure 4.1 is a good simple set up for demonstrating the Hall effect and while such a measurement could be used to measure an estimate of carrier however in reality Hall effect measurements are rarely, if ever, performed using this set up. In reality, the Van der Pauw geometry is generally used. Named after its creator, L. J. Van der Pauw, this particular geometry is generally used as it allows for the measurement of any homogeneous solid of an arbitrary shape. The only other requirements are that the material contains no voids and is significantly thinner than it is wide [133].

In this geometry, four contacts are placed on the perimeter of the sample as shown in figure 4.2. A current is passed between contact 1 and contact 2, I_{12} while the voltage between contact 3 and contact 4. V_{34} is measured. From this measurement the resistance can be calculated using $R_{12,34} = V_{34}/I_{12}$. If the contacts between which the current is applied and the voltage is measured are changed to arbitrary pairs i and j for current and k and l for voltage the expression for calculating resistance can be generalised to

$$R_{ij,kl} = \frac{V_{kl}}{I_{ij}} \tag{4.2}$$

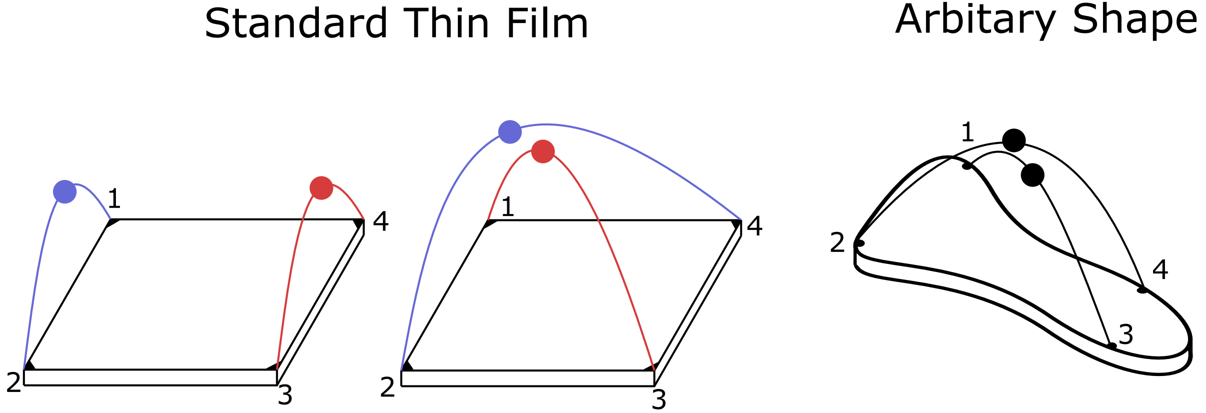

Figure 4.2: Schematic diagram showing the van de Pauw geometry for hall effect measurements. The left show a standard set up for measurements of sheet resistance and hall voltage on thin films while the right shows a set up for a sample with arbitrary shape and dimensions.

Sheet resistance, R_s, can be related to resistance measured horizontally and vertically as obtained with equation 4.2 using the relationship

$$e^{-\frac{\pi R_{12,34}}{R_s}} + e^{-\frac{\pi R_{23,41}}{R_s}} = 1 \tag{4.3}$$

Van de Pauw also proposes that

$$R_{ij,kl} = R_{kl,ij} \tag{4.4}$$

meaning that by switching which contacts the current is applied to and the voltage is measured across, several measurements can be averaged so that more accurate values can be obtained and the impact of effects such as sample asymmetry and magnetoresistnace are minimised. Further measurement can be made by repeating each measurement with the polarity switched. With all these measurements the vertical, R_v, and horizontal, R_h, resistances become:

$$R_v = \frac{R_{12,34} + R_{34,12} + R_{21,43} + R_{43,21}}{4} \tag{4.5}$$

and

$$R_h = \frac{R_{23,14} + R_{14,23} + R_{32,41} + R_{41,32}}{4} \tag{4.6}$$

R_s can then be calculated using equation 4.3 by replacing the resistivities with R_v and R_h.

The Hall voltage, V_H, can also be more accurately obtained by averaging several measurements. By measuring the voltage between both sets of opposite corners and flipping both the

current and polarity of the magnetic field for each pair, eight measurements can be made and averaged. The Hall voltage as obtained by this method is

$$V_H = \frac{V_{13}^+ + V_{13}^- + V_{24}^+ + V_{24}^- + V_{31}^+ + V_{31}^- + V_{42}^+ + V_{42}^-}{8} \tag{4.7}$$

where + and - denote the polarity of the magnetic field

The sheet carrier concentration can then be calculated using equation 4.1 as described above. Utilising this and the sheet resistance as calculated using equation 4.3, it is possible to calculate the carrier mobility. The Hall mobility, μ_H is given by

$$\mu_H = \frac{|V_H|\, t}{IB\rho} \tag{4.8}$$

Since sheet resistance is given by $R_s = \rho/t$ this can be rewritten in terms of the already obtained quantities n_s and R_s utilising equation 4.1.

$$\mu_H = \frac{1}{en_sR_s} \tag{4.9}$$

4.3 Optical Measurements

A range of techniques can be performed to measure the optical properties of a material and extract information about the films properties ranging from film thickness to optical bandgap and plasma frequency. Primarily these techniques consists of transmission, absorption and reflectivity spectroscopy with a range of analysis techniques performed on the resulting spectra.

This section discusses the experimental techniques of uv-vis spectroscopy and Fourier transform infra red spectroscopy, FTIR, used to obtain these spectra and a range of analysis performed to extract properties of the samples being measured.

4.3.1 UV-Vis Spectroscopy

UV-Vis spectroscopy is used to perform optical measurements of transmission and reflectivity over a range covering the visible and ultra-violet regions. This usually encompasses a range of wavelengths, λ, of around 250–2500 nm.

For transmission spectroscopy, the set up consists simply of a light source, a monochromator and a detector. The source generates white light which enters the monochromator. The monochromator utilises either a prism or a diffraction grating to select a specific wavelength of light. The monochromator scans through the range of wavelengths for which the spectrum is being measured. Initially a baseline spectrum is measured with no sample in the path of the beam and this is set as 100% transmission for each wavelength. This is followed by a spectrum with the

sample placed in the path of the beam. The ratio of the baseline spectrum and the spectrum for the sample gives the transmission spectrum of the sample at a percentage.

Reflectivity spectroscopy functions very similarly except that through the utilisation of a series of mirrors the light reflected off the sample is collected rather than the light transmitted.

The absorption coefficient, α, can also be obtained through UV-Vis by measuring both the transmission, T, and reflectivity, R, assuming that all light which is not transmitted or reflected is absorbed. The relationship between α and T and R is:

$$\alpha = -\frac{1}{d}\ln\left(\frac{T}{(1-R)^2}\right) \tag{4.10}$$

where d is the film thickness.

The primary use of absorption spectroscopy is to extract the optical bandgap of a material, how this varies from the fundamental bandgap of a material is explained in section 1.3.2. From the absorption coefficient spectrum the most standard method for extracting the optical band gap is the Tauc plot. When first proposed by Tauc in 1966, the Tauc plot was presented as a method for establishing the band gap of amorphous materials [134] but is now widely and commonly used for crystalline materials as well.

Tauc suggested that the best method for extracting the band gap from optical spectra was to plot optical absorption as a function of photon energy. This was later further developed when it was shown that the absorption strength was dependent on the difference between the the photon energy, $h\nu$, and band gap, E_g, following[135]:

$$(\alpha h\nu)^{1/n} = A(h\nu - E_g) \tag{4.11}$$

where A is a proportionality constant and the exponent n is dependent on the nature of the electronic transition. n varies dependent on whether the transition is allowed or forbidden and whether it is direct or indirect. Table 4.1 shows the value of n for each type of transition.

Table 4.1: The exponent value n in equation 4.11 for transitions that are allowed or forbidden and direct or indirect.

Transition Type	n
Direct and allowed	1/2
Direct and forbidden	3/2
Indirect and allowed	2
Indirect and forbidden	3

As allowed transitions dominate the absorption process, generally n values of either 1/2 or 2 are most commonly used dependent on whether the transition is direct or indirect[136]. The origin of these values is explained in more detail in section 3.5.7.

Based on this the standard procedure for producing a Tauc plot is to acquire absorbance data over an energy range containing the bandgap of the material then plotting $(\alpha h\nu)^{1/n}$ against $h\nu$. A linear fit is applied to the absorption edge and the x-intercept is taken as the bandgap. If the type of transition is known prior to plotting the correct n can be used initially, if it is not known it can be identified by testing the different possible n values and identifying which gives the best fit.

4.3.2 Extracting Film Thickness

In a stack of materials, reflection of some light will occur at each interface. Dependent on the ratio of the wavelength of the light and the thickness of the film, the reflected light may interfere either constructively or destructively. If the thickness is equal to $n\lambda/2$, where n is an integer and λ is the wavelength, destructive interference will occur reducing the intensity of the transmitted light. If the thickness is $n\lambda/4$ where n is an odd integer constructive interference occurs increasing the intensity of transmitted light. As such, the separation of interference fringes in transmission or reflection spectra is dependent on the thickness of the samples and as such the thickness can be extracted from such spectra.

If other properties of the film are known the film thickness can be extracted by fitting of that data using the transfer matrix method as discussed in section 3.4. This however requires prior knowledge of the films dielectric constant.

4.3.3 FTIR

Optical measurements covering the infrared, IR, region of light are performed using Fourier-transform IR (FTIR) spectroscopy. This differs from UV-Vis spectrosopy mainly in the fact that rather than shining monochromated light through the sample and scanning through wavelengths polychromatic light containing a range of wavelengths is shone on the sample. In FTIR spectroscopy a polychromatic IR source shines light into an Michelson interferometer which directs the light into a sample compartment and then onto a detector.

In the Michelson interferometer the incident light falls onto a beamsplitter which reflects half of the incident light onto a fixed mirror and transmits the other half onto a movable mirror. The mirrors reflect the two beams of light back onto the beamsplitter where they are recombined, directed at the sample compartment. The set up of the sample compartment is dependent on whether transmission or reflectivity is being measured. After interacting with the sample the light exits the sample compartment and reaches the detector. This set up is depicted in Figure 4.3.

The path difference between the paths travelled by light reflected off the two mirrors is $2x$ as shown in Figure 4.3. As such the time difference in the two paths, τ, before reaching the detector is $2x/c$ where c is the speed of light. As the position of the movable mirror changes, different wavelengths will interfere constructively and destructively. By scanning through path differences

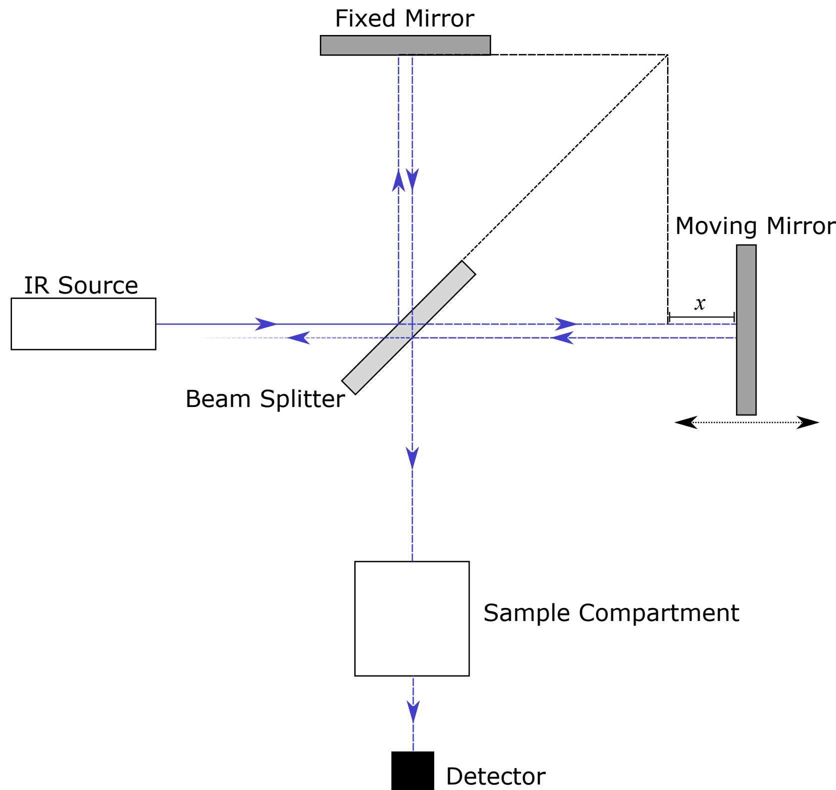

Figure 4.3: Diagram showing the beam path through an FTIR spectroscope showing the components of a Michelson interferometer

and measuring signal intensity, an interferogram can is constructed. The interferogram is translated into a spectrum via a fast fourier transform, FFT, algorithm.

As FTIR spectrometers measure all frequencies of light simultaneously, measurements are quick and provide a better signal to noise ratio compared to dispersive spectroscopy techniques such as UV-Vis spectroscopy. However, FTIR is limited at short wavelengths, or high energies. Generally, FTIR spectroscopy is not possible for wavelengths shorter than around 700 nm, energies higher than 1.77 eV. As such it is not suitable for looking at the bandgap of wide bandgap semiconductors such as those used as TCOs where optical bandgaps of greater than 3 eV are standard.

4.3.4 Extracting Plasma Frequency

Within this thesis, FTIR measurements are primarily used to indirectly measure the plasma frequency of a material. This is achieved by measuring a reflectively spectra over a range of wavelengths within which the plasma frequency is expected to fall. This experimental data is then fitted using the transfer matrix method described in section 3.4. The refractive index of the material is calculated using the one of the ossilator models of the dielectric function discussed

in section 3.3. For the work in this thesis the two oscillator model described in section 3.3.2 is used. Plasma frequency is a variable within this model and can be extracted using least square minimisation fit of the data.

4.4 X-ray Diffraction

X-ray diffraction is a crystallographic technique used to determine the atomic or molecular structure of a crystalline material. When x-rays are incident on a material they are scattered by the atoms within the material. In the regular periodic array of atoms present in a crystal, the x-rays are reflected off of the atomic planes. As such, light reflected off of the different planes will interfere with each other. Dependent on the angle of incidence and the ratio of the atomic spacing and x-ray wavelength the interference will be constructive or destructive. The reflected light interferes constructively when the conditions of Bragg's law are met. Bragg's law is shown in equation 4.12 in which n is any positive integer.

$$n\lambda = 2d\sin\theta \tag{4.12}$$

where λ is the wavelength of the incident x-rays, d is the inter-atomic spacing and θ is the angle of incidence.

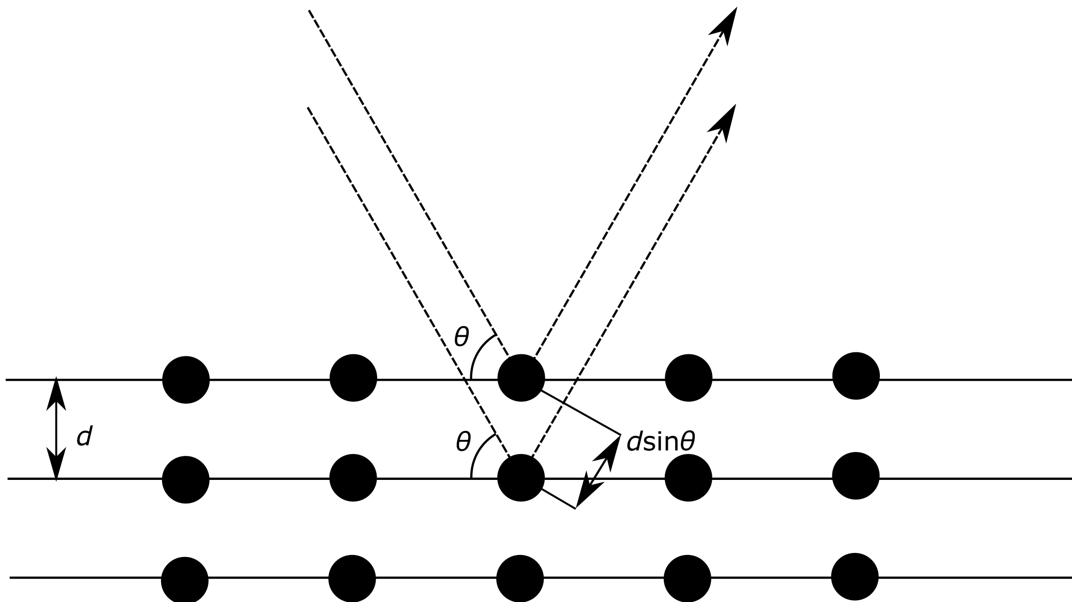

Figure 4.4: Bragg diffraction from two parallel crystal planes. The dashed lines represent the incident and reflected x-rays.

By measuring the intensity of diffracted light as a function of scattering angle, a diffraction pattern can be created. Peaks will be present at angles where the conditions of Bragg's law

are met. From these patterns, information about orientation of polycrystalline samples can be obtained along with lattice constants and the crystallinity of the sample.

4.4.1 Measurement Geometry

To measure a diffraction pattern an x-ray diffractometer is used. In their most basic form these consist of a monochromated x-ray source, a sample plate and a scintillation detector. To vary the scattering angle measured, the source and detector are usually moved round the sample. Different geometries can be used for these measurements but the most commonly used are the Bragg-Brentano and parallel beam geometries.

Bragg-Brentano is the simplest and most commonly used geometry. These measurements are commonly referred to as $\theta - 2\theta$ scans. This is because in such measurements the source is kept stationary while the sample and detector are rotated by θ and 2θ around the sample respectively. Some diffractometers achieve the same effect by rotating the source and detector around a stationary, usually horizontal, sample by $-\theta$ and θ respectively. Figure 4.5 (a) shows a diagram of the Bragg-Brentano Geometry.

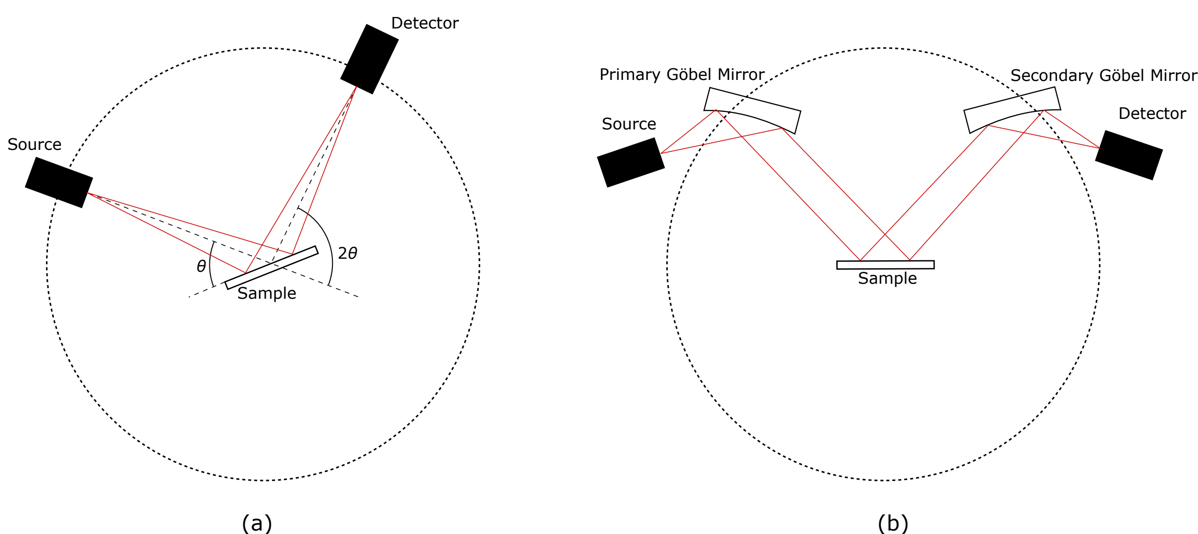

Figure 4.5: Diagrams of XRD geometries. (a) shows Bragg-Brentano geometry and (b) shows parallel beam geometry.

Another commonly used geometry for XRD measurements is the parallel beam, PB, geometry. In PB geometry the incident x-rays are directed into high intensity parallel beams by a Göbel mirror. A Göbel mirror consists of a multilayer crystal with atomic layer spacing designed to reflect x-rays of a particular wavelength. The crystal is curved so that the reflected beams are all parallel. As whether light is reflected off a Göbel mirror is dependent on wavelength, background Bremsstrahlung radiation is suppressed.

Each of these geometries provide benefits over the other and are therefore the choice of geom-

etry should depend on the measurement being performed. Bragg-Brentano geometry provides higher resolution and beam intensity than PB but requires careful alignment of the optics and a carefully prepared sample. A sample must be flat and have low roughness to successfully utilise Bragg-Brentano as the separation of source and sample and the separation of sample and detector must be equal for correct focusing. PB overcome these limitations as focusing occurs away from the sample at the Göbel mirrors, allowing for a greater diversity of samples to be measured. PB does, however, provide lower counts and broader peaks than Bragg-Brentano meaning measurements will be more time consuming or the data will be of a lower quality so where samples are suitable Bragg-Brentano will be preferable.

4.5 X-ray Photo-electron Spectroscopy

X-ray photo-electron spectroscopy (XPS) is a spectroscopic technique where the binding energy of electrons within a material are probed. This gives information on the chemical composition of a material as well as the electronic and chemical states of the elements within it. XPS and a variant, hard X-ray photo-electron spectroscopy (HAXPES), are used throughout the work presented in this thesis. The working principles and the basics of data analysis for these techniques are discussed in this section.

4.5.1 Basic Working Principles

In XPS, X-rays of a known wavelength and therefore energy are incident on a sample. The X-rays interact with the electrons within the sample causing the emission of photo-electrons. The kinetic energy of the emitted photo-electrons, E_k is measured by an analyser. As the energy of the incident X-rays, $h\nu$, is known, the binding energy of the electrons, E_b can be calculated.

$$E_b = h\nu - (E_k + \Phi) \tag{4.13}$$

where Φ is the work function of the analyser. The inclusion of this work function term is to account for the fact that the photo-electron loses a small amount of energy, of the order of a few eV, to the instruments detector upon absorbtion.

Figure 4.6 shows a simplified diagram of the experimental set up for XPS utilising a hemispherical analyser.

When a photo-electron is liberated, it first travels through a series of electrostatic electron lenses. These lenses serve two main purposes, focusing the electrons on the entrance slit of the analyser and to reduce the kinetic energy of electrons of a certain energy to be equal to the pass energy of the analyser.

The hemispherical analyser's purpose is to only allow electrons with a certain kinetic energy to reach the detector. The kinetic energy the analyser allows through is known as the pass energy.

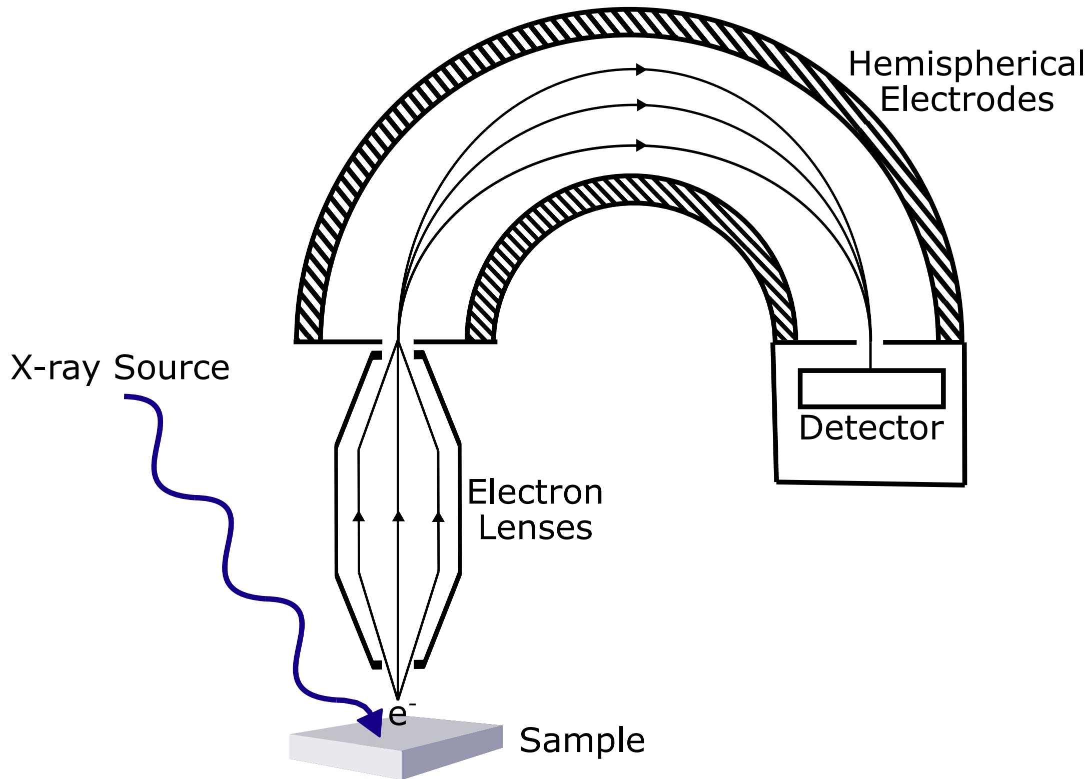

Figure 4.6: Diagram showing the experimental set up for XPS utilising a hemispherical electron analyser.

The two hemispherical electrodes have potentials applied to them which bends the path of the electrons travelling through the analyser so that only those possessing a specific kinetic energy, the pass energy, exit through the exit slit and reach the detector.

The potentials applied to each hemispherical electrode are dependent on their radii and the desired pass energy, E_0. The potentials applied to the inner hemisphere, V_1, and outer hemisphere, V_2, are given by

$$V_1(R_1) = V_0\left[\frac{2R_0}{R_1} - 1\right] \tag{4.14}$$

and

$$V_2(R_2) = V_0\left[\frac{2R_0}{R_2} - 1\right] \tag{4.15}$$

in which R_1 and R_2 are the radii of the inner and outer hemispheres, V_0 is the voltage corresponding to the desired pass energy and R_0 is the radius of the path required for an electron to reach the exit slit.

Selecting a pass energy is a trade off between energy resolution and counts in the final scan.

4.5.2 X-ray Generation and Monochromators

To generate the X-rays, a metallic anode is bombarded with high energy electrons. In XPS this anode is generally made of either Mg or Al. The bombarding electrons interact with electrons within the anode, liberating them. Electrons from higher energy orbitals will fall into the generated vacancy releasing a photon with energy equal to the difference in energy of the two orbitals.

The energy spectrum of emitted X-rays consists of a characteristic peaks. The characteristic peaks have energy equal to the difference in energy of the orbitals. In X-ray notation the transitions are given a letter K, L, M depending on the orbital the electron is transitioning into, A transition into the 1s orbital is a K transition. The distance between the orbitals in the transition is notated by Greek letters. If the orbitals involved are adjacent, for example from 2 to 1 or from 3 to 2 this called an α transition but if there are separated by another shell, such as a transition from 3 to 1, this is called a β transition.

The characteristic peaks are present on a broad background. The background can be attributed to bremsstrahlung (braking) radiation. This radiation is emitted when a charged particle such as an electron decelerates due to the conservation of energy. The spectrum for bremsstrahlung radiation is continuous increasing in intensity towards higher energy.

For XPS, ideally X-rays of a single known energy should be used so that the binding energy of the emitted electrons can be known with certainty from equation 4.13. To achieve this the emitted X-rays are generally monochromated. Monochromation of X-rays is achieved by utilising Bragg diffraction so that only X-rays of a certain wavelength are reflected from a crystal. Bragg's law is show in equation 4.12 and explained in section4.4. This means that by adjusting the angle of incidence of X-rays onto a crystal of known atomic spacing X-rays of only a specific energy will be reflected. The monochromating crystal is also curved to focus the reflected X-rays onto the sample [137]. This results in X-rays of energy 1486.7 eV for a monochromated Al Kα source and 1253.6 eV for a monochromated Mg Kα source.

4.5.3 Peak Broadening

While an electron within a specific orbital will have a specific binding energy, the peaks obtained in an XPS spectra will have a width. The exact shape, known as the line shape, of the peak is dependent on many aspects of the chemical environment but two properties that primarily contribute are instrumental broadening and the core-hole lifetime.

Instrumental broadening occurs based on the pass energy and slit width of the analyser. The natural line width of the x-ray source also contributes to broadening. When fitting a peak, this can be modelled as Gaussian function with the full width half maximum, FWHM, determined by the instrumentation. A Gaussian function is described as

$$F_g(E) = \frac{1}{\sqrt{2\pi\sigma^2}} e^{\frac{(E-E_0)^2}{2\sigma^2}} \tag{4.16}$$

where σ is the standard deviation of the energies recorded and E_0 is the expected energy of the peak which will be the peak centre. The FWHM of the function is given by $\Gamma = 2\sqrt{2\ln 2}\,\sigma$.

The core-hole lifetime is important as when an electron is liberated in XPS a core hole is left in its place. This causes the system to relax and change the apparent binding energies of other photo-electrons until the hole is filled. Peak broadening due to core-hole lifetimes can be modelled using a Lorentzian function [138].

$$F_L(E) = \frac{1}{\pi} \frac{0.5\Gamma}{(E-E_0)^2 + (0.5\Gamma)^2} \tag{4.17}$$

where Γ is the FWHM of the peak.

To account for both of these contributions to broadening, peaks in XPS are generally fitted with a convolution of a Gaussian and Lorentzian function. This convolution of functions is commonly called a Voigt function. Figure 4.7 shows examples of a Gaussian, a Lorentzian and a convolved Voigt function for comparison.

4.5.4 Binding Energy Shifts

As previously mentioned elements can be identified based on the characteristic peaks present in photo-emission spectra. The apparent binding energy of a characteristic peak however can be shifted due to a range of phenomena.

One of the most common causes of a shift in binding energy in a change in the oxidation state of the element. The higher the oxidation state the higher the binding energy of the electron due to increased coulombic attraction between the emitted electron and the ionic core. This means that it is possible to differentiate between different oxidation states of elements within a material using XPS. The chemical environment of the element can also cause a shift in binding energy even within the same oxidation state. This means the element that it is directly bonded to can impact the binding energy.

Losses due to interactions within the material as the electron escapes can also cause an shift in the apparent binding energy of the characteristic peak. One example of this is loss of kinetic energy due to interactions with plasmons within the material. In this case the electron will lose energy equal to the plasma energy so all electrons that experience this loss will lose the same amount of energy. Therfore a secondary peak with a higher apparent binding energy will form. This peak will have an apparent binding energy greater than that of the characteristic peak equal to the plasma energy of he material.

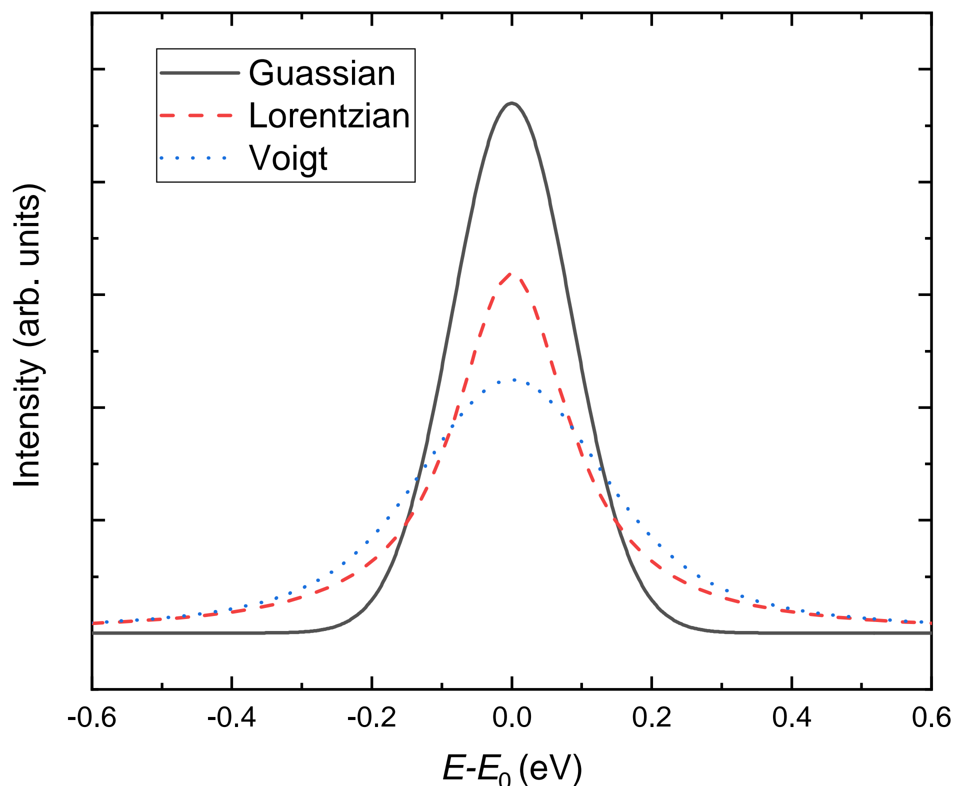

Figure 4.7: Examples of peaks with line shapes of Gaussian, Lorentzian and Voigt functions. Γ and σ are both set to 0.1 for each function and E_0 is set to 0 eV to centre the peaks around 0 eV.

4.5.5 HAXPES

Hard x-ray photo-electron spectroscopy, HAXPES, is a variant of XPS utilising higher energy x-rays. while conventional uses X-rays of energy around 1500 eV or lower known as 'soft' X-rays, HAXPES uses 'hard' X-rays in the energy range of 2-10 keV [139]. Such energies can not generally be achieved using conventional X-ray sources and as such HAXPES is usually performed utilising synchrotron radiation.

These differences have a significant impact on the results of the experiment. Firstly the higher photon energy increases the probing depth (this is discussed in more depth in section 4.5.9). As such, one of the primary uses for HAXPES is depth profiling by comparing the HAXPES spectra to a lower energy XPS spectra. This also makes the technique useful for probing features below the surface such as buried junctions.

As explained in detail in section 4.5.8, the relative intensities of the photoionisation cross-sections for different orbital shells change with photon energy. As such, certain features are more prominent in HAXPES than XPS. While all cross-sections decrease with increased photon energy this does not mean that HAXPES spectra have lower intensity as the increased intensity of synchrotron radiation significantly outweighs the reductions in cross-sections.

4.5.6 Spin Orbit Splitting

The difference between s, p, d and f orbitals is the orbital angular momentum quantum number, ℓ, with $\ell = 0$ for the s orbital then increasing by one though the series. An electron also possesses a spin angular momentum quantum number, s, which is equal to ±½.

The total angular moment quantum number, j, is equal to $|\ell+s|$. As a result, for all orbitals other than the s orbital, two possible values of j exist. This manifests as a splitting of the orbital energy level into two possible energy states. In XPS this manifests as two peaks of different binding energy for these orbitals. The area ratio of these peaks is based on the degeneracy of the spin states, all orbitals with a certain ℓ value will always have the same area ratio. The degeneracy of each state is $2j$+1 and the ratio of the areas is equal to the ratio of these values [140]. The values of ℓ, j and the area ratio of the doublets for each orbital is shown in Table 4.2.

Table 4.2: The possible quantum numbers of different orbitals and the corresponding peak area ratios in XPS.

Orbital	ℓ	j	Area Ratio
s	0	1/2	N/A
p	1	1/2, 3/2	1:2
d	2	3/2, 5/2	2:3
f	3	5/2, 7/2	3:4

Separation of the doublets is constant for each orbital of each element and the value for most are known [141]. The binding energy difference, ΔE, between the two features of a doublet is dependent on the four quantum numbers j, ℓ, s and n as well as the nuclear charge of the atom, Z. n is the principal quantum number and describes the principal shell. For example, the 1s orbital has an n value of 1 and the 2s and 2p orbitals have an n value of 2, increasing as the orbitals increase in distance from the nucleus. The shift in binding energy due to spin orbit coupling is given by

$$\Delta E = \frac{\beta(n,\ell)}{2}(j(j+1) - \ell(\ell+1) - s(s+1)) \tag{4.18}$$

in which

$$\beta(n,\ell) = Z^4 \frac{\mu_0}{4\pi} g_s \mu_B^2 \frac{1}{n^3 \alpha_0^3 \ell(\ell+1/2)(\ell+1)} \tag{4.19}$$

where μ_0 is the permeability of free space, g_s is the g-factor, a dimensionless quantity describing the magnetic moment of a particle and for an electron is ~2, μ_B is the Bohr magneton and α_0 is the Bohr radius.

The implication of equation 4.18 is that the larger j value shifts to lower binding energy and the lower j value shifts to a higher binding energy. The separation of the doublets increases with increasing atomic number due to the dependence on Z.

As such, calculation of the separation of the peaks that arise due to spin orbit splitting can be a useful tool in the identification of features in XPS spectra and be a useful restraint in their fitting.

4.5.7 Valence Band and Conduction Band Emission

While core levels manifest as distinct peaks, the valence band is made up of a mixture of levels from all elements within the compound. As the region consists of many features, contributed by many different orbitals, overlapping extracting information from the valence band emission is more difficult. However, it can be considered a measurement of the occupied density of states. Valence band spectra do tend to have distinct shapes and as such can be used to distinguish between materials which have core levels in similar positions [141].

As the binding energies of valence band levels are low the intensity of its features are also low. As such, long scan times are required to obtain high quality data with a high signal to noise ratio even when utilising the higher counts achieved in HAXPES compared to XPS.

In metals and degenerately doped semiconductors scans of this region can also be used to observe emission from the conduction band as these bands are occupied in such materials. This allows for direct observation of the position of the Fermi level in these materials.

4.5.8 Interaction Cross-sections

The cross-section of an interaction describes the probability of it occurring. In XPS, the interaction cross-sections of importance are the photo-ionisation cross-sections, the probability that the incident photon will liberate an electron. These cross-sections are dependent on photon energy, the electron binding energy and the orbital of the electron.

The simplest method by which photo-ionisation cross-section for an electronic subshell $n\ell$ and x-ray of energy $h\nu$ can be calculated is by utilising the dipole approximation using equation 4.20 [142, 143]

$$\sigma_{n\ell}(h\nu) = \frac{4\pi^2\alpha_0 a_0^2}{3}\frac{N_{n\ell}}{2\ell+1}h\nu[\ell R_{\ell-1}^2(E_k) + (\ell+1)\ell R_{\ell+1}^2(E_k)] \tag{4.20}$$

In this expression α_0 is the fine structure constant (~1/137) and a_0 is the Bohr radius. $N_{n\ell}$ is the occupation of the $n\ell$ subshell and E_k is the kinetic energy of the ionised liberated electron.

$R_{\ell+1}$ and $R_{\ell-1}$ are the one electron radial dipole matrix elements summed over the two final allowed energy states, $\phi_{E_k,\ell\pm1}$ (that of the ionic core and that of the unbound electron), for photo-emission from a the initial ground state $\phi_{n\ell}$. These matrix elements can be expressed as

$$R_{\ell\pm1} = \int_0^\infty P_{n\ell}(r) r P_{E_k,\ell\pm1}(r) dr \tag{4.21}$$

$\frac{P_{n\ell}(r)}{r}$ and $\frac{P_{E_k,\ell\pm1}}{r}$ are the initial and final radial wave functions for photo-emission from subshell $n\ell$ meaning that

$$\phi_{n\ell} = R_{n\ell}(r)Y_{n\ell}(\theta,\phi) = \frac{P_{n\ell}(r)}{r}Y_{n\ell}(\phi,\theta) \tag{4.22}$$

where $Y_{n\ell}(\theta,\phi)$ is the spherical harmonics of the wave function.

To solve equation 4.20 solutions to the radial Schrödinger equation are required for the initial and final state of the electron. The equations for these two cases are

$$\left(\frac{d^2}{dr^2} + V(r) + E_{n\ell} - \frac{\ell(\ell+1)}{r^2}\right)P_{n\ell}(r) = 0 \tag{4.23}$$

and

$$\left(\frac{d^2}{dr^2} + V(r) + E_k - \frac{(\ell\pm1)(\ell\pm1+1)}{r^2}\right)P_{E_k,\ell\pm1}(r) = 0 \tag{4.24}$$

where $V(r)$ is the central potential experienced by an electron in subshell $n\ell$. $P_{n\ell}(r)$ and $P_{E_k}, \ell\pm1$ can be seen to be solution of equations 4.23 and 4.24 respectively. The potential in the two equations is the same which is a central assumption for this approximation. Evaluation of these equations allows for the radial matrix elements to be obtained and for equation 4.20 to be solved for a given orbital. Solving this is far from trivial but several data bases of the photo-ionisation cross-sections for a wide range of elements exist calculated using this or similar methods [143–147]. Figure 4.8 shows the photo-ionisation cross-sections for the outer orbitals of In and O, the composite elements of In_2O_3, as a function of incident photon energy as taken from reference 144.

It can be seen that for In, the 4d orbitals have the highest interaction cross sections are the highest followed by the 5s and the 5p. This tends to be the case for the majority of elements. The cross-section of the d orbital decreases the quickest with increasing photon energy.

4.5.9 Probing Depth and Photon Energy

While electrons from a broad range of depths may be emitted due to photo-excitation, only electrons very close to the surface will escape the sample with no energy loss. Only these electrons will contribute to the characteristic peaks of the spectrum. Other electrons will have a reduced kinetic energy due to interactions as they leave the sample and therefore an increased apparent binding energy. These electrons contribute to the background. The difference between background electrons and characteristic electrons is shown in Figure 4.9.

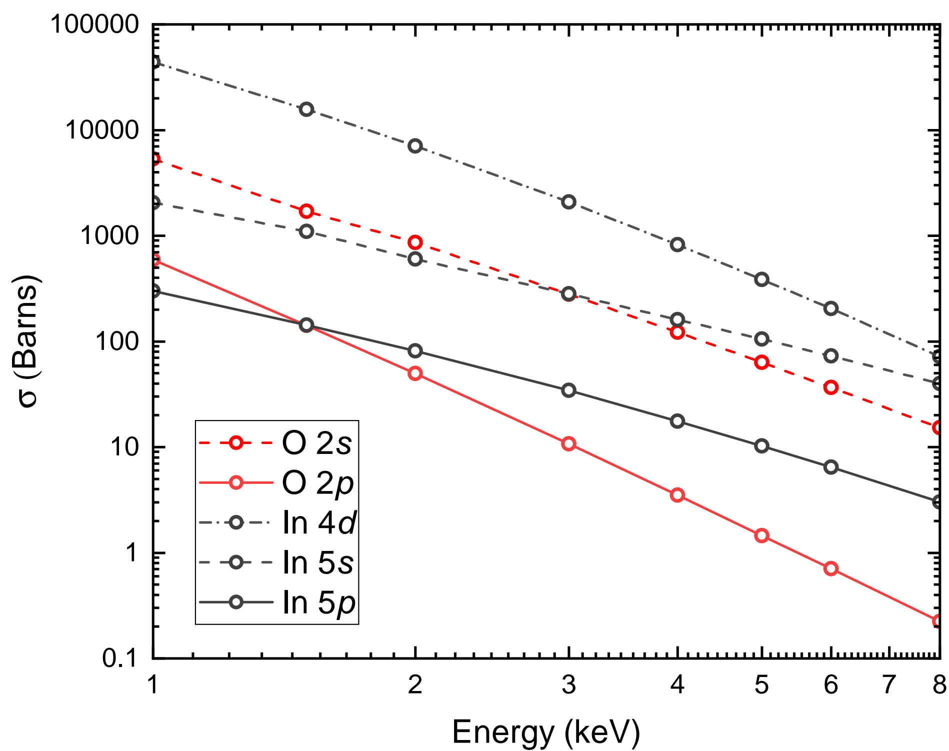

Figure 4.8: Photo-ionisation cross-sections, σ, for the outer orbitals of In and O as a function of incident photon energy over the range at which the majority of photo-emission spectroscopy is performed.

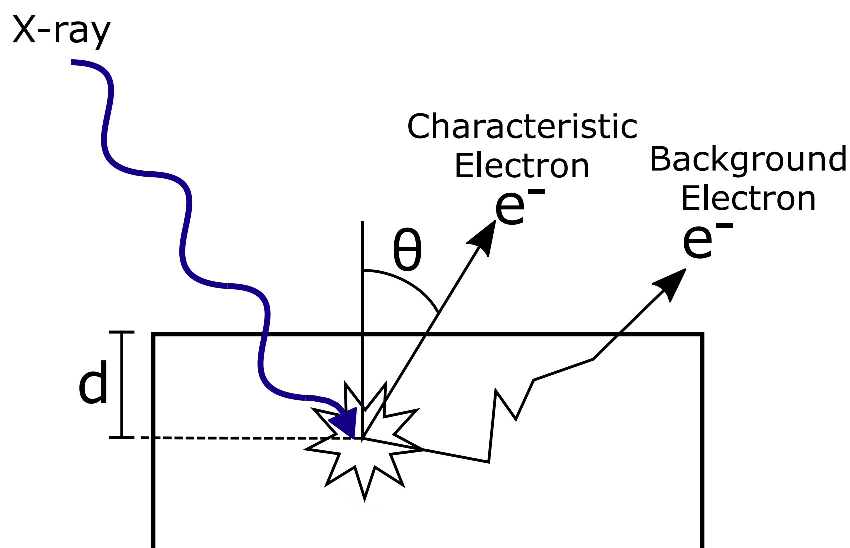

Figure 4.9: Diagram showing the difference between characteristic electrons, which have no kinetic energy loss, and background electrons, which have lost kinetic energy before exiting the sample.

The contribution of electrons with no kinetic energy loss decreases exponentially with depth, d, following the expression

$$I = I_0 \exp\left(\frac{-d}{\lambda \cos\theta}\right) \tag{4.25}$$

where λ is the mean free path of the electron and θ angle of the electron's initial trajectory relative to the normal of the surface. Based on this, it is expected that 95% of the signal in XPS comes from a depth within the first 3λ.

λ varies with kinetic energy and therefore the incident photon energy. As such, the probing depth of XPS is dependent on photon energy. While λ is also dependent on the properties of the material such as atomic density, generally the inelastic mean free path of photoelectrons in XPS, with a photon energy of 1487 eV, will have a mean free path of around 3 nm. This means that the significant majority of the signal in XPS will generally originate from the first 10 nm of the sample. Also, as the mean free path is dependent on kinetic energy, the probing depth of XPS is dependent on the the binding energy of the level being probed. Higher binding energy levels will have lower kinetic energy when liberated and therefore the mean free path will vary as shown in the top graph of Figure 4.10.

An approximation of the peak intensity can be calculated using the mean free path, λ, the interaction cross-section described in the previous section, σ [143].

$$I \propto n\sigma\lambda\varsigma \tag{4.26}$$

where n is the atomic density of the element the peak is attributed to and ς is a parameter encompassing terms specific to the spectrometer as experimental geometry. As ς is constant when utilising the same experimental set up it possible to find the ratio of elements in a compound using equation 4.26 when σ and λ are known. Data bases exist containing information of both σ and λ for a large array of elements as such comparing peak intensities in XPS can be a useful method in estimating the elemental composition of a compound.

4.5.10 Auger Electrons

When a core-level electron is emitted, such as in photoemission, a vacancy is left in its place. An electron in a higher energy orbital may fall into this vacancy resulting in the release of energy. Commonly, this energy will be emitted in the form of a photon but it is also possible that it will be given to another electron which is then emitted. This second emitted electron is an Auger electron [141, 148]. Figure 4.11 shows a diagram showing the Auger effect.

The kinetic energy of an Auger electron, E_{Auger} is dependent on the energy of the transition of the electron filling the vacancy, ΔE and the binding energy of the orbital the electron was

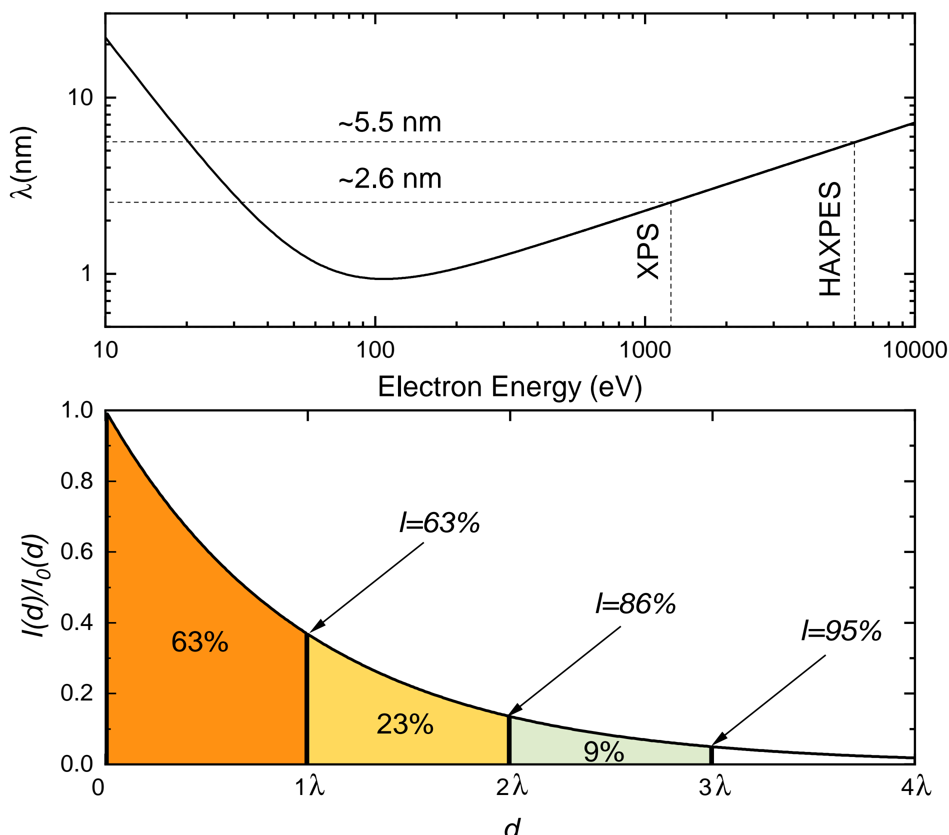

Figure 4.10: (Top) The inelastic mean free path, λ, as a function of electron energy The values of λ for energies corresponding to XPS and HAXPES measurements performed in this work are shown. (Bottom) the ratio of photo-electrons generated at depth, d, which escape the sample without reduced kinetic energy. The area under the curve corresponds to the percentage of the signal which originates from that depth.

emitted from, E_b.

$$E_{Auger} = \Delta E - E_b \tag{4.27}$$

As the kinetic energy is independent of the incident phonon energy, E_p the measured kinetic energy of Auger electrons in XPS will only depend on the element from which the electron is emitted and the orbitals involved. Because of this, as can be seen from equation 4.13 the apparent binding energy of an Auger electron is dependent on the incident photon energy. The higher E_p the higher the apparent binding energy of the Auger electron. A result of this is that Auger features tend to only be visible in spectra measured with a low photon energy and not in HAXPES measurements. This can considered an advantage of HAXPES as there is a decreased chance of overlap between the Auger features and core level peaks [139].

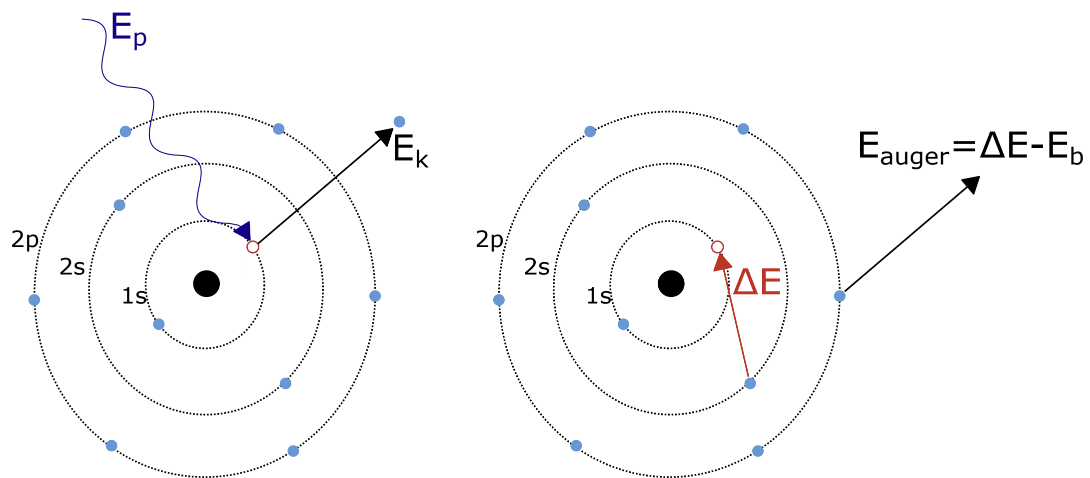

Figure 4.11: Diagram showing the Auger effect and the emission of an Auger electron.

Chapter 5

Ce doping of In_2O_3

5.1 Introduction

Traditionally Sn has been used to dope In_2O_3 n-type due to its correct preferred oxidation state and close proximity to In on the periodic table. However, more recent research has focused on the use of alternative dopant, most commonly transition metals which are stable in the correct oxidation state.

Such dopants have been shown to achieve significantly higher mobilities for comparable carrier concentrations in comparison to Sn. Beyond this one range of materials that have had little consideration as dopants in In_2O_3 are the f-block elements, the lanthanides and actinides.

5.2 f-Block elements

At the bottom of the periodic table there are two rows of elements, the lanthanides and the actinides, named for the first element in each row, lanthanum and actinium respectively. Together these elements are known as the f-block elements as their outer most filled electron orbital is an f-orbital. The Lanthanides have a partially filled $4f$-orbital while the actinides have partially filled $5f$-orbitals.

5.2.1 Abundance

Of the 14 actinides only two occur within the Earth's crust with any reasonable abundance. These are thorium, Th, and uranium, U. Both of these elements are radioactive and as such are unsuitable for many materials applications including their potential use as a dopant in a material.

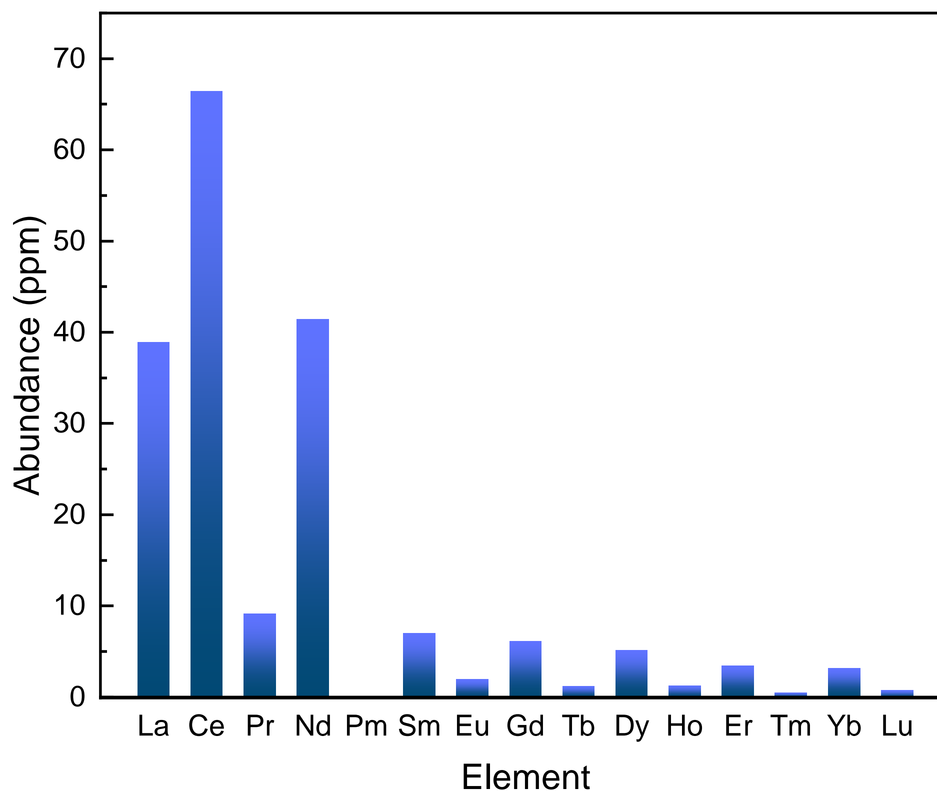

Figure 5.1: The relative abundance of the Lanthanides in the Earth's crust

Another common name used for the lanthanides is 'rare Earth metals.' While this names is applicable for some elements within the block the descriptor 'rare' is far from true for many others .

Most of the the lanthanides are by no means rare. All but one, promethium, occur naturally within the Earth's crust. Most of these are primarily found with the mineral bastnasite which is a mixed lanthanide fluorocarbonate with the chemical formula $LnFCO_3$ in which Ln is a mixture of lanthanides. In bastnasite the most abundant lanthanide is Ce at 49% followed by La and Nd at 33% and 12% respectively. The other lanthanides of there than Pm each make up less than 5% each. Because of this, Ce is the most abundant of the rare earth metals.

The relative abundance of each lanthanide within the Earth's crust is shown in Figure 5.1. Ce, the most abundant lanthanide, has an abundance of 66.5 ppm. For comparison, In, a major constituent of In_2O_3, has an abundance of around 50 ppm, making it over 1000 times less abundant. This means, excluding the non-naturally occurring Pm, use of such elements in a material should not be a limiting factor in production [149].

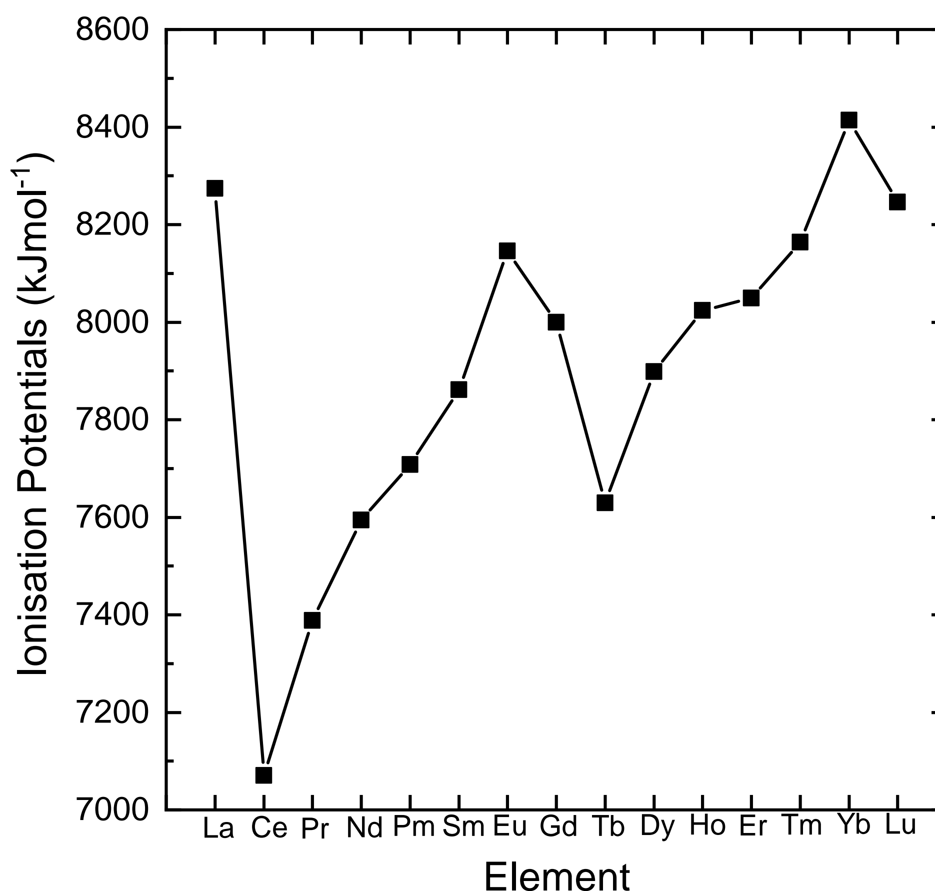

Figure 5.2: The sum of the first four ionisation potential energies of elements in the lanthanide block of elements. Recreated from reference [149]

5.2.2 Oxidation States

In general the most stable oxidation state for all the lanthanides is the (III) oxidation state. Beyond this, (II) and (IV) oxidation states are known for several of the lanthanides and are stable in some specific compounds.

To dope In_2O_3 on the cation site the dopant needs to be in a (IV) oxidation state. Figure 5.2 shows the sum of the first four ionisation potential of the lanthanides. This shows the energy required to remove the four outermost electrons and get the element into the (IV) oxidation state. A clear minimum is seen at Ce which means that it is a more accessible oxidation state than (IV) of the other lanthanides. This is due to Ce electronic configuration of [Xe]$4f^1 5d^1 6s^2$ which means that in the (IV) oxidation state has an empty $4f$ orbital which increases the stability of the state. Many compounds counting Ce (IV) are known in both liquid and solid forms. Among these is the stable oxide of Ce, CeO_2.

The (IV) oxidation state of the other lanthanides tend to less accessible due to the high binding energy of the $4f$ electrons beyond the first. Based on this, of the lanthanides, only Ce

appears to be suitable as a potential dopant in In_2O_3.

5.2.3 Ionic Radii

The atomic radii of the lanthanides are generally smaller than could be expected of elements with such a high atomic number. This effect is more pronounced the further into the group. This is the case due to a phenomena known as 'lanthanide contractions [149].'

This phenomena occurs due to the poor shielding of uclear attractive forces by f electrons. The 6 s electrons, which are the outermost electrons in all the unionised lanthanides, are draw closer to the nucleus resulting in a smaller atomic radius. The nuclear charge increases down the group increasing the attractive force felt by electrons while the additional $4f$ electrons do not provide sufficient shielding to compensate.

When ionised, the radii of elements decreases as electrons are drawn closer to the nucleus. In its two stable oxidation states, (III) and (IV), Ce has an ionic radius of 101 pm and 87 pm respectively for a co-ordination number of 6. This is the co-ordination number of both In sites in In_2O_3. In (III) with a co-ordiantion number of 6 has an ionic radii of 80 pm. This means that Ce (IV) is closer in ionic radii to In than the established dopant Sn which has an ionic radii of 69 pm in the (IV) oxidaiton state with a co-ordiantion number of 6 [150]. As such, if Ce were to be used as a dopant in In_2O_3, reduced lattice strain could be expected in comparison to ITO, improving conductivity.

5.3 Novel Dopants in In_2O_3

While Sn dominates as a dopant in In_2O_3, particularly for industrial applications, a range of novel alternative dopants have garnered some interest. Most of these dopants are transition metals from the d-block of the periodic table which are stable in the (IV) oxidation state making them suitable cation dopants. Traditional wisdom suggests that reduced mobility should be expected when using these dopants compared to Sn as their ionic radii is further from that of In. This is not the case however, these alternative dopant have all displayed significantly improved mobilities in comparison to ITO.

Where each of these dopants do display inferior properties to ITO is carrier concentration. With the exception of Ti these dopants fall significantly short of the highest carrier concentrations seen in ITO.

Figure 5.3 shows the mobility against carrier concentration for a range of dopants in In_2O_3 as reported in the literature. Throughout this section the electrical properties achieved with each of these dopants are discussed along with the understanding of how each dopant behaves, as reported in the literature.

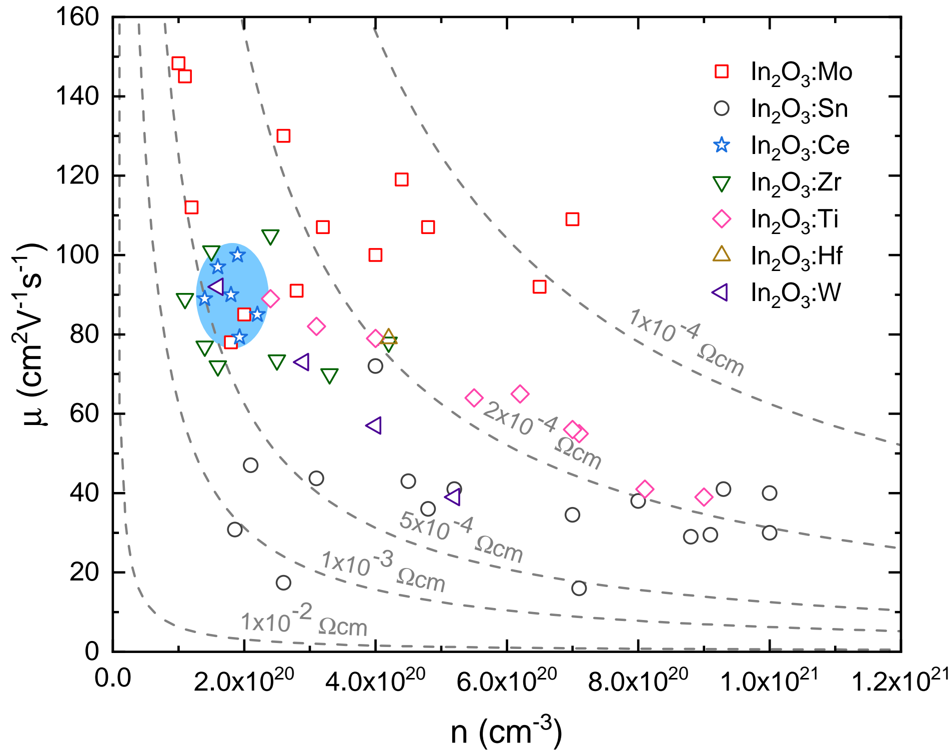

Figure 5.3: Carrier concentration and mobility of a range of Mo [5, 151–153], Sn [154–158], Zr [159, 160], Ti [161, 162], W [163–165] and Ce [165, 166] doped In_2O_3 samples as reported in the literature. Grey dashed lines show constant resistivity. The light blue area shows the region in which all Ce doped In_2O_3 samples fall.

5.3.1 Mo Doping of In_2O_3

Of these transition metal dopants molybdenum has had the most research published on it. Mo doped In_2O_3 has regularly displayed the highest mobilities of any doped In_2O_3. Mobilities as high as 149 $cm^2V^{-1}s^{-1}$ have been reported for high quality films with lower carrier concentrations, ~2×10^{20} cm^{-3} [75]. The high mobilities are maintained in the high limits of IMO carrier concentrations with mobilities of up to 110 $cm^2V^{-1}s^{-1}$ at carrier concentration around 7×10^{20} cm^{-3}. The highest reported limit on carrier concentrations are lower than those reported for ITO which reach up to >1×10^{20} cm−3 however the higher mobilities mean that the resistivities are still comparable.

Mo is stable in IV and VI oxidation states with a preference towards the VI oxidation state. In In_2O_3 it was believed that Mo incorporated as Mo(VI) [167] which would make it a triple electron donor which would be negative for mobility as explained in section 2.2.3. Recent work has shown that Mo in fact incorporates as Mo(IV) except at the surface where Mo(VI) is present [168]

Explanations of the enhanced mobilities seen in IMO have been provided mostly revolving

around the d state nature of of the donor states. Bhachu et al suggested a 'remote screening mechanism' to be the origin of the high mobility. As the donor state did not contribute significantly to the CBM the amplitude of conduction band wave function is small at the donor centre. As such the conduction band electrons travel remotely from the donor centres reducing the coulomb scattering they experience [168].

Swallow et al suggested that the d donor state sitting higher in the conduction band, and its different shape to the p states making up the host CBM, preventing mixing of the donor state and the CBM. In the case of Sn doping the donor orbital is p in nature and does mix with host CBM states. This causes broadening of the conduction band increasing the carrier effective mass and reducing mobility as more Sn is introduced into the material. In the case of Mo doping the original shape of the host CBM is maintained and the carrier effective mass remains low allowing for the higher mobilities observed [75].

How much and whether each of these mechanisms contribute to the high mobilities seen in IMO is still disputed as little literature exists on the matter. Stronger experimental evidence is provided for the explanation given by Swallow et al utilising XPS and inverse photo-emission spectroscopy (IPES) to observe the different shapes of the conduction band in IMO and ITO but this does not necessarily mean there is no contribution from the remote screening proposed by Bachu et al.

5.3.2 Other Transition Metal dopants

Work has been performed investigating the potential use of all other transition metals which are stable in the (IV) oxidation state as dopants in In_2O_3. These elements are Ti, Zr, Hf and W. As shown in figure 5.3 each of these have displayed improved mobilities over ITO in certain carrier concentration ranges.

Of all these transtion metal dopants, including Mo, Ti displays the highest carrier concentrations of up to 9×10^{20} cm^{-3} [162]. This is close to the highest carrier concentrations observed in ITO. However at these carrier concentrations Ti doping only achieves mobilities of up to ~40 $cm^2V^{-1}s^{-1}$, comparable to that observed in ITO with similar carrier concentrations. At lower carrier concentrations, between 2 and 4×10^{20} cm^{-3} mobilities of greater 80–90 $cm^2V^{-1}s^{-1}$ are observed [161]. For carrier concentrations between these ranges mobilities that improved on those seen in ITO are observed but are still lower than those seen in IMO for similar carrier concentrations.

Zr doping of In_2O_3 has displayed carrier concentrations of up to 4×10^{20} cm^{-3} and has displayed mobilities of up to 79 $cm^2V^{-1}s^{-1}$ for such carrier concentrations. Below n=3×10^{20} cm^{-3} mobilities >100 $cm^2V^{-1}s^{-1}$ have been reported. Of the transition metal dopants other than Mo, Zr has the most literature discussing it.

Hf has had the least reported work performed of these dopants but what has been done shows similar promise. Carrier concentrations of 4×10^{20} cm^{-3} with mobilities of up to 80 $cm^2V^{-1}s^{-1}$

have been reported placing its properties in a similar range to those of Zr and Ti doped In_2O_3.

Finally, W falls in the same group in the periodic table as Mo. As such it similarly has two stable oxidation stated, (IV) and (VI). The highest mobilities reported fall around 90 $cm^2V^{-1}s^{-1}$ at carrier concentrations of around 2×10^{20} cm^{-3}. This rapidly reduces with increasing carrier concentrations with the mobilities reported for carrier concentrations >5×10^{20} cm^{-3} falling around 40 $cm^2V^{-1}s^{-1}$ which is comparable to those seen in ITO [163–165].

While higher mobilities have been observed with these dopants than with Sn doping in each case discussion of the mechanism behind this has had minimum discussion. As similarly to Mo the donor states are likely d states due to these elements being transition metals it seems likely that the mechanism behind the improved mobilities in each of these cases is the same.

5.3.3 Ce Doping of In_2O_3

Minimal literature exists on Ce doping of In_2O_3 but what there is shows promise. An increase in conductivity and carrier concentration can be seen with the incorporation of Ce indicating that Ce is in (IV) oxidation state and acting as a donor. Films in these studies have also displayed mobilities of up to ~100 $cm^2V^{-1}s^{-1}$, far superior that those seen in ITO. However it appears that Ce doped In_2O_3 is limited in carrier concentration as no value of n much greater than ~2×10^{20} cm^{-3} have been reported[165, 166]. With little work on understanding the behaviour of Ce as a dopant in In_2O_3 however it is difficult to say for sure whether it is possible to improve upon this low carrier concentration. Hence this chapter looks to better understand how Ce incorporates into In_2O_3 and whether it would be possible to increase the carrier concentration above this limit as the mobilities seen are so promising. It also aims to develop an understanding of the origin of the high mobilities seen in the material.

5.4 In_2O_3:Ce Thin Films

5.4.1 Fabrication

For this study a selection of three highly conductive, polycrystalline Ce doped In_2O_3 thin films of varied Ce content were studied. A undoped In_2O_3 thin film was also studied for comparison. The films were prepared by rapid plasma deposition (RPD) using the Sumitomo Heavy Industries, URT-IP2, onto 1.1 nm thick soda-lime glass substrates. Ceramic tablets of pure In_2O_3 and In_2O_3 mixed with a CeO_2 content of 1, 2 and 3 wt.% were used. Films were deposited under a mixer Ar and O_2 atmosphere with a flow ratio of O_2 to Ar of 24%. The films were deposited at a temperature of 200 °C and underwent a post-anneal at 500 °C for 30 minutes to improve crystallinity and the resulting transport properties.

Throughout this chapter the samples are referred to by the concentration of Ce in the tablet used in the fabrication.

5.4.2 Electrical Properties

Hall effect measurements were carried out on the samples using the van der Pauw method to determine the sheet resistance, free carrier concentration and mobility. A square array of Ohmic contacts was arranged on 1 cm^2 samples that were subjected to an input current of 1 mA and a magnetic field varied between 0.8 and -0.8 T.

As seen in previous studies, an increase in carrier concentration can be seen for all three ICO thin films compared to the undoped film. While high mobilities of over 125 $cm^2V^{-1}s^{-1}$ were seen in all three films the highest carrier concentration observed was 2.12×10^{20} cm^{-3}. The full results of Hall measurements for all samples including the undoped In_2O_3 are presented in Table 5.1

These carrier concentrations still fall significantly short of those seen in ITO and slightly short of those seen with the other novel dopants discussed in section 5.3. Of those materials, only IMO has displayed mobilities as high as those observed in these films.

The Ce concentration within each film has also been established using ICP-MS and presented in Table 5.1. The values presented are the at% on the cation site, that is to say the percentage of In sites within the lattice that are occupied by a Ce atom.

Table 5.1: Properties of undoped and Ce doped In_2O_3 thin films studied in this work: Ce concentration determined from ICP-MS expressed as a percentage of the cation lattice sites, film thickness, t, sheet resistance, $R_\square$, resistivity, ρ, carrier concentration, n, and carrier mobility, μ.

Sample	[Ce] (%)	t (±1) (nm)	$R_\square$ (±0.1) (Ω/□)	ρ ($\pm1\times10^{-5}$) (Ωcm)	n ($\pm1\times10^{18}$) (cm^{-3})	μ (±0.1) ($cm^2V^{-1}s^{-1}$)
In_2O_3	-	250	236.4	5.9×10^{-3}	1.1×10^{19}	96.7
In_2O_3:Ce 1%	0.28	210	22.4	4.7×10^{-4}	1.0×10^{20}	130.2
In_2O_3:Ce 2%	0.96	204	14.6	3.0×10^{-4}	1.5×10^{20}	136.0
In_2O_3:Ce 3%	1.30	196	11.8	2.3×10^{-4}	2.1×10^{20}	127.8

5.4.3 Optical Properties

Transmission and reflectivitly spectra of the films are shown in Figure 5.4. High transmission is measured across the visible and near infra-red range for all samples with no obvious impact from Ce doping . For undoped In_2O_3 the average transmission over a range of λ = 350-1500 nm is 79.4%. Over the same range, the Ce 1% sample had an average transmission of 80.4%, the Ce 2% sample had an average transmission of 81.0% and the Ce 3% sample had an average transmission of 81.3%.

The transmission is consistent for all samples with the slight differences in average transmission across this range being attributed to the slight differences in film thickness, resulting in a shift in the interference fringes in the transmission spectrum.

Comparisons to the optical spectra of the soda lime glass (SLG) substrate show that most of the optical losses in these measurements are in the substrate rather than the deposited thin

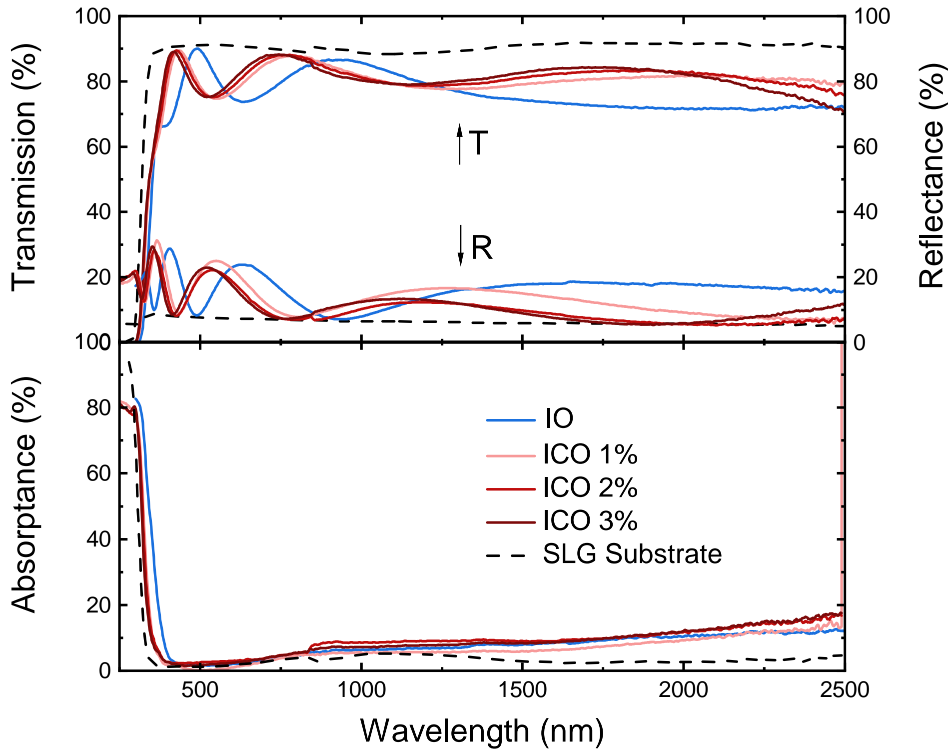

Figure 5.4: (Top) Transmission and reflectivity spectra of undoped and Ce doped In_2O_3 thin films. (Bottom) Absorptance spectra for each of the undoped and Ce doped In_2O_3 thin films.The transmission, reflectively and absorptance spectra for the soda lime glass (SLG) substrate the films were grown on is also shown.

films.

The average transmission across the range measured is high for all three films, comparable or higher than the average transmission reported for ITO or IMO films of similar conductivity. In particular the transmission in the near infra-red is higher than that reported for other In_2O_3-based TCOs.

Reflectance for all the samples is low with all displaying an average reflectance of below 20% for wavelengths up to 2500 nm. Where reflectance does lie above 20% it is at the peak of interference fringes. Such low reflectence at high wavelengths is not commonly seen in In_2O_3-based TCOs.

Absorbance, shown in he bottom half of Figure 5.4, shows low absorbance beyond the absorption edge for all the samples. Within the visible range absorption of the samples and the substrate show very little difference meaning most of the absorption at those wavelengths occurs within the substrate. At longer wavelengths there is a greater difference between the substrate and the films but the doped films are still relatively consistent with the undoped film. As such little or no absorption can be attributed to the introduction of the dopant defects at the doping densities investigated.

5.5 Photo-emission

HAXPES spectra were taken for the Ce doped samples over regions showing the In $3d$, Ce $3d$ and O $1s$ peaks as well as the valence band (VB) and CB emission. The HAXPES was performed at the I09 beamline at the Diamond Light Source (Didcot, UK). A photon energy of 5.951 keV was selected using a Si(111) double-crystal monochromator and a Si(004) channel-cut crystal as a post monochromator. The beam size at the sample was 40 × 20 μm^2 with an incident angle of 87.5° with respect to the surface normal. Photoelectrons were detected using a EW4000 photoelectron analyser from VG Scienta (Uppsala, Sweden). Calibration of the binding energy scale was performed using the Fermi edge and the $4f$ core level lines of a gold reference sample. The gold Fermi edge was fitted to obtain an experimental resolution of ~200 meV.

For the most heavily doped sample, Ce 3%, the measurements were repeated in regular XPS. These XPS measurements were performed at the Harwell national XPS labratory, using a Thermo Fisher Scientific NEXSA spectrometer using a microfocused monochromatic Al X-ray source (72 W) over an area of approximately 100 μm^2. A pass energy of 40 eV was used with a step size of 0.1 eV. The Fermi edge of a gold foil was fitted to determine an experimental resolution of ~460 meV.

5.5.1 Surveys

When initially measuring a sample in both HAXPES and XPS a scan covering a wide energy range with a large step size and short dwell time is performed. These quick scans gives general information about the chemical make up of the sample and the binding energy of interesting features on which longer scans can be performed. It is also used to check for potential contamination of the sample to check whether longer measurements are worth performing.

Figure 5.5 shows the survey scans of the 3% Ce doped In_2O_3 sample measured in both XPS and HAXPES. In each spectrum all features of significant intensity have been labelled. The features have been identified using spectra presented in Ref. 141.

The majority of the features seen in both surveys are attributed to either In or O. Beyond these elements peaks attributed to Ca and Si are seen in the XPS and a peak attributed to C is seen in both the XPS and HAXPES. The presence of adventitious carbon is expected on the surface of any air exposed sample. The reduction of the intensity of the C $1s$ peak in the HAXPES relative to the XPS is indictive that the carbon is only present on the surface. The Ca and Si peaks are only present in the XPS spectrum indicating that these elements are also surface contaminants. The presence of these elements likely arose due the cutting process to ensure the samples of small enough to the be mounted for the photoemission experiments. The samples are deposited on soda-lime glass substrates which contain Ca and Si and it is likely some dust from the substrate contaminated the samples during cutting.

In the XPS spectra two features exist at around 975 eV and 1085 eV. These features are

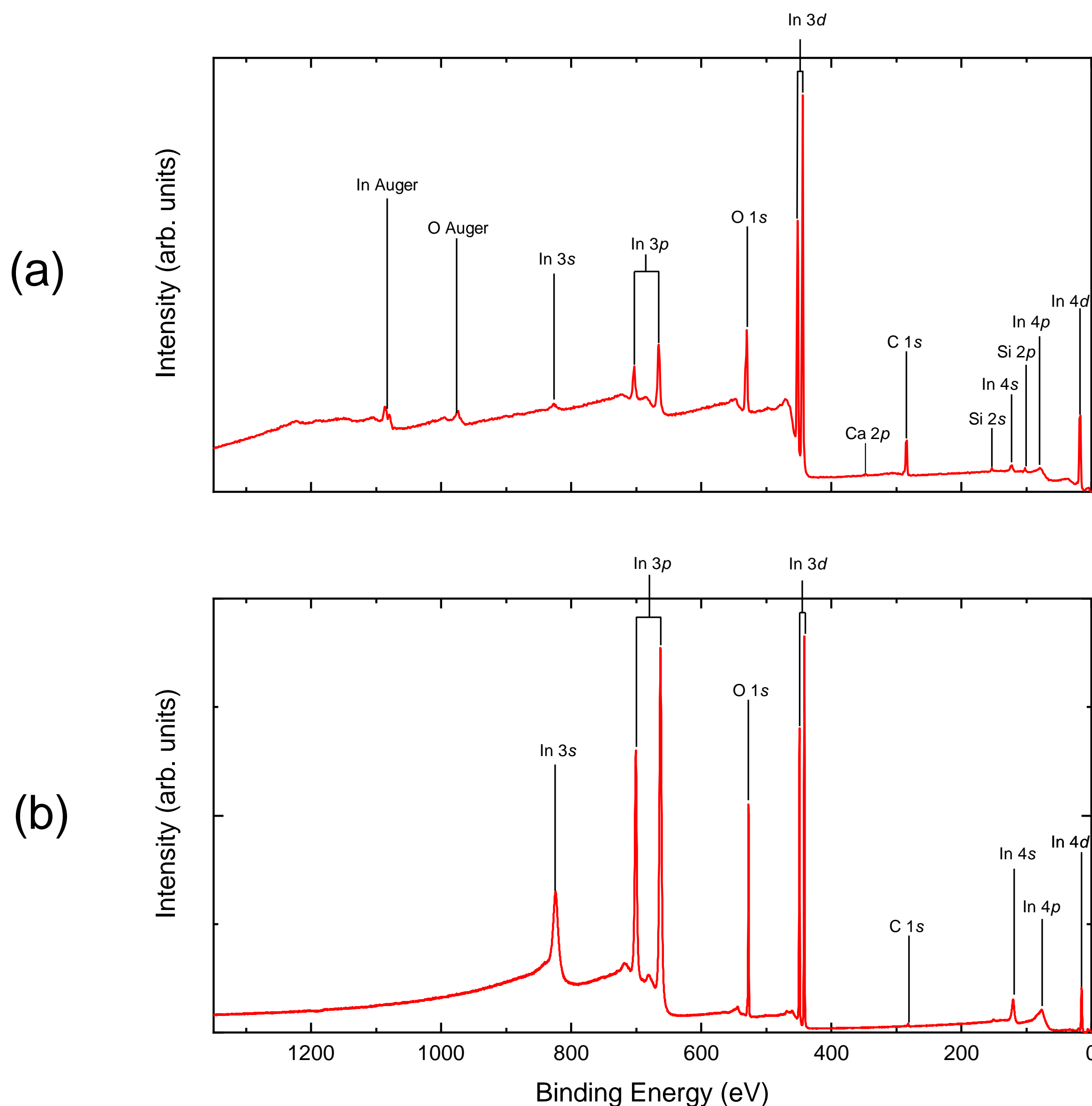

Figure 5.5: Spectra of survey scans of the ICO 3% sample performed in (a) XPS with a photon energy of 1487 eV and (b) HAXPES with a photon energy of 5951 eV for a binding energy range of 1350 eV to 0 eV. Features in each spectrum have been indexed and labelled.

attributed to the O and In augers when using an Al kα source. These features are not present in the HAXPES spectrum as the binding energy of auger features is dependent on the incident photon energy as explained in section 4.5.10. With an incident photon energy of 5951 eV as is used in the HAXPES the auger features will have binding energies well above the 1350 eV displayed in Figure 5.5.

The relative intensity of the In and O *s* and *p* peaks is higher in the HAXPES data than the XPS spectrum. This is because the interaction cross section of *s* and *p* orbitals increases relative

to d orbitals with increasing photon energy. An additional peak attributed to O 2s is expected around 23 eV [141] but it is not possible to resolve this from the more prominent In 4d peak located at around 17 eV in these survey scans.

No features attributed to the dopant, Ce, have been noted in the survey spectra. The most intense Ce peaks is expected to be the Ce 3d peaks expected in the region of 880-920 eV, encompassing both the $3d_{3/2}$ and $3d_{5/2}$ peaks. No obvious peaks are present in this region. It is therefore not possible to confirm the presence of Ce in the sample from these surveys alone.

Surveys were also performed on the Ce 1% and Ce 2%, however as the Ce features are not detectable in the survey scans the difference between the scans for the different samples is negligible. Therefore the survey scans for the other two samples are not presented here.

5.5.2 Fermi Edge Calibration

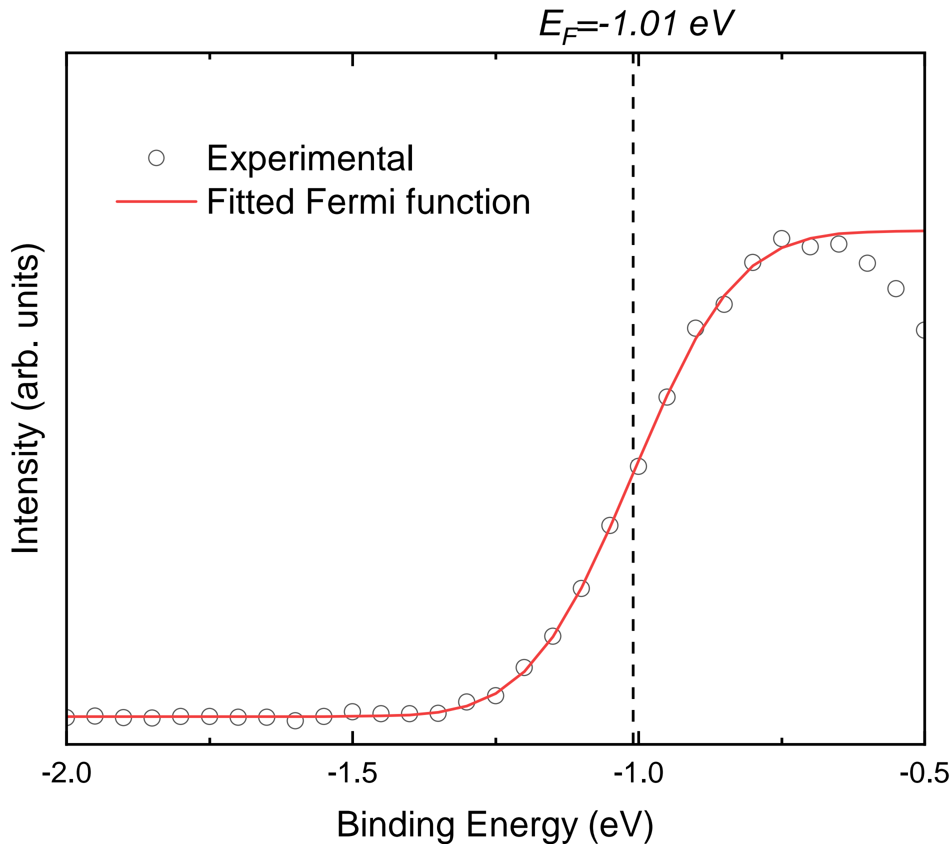

Figure 5.6: The HAXPES spectrum for the Ce 3% sample showing the Fermi edge cut off of the conduction band emission. It has been fitted with a Fermi function for calibration purposes

Binding energies of core levels are reported relative to the Fermi level of the system. Therefore, photoemission data should be calibrated so the E_F is set to 0. While many techniques are used to perform such a calibration in the HAXPES data the conduction band emission can be observed

due to the high intensity of syncotron radiation. As such, the Fermi edge of the sample can be directly fitted with a Fermi function, equation 3.57, and the position of the Fermi edge can be extracted.

Figure 5.6 shows the HAXPES spectra containing the Fermi edge of the Ce 3% sample. It has been fitted with a Fermi function, shown in red, and the Fermi level has been extracted as E_F=-1.01 eV. This means that all data for the sample is off set by this amount and needs to be shifted to account for this.

Similar fits were applied to the Fermi edges of the Ce 1% sample and the Ce 2% sample. The Fermi edges were found to be offset by -1.11 eV and -0.99 eV respectively for these samples and other spectra for these samples were adjusted accordingly.

5.5.3 Carbon 1*s* calibration

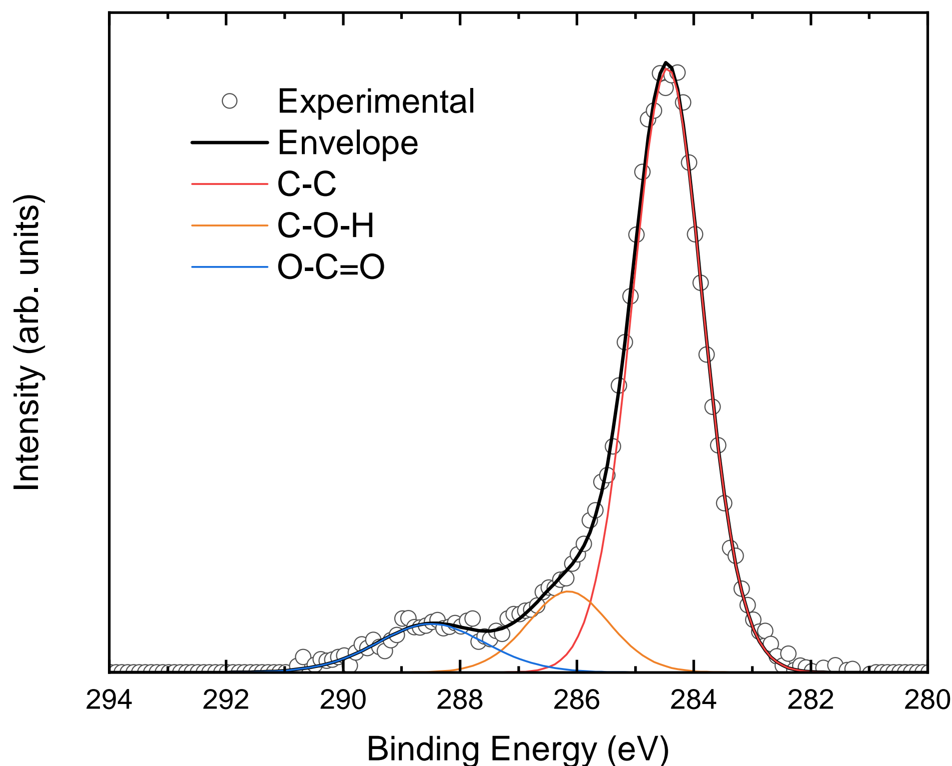

Figure 5.7: The XPS spectrum for the Ce 1% sample covering the region containing the C 1*s* peaks. It has been fitted with three peaks representing three types of adventitious carbon.

In the XPS measurements the intensity is of the emission from the conduction band is significantly lower than the HAXPES. As a result, fitting of a Fermi function to the Fermi edge of the conduction band emission is not possible. Therefore another calibration technique is required for the XPS measurements.

In the XPS survey spectra a C 1*s* peak can been seen. This is attributed to adventitious carbon on the surface. The majority of adventitious carbon is expected to be in the form of carbon, C-C, but carbon-hydroxides and carbonates are also expected to be present, C-O-H and O-C=O. The largest peak attributed to C-C is expected at 284.8 eV with additional peaks at ~286 eV for C-O-H and ~288.5 for O-C=O. It is possible to calibrate data to the adventitious carbon peak at 284.8 eV.

Figure 5.7 show the XPS spectra for the region covering the three adventitious C 1*s* peaks for the Ce 1% sample It has been fitted with three peak, the largest of which is attributed to C-C. This peak is located at 284.45 eV. The data therefore assumed to be offset by -0.35 eV and as such all other core level spectra need to be shifted by this amount to correct for this.

Similar fitting was performed on the spectra for the C 1*s* region for the Ce 2% and Ce 3% samples. These were found to be offset by -0.35 eV and -0.20 eV respectively. The other core level spectra for these samples were shifted to account for these offsets.

5.5.4 In and O Core Levels

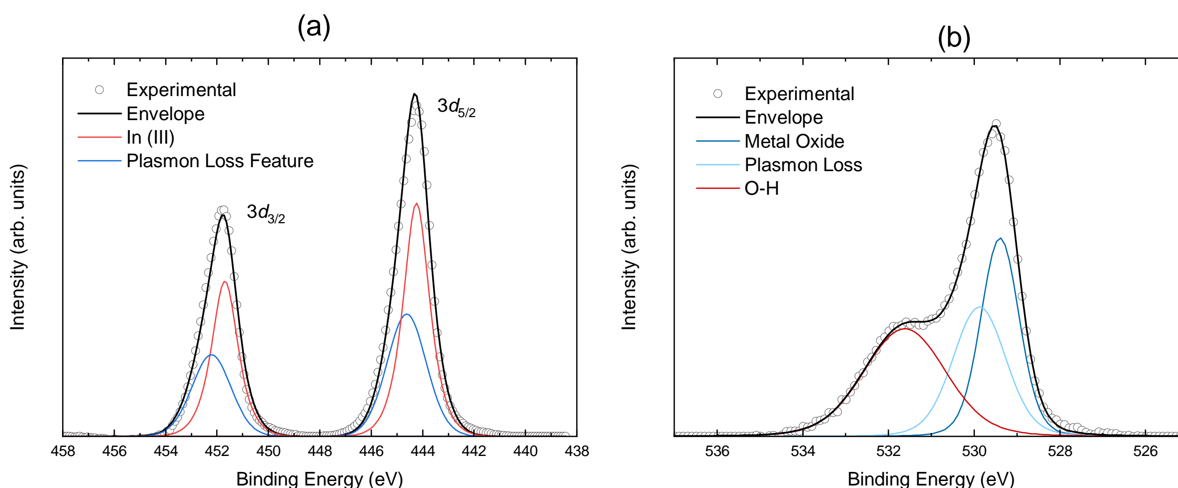

Figure 5.8: The XPS spectra for the Ce 1% sample covering the regions containing (a) the In 3*d* peaks and (b) the O 1*s* peaks. The In 3*d* spectrum has been fitted with 4 peaks, each doublet feature contains a peak corresponding to In (III) within the In_2O_3 and a peak corresponding to a plasmon loss feature. The O 1*s* spectrum has been fitted with three peaks, one for O (II) within the In_2O_3, one for O-H on the surface and one for a plasmon loss feature.

Small region scans of the energy ranges containing the In 3*d* and O 1*s* peaks have been measured in both HAXPES and XPS. The XPS scans for these regions in the Ce 1% sample are shown in Figure 5.8.

The In 3*d* region consists of two peaks as expected due to doublet splitting. The peaks display a slight asymmetry being slightly broader on the high binding energy side. To account for this asymmetry each feature has been fitted with two peaks. The two pairs of peaks are separated by

7.6 eV, the doublet separation for the In $3d$ orbital [169] and the area ratio was constrained so that the area of the $3d_{5/2}$ peaks are 1.5× that of the $3d_{3/2}$ peaks. In each peak the larger fitted peak sits at a lower binding energy and is attributed to In (III), the expected oxidation state of In in In_2O_3. The In (III) $3d_{3/2}$ has a binding energy of 451.8 eV and the $3d_{5/2}$ has a binding energy of 444.2 eV. The reported binding energy of these two features as reported in the literature are 451.8-452.1 eV and 444.2-444.5 eV respectively [170, 171]. The second peak, included to account for the asymmetry, in each feature is attributed to plasmon losses. These features are present in samples with high carrier concentrations as the emitted photo-electrons lose energy to the free electrons in the system. When these electrons lose energy in this way the energy loss is equal to the plasma frequency in the system giving it a higher apparent binding energy. Therefore this manifests itself as a peak at a binding energy greater than that of the main peak by an amount equal to the plasma frequency This feature is located at binding energies of 452.3 eV and 444.6 eV for the $3d_{3/2}$ and $3d_{5/2}$ components respectively. This corresponds to a plasma frequency of 0.395 eV in this case.

The O 1s region consists of a sharp peak with a broad shoulder at a higher binding energy. The region has been fitted with three peaks. The main peak, located at a binding energy of 529.5 eV, is attributed to O (II), the oxidation state of O in In_2O_3. O 1s for O (II) is reported to have a binding energy of ~530.0 eV [172, 173]. The second peak, fitted to the large shoulder at a higher binding energy, is attributed to adventitious O-H, oxygen bonded to hydrogen, on the surface. This peak is located at a binding energy of 531.6 eV. The O-H is widely reported in metal oxides and is expected at around 532.0 eV [174]. The shape of the O 1s features and the binding energy of the fitted peaks are as expected from In_2O_3.

Figure 5.9 shows the same region for the Ce 2% and Ce 3% samples. The same features a present in this region in these samples as in the Ce 1% sample. However the separation of the main In (III) peaks and the plasmon loss features is 0.466 eV and 0.493 eV for Ce 2% and 3 % respectively. This corresponds to an increasing plasma frequency with greater Ce content and therefore carrier concentrations as expected.

5.5.5 Ce Core Levels

Binding energy of a core level is dependent on the oxidation state of the element. Because of this, it is possible to differentiate between Ce (III) and Ce (IV) based on the peak positions of Ce $3d$ core levels in photo-emission.

In addition to this Ce (III) and Ce(IV) display different multiplet splitting in the Ce $3d$ core levels. Ce (III) has four features, two for Ce $3d_{3/2}$ and two for Ce $3d_{5/2}$, while Ce(IV) has six features, three for each. The doublet separation for Ce $3d$ orbitals is 18.6 eV [175]. The satellites in the Ce $3d$ spectra are attributed to metal-charge transfer

For Ce(III), peaks are present at 903.4 and 899.1 eV for Ce $3d_{3/2}$ and 880.9 and 885.2 eV for Ce $3d_{5/2}$. For Ce(IV), peaks are present at 916.9, 907.3 and 901.3 eV for Ce $3d_{3/2}$ and 898.3, 888.5

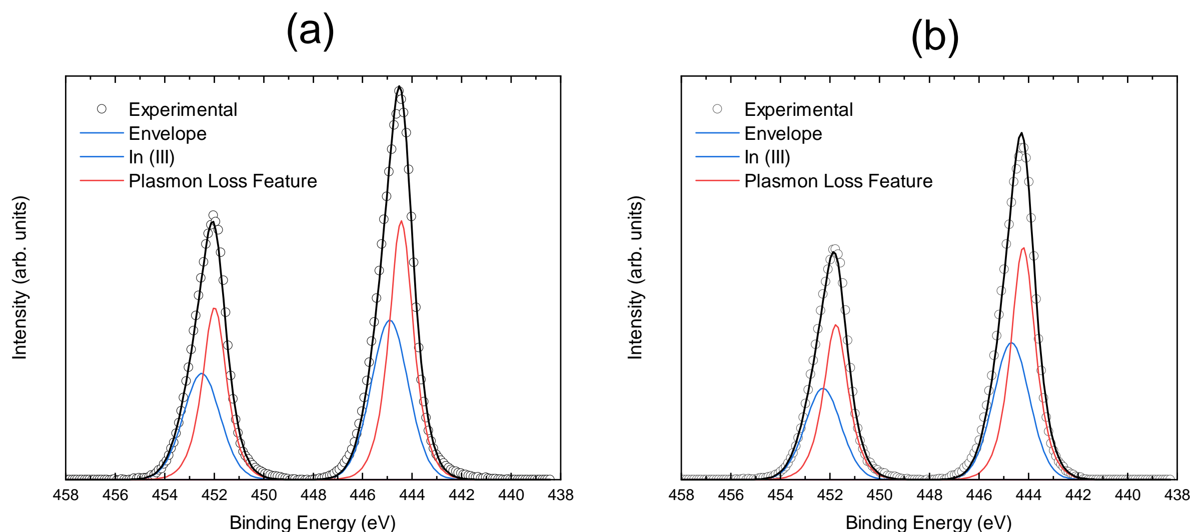

Figure 5.9: The XPS spectra for the region containing the In $3d$ peaks for (a) the Ce 3% samplea and (b) the Ce 2% sample. Each feature has been fitted with two peaks, one corresponding to In (III) and one corresponding to a plasmon loss feature.

and 882.7 eV for Ce $3d_{5/2}$ [176, 177].

Based on these differences between the spectra for the two oxidation states it is possible to determine in which oxidation state Ce has incorporated into a compound. In a case where both are present it is possible to determine the ratio of the two oxidation states based on the area under the peaks attributed to each oxidation state.

As shown in section 5.5.1 Ce features could not be seen in the survey scans of the survey

Figure 5.10 displays the background subtracted Ce $3d$ spectra for the three Ce doped samples. Each data set has been fitted with 10 peaks, 4 corresponding to Ce(III) and 6 corresponding to Ce (IV). The fits have been restrained, the separation of each doublet is set so that the Ce $3d_{3/2}$ feature is at a binding energy of 18.6 eV greater than that of the corresponding Ce $3d_{5/2}$ feature. The area ratio each doublet is also restrained so that the area of Ce $3d_{5/2}$ feature is 1.5$\times$ that of the Ce $3d_{3/2}$ feature due to the degeneracy of each state and the FWHM of each doublet pair was restrained to be equal. The position of each peak was also restrained to be within $\pm$0.5 eV of the positions reported in the literature.

Uncertainty in the curve fitting of the Ce $3d$ spectra is relatively high due to the low signal to noise ratio resulting from the low concentrations of Ce in the films and the large number of components required for the fitting. The data for the 1% sample is particularly noisy due to the very low Ce content in the film. Despite this, fitting of the data has still been possible and, in any case, a clear trend is apparent from inspection of the data that the Ce signal contains an increasing proportion of Ce (III) as the total Ce content increases.

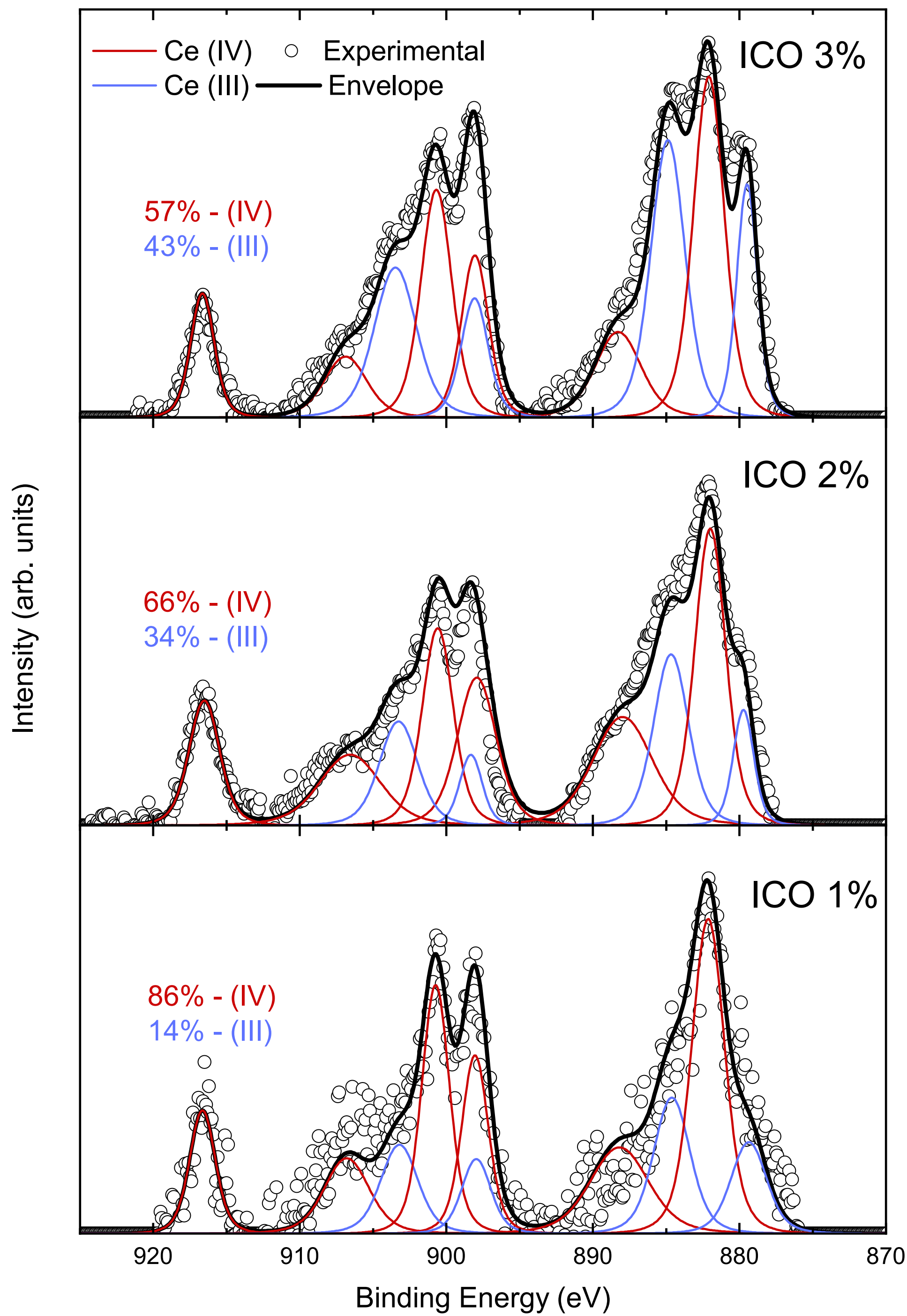

Figure 5.10: Background subtracted and fitted HAXPES spectra of Ce 3*d* core levels for the three Ce doped samples. Features attributed to Ce(III) are shown in blue and the features attributed to Ce(IV) are shown in red. The percentage of the signal attributed to each oxidation state is stated for each sample.

5.5.6 Doping Density Dependence

Figure 5.11 shows the percentage contribution of Ce(III) and Ce(IV) to the fitted components of the Ce 3*d* HAXPES spectra against the atomic percentage of Ce on the cation site within the films. This shows a clearly linear trend between the percentage of Ce in the (III) oxidation state and the percentage of Ce within the films. This indicates that as more Ce is incorporated into the films the preferred oxidation state starts to shift from (IV) to (III).

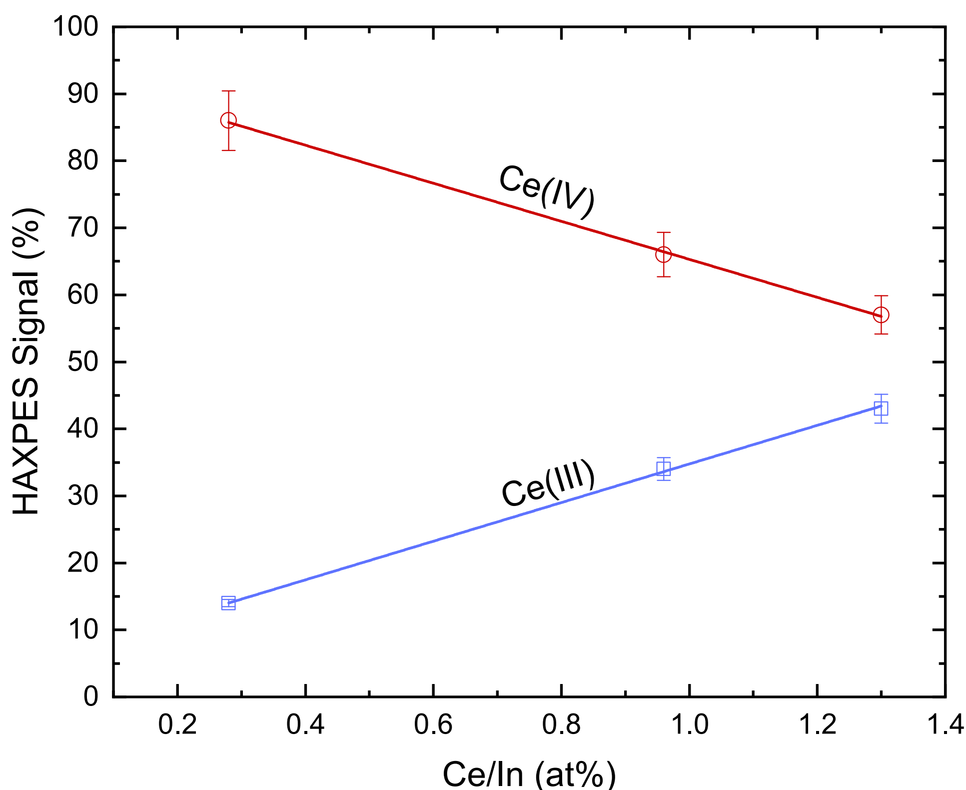

Figure 5.11: The percentage of the signal attributed to each Ce oxidation state in the Ce 3*d* HAXPES spectra against the atomic percentage of Ce on the cation site. A linear trend of an increasing Ce(III) percentage is seen with increasing Ce content.

However, as HAXPES is still a relatively surface technique the ratios extracted may not be entirely representative of the bulk of the films. This only shows that at the depth at which HAXPES probes the percentage of Ce (III) increases.

5.5.7 Depth Dependence

As discussed in detail in section 4.5.9 the depth at which the majority of the signal comes from in photo-emission is dependent on the incident photon energy. Therefore performing XPS at a lower photon energy can provide information on how the chemical composition of the material

varies with depth. This is utilised here to see how the ratio of Ce oxidation states varies with depth throughout the samples.

Due to the lower signal to noise ratio in conventional XPS compared to HAXPES data of high enough quality to fit was only obtainable for the 3% Ce sample.

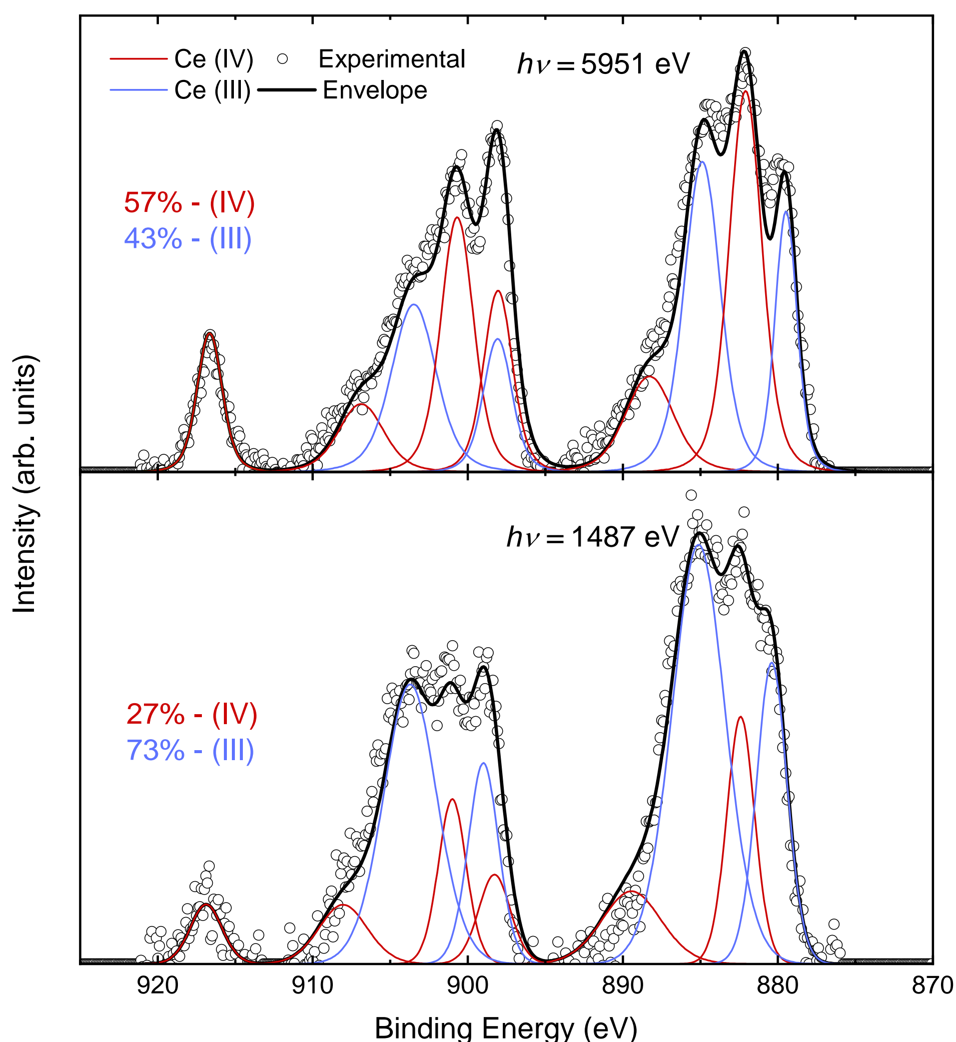

Figure 5.12: HAXPES spectra measured at a photon energy of 5951 eV and XPS spectra measured at a photon energy of 1487 eV for the ICO 3% sample. Features attributed to Ce(III) are shown in blue and the features attributed to Ce(IV) are shown in red. An increased relative signal from Ce(III) can be seen at the lower energy indicating that the Ce(III) is present at the surface.

The ratio of Ce(IV) to Ce(III) as measured from the area under the Ce 3*d* features was found to be 57:43 for the HAXPES and 27:73 for the XPS. This suggests that Ce(III) is forming preferentially near the surface. As such, it is not possible to state quantitatively the ratios of the two oxidation states in the bulks of the samples from photoemission.

5.5.8 Conduction Band Emission

Conduction band emission features can be seen in all three doped samples as shown in Figure 5.13. The emission increases with increased Ce content, the inset of Figure 5.13 shows a linear relationship between the relative area of the conduction band emission and carrier concentration obtained through Hall effect measurements. The relative areas were calculated by integrating under the data between binding energies of -1.75 eV and -3.75 eV

This linear trend between emission from the conduction band and the carrier concentration is expected as the additional carriers will fill the conduction band so that the emission from the conduction band should be proportional to the carrier concentration.

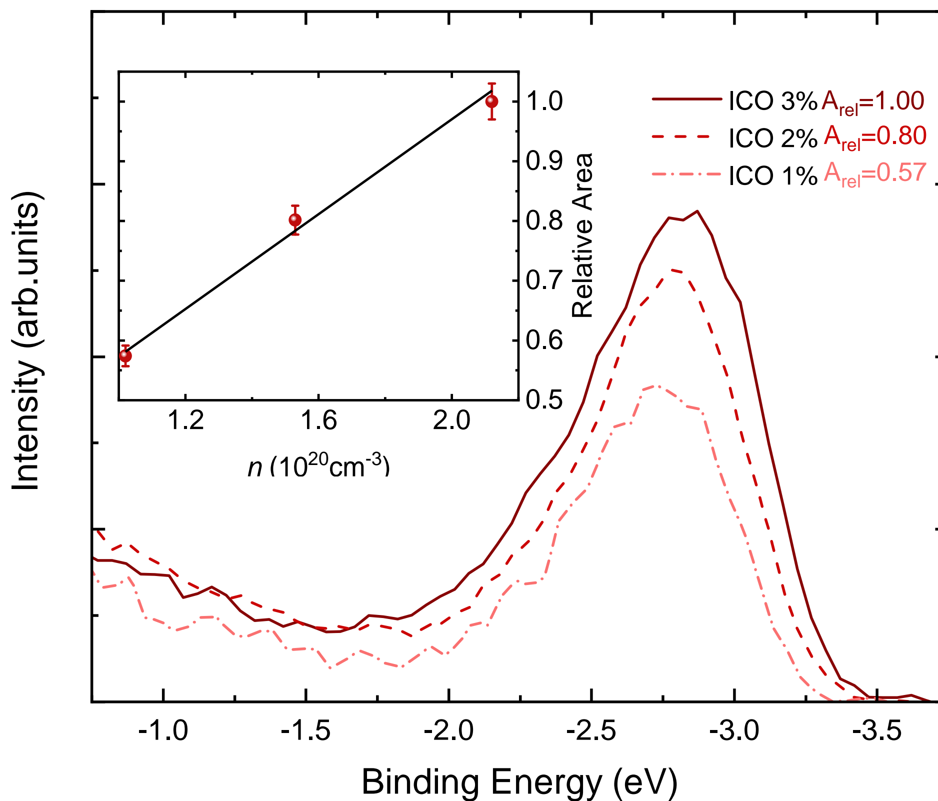

Figure 5.13: HAXPES spectra for the conduction band emission of the three Ce doped samples showing increased emission with increased Ce content. The binding energy is given relative to the samples VBM. The inset shows the trend between the area of the emission feature against carrier concentration of the sample, showing a linear relationship.

5.5.9 Carrier Concentration Limit

The ICO samples in this study along with those presented in previous literature all have carrier concentrations no higher than ~2×10^{20} cm^{-3}.

As previously noted, and shown in Figure 5.10, all three samples contain features attributed to both oxidation states, with the features for Ce(IV) being more prominent. However, with increasing Ce content the relative intensity of Ce(III) feature increases. The increase in the percentage of Ce(III) with increasing Ce content indicates a change in the energetically preferable Ce defect with increased Fermi level.

The increasing content of Ce(III) may be limiting the carrier concentration of the films as Ce(III) is a neutral defect. Therefore, if for certain Ce content or carrier concentration all further incorporated Ce is in the III oxidation state, no more carriers will be added. In this case there would be a relatively low limit on the upper carrier concentration achievable through Ce doping of In_2O_3.

For the samples in this study no saturation of carrier concentration is reached. However, the lack of reports of ICO films with higher carrier concentration along with the trend in Ce(III) content seen here casts doubt over whether higher carrier concentrations will be achievable by Ce doping. Attempts to dope In_2O_3 more highly with Ce have resulted in significant reductions in the conductivity of the films compared to the films reported here and in the literature.

5.5.10 Defect Thermodynamics

Utilising DFT the formation energies of likely defects in Ce doped In_2O_3 were calculated a a function of Fermi level. These formation energies were calculated under both O-poor and O-rich conditions to cover the full range of likely deposition conditions with the results for both shown in figure 5.14. In reality, depositions will occur somewhere between these two extremes.

In both extremes the lowest formation energy defect for energies below the CBM is substitutional Ce on the In 24d site, Ce_{In24d}. Substitutional Ce on the In 8b site, Ce_{In8b}, has a slightly higher formation energy but the difference is small enough that it is likely that both will form with the introduction of Ce.

For Fermi levels below the CBM both Ce_{In24d} and Ce_{In8b} incorporate in the +1 charge state meaning they act as donor defects. This is the behaviour desired in a dopant. However, on the $24d$ site the preferred charge state transitions to neutral for Fermi levels around 0.03 eV above the CBM. Similarly, on the $8b$ site this transition occurs for Fermi levels around 0.13 eV above the CBM. Once the Fermi level enters this regime Ce can be expected to incorporate as a neutral defect and not behave as a dopant. This places an upper limit on the carrier concentrations achievable through Ce doping as these transitions act a charge neutrality levels in ICO as discussed in section 2.3.2.

This is in line with observations made experimentally earlier in this chapter. The carrier concentrations observed in ICO are rarely higher than ~2×10^{20} cm^{-3} and a mixture of Ce (IV), in the +1 charge state, and Ce (III), in the neutral charge state, were observed in the HAXPES and XPS. It is therefore likely that the upper limit on carrier concentration has been achieved for

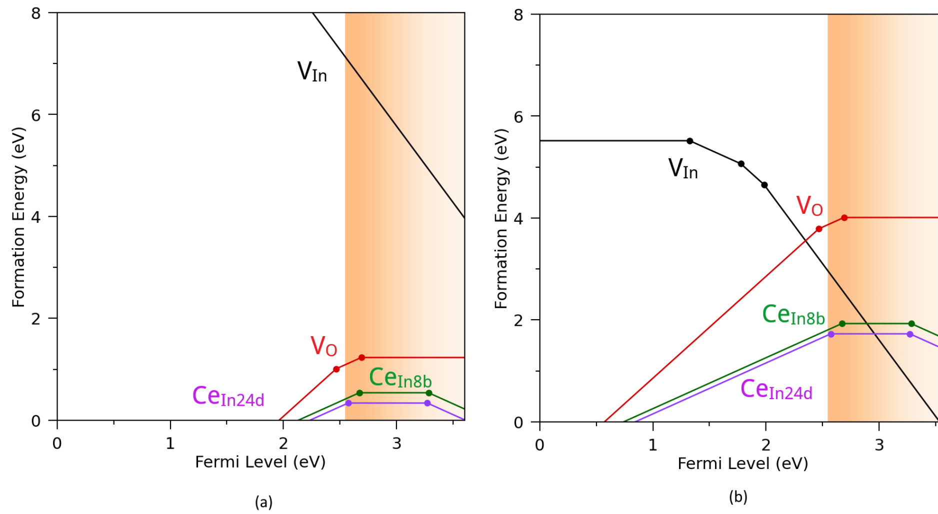

Figure 5.14: Defect transition level diagrams, showing defect formation energy against Fermi level. The conduction band is shown by the shaded orange region. Filled circles represent transition levels between defects of different charge, with the slope of the line indicating the charge. A positive gradient denotes positive charge, negative gradient denotes negative charge, with a steeper gradient representing a higher charge state. Horizontal lines indicate the neutral charge state. (a) shows the defect formation energies for O-poor conditions and (b) shows the for O-rich conditions.

ICO with attempts to introduce more Ce resulting in it incorporation as neutral Ce (III) and not contributing to conductivity.

For comparison, the transitions to the neutral charge state in Mo and Sn doped In_2O_3 both occur over 0.5 eV above the CBM explaining why much higher carrier concentrations have been achieved in those systems.

5.6 Origin of High Mobilities

The property of the ICO films that make it of interest compared to conventional ITO thin films is the high mobilities observed within them. With regards to mobility the only TCO, In_2O_3-based or otherwise, to consistently match or surpass the mobilities observed of these ICO thin films at similar carrier concentrations is IMO. As previously discussed the mechanism behind the high mobilities seen in IMO has been identified as the donating resonant d orbital not hybridising with the CBM. As ICO displays similarly high mobilities it is likely a similar mechanism to this is behind its promising electronic properties.

5.6.1 Fermi Level to VBM Separation

The position of the Fermi level can be extracted from photoemission in degenerately doped samples as the conduction band is occupied and therefore emission from the conduction band can be observed as previously shown in Figure 5.13. The position of the Fermi level can be extracted by fitting a Fermi function to the lower binding energy edge of the conduction band emission. The centre of the Fermi function corresponds to the Fermi level of the sample. In the inset of Figure 5.15 HAXPES spectra for the region containing the conduction band emission and the valence band maximum. A Fermi function has been fitted to the Fermi edge of the emission and the position has been set to 0 eV binding energy.

The position of the valence bands have been extracted thorough a linear fit of the VBM in the HAXPES specta. The x-axis intercept of these linear fits has been taken as the VBM. This gives the position of the VBM relative to the Fermi level. The linear fit and the extracted value are displayed for each spectrum in the inset of Figure 5.15

As discussed in section 3.5 the relationship between Fermi level and carrier concentration can be modelled using Fermi statistics. In a degenerately doped system the relationship between E_F and n is given by equation 3.56 where the density of states is defined by equation 3.55. This means that the relationship between E_F and n is dependent on the carrier effective mass, m^*. Therefore by fitting the data points for extracted Fermi level using equation 3.56 a band edge effective mass can be extracted.

Figure 5.15 shows the extracted Fermi levels relative to the VBM for the three ICO samples against n. The data was fitted using equation 3.56 and the non-parabolic approximation utilising a fundamental band gap of 2.75 eV. This fit gives a band edge effective mass of $m_0^* = 0.23m_0$ where m_0 is the rest electron effective mass.

5.6.2 Infra-Red Reflectivity

Another property of materials dependent on carrier effective mass is the plasma frequency. The relationship between plasma frequency and carrier effective mass is given in equation 1.5.

Reflectivity in the infra-red range has been measured for each of the Ce doped samples. This data has been fitted using the two-oscillator model discussed in section 3.3.2 accounting for plasma and phonon contributions in combination with the transfer matrix method as explained in section 3.4. As shown in Figure 5.16, the model is good agreement with the data for energies above 0.2 eV, below which contributions from optical modes of the soda-lime glass substrate and the sample reduce the agreement. From the fits the plasma frequency for each sample has been extracted. The extracted plasma frequencies for each sample were 0.38 eV, 0.45 eV and 0.52 eV with increasing Ce content. These values are in good agreement with the plasma frequencies extracted from the separation of plasmon loss peaks in the core level XPS presented in section 5.5.4. This gives increased confidence in the values extracted being accurate.

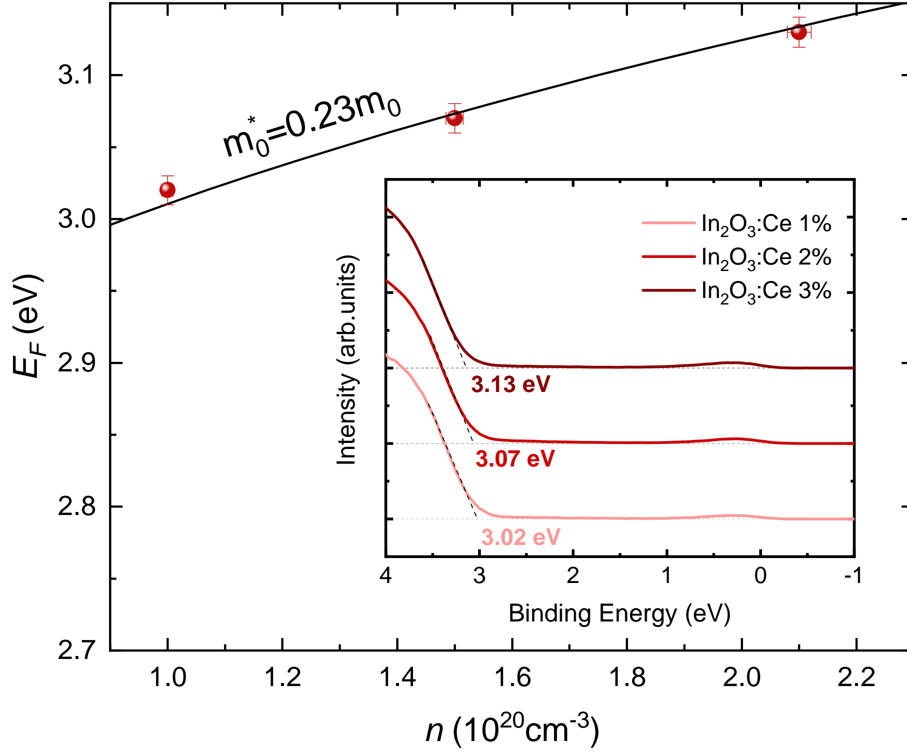

Figure 5.15: The Fermi level relative to the VBM against carrier concentration, n, for the three ICO samples. The solid black line shows the calculated relationship between E_F and n for In_2O_3 using a fundamental band gap of 2.75 eV and a band edge electron effective mass of 0.23 m_0. The inset shows the background subtracted HAXPES spectra for the region encompassing the VBM and Fermi edge for the three ICO samples used to extract these data points. The Fermi edge for each sample has been set to 0 eV on the binding energy axis. Linear extrapolation to the x-axis has been used to extract the exact position of the VBM. The dashed horizontal lines show zero intensity for each spectrum.

The inset in Figure 5.16 shows the plasma frequency against carrier concentration fitted with equation 1.5 (the solid black line) to extract the carrier effective mass. For this fit an ϵ_s value of 8.9 has been used, a value widely reported for In_2O_3. The band edge effective mass obtained with this fit is $m_0^* = 0.23m_0$. This value is in great agreement with the value obtained from the HAXPES data supporting this being an accurate value for the effective mass in ICO.

5.6.3 Carrier Effective Mass

Fitting of the conduction band dispersion in angle resolved photo-emission spectroscopy (ARPES) has given a value of m_0^* of 0.2-0.24 m_0 for undoped In_2O_3 [178, 179]. The value obtained for ICO here through both techniques falls within this range, indicating that the dispersion of the band structure is not significantly changed by the introduction of Ce.

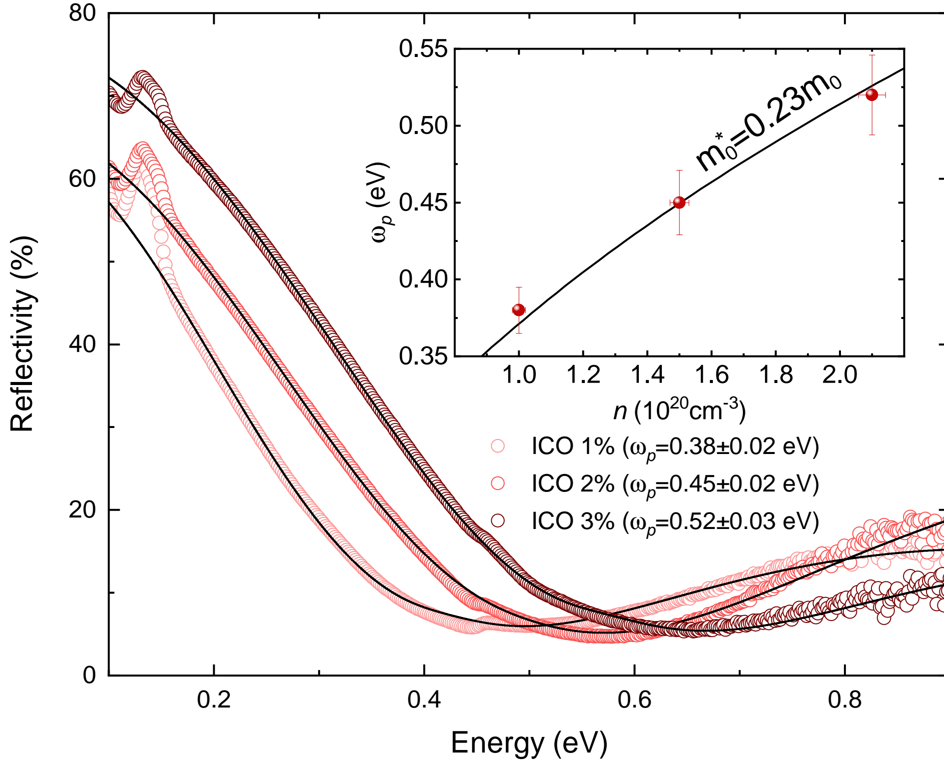

Figure 5.16: Infra-red reflectivity of the ICO samples in this study. The data has been fitted with a two oscillator model to extract the plasma frequency of the films. The inset shows the extracted plasma frequencies as a function of Carrier concentration which have been fitted to extract the band edge effective mass of the material.

In comparison, ITO has been reported to have a band edge effective mass of around 0.30-0.40 m_0 on multiple occasions [75, 180–183]. This shows the incorporation of Sn increases the electron effective mass compared to undoped In_2O_3 which limits the mobility. The value obtained for ICO is also very close to the value reported for IMO of 0.22 m_0 which has previously been shown to demonstrate high mobilities due its resonant $4d$ level [75]. It therefore seems likely that the donating $4f$ orbital in Ce sits well above the CBM allowing for these high mobilities.

5.7 Optical Gap

An alternative way of observing the position of the Fermi level in a degenerately doped semiconductor is through measurement of the optical gap. The standard method for obtaining the optical gap is the Tauc plot, described in section 4.3.1. For degenerately doped samples the validity of this method is questionable as the occupied conduction band states change the relationship between the absorption coefficient and photon energy. This relationship is discussed in detail later in section 3.5.7. This causes tailing in the plot which results in a varying gradient. As such where in the linear fit is applied to in the data set can result in significantly different x-axis intercepts

and therefore optical gaps. Despite these limitations Tauc plots can still be utilised in observing trends in optical gap if a consistent method is used, if the fits are applied at a consistent y value.

In this case the position of the Fermi level relative to the the VBM has already been obtained using HAXPES in section 5.6.1. In most systems this can be expected to be equivalent to the optical gap, however, in In_2O_3 this is not the case due to the forbidden transition between the VBM and CBM. As such, the optical gap is greater than the VBM to Fermi level separation. The increase in optical gap due to the forbidden transition is reported to be ~0.8 eV [48, 184].

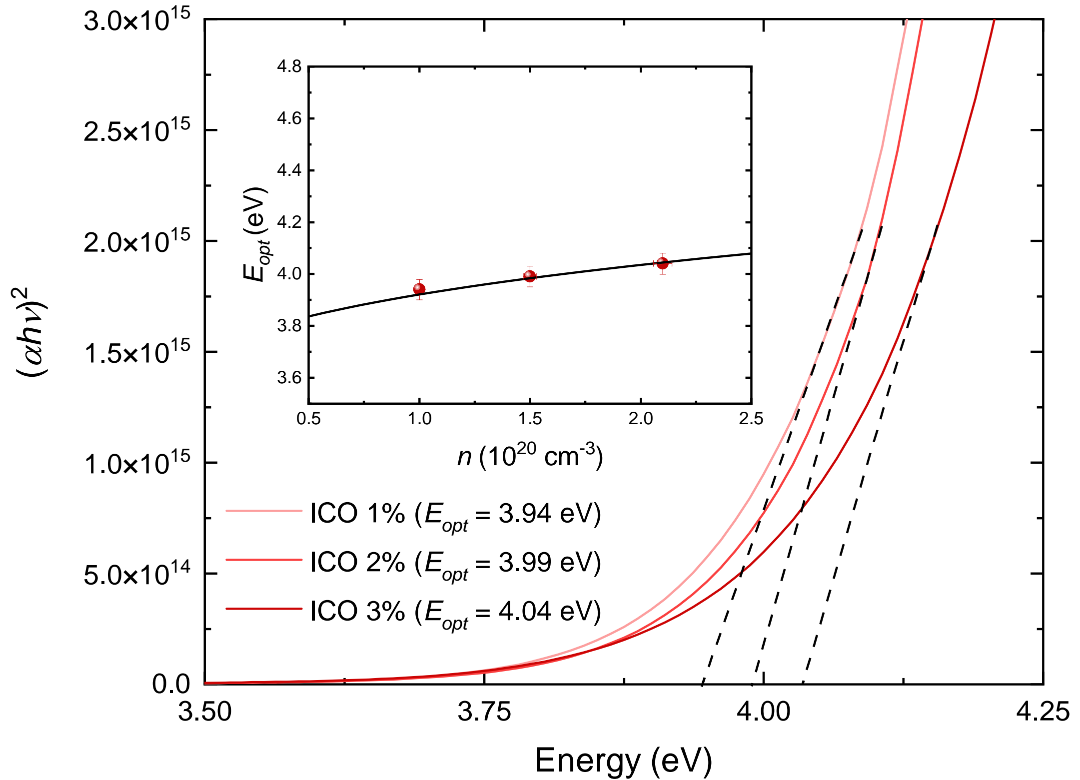

Figure 5.17: Tauc plots extracting the optical gap for the three Ce doped samples. The inset shows the modelled relationship between the optical gap and carrier concentration fitted to the extracted optical gaps.

Tauc plots have been created for the three Ce doped samples to show the trend in optical gap measured in this way is in agreement with that seen in the HAXPES data. Figure 5.17 shows these Tauc plots. The optical gaps extracted are 0.91-0.92 eV greater than the Fermi level positions extracted from the HAXPES data. This is slightly larger than the 0.8 eV increase expected but this can be attributed to the high uncertainty attributed to Tauc plots for degenerate samples. If the data had be fitted lower on the curve smaller gaps would have been extracted and the values would have been closer to the Fermi level plus 0.8 eV.

The inset shows the extracted optical gaps plotted against carrier concentration. The line shown in the inset is the calculated Fermi level as a function of carrier concentration for an

electron effective mass of m^*=0.23 m_0 increased by 0.91 eV to account for the forbidden transition. This show the trend in optical gap obtained by this method is in agreement with that obtained from the HAXPES data. This increases confidence in both the method used to obtain the Fermi level using photo-emission data and the value of the effective mass obtained.

The increased confidence in the method used to extract the Fermi level using HAXPES is important as in some cases measuring the optical gap is not possible. As example of a case like this is seen in Chapter 6 where the samples investigate have an optical gap greater than that of the substrate. As a result, absorption in the substrate dominates so the absorption edge from the deposited film can not be observed.

5.8 Resonant Doping

This lower effective mass supports a similar mechanism to that suggested in Ref. 75 for IMO. The lower effective mass indicates the a narrower CBM. In Ref. 75 this was suggested to be a result of the donor *d* orbitals not mixing with the host *p* orbitals at the CBM due to them sitting at an energy well above the CBM. Based on the similar effective masses observed in ICO, IMO and undoped In_2O_3 it seems likely that *f* orbitals behave similarly. Meanwhile the Sn *p* donor state mixes with the host CBM, broadening it and increasing the carrier effective mass. These donor states sitting well above the CBM have been dubbed 'resonant' and hence these dopants have been referred to as resonant dopants. Figure 5.18 shows a simple diagram depicting the difference between resonant and traditional dopants.

5.8.1 In_2O_3 Band Structure

DFT calculations of the band structure of Ce doped In_2O_3 were performed for Ce on both In sites in In_2O_3 and in both the +1 and neutral charge states. These calculated band structures are all shown in figure 5.19 alongside the band structure for the undoped host material.

The band structure of undoped In_2O_3 displays a fundamental band gap of 2.54 eV which is in good agreement with previously reported results [75, 185].

The band structures calculated for Ce on the 24*d* and the 8*b* sites are virtually identical when in the same charge state. In figures 5.19 b and d which show the band structures for Ce in the neutral charge state, Ce (III), a single Ce 4*f* can be seen just above the CBM. The remaining 4*f* states sit around 5 eV above the CBM and are marked by red crosses as they overlap with host states at that energy.

In figures 5.19 c and e which depict the calculated bacnd structure for Ce in the +1 charge state, Ce(IV), the Ce 4*f* states can be seen around 1.5 eV above the CBM. These states are sitting resonant within the conduction band meaning they do not mix with the In 5*s* states which dominate the CBM. As a result, the host band structure is maintained so the carrier effective

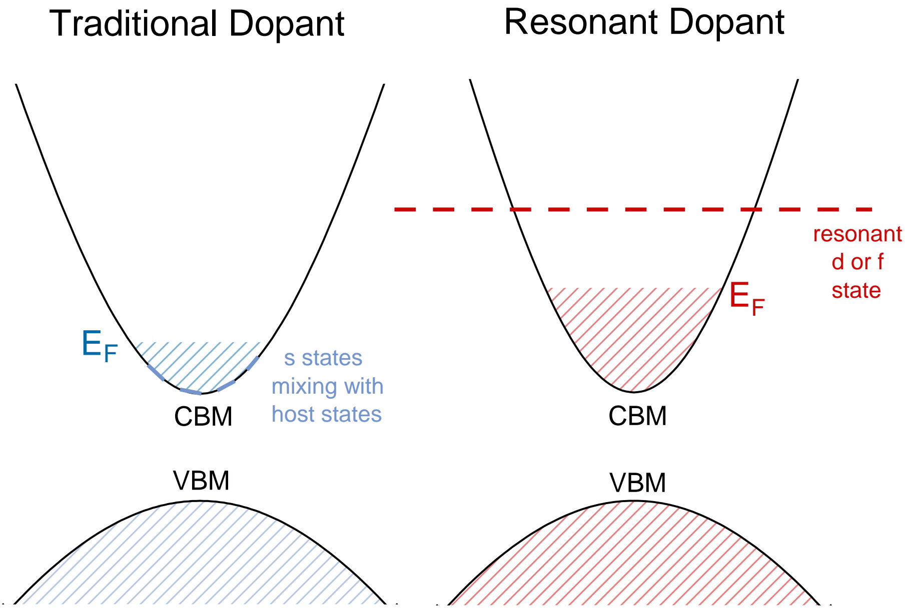

Figure 5.18: Diagram demonstrating the difference between the band structure of TCOs doped with traditional and resonant dopants. The resonant dopant results in a narrower conduction band at the CBM resulting a lower carrier effective mass and a higher Fermi level, E_F for the same carrier concentration.

mass in the system remains low. This is similar to the phenomena seen within Mo doped In_2O_3 and as expected for a resonant dopant.

5.8.2 Partial Charge Density

Also calculated was the partial charge density at the CMB in Ce doped In_2O_3. Figure 5.20 shows the partial charge density at the CBM focusing on the In 24d site. It can be seen that there is minimal charge density at the site which is marked in blue.

The Ce atom at the In 24d site only contributes around 0.3% of the partial charge denisty at the CBM. This behaviour is similar to that seen in Mo doped In_2O_3 and notably different to that seen in Sn doped In_2O_3 [75]. In ITO the Sn atom contributes significantly to the partial charge density at the CBM.

5.8.3 Impact on Carrier concentration

As previously shown in Figure 5.14 the CNL for Ce doped In_2O_3 lies roughly 0.1 eV above the CBM and the lower carrier concentrations achieved with Ce compared to other dopants has been attributed to this. However, the resonant behaviour of Ce also contributes to this lower limit.

The relationship between carrier concentration and Fermi Level is described in equation 3.56 in section 3.5. This relationship is dependent on carrier effective mass meaning that a lower

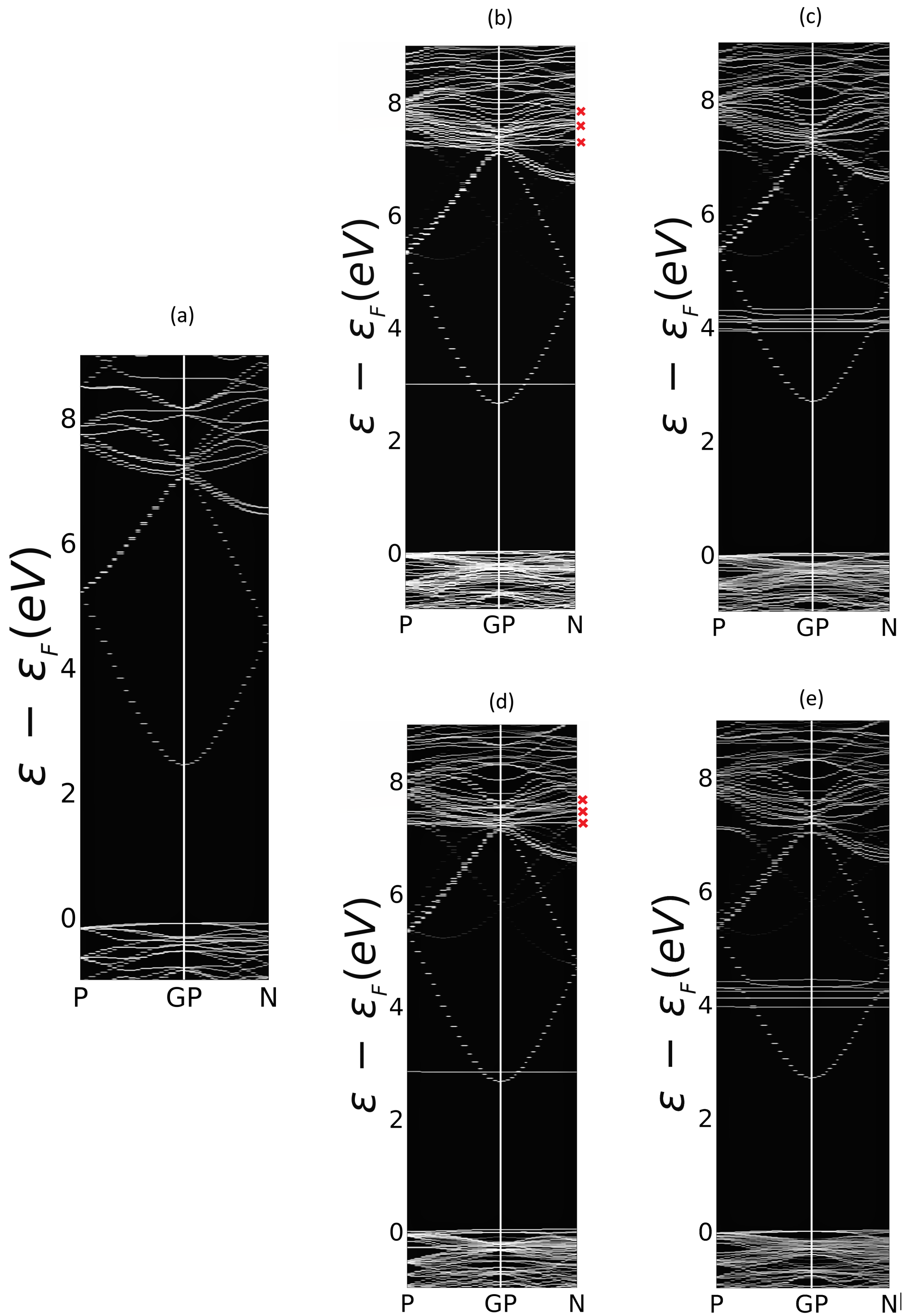

Figure 5.19: Calculated band structures for (a) undoped In_2O_3 and In_2O_3 with (b) neutral Ce on the 24d site, (c) +1 Ce on the 24d site, (d) neutral Ce on the 8b site and (e) +1 Ce on the 8b site. In the two band structures for incorporating neutral Ce the Ce 4f levels are marked with red crossed as they considerably overlap with levels from the host.

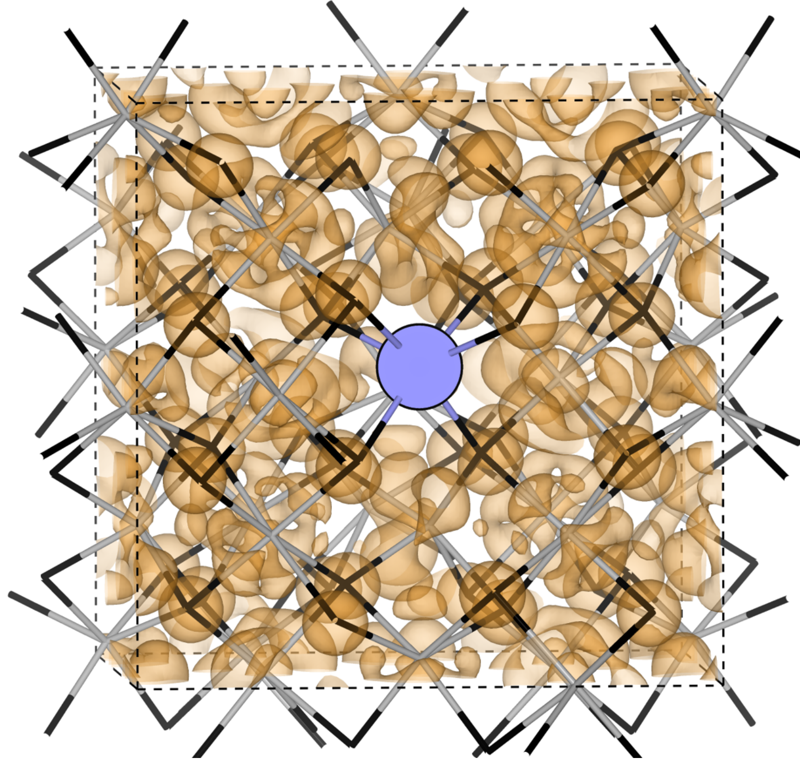

Figure 5.20: Partial charge density around the Ce_{In} $24d$ site when in the +1 charge state. Wire framework denotes In atoms in grey, O atoms in black, and Ce in blue, with charge density as the orange isosurface.

effective mass means a higher Fermi energy for the same carrier concentration. Hence, the CNL is reached at a lower carrier concentration than it would be for a higher effective mass.

For Sn doped In_2O_3 the CNL sits at 3.5 eV, around 0.85 eV above the CBM where the Sn_{In} 1+/0 transition occurs. Meanwhile Mo doped In_2O_3 has a CNL at 3.4 eV, 0.74 eV above the CBM where the Mo_{In} 1+/0 transition occurs [186].

Figure 5.21 shows the relationship between carrier concentration and Fermi level as calculated using equation 3.56 for the alpha approximation for effective masses of 0.23 m_0 and 0.40 m_0 to represent the resonant dopants and non-resonant Sn dopant respectively. This shows that for the carrier concentration observed in the Ce doped samples, ~2×10^{20} cm^{-3} corresponds to a Fermi level of 3.2 eV for an effective mass of 0.22 m_0 and ~5×10^{20} cm^{-3} for one of 0.40 m_0. This shows that the upper limit on carrier concentration is potentially halved by the resonant nature of the dopant.

Similarly for IMO the CNL of 0.74 eV above the CBM gives an upper limit on carrier concentration of around ~8×10^{20} cm^{-3} for an effective mass of 0.22 m_0 while it could reach 1.6×10^{21} cm^{-3} if it had the higher effective mass seen in ITO.

Meanwhile ITO having the highest energy CNL and higher effective mass it can reach carrier

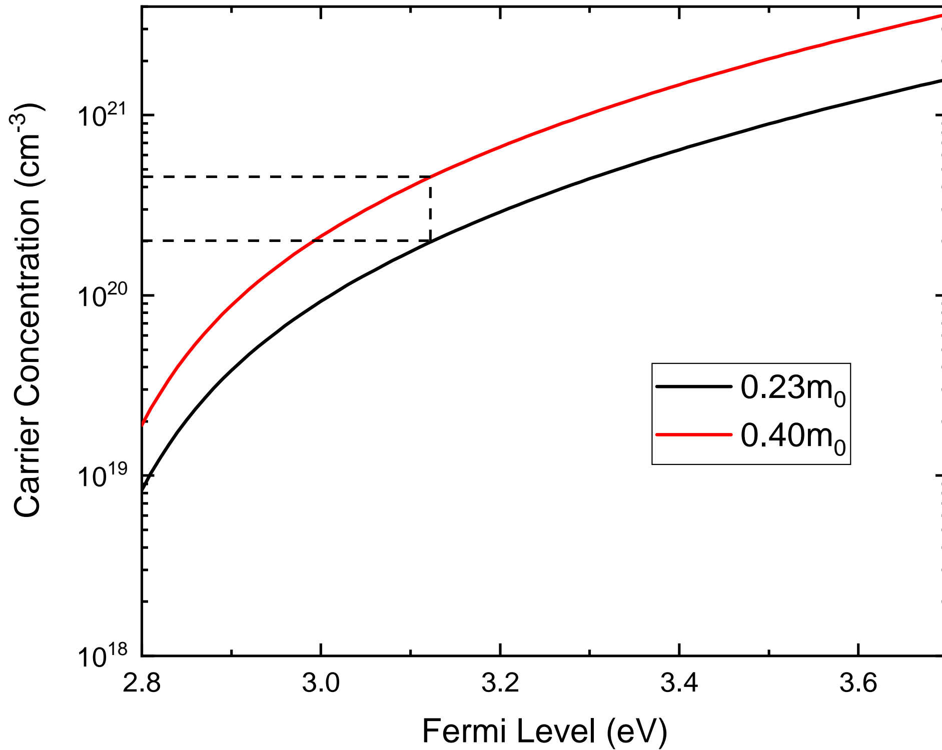

Figure 5.21: Calculated relationships between Fermi level and carrier concentration for effective masses of $0.23m_0$ and $0.40m_0$.

concentrations of up 2.2 $\times 10^{21}$ cm^{-3}. To reach carrier concentrations of this level utilising a resonant dopant with an effective mass of 0.22 m_0 the Fermi level would have to be around 1.1 eV above the CBM. Even if no change in preferred charge state occurred for the dopant before this point under most growth conditions the favourable formation of In vacancies would prevent the Fermi level ever reaching energies that high. Therefore it seems likely that it would be impossible for any resonant dopant to ever achieve the higher carrier concentrations observed in ITO reported in the literature and therefore only slight improvements in overall conductivity can be expected due to the improved mobilities.

5.9 Infra-Red Transparency

Although the carrier concentration does limit the conductivity of these samples the conductivities achieved are only surpassed by ITO or IMO. When comparing samples of similar resistivity, the higher mobilities of ICO mean that greater transparency can be achieved in the near infra-red region due to the relationship between plasma frequency and carrier concentration. This can be seen in Figure 5.22 which shows the transmission spectra for the ICO 3% thin film and a commercial ITO thin film of comparable resisitivity. While this is not of great importance for many applications of TCOs it can have a significant impact on the performance of photovoltaic

devices.

Commercially available ITO was used for comparisons. The ITO used was Ossila unpatterned ITO glass substrates with quoted thickness of 100 nm and sheet resistance of 20 Ω/□ corresponding to a resistivity of 2.0×10^{-4} Ωcm. The soda-lime glass substrates are quoted as 1.1 mm thick.

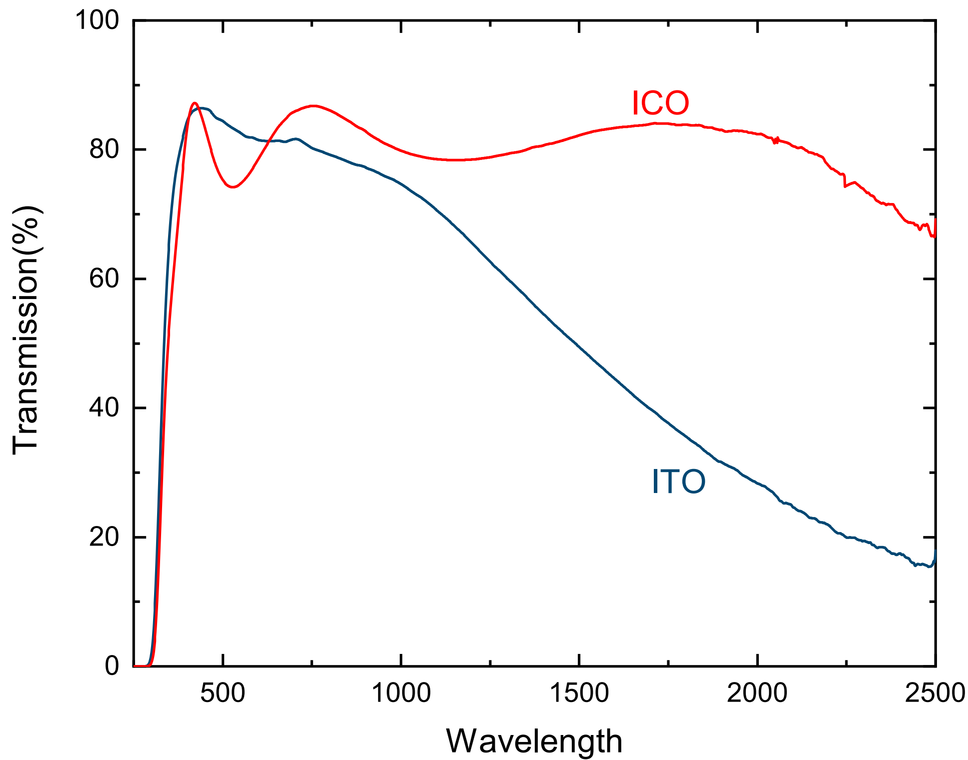

Figure 5.22: Transmission spectra of the ICO 3% thin film and a commercial ITO thin film of comparable resistivity showing improved transmission for the ICO thin film in the near infra-red due to its lower carrier concentration.

The infra-red region of light begins at energies below ~1.63 eV (wavelengths greater than 700 nm) while the majority of thin film photovoltaic absorber have band gaps in the range of E_g = 1.0-1.5 eV [30–33] as this range allows for the highest efficiency as described by the Shockley-Queisser limit [28]. Therefore, these absorbers will utilise photons from the near-IR region and any optical losses in the transparent contact will result in reduced efficiency.

This is of particular importance for absorbers with bandgaps at the narrower end of this range as a greater proportion of the power absorber comes from the near-IR region. This is of even greater importance when considering the loss of energy from photons of higher energy due to thermalisation. Therefore, when selecting a transparent conductor for photovoltaic applications ICO has significant benefits over ITO.

An area in which narrow band gap absorbers are regularly used are multi-junction solar cells. Such devices utilise absorbers such as Ge which has a band gap as small as 0.65 eV and therefore

are very absorbing in the infra-red region [187]. Such devices have a significantly higher cost per unit area than single-junction solar cells and as such are generally used in low area applications such as in concentrator solar cells or for extraterrestrial applications. This negates the primary limiting factor preventing In_2O_3-based TCOs from being utilised is most solar cells which is the cost of indium, as per unit area that cost would be negligible compared to that of the rest of the device.

5.10 Conclusion

Ce doped In_2O_3 thin films have been shown to display mobilities that surpass those seen in Sn doped In_2O_3, a material which currently dominates the commercial TCO market. However, in reports of ICO so far, carrier concentrations have not exceeded around 2×10^{20} cm^{-3}.

Both Ce(III) and Ce(IV) were observed in HAXPES spectra of Ce $3d$ peaks for all samples with an increase in the proportion of Ce(III) with increased total Ce content. Ce(III) on an In(III) site is a neutral defect and therefore no extra carriers are contributed. This may be a limiting factor on the carrier concentrations achievable with Ce doping.

The high carrier mobility of the samples is attributed to a lower carrier effective mass compared to ITO, which can be observed in the relationships between carrier concentration and both the Fermi level to valence band separation and plasma frequency. The low effective mass observed in ICO is due to the donor f states being resonant with the host conduction band due to sitting at an energy significantly above the CBM. This prevents hybridisation between the donor states and the cation states in the CBM, so that the shape of the host conduction band and low band edge effective mass are preserved.

Both observations, the mixed oxidation states and the lower band edge effective mass, were further supported by the results of DFT calculations. Defect formation energy calculations showed a change in preferred oxidation state for Fermi levels slightly above the CBM. This helped explain the multiple oxidation of Ce observed in the photo-emission measurements. Similarly, band structure calculation showed the Ce $4f$ states sitting resonantly in the conduction band supporting it being a resonant dopant in In_2O_3.

While the low carrier concentrations still present a challenge, the high mobilities mean that resistivities lower than most other transparent conductors have been achieved with ICO. Obtaining comparable resistivities with a lower carrier concentration, but a higher mobility, has the benefit of improved transmission in the near infrared. This means ICO has great potential to be an ideal candidate for a transparent conductor where high infrared transparency is important such as in photovoltaic devices utilising an absorber with a narrow band gap.

Very little research has been performed looking at the potential of Ce as a dopant in In_2O_3 and despite this it has already achieved resistivities lower than most of its competitors which have had decades of research invested in them. Therefore, despite the low carrier concentrations

observed here, it seems likely that further research into optimisation of the material could develop it into a TCO with significant beneficial properties compared to ITO, which currently dominates the field.

Chapter 6

Ta doping of SnO_2

6.1 Introduction

In the previous chapter the mechanism of resonant doping in Ce doped In_2O_3 was discussed and identified as a way to achieve high mobilities and improved infra-red transparency compared to the traditional dopants due to a similar mechanism to that previously observed in Mo doped In_2O_3. These properties make Ce doped In_2O_3 an appealing material for us in photovoltaic applications. Unfortunately the issue of the high cost and low abundance of In still persists making any In_2O_3 based TCO unsuitable for wide area applications such a conventional photovoltaics.

SnO_2 is the metal oxide that shows the greatest potential as a TCO after In_2O_3. Doped with F or Sb, to form FTO or ATO, it has displayed resistivities of around ~10^{-4} Ωcm. It has recently been reported that FTO is inherently self limiting as mobilities fail to surpass ~35 $cm^2V^{-1}s^{-1}$ for carrier concentrations of 3×10^{20} cm^{-3} or greater. These limited properties have been shown to be due to the preferential formation of interstitial F defects when the Fermi level rises to around 0.5 eV above the CBM [56]. In SnO_2 interstitial F acts as an acceptor and will therefore reduce the n-type carrier concentration. As such, in FTO the Fermi level is effectively pinned 0.5 eV above the CBM preventing any further increase in carrier concentration while further defects can be expected to still negatively impact the carrier mobility. This mechanism is refereed to as self-compensation as the dopant acts to compensate for itself by introducing acceptors rather than donors when doped beyond a certain level.

ATO also appears to be inherently self limited as reported mobilities generally fall below 20 $cm^2V^{-1}s^{-1}$ at carrier concentrations corresponding to degenerate doping. A self-compensation mechanism has also been identified in ATO arising due to the multi-valency on Sb. Sb can form

stably in both the Sb(III) and Sb(V) oxidation states, this has been observed using both Mössbauer spectroscopy and via XPS studies [61, 63],

Based on these observations about conventional dopants and the positive results seen using resonant dopants such as Ce or Mo in In_2O_3 an image of the ideal n-type dopant for SnO_2 arises. The ideal dopant would be an element with a similar ionic radius to Sn in SnO_2, have a donating orbital which is resonant in the conduction band to minimise mixing with the host Sn 5*s* states, be stable in the V oxidation state and be free of self compensation mechanisms. Based on the successful dopants in In_2O_3 such a dopant would likely be either a transition metal with a donating *d* orbital or a lanthanide with a donating *f* orbital. This chapter discusses elements which may potentially provide these desired properties, identifies the most promising candidate and through a combination of experimental characterisation and DFT calculations the actual its actual potential is analysed.

6.2 Potential Dopants in SnO_2

The number of potential dopants that fulfil the requirements for SnO_2 is much lower than for In_2O_3. This is primarily due to the lower number of transition metals, and no lanthanides, which are stable in the V oxidation state compared to the IV oxidation state. Four elements that do fulfil the requirements exist: vanadium, niobium, tantalum and dubnium. Of these element Db is not radioactively stable and is therefore unsuitable for use as a dopant leaving three options.

6.2.1 Vanadium

Several reports exist of attempts to created a transparent conductor based on V doped SnO_2 (VTO). However, these attempts have never resulted in carrier concentrations comparable to those seen in conventional TCOs. Experimental studies utilising photo-emission spectroscopy have explained the lack of success seen with VTO by showing that the V 3*d* state sit only 1.1 eV above the VBM of SnO_2 [188]. This places them below the Fermi level of undoped SnO_2 meaning V will not act as an n-type dopant despite its correct oxidation state.

An energy level diagram showing the position of the dopant level relative to the CB and VB for VTO is shown in figure 6.1 along side one for Nb doped SnO_2

6.2.2 Niobium

As with V, there have been reported attempts to fabricate transparent conducting Nb doped SnO_2 (NTO). Compared to VTO, NTO has shown moderate promise experimentally with reported mobilities of up to around 25 $cm^2V^{-1}s^{-1}$, relatively high for doped SnO_2. However, the carrier concentrations obtained in films with reasonable mobilities fall below 1×10^{20} cm^{-3} [189–191].

Recent DFT calculations have shown that Nb acts as a deep donor in SnO_2 with substitutional Nb on a Sn site, Nb_{Sn} transitioning from the +1 to the 0 charge state at about 0.2 eV below the

CBM. As such Nb doping is unlikely to be be able to move and the Fermi level above this point as any additional Nb will be introduced as a neutral defect. As such, Nb is unlikely to be able to degenerately dope SnO_2. Density of states calculations show a Nb 4d state around 2.5 eV above the VBM explaining the transition of Nb_{Sn} into the neutral charge state. This is in line with the experimental results and explains the limited carrier concentrations and conductivities seen in fabricated NTO films.

Bases on both the experimental and calculated results reported in the literature it seems unlikely that NTO would ever be able to achieve the Carrier concentrations or conductivities required to make it competitive with the likes of FTO or ITO.

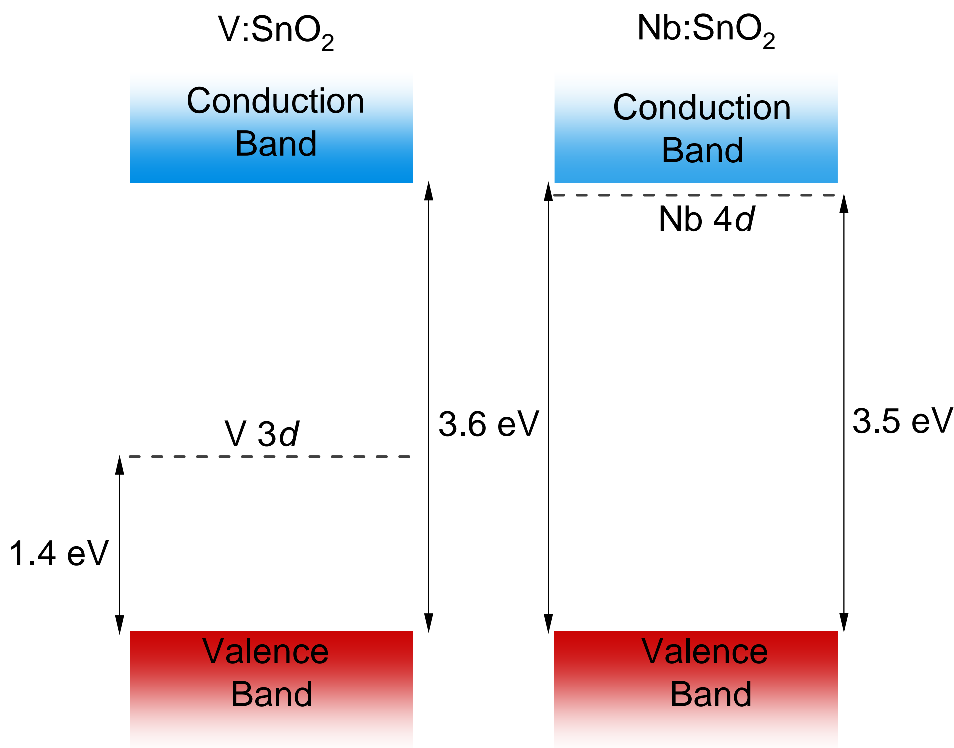

Figure 6.1: Energy level diagrams for V and Nb doped SnO_2 showing the positions of the V 3d and Nb 4d donor levels relative to the conuction and valence bands of SnO_2

6.2.3 Tantalum

With V and Nb ruled out due to their d orbitals sitting within the band gap of SnO_2 preventing degenerate doping only Ta remains as a potential resonant dopant in SnO_2. Experimentally Ta has shown significant promise, outperforming both V and Nb. Polycrystalline thin films of Ta doped SnO_2, TaTO, have displayed resistivities as low as $1.8\times10^{-4}\,\Omega\,$cm and have been fabricated by a wide array of deposition methods [192–203].

TaTO also displays exceedingly high mobilities of up to 83 $cm^2 V^{-1} s^{-1}$ when deposited by pulsed laser deposition [192] in particular and up to 49 $cm^2 V^{-1} s^{-1}$ when deposited by sputtering [203] (at carrier concentrations of 2.7×10^{20} cm^{-3} and 2.2×10^{20} cm^{-3} respectively). This surpasses the upper mobilities reported for both ATO and FTO by a significant margin, In cases where TaTO does not surpass this upper limit comparative studies of TaTO and ATO show that TaTO displays higher mobilities at similar carrier concentrations when deposited by the same method [202].

Understanding of the superior properties observed in TaTO has never been developed. In this chapter experimental studies of TaTO and ATO thin films deposited by aerosol assisted chemical vapour deposition (AACVD) along with DFT calculations are utilised to develop an understanding of the behaviour of Ta as a dopant in SnO_2 and whether it displays similar resonant behaviour to Mo and Ce in In_2O_3.

6.3 SnO_2:Ta and SnO_2:Sb thin films

For this study a range of samples of Ta and Sb doped SnO_2 were deposited by AACVD. The Sb doped samples were used as comparative standards so that the behaviour of Ta could be compared to that of a conventional dopant. 5 samples containing each dopant were fabricated utilising a range of doping densities along with a sample of undoped SnO_2.

6.3.1 Fabrication

Thin films of SnO_2:Ta and SnO_2:Sb were deposited by aerosol assisted chemical vapour deposition (AACVD). All precursors were purchased from Sigma-Aldrich and used as received. AACVD depositions were carried out on a custom built cold-wall reactor where the substrate (~ 50 nm SiO_2 barrier-coated float glass) was positioned on a graphite block containing a Watmann cartridge heater regulated by a Pt-Rh cartridge heater. A stainless steel top plate was positioned 0.8 cm above the substrate to promote laminar flow. The tantalum doped SnO_2 films were grown using a dual pot AACVD process using butyltin trichloride (0.3 mL, 1.77 mmol) dissolved in dry methanol (10 mL, 394 mmol) and tantalum (V) ethoxide (5, 10, 15, 25, 40 mol.%) dissolved in dry toluene (10 mL, 124.7 mmol). The two solutions were atomized using a Johnson Matthey Liquifog® piezoelectric ultrasonic humidifier with the tin precursor flow rate kept at 0.6 L min^{-1} using air (BOC, 99.99%) and the tantalum precursor flow rate was kept at 0.6 L min^{-1} using nitrogen (BOC, 99.99%). The two flows were then mixed at a Y junction and delivered to the CVD reactor. The glass substrate was maintained at 500 °C. The antimony doped SnO_2 films were grown similar to the method previously reported in Ref. 204 on glass substrates at 450 °C using a one-pot AACVD process where the butyltin trichloride (0.2 mL, 1.06 mmol) and antimony(III) ethoxide (2, 6, 9, 11, 15 mol.%) were dissolved in methanol (10 mL, 394 mmol). The carrier gas was air and the flow rate was 1 L min^{-1}. At the end of the depositions for both systems, the reactor was turned off and

cooled under a flow of nitrogen until 100 °C after which point the samples were removed. The coated substrates were handled and stored in air.

6.3.2 Electrical Properties

Table 6.1 shows the electrical properties of the films deposited for this work. The samples are labelled by the percentage of Ta or Sb in the precursor solution. For the Sb doped films, the highest mobility is 17.7 $cm^2\,V^{-1}\,s^{-1}$ at a carrier concentration of 3.44×10^{20} cm^{-3}, corresponding to the lowest resistivity of 10.3×10^{-4} Ω cm. In the Ta doped films, the highest mobility observed was 25.9 $cm^2\,V^{-1}\,s^{-1}$ at a carrier concentration of 2.65 $\times10^{20}$ cm^{-3}, corresponding to a resistivity of 9.1×10^{-4} Ω cm. Films with higher carrier density of up to 3.70×10^{20} cm^{-3} and slightly lower mobility gave resistivities down to 7.4×10^{-4} Ω cm. Literature values for TaTO and ATO are also shown in Figure 6.2. The literature shows a trend of TaTO achieving higher mobilities than ATO at comparable carrier concentrations, similar to the samples studied in this work. Some exceptions to this are the TaTO samples deposited onto seed a layer to promote preferred orientation and increased crystallinity, which display significantly higher mobilities than seen else where and highlight the potential of Ta as a dopant [192, 203]. Discussion of the potential impact of theses seed layers is included in section 6.4 later in this chapter,

Table 6.1: Electrical properties of the 'undoped', Ta doped and Sb doped SnO_2 films used in this work as determined by room temperature Hall effect measurements. Percentages given are the Ta or Sb concentration in the precursor solution.

Sample	Sheet resistance (±1) (Ω/□)	ρ ($\pm1\times10^{-5}$) (Ωcm)	μ (±0.1) ($cm^2V^{-1}s^{-1}$)	n ($\pm1\times10^{18}$) (cm^{-3})
'undoped' SnO_2	35	2.97×10^{-3}	17.2	1.21×10^{20}
Ta:SnO_2 (5%)	14	1.09×10^{-3}	21.3	2.68×10^{20}
Ta:SnO_2 (10%)	8	7.42×10^{-4}	22.5	3.66×10^{20}
Ta:SnO_2 (15%)	8	9.08×10^{-4}	25.9	2.65×10^{20}
Ta:SnO_2 (25%)	14	1.36×10^{-3}	25.5	1.80×10^{20}
Ta:SnO_2 (40%)	13	1.29×10^{-3}	15.7	3.10×10^{20}
Sb:SnO_2 (2%)	11	1.03×10^{-3}	17.7	3.44×10^{20}
Sb:SnO_2 (6%)	23	1.40×10^{-3}	11.3	3.94×10^{20}
Sb:SnO_2 (9%)	34	1.49×10^{-3}	13.0	2.38×10^{20}
Sb:SnO_2 (11%)	128	7.72×10^{-3}	5.0	1.63×10^{20}
Sb:SnO_2 (15%)	23	1.49×10^{-3}	6.7	6.26×10^{20}

A nominally undoped film was deposited by the same method. This film was measured to have a resistivity of 2.97×10^{-3} Ωcm corresponding to a carrier concentration of 1.2×10^{20} cm^{-3} and a carrier mobility 17.2 $cm^2\,V^{-1}\,s^{-1}$. The low resistivity of the undoped sample can be attributed to the deposition method introducing a high concentration of defects which unintentionally dope the film.

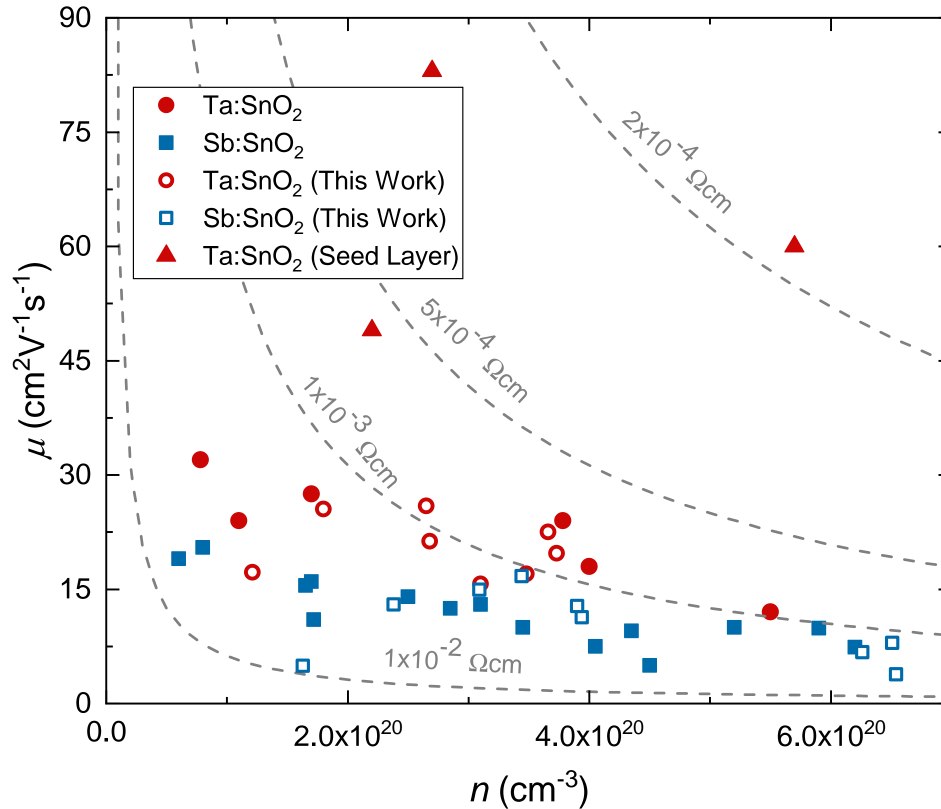

Figure 6.2: The mobility for samples with a range carrier concentrations deposited by AACVD (This work) and Hall properties of ATO and TaTO samples reported throughout the literature [201, 205–208]. Dashed lines display lines of constant resistivity. Triangular points are TaTO films deposited on seed layers as reported in the literature [192, 203]

6.3.3 Optical Properties

Transmission spectra using the UV-VIS Spectrometer were taken for each doped sample and the undoped sample and reflectvity spectra using the FTIR spectrometer were taken for selected TaTO and ATO samples.

Transmission spectra for examples of TaTO and ATO of comparable carrier concentrations, 3.66×10^{20} and 3.44×10^{20} cm^{-3} respectively, are shown in Figure 6.3. The transmission at high energies is comparable for the two samples. However at lower energies TaTO displays superior transmission. For photovoltaic application, depending on the absorber used, transparency in the near infra-red at energies as low as 1.1 eV can be important. Currently, one of the main applications of FTO is as a transparent electrode in thin film solar cells, so it is likely that commercially TaTO would be used in similar applications rendering the increased transmission in the near-IR is important.

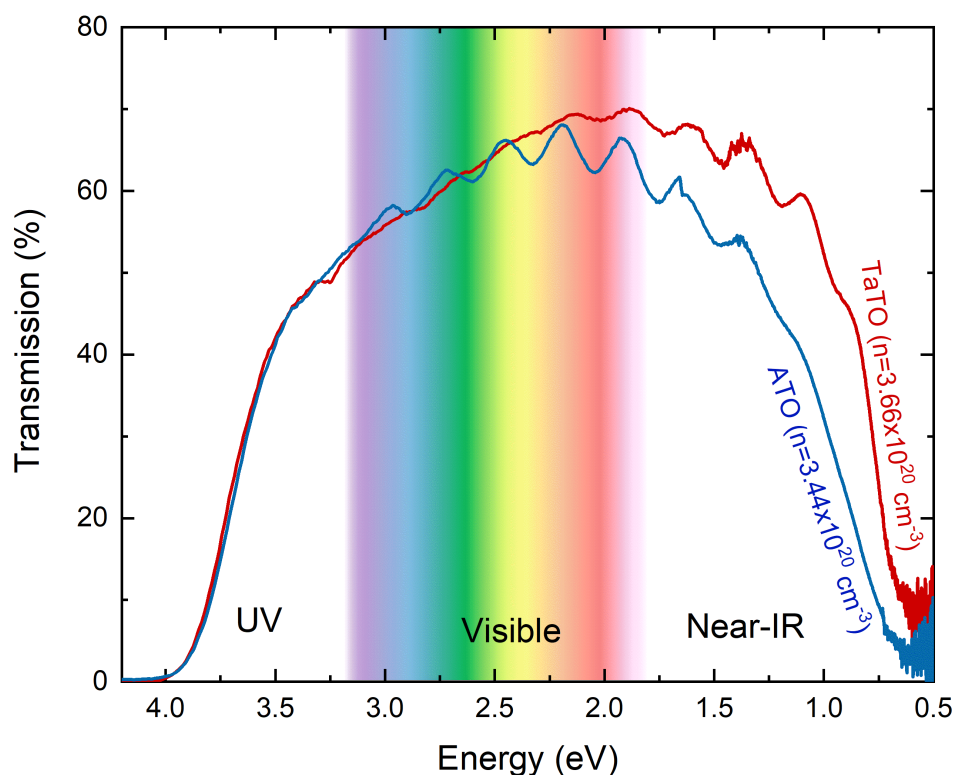

Figure 6.3: Transmission spectra of ATO and TaTO thin films with comparable carrier concentrations.

6.4 X-ray Diffraction

Figure 6.4 shows the XRD patterns for each of the Ta doped, Sb doped and undoped samples as well as the calculated pattern for SnO_2. All peaks in the diffraction patterns for all the samples can be attributed to SnO_2 as they are present in the calculated pattern. It can be concluded with confidence that all films are therefore polycrystalline SnO_2.

6.4.1 Crystallinity

The peaks in the XRD Pattern vary in width between the samples. Generally, the peaks in the Sb doped samples appear broader than those in the undoped or Ta doped samples. Increased peak width is indicative of reduced crystallinity. This means it is likely that some difference in the fabrication of the two materials has resulted in a difference in crystallinity,

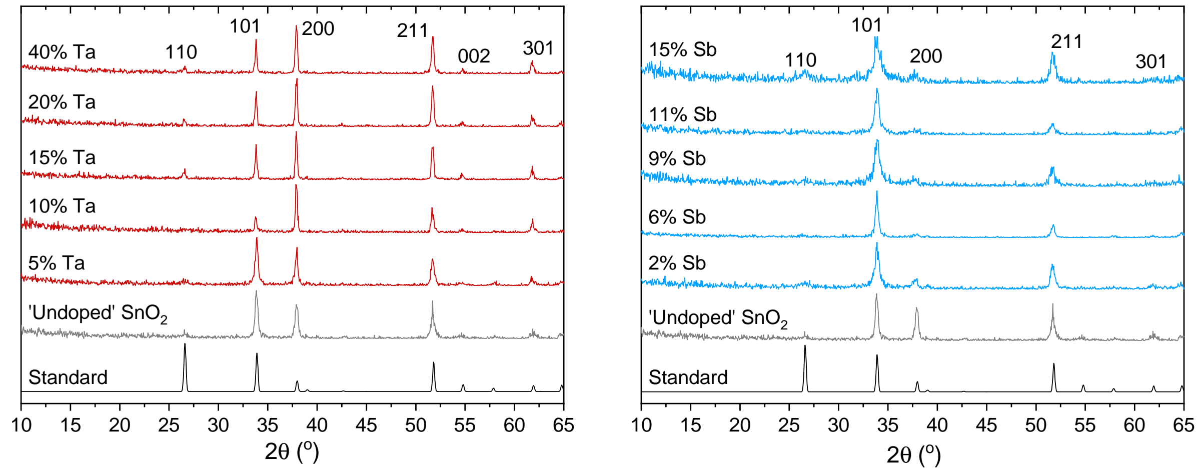

Figure 6.4: XRD for (left) TaTO and (right) ATO under different doping concentrations. Shown in each panel are the XRD for undoped SnO_2 and the calculated XRD of SnO_2.

6.4.2 Orientation

A difference in preferred orientation can be seen between the Sb doped and the Ta doped samples. In the Sb doped samples there is significantly less intensity in the peak corresponding to the 200 reflection at 37.9° which is the most intense in several of the Ta doped samples. Sb doped samples also display less intensity in the 301 peak at 61.7°. The preference in orientation in the Ta doped samples appears similar to the preference in the undoped sample, with the Ta doped samples displaying a slight increase in preference to the (100) orientation over the (101) orientation.

Notably, many of the Ta doped SnO_2 samples with the highest reported mobilities within the literature display preferred growth in the (100) orientation [192, 203]. In combination with the XRD patterns shown here there is a clear correlation between the presence of the 200 peak in XRD and improved mobility. Charge transport within SnO_2 has been shown to be anisotropic with the electron effective mass varying depending on the direction. [209, 210] Therefore, it is possible that the differences in orientation contribute to the improvement in carrier mobility seen in the Ta doped samples. However, Sb doped SnO_2 samples in the literature rarely display the 200 orientation in XRD and high mobility Ta doped SnO_2 not displaying this preferred orientation has been reported [197]. Further work looking at samples of Sb and Ta doped SnO_2 with controlled orientation would be required to establish the magnitude of this potential contribution.

6.5 Infra-Red Reflectivity

IR reflectivity spectra were measured for three of each of the TaTO and ATO samples, chosen to encompass a range of carrier concentrations. The samples chosen were the 10%, 15% and 40% for the Ta doped and the 2%, 6% and 9% for the Sb doped. The IR-reflectivity spectra for a photon energy range of 0.25–1.25 eV for these samples are shown in figure 6.5.

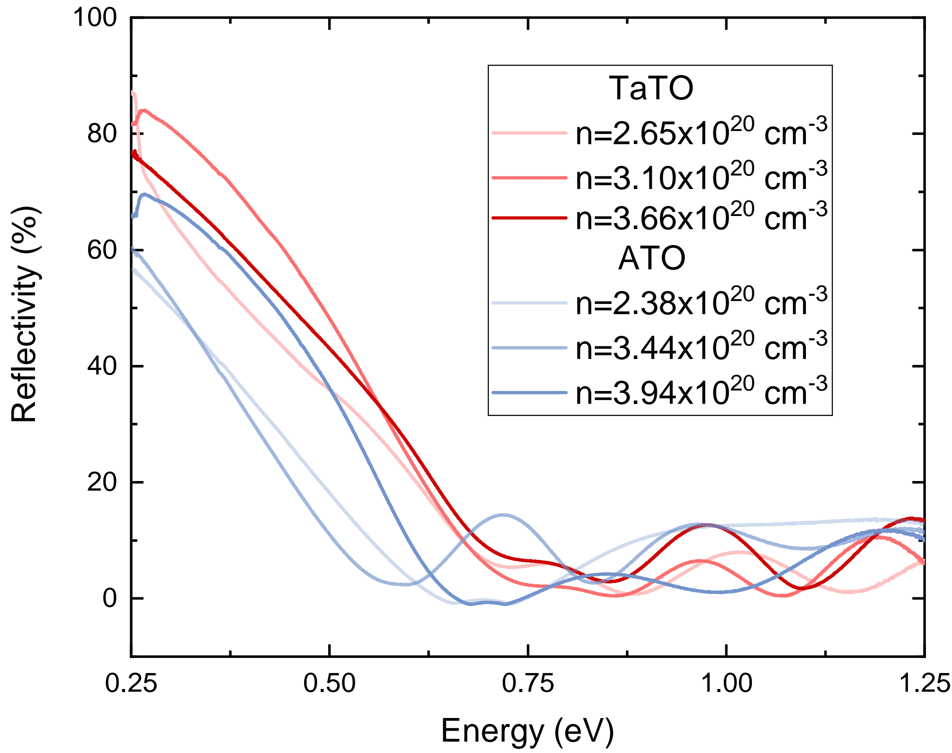

Figure 6.5: Reflectivity spectra of Ta doped and Sb doped SnO_2 thin films over an energy range covering the near infra-red.

A clear difference can be observed between the spectra for TaTO and for ATO. In all cases the reflectively onset due to plasma reflectvity is at a higher energy for the TaTO samples than the ATO samples. As discussed in section 1.3.4, the reflectivity onset is dependent on the plasma frequency which is dependent on the carrier concentration and carrier effective mass. If two films have similar carrier concentrations but different plasma frequencies this is indicative of the film with the higher energy plasma frequency having a lower effective based on equation 1.5. Figure 6.6 shows reflectivitly spectra for the Ta doped sample for which n=3.66×10^{20} cm^{-3} and the Sb doped sample for which n=3.44×10^{20} cm^{-3}. The difference in reflectivity onset indicates a lower free carrier effective mass in TaTO than ATO.

6.6 HAXPES

Hard X-ray photon emission spectroscopy (HAXPES) was performed at the I09 beamline at the Diamond Light Source (Didcot, UK). A photon energy of 5.95 keV was selected using a Si(111) double-crystal monochromator and a Si(004) channel-cut crystal as a post monochromator. The beam size at the sample was 40×20 μm^2 with a grazing incident angle of 87.5° with respect to the surface normal. Photoelectrons were detected using a EW4000 photoelectron analyser from

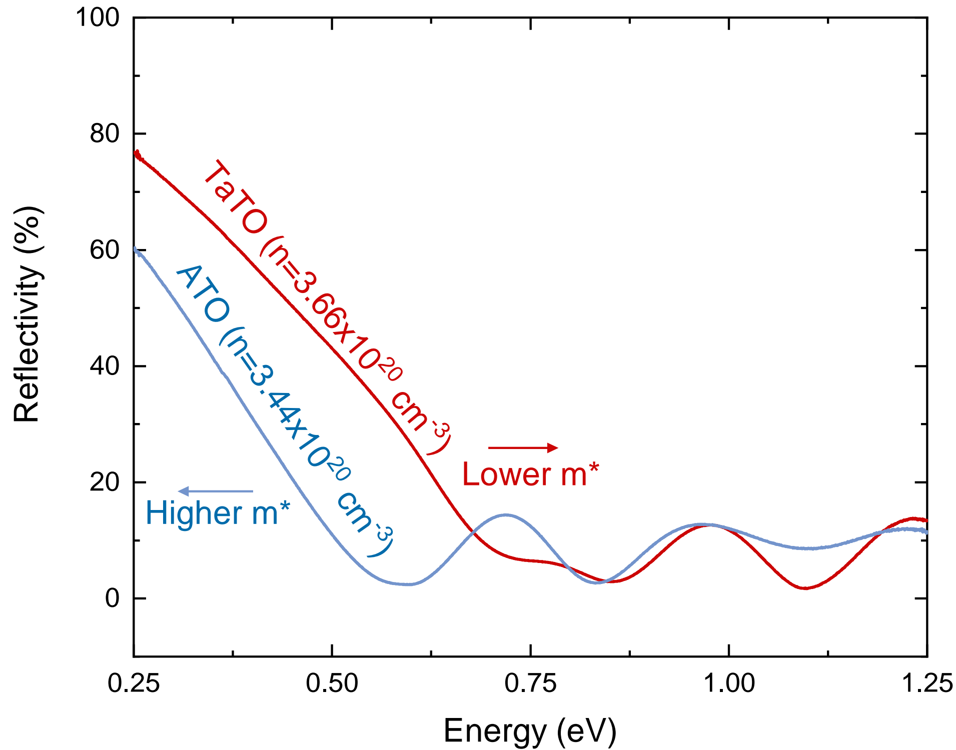

Figure 6.6: Reflectivity spectra of Ta doped and Sb doped SnO_2 thin films with comparable carrier concentrations over an energy range covering the near infra-red.

VG Scienta (Uppsala, Sweden). Calibration of the binding energy scale was performed using the Fermi edge and the 4f core level lines of a gold reference sample. The gold Fermi edge was fitted to obtain an experimental resolution of ~ 200 meV.

Spectra were measured for 5 Ta doped and 5 Sb doped samples covering a range of carrier concentrations. Survey spectra were taken for each sample followed by regions covering core levels of each expected element: Sn, O, C and the dopant species as well as a region covering the valence and conduction band emission.

6.6.1 Surveys

Figure 6.7 shows HAXPES survey scans for both and Ta and Sb doped samples with features of significant intensity identified and labelled. The origin of the features in these spectra were identified using spectra which are presented in Ref. 141.

The survey spectra shown are those for the 11% Sb sample and the 5% Ta sample. These spectra are representative of the survey spectra of all the Sb and Ta doped samples used in this study as all displayed the same features.

Most of the features in these surveys can be attributed to either Sn or O as expected. A small peak at ~284 eV has been attributed to C 1s in both spectra. This is attributed to adventitious

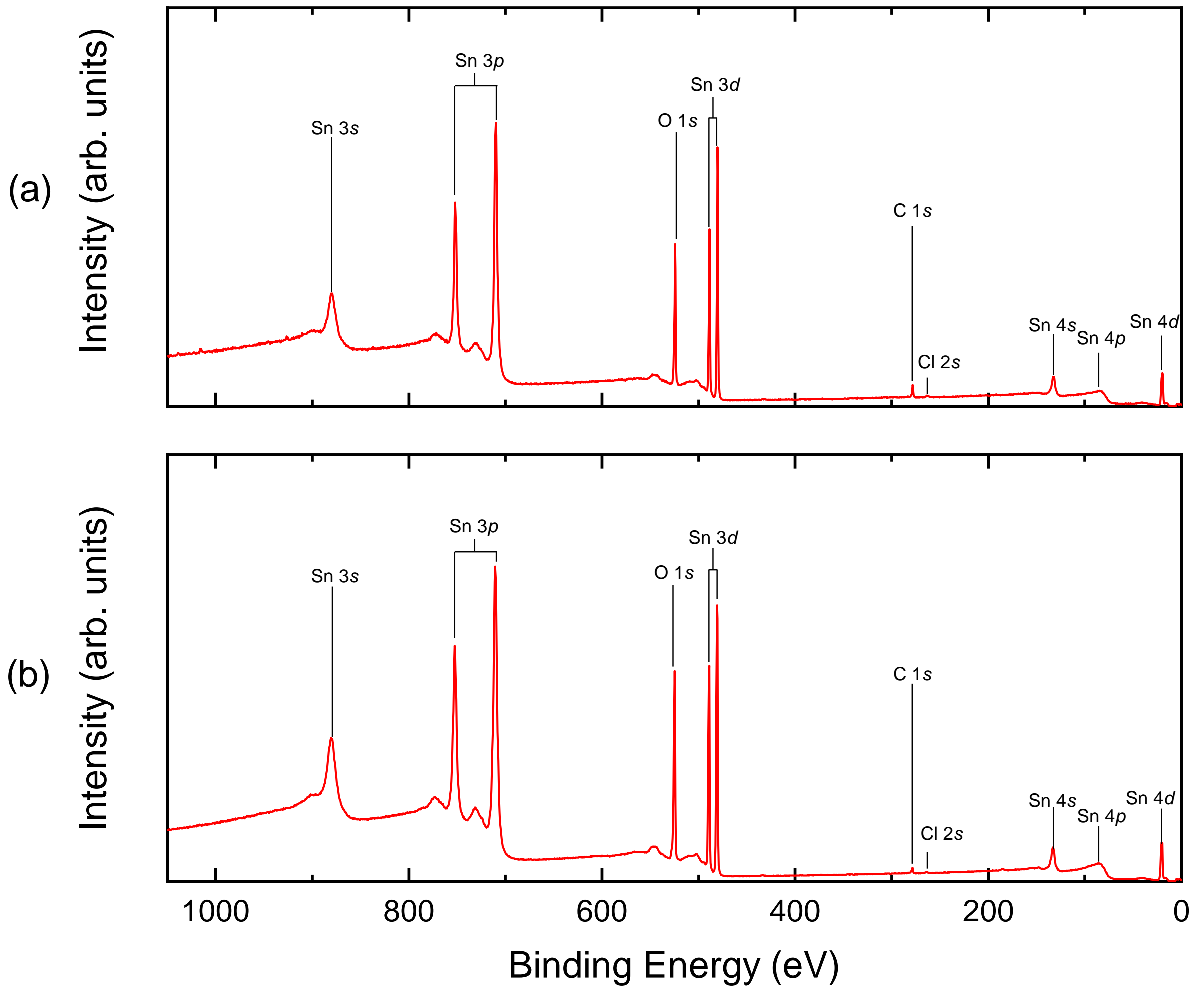

Figure 6.7: Survey spectra for (a) Sb doped SnO_2 and (b) Ta doped SnO_2. Prominent features have been identified using spectra in Ref. 141 and labelled.

carbon which is present in most photo emission spectra. A smaller feature at ~270 eV has been attributed to Cl 2*s*. The presence of Cl in these samples is likely due to the use of butyltin trichloride in the deposition process. The Cl 2*s* peaks are very small indicating that the concentration Cl in the samples is very small and likely have little to no impact on the materials properties but its presence must still be considered while analysing these samples.

6.6.2 Conduction Band Emission and midgap states

As all TaTO and ATO samples are degenerately doped there are occupied states within the conduction bands are photo-emission from these bands can be seen as shown in figure 6.8.

In the valence and conduction band spectra for both Ta doped Sb doped SnO_2 the counts never reach zero within the band gap. This is due to the presence of a large feature within the band-gap. Figure 6.10 shows the HAXPES spectra for a Ta doped sample for the region covering

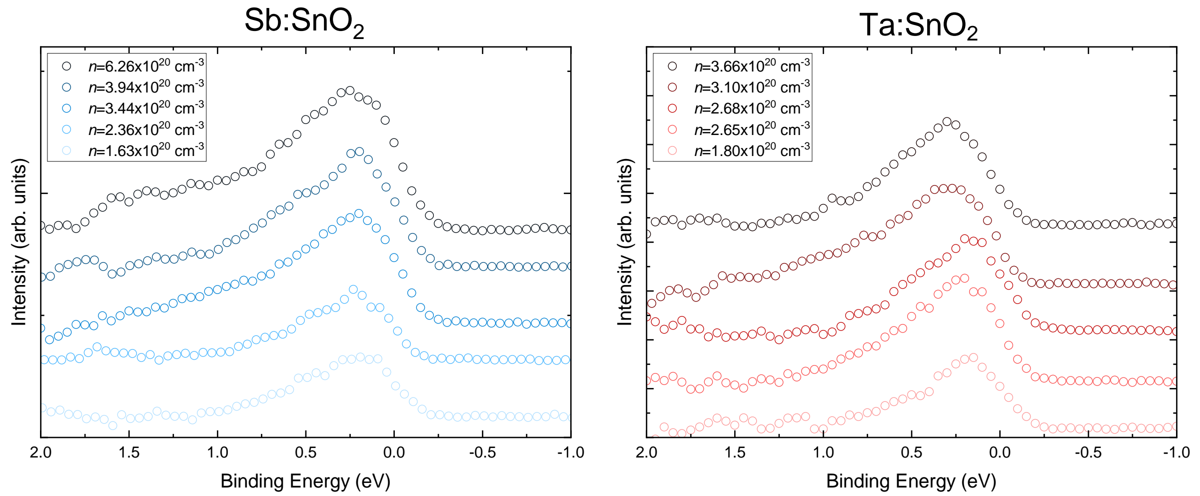

Figure 6.8: HAXPES spectra for all doped samples of SnO_2 covering a binding energy range of 2 to -1 eV to show the conduction band emission observed in each sample.

the VBM and conduction band emission. The mid-gap state can be clearly seen.

This feature has been regularly reported in SnO_2 spectra and those of other Sn (IV) containing compounds, it is even present for Sn doped In_2O_3 where Sn content is usually around 10 at%. The feature is regularly attributed to the formation of Sn (II) at the surface due to surface termination [211]. While the proportion of the Sn in these compounds in the (II) oxidation state in minimal the surface sensitive nature of XPS and HAXPES means that the features caused by its presence are still of a significant size. If this is the origin of the the midgap state other features attributed to Sn (II) would be expected to be present in the HAXPES spectra for the samples. Figure 6.9 shows the HAXPES spectrum for the region containing the Sn 3*d* peaks. If Sn (II) is present at the surface an asymmetry would be expected in the Sn 3*d* peaks due to the shift in binding energy for different oxidation states.

In figure 6.9 a clear asymmetry can be observed in the Sn 3*d* peaks with the peaks being broader on the high binding energy side. This is indicative that there are multiple contributions in each peak. As such the peaks have each been fitted with two convolved Lorentzian Gaussian peaks each. The 3*d* peaks for Sn (II), Sn in SnO, have been reported to have a binding energy of around 0.5 eV less than that reported for Sn(IV), Sn in SnO_2. Restraining the two features within a peak to have a separation of 0.5 eV gives a good fit supporting there being Sn(II) present within the samples and this being the origin of the mid gap state seen in the valence band spectra.

In this case the mid gap feature makes the comparison of valence band cut offs and conduction band features difficult. In particular the size of this feature varies significantly between samples further complicating comparisons. For this reason comparing the area under the conduction band emission to carrier concentration as was done for the ICO samples in chapter 5 will no give a meaningful comparison as that area is significantly impacted by the presence of the mid-gap

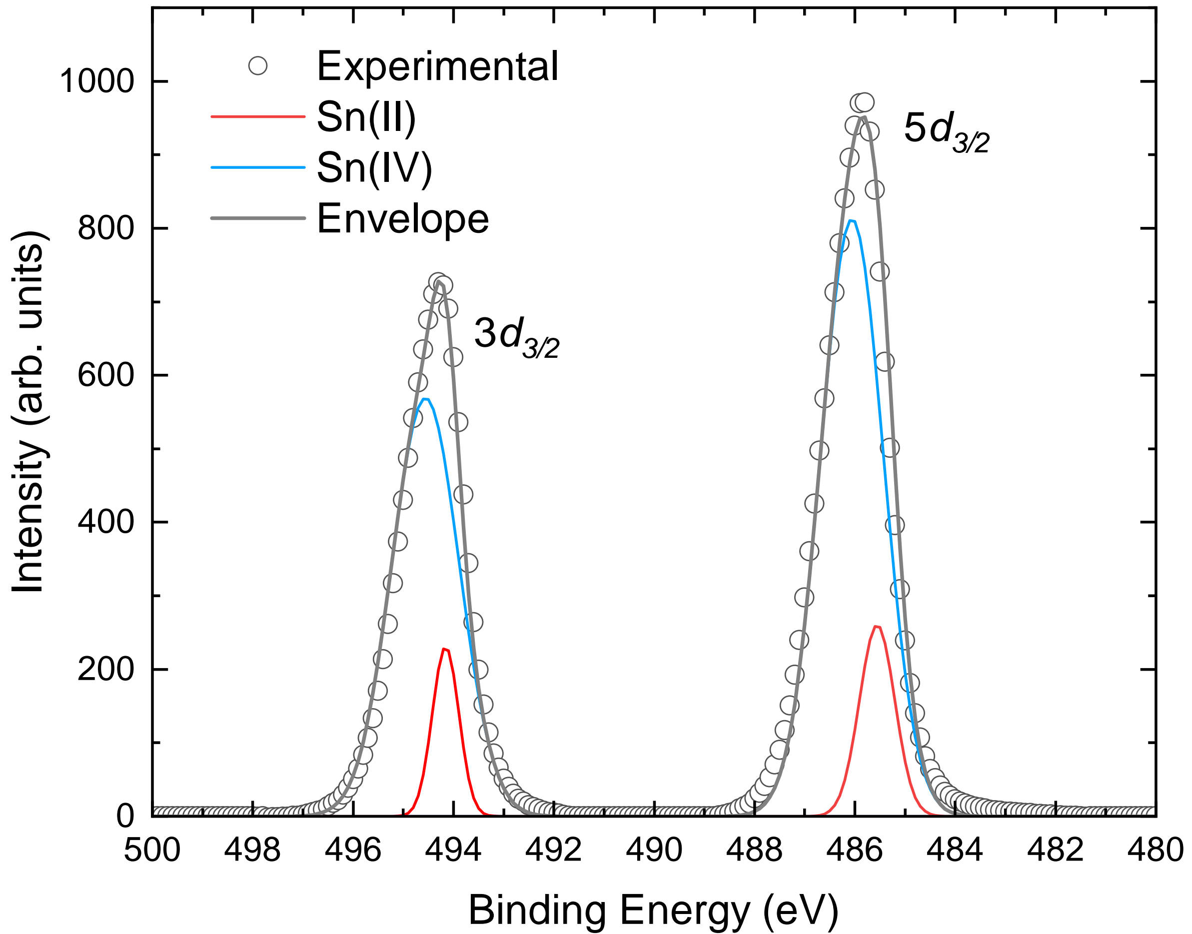

Figure 6.9: HAXPES spectra of the Ta 10% sample for the region containing the Sn 3d peaks. Each peak has been fitted with two components restrained to match the reported separation for the Sn 3d doublet and the reported separation for Sn(IV) and Sn(II).

states.

6.7 Resonant Doping

As previously discussed, a strong indication of a resonant dopant in a system is a reduced effective mass compared to the traditional dopant in the system. In this case this means that it is expected that a lower effective mass will be observed in the Ta doped samples than the Sb doped samples.

6.7.1 Valence Band to Fermi Level Separation

As in previous chapter, the effective mass of of free carriers within these materials can be extracted from trends in the relationship between Fermi level and carrier concentration and the position of the Fermi level can be extracted from the HAXPES spectra. This is done by fitting the

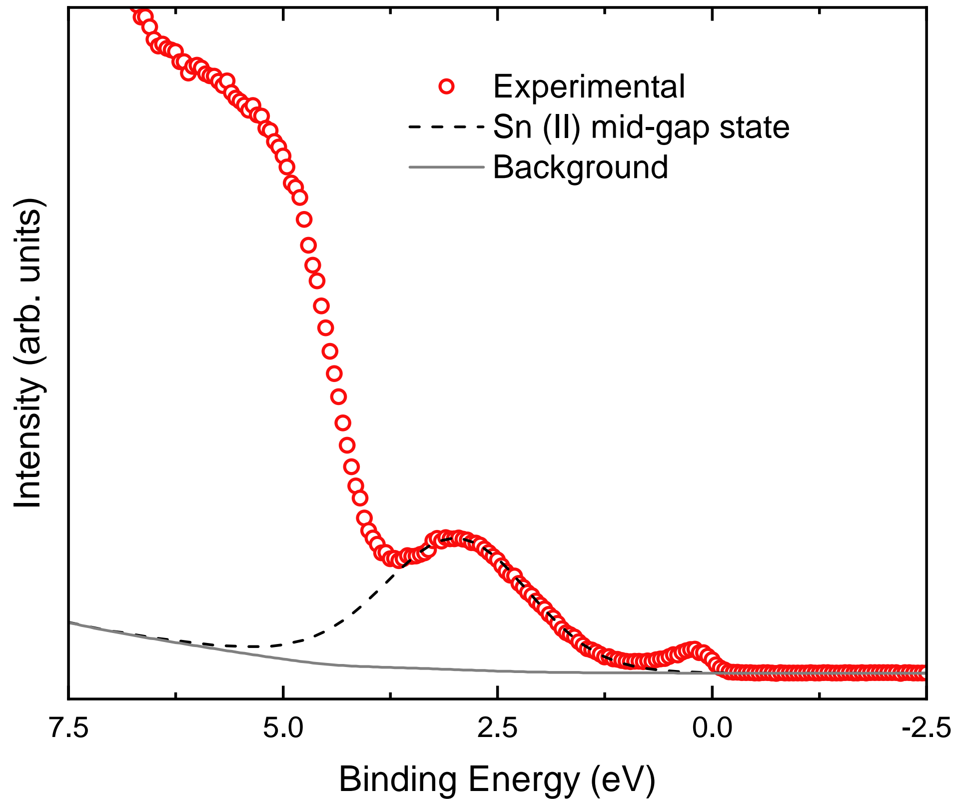

Figure 6.10: HAXPES spectra of the conduction band emission and VBM for the TaTO 15% sample showing the presence of a Sn(II) mid-gap states. The mid-gap state has been fitted with a convolved Lorentzian Gaussian curve to represent the contribution of the feature.

conduction band emission with a Fermi function and the valence band maximum with a linear fit. This method is explained in more detail in section 5.6.1. However this proves more challenging here due to the presence of the mid-gap states discussed above.

While this mid-gap state is expected to have minimum impact on the apparent position of the Fermi level, as any overlap between this state and the conduction band will be at the CBM, it may impact the apparent position of the VBM in the photo-emission. As the mid-gap state and the VBM overlap it is likely that it will cause broadening of the VBM making the VBM appear to be at a lower binding energy than it actually is. In an attempt to account for this the VBMs of each sample have been fitted with and without the mid-gap state fitted and subtracted.

Figure 6.11 shows the HAXPES spectra for the regions containing the VBM and conduction band emission with the Sn(II) state present and subtracted. The Fermi level is set to 0 eV binding energy and the VBM has been fitted with a linear fit to extract the separation. As expected all data sets show an increase in separation with increasing carrier concentration. The trends appear to be very similar with and without the mid-gap state subtracted. With the mid-gap state present the apparent separation is smaller, the variation between the separation compared to

when the state is subtracted is between 0.22 and 0.26 eV. This is the expected outcome as the mid-gap state is expected to broaden the VBM in photo-emission making its apparent binding energy appear lower, closer to the Fermi level. This still leaves the question, which is a more accurate measure of the VBM position?

6.7.2 Valence Band Emission Fitted With Calculated DOS

As part of this work the valence bands density of states were calculated using DFT. By broadening the calculated DOS to simulate instrumental broadening, and adjusting the intensity to correct for the cross-sections of the orbitals at the energy used in the experiment, the DOS can be fitted to the Valence band spectra. Figure 6.12 shows the fitted valence band emission for an Sb doped and a Ta doped SnO_2 sample. Cross-section correction has been performed using values found in reference 144. Instrumental broadening was simulated using a convolved Lorentizian and Gaussian function to account for broadening due to reasons discussed in section 4.5.3

In SnO_2 the valence band consists of three features in photoemission, the largest of which is at the highest binding energy (labeled (I) in figure 6.12). The position of feature (I) will not be impacted by the presence of the mid-gap state due to its position. Therefore, the DOS is aligned with the experimental data on the x-axis and normalised on the y-axis using this peak. In this alignment the VMB in the unbroadened DOS is set to 0 so that the x-axis intercept of the linear fit applied to the experimental data will give an approximation of the how much the VBM is offset due to the effects of the mid-gap staate. Figrue 6.12 shows this for the ATO sample with a carrier concentration of 6.26×10^{20} cm^{-3} and finds that the x-intercept of the linear fit is at a binding energy about 0.23 eV above the VBM of the DOS. The difference between the position of the VBM extracted with the linear fit with the mid-gap state present and subtracted is 0.22 eV as shown in figure 6.11. Similarly, as also shown in figure 6.12, fitting the DOS for the TaTO sample with a carrier concentration of 3.66×10^{20} cm^{-3} gives a difference of 0.22 eV for the positon of the VBM in the DOS and the linear fit. The difference between the VBM extracted from the linear fit with and without the mid-gap state subtracted is 0.23 eV. Both of these show that the position of the VBM in the calculated DOS is in good agreement with the position of the VBM extracted from the linear fit once the mid-gap state had been subtracted. Therefore, proceeding forward the VBM positions extracted with the state subtracted will be used.

Notably the broadened DOS is a good fit for the experimental data away from the VBM but feature (III) appears to be over estimated in both the Sb doped and Ta doped samples. Previous work comparing calculated DOS to experimental XPS data for the valence band of SnO_2 has found good agreement for feature (III) but discrepancy in features (I) and (II) [212]. As the DOS and experimental data is normalised to the largest feature in this work they have been normalised to feature (I) while in reference 212 they have been normalised to feature (III) due to the different photon energies used and the changes in interaction cross section. It is likely that these are the disagreement seen here and in reference 212 are the same but just appear different due to

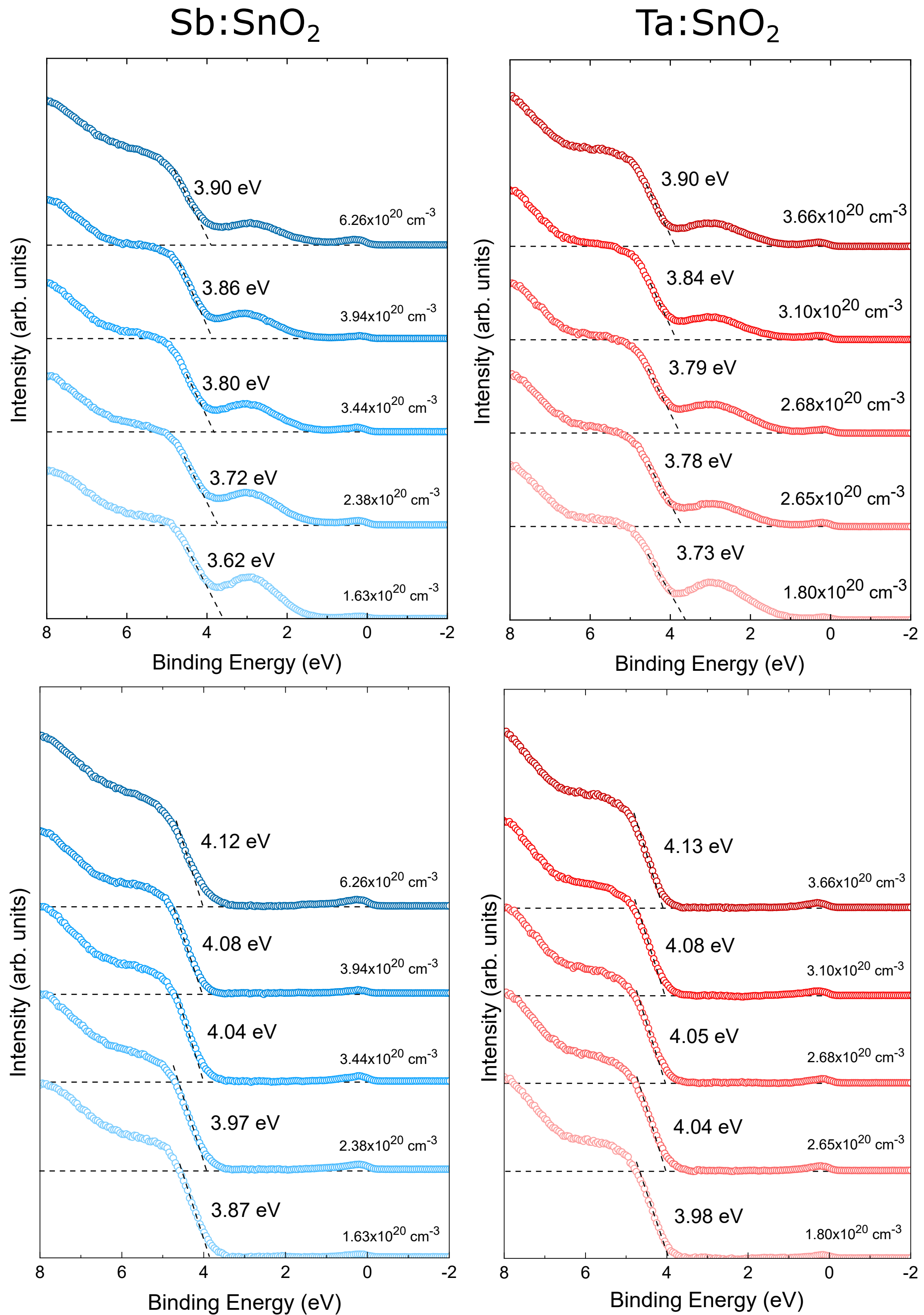

Figure 6.11: The HAXPES spectra for the ATO and TaTO samples covering the region showing the VBM and conduction band emission. The Fermi edge has been fitted with a Fermi function so that the Fermi level could be set to 0. The position of the VBM relative to Fermi level is labelled for each sample. In the top graphs the mid-gap state associated with Sn(II) at the surface is present but has been removed in the bottom graphs. Each data set is labelled with its carrier concentration on the right

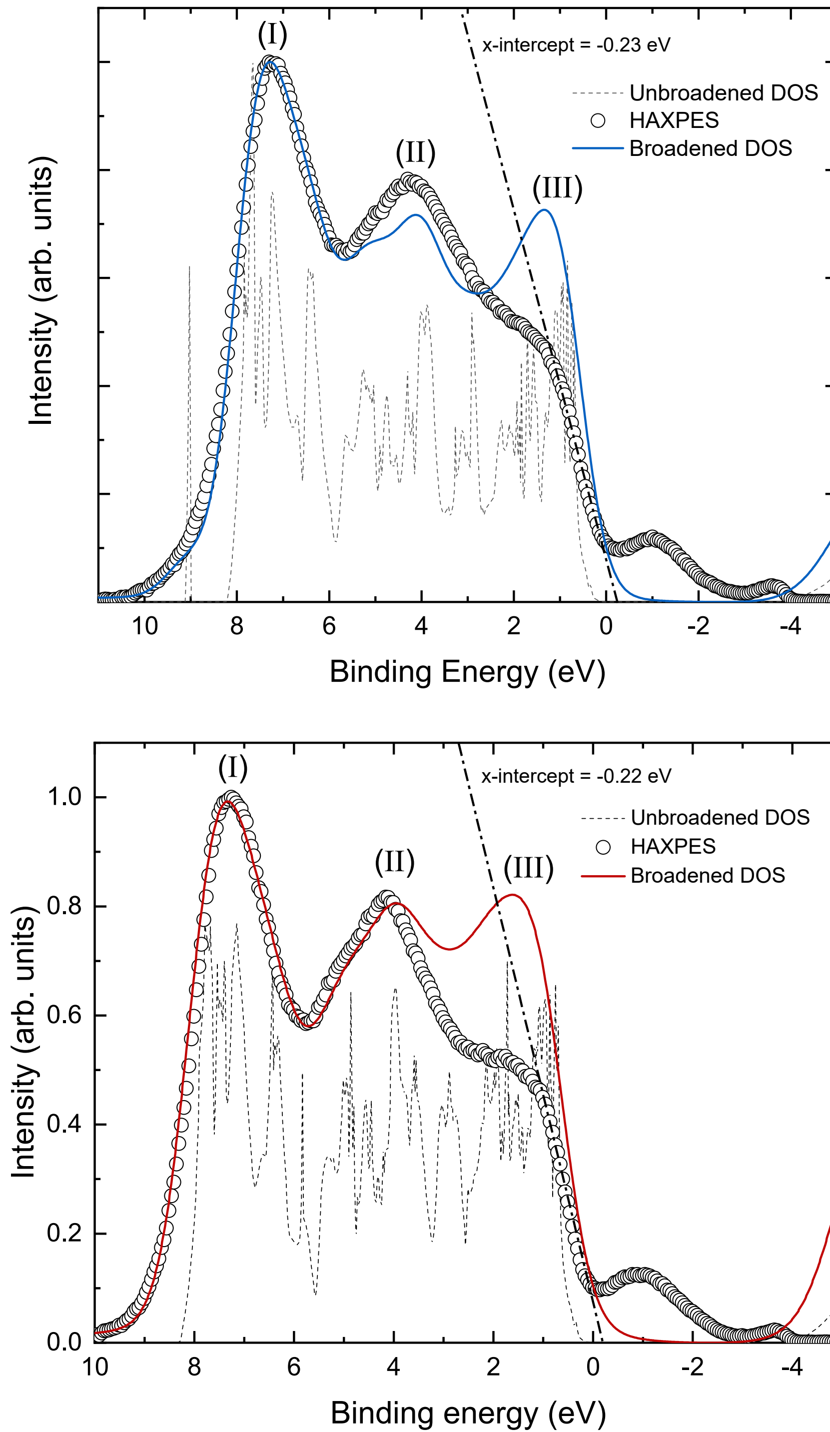

Figure 6.12: The HAXPES spectra for ATO (Top) and TaTO (Bottom) samples covering the region showing the VBM and conduction band emission. The ATO sample has a carrier concentration of 6.26×10^{20} cm^{-3} and the TaTO sample has a carrier concentration of 3.66×10^{20} cm^{-3}. The calculate Density of States (DOS) is also presented both broadened and unbroadened. The VBM in the unbroadened DOS is set to 0 eV on the x-axis. The HAXPES and Broadened DOS have been normalised to feature (I) and have been aligned on the x-axis to the same feature. The linear fit to the VBM in the experimental data is also shown to demonstrate the difference in the VBM position due to the presence of the mid-gap state.

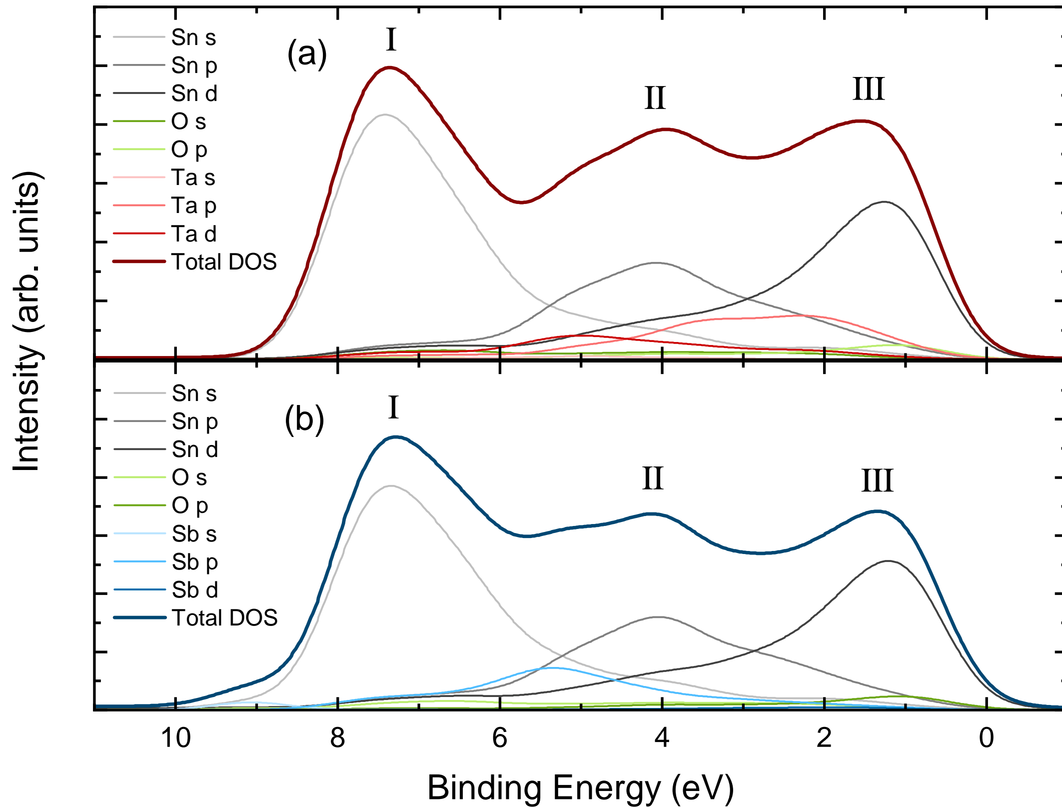

Figure 6.13: The orbitally resolved denisty of states for TaTO (top) and ATO (bottom) for the valence band. This shows the contribution of each orbital to the valence band.

different features being used for normalisation. Similar disagreement between DOS between the calculated DOS and experimental data at high beam energies has been previously observed in other metal oxides including PbO_2, In_2O_3 and CdO [213–215]. However understanding of this disagreement is lacking.

Figure 6.13 shows the total broadened DOS for Sb:SnO_2 and Ta:SnO_2 and the orbitally resolved DOS. This shows which orbital is contributing to which features within the valence band. This shows that feature (III) is predominately made up of Sn d character. This is specifically Sn 4d, the highest occupied d orbital for Sn. Notably in In_2O_3 the feature at the VBM is also overestimated in the calculated DOS and the VBM is dominated by In 4d character indicating a similar phenomena. Sn 4d is a semi-core level. This means that some electrons within the orbital will contribute to the valence band while the more tightly bound electrons will behave like core level electrons. Figure 6.14 shows the HAXPES spectra for the region containing the semi-core levels, including the Sn 4d level, for a Ta doped sample. The calculated DOS are shown along side this data. A difference of 1.4 eV can be seen in the peak postion between the HAXPES and DOS. The experimental data shows the peak at a higher binding energy. As the DOS places the semi-core level peak for Sn 4d closer to the valence band it is also overestimating the contribution

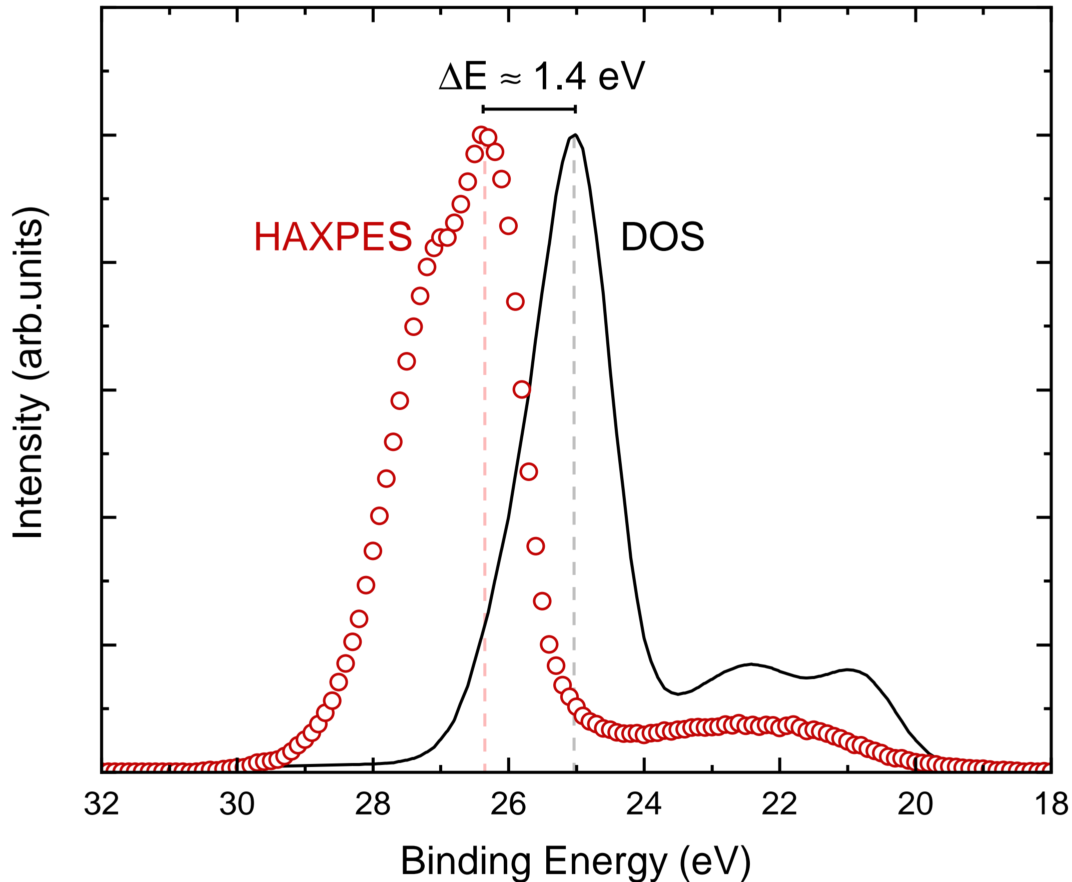

Figure 6.14: The HAXPES spectrum and calculaetd DOS for Ta doped SnO_2 for the region containing the semi-core levels including Sn $4d$. The DOS has been broadened and cross-section corrected. A difference in binding energy can be seen between the DOS and experimental data.

of the Sn $4d$ levels to the valence band causing the increased intensity of feature (III) and the discrepancy between the valence band HAXPES and DOS..

6.7.3 Extracting Effective Mass

As in chapter 5, using the non-parabolic alpha approximation described in section 3.5.4 in conjuncture with equation 3.56, the relationship between carrier concentration and Fermi level can be calculated for specific carrier effective mass. This can then be fitted to the data for Fermi level position relative to the VBM as extracted in figure 6.11 and an effective mass can be extracted. Figure 6.15 shows the Fermi level to valence band separation measured with the mid-gap state removed against carrier concentration fitted with lines calculated using this method fitted to the data for both ATO and TaTO.

From the data points alone a clear difference can be seen in the realtionship between carrier concentration and Fermi level for the two dopants. When the band-edge effective masses extracted

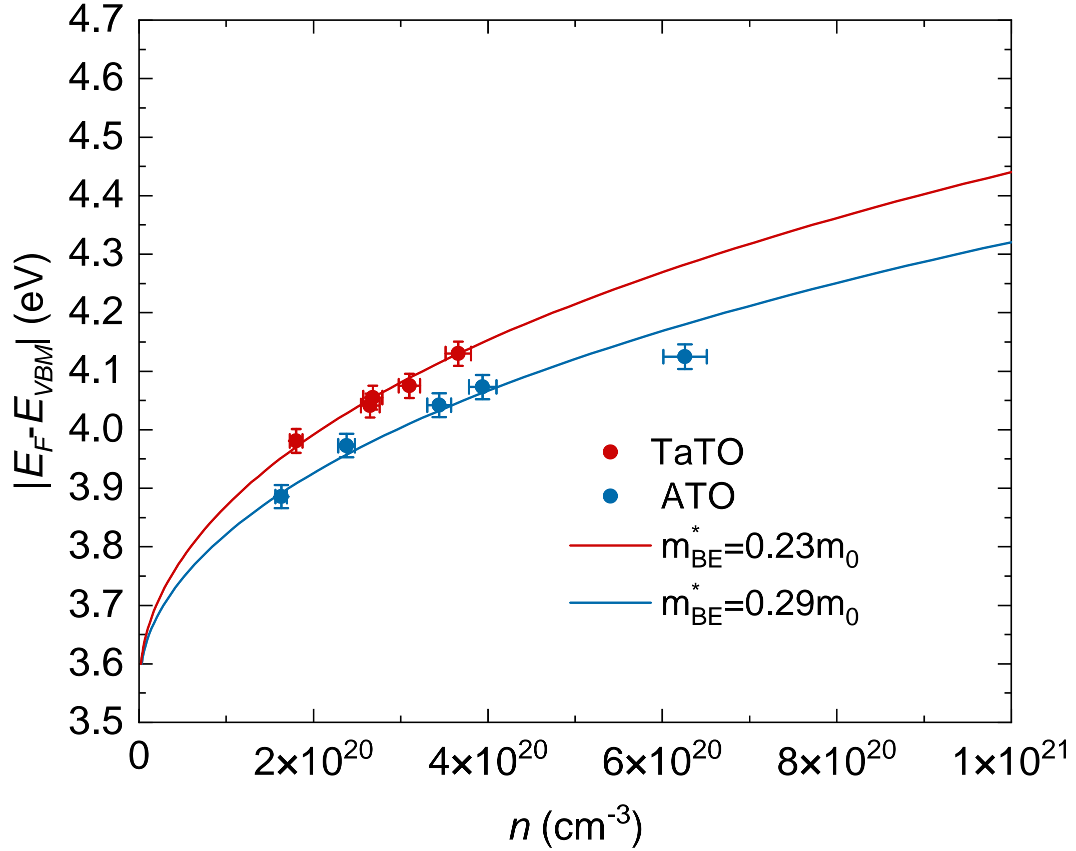

Figure 6.15: Fermi level to valence band maximum separation against carrier concentration for the ATO and TaTO samples. The VBM position taken was with the mid-gap state removed. Calculated relationships are also presented and fitted to the experimental data. A band edge effective mass of $0.23m_0$ was extracted for TaTO and $0.29m_0$ for ATO.

were 0.23 m_0 for TaTO and 0.29 m_0 for ATO. The lower effective mass extracted for TaTO is what would be expected for a resonant dopant. The higher effective mass seen in ATO is due to mixing of the dopant Sb 5s states with the Sn 5s states that make up the CBM. The Ta donor level is 5d and therefore mixes to much smaller degree due to it being energetically separate from the CBM and differing in shape from the Sn 5s levels.

This difference in effective mass can explain the difference in mobility observed in the samples fabricated for this work but is not significant enough to account for the larger mobilities observed in TaTO in the literature. As the highest mobility TaTO samples all display a strongly preferred (200) orientation this further supports the previously dicussed possibility that carrier mobility in TaTO is orientation dependent.

Notably the ATO sample with the highest carrier concentration, n=6.26.×10^{20} cm^{-3}, does not fall on the fitted line for m^*_{BE}=0.29 m_0. This is also the sample with the highest Sb content in the

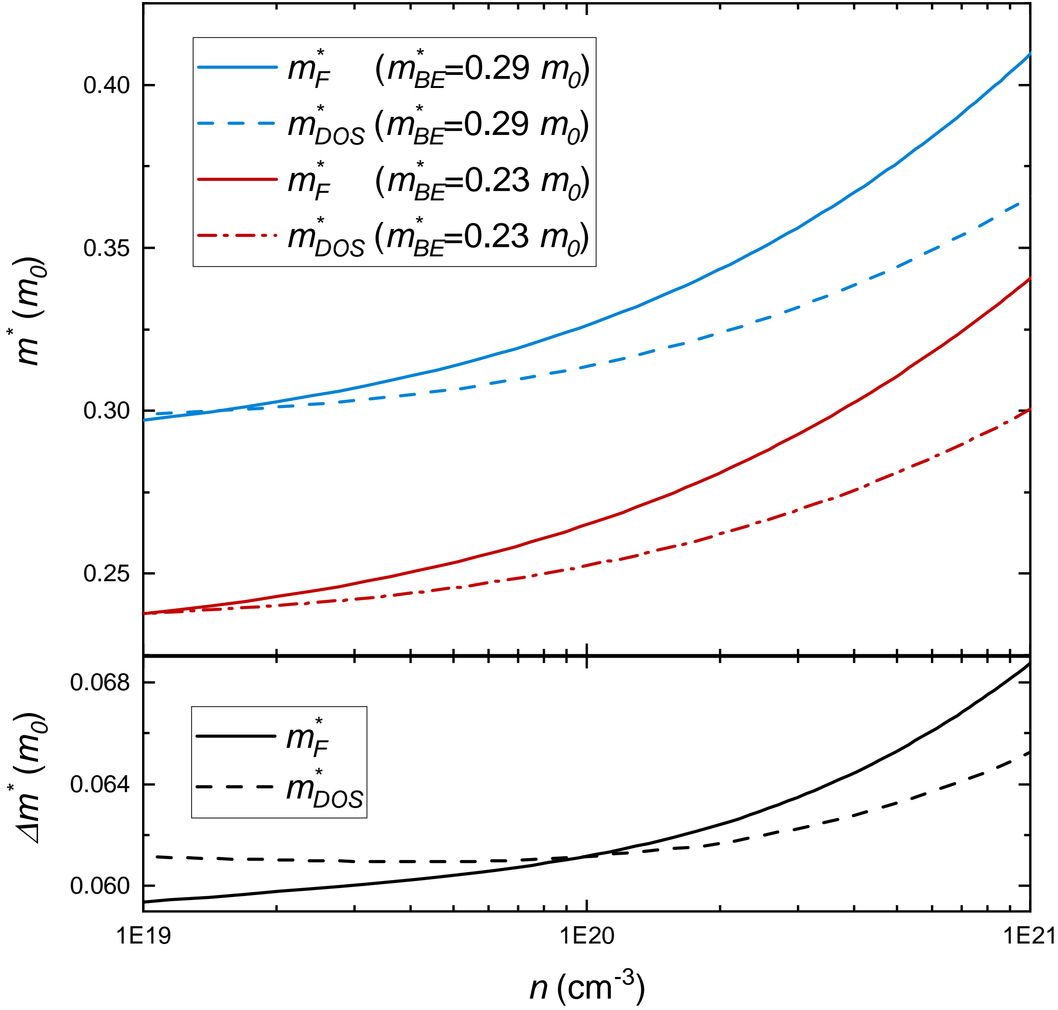

Figure 6.16: (Top) The Fermi level effective masseses and the density of states averaged effective masses for band edge effective masses of 0.29 m_0 and 0.23 m_0. (Bottom) The difference in these two kinds off effective mass for the two different band edge effective masses.

precursor, this disagreement with the fitted line likely arises from the greater concentration of Sb leading to further mixing of states at the CBM which further increases the carrier effective mass.

The effective masses presented in figure 6.15 are band-edge effective masses. A full explanation of what this means is presented in section 3.5.1. This effective mass can be used to calculated the DOS averaged effective mass, m^*_{DOS}, which is used in fitting optical data, and the Fermi level effective mass, m^*_F which is important for describing conductivity as free carriers move at the Fermi surface. These both vary with carrier concentration. Figure 6.16 shows how m^*_{DOS} and m^*_F develop with carrier concentration for band edge effective Masses of 0.23 m_0 and 0.29 m_0.

The bottom of figure 6.16 shows the difference between the values for m^*_F and m^*_{DOS} for the two band edge effective masses. The difference is relatively consistent but does increase slightly with increasing carrier concentration. This means that the impact of a resonant dopant can be

expected to have a higher impact relative to traditional dopants at higher carrier concentrations. The greater difference in m_F^* will result in a greater difference in mobility and therefore conductivity. Meanwhile, the increasing difference in m_{DOS}^* will cause a greater difference in the plasma-frequency at higher carrier concentration which will actually have a negative impact on the infra-red transparency of the TCO using a resonant dopant. However, it seems unlikely that such a small increase in the difference, less than 0.01 eV across a change of two orders of magnitude change in carrier concentration, is unlikely to have a significant impact compared to the total difference. Also the potential further increase in band edge effective mass from further incorporation of Sb required to reach the higher carrier concentrations will likely have a much more significant impact than this small change.

6.7.4 Orbital Energies

The orbital configuration energies for the outer orbitals of most elements are widely reported in published databases [216, 217]. Comparing these for the host elements and dopants allows for a estimate of the relative energies of the states making up the CBM and the donor states.

Figure 6.17 shows the orbital configuration energies for the outer orbitals of Sn, O, Ta and Sb. The CBM in SnO_2 is predominantly Sn 5s and O 2p. The energies of the orbitals are 14.6 eV and 15.9 eV respectively. The dopant levels for Ta and Sb are the Ta 5d and the Sb 5s. The orbital energies of these dopant orbitals are 7.6 eV and 16.7 eV respectively. This shows that the donating Ta orbital is energetically removed from the CBM while the Sb donor orbital is in close proximity. This further supports that Ta is likely a resonant dopant in SnO_2.

6.7.5 Calculated Band Structure

Further support for the resonant nature of Ta in SnO_2 can be seen in the unfolded band structure for TaTO calculated using DFT. Figure 6.18 shows the unfolded band structure for substitutional Ta on a Sn site, Ta_{Sn} in the +1 charge state as presented in reference 218, This charge state is used as a dopant defect will be ionised into the +1 charge state by donating an electron. Also shown is the calculated DOS for the conduction band for Ta doped SnO_2 and the specific states belonging to Ta.

In both the spin-up and spin-down configurations the Ta 5d bands can be seen at around 2.47 eV above the CBM. These bands had 70% Ta d character with the rest being made up of a mixture of Sn s and O s states. These calculations also find that the the CBM has <1% Ta d. This is of note as calculations for substitutional Sb and F, Sb_{Sn} and F_O, find that there is around 3% Sb and F character at the CBM [218] in ATO and FTO respectively. This is indicative that there in reduced mixing of the host CBM states in TaTO compared to ATO or FTO. This further supports the prospect of Ta being a resonant dopant in SnO_2.

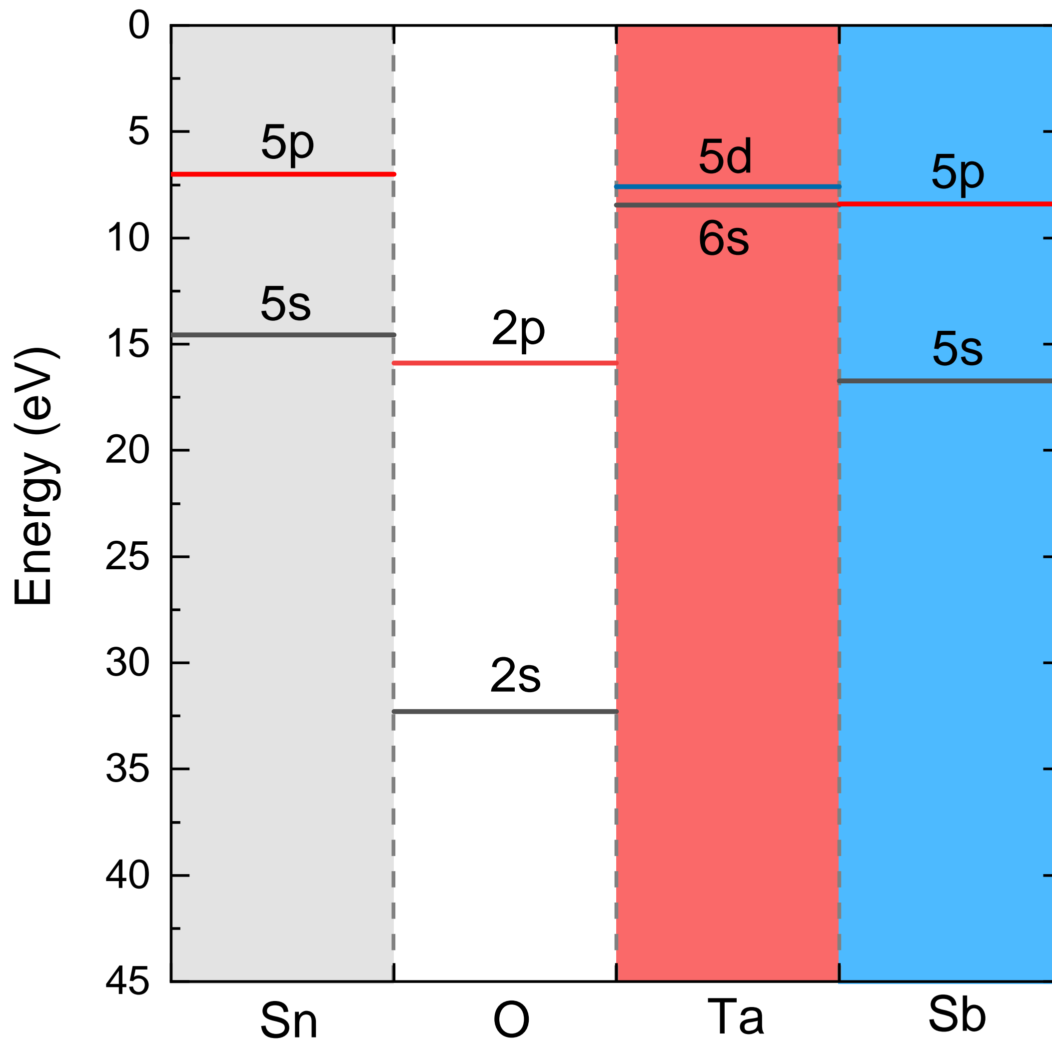

Figure 6.17: Fermi level to valence band maximum separation against carrier concentration for the ATO and TaTO samples. The VBM position taken was with the mid-gap state removed. Calculated relationships are also presented and fitted to the experimental data. A band edge effective mass of $0.23m_0$ was extracted for TaTO and $0.29m_0$ for ATO.

6.7.6 Partial Charge Densities

The partial charge densities of the three systems, TaTO, ATO and FTO are shown in figure 6.19. This pictorially shows the distribution of carriers at the CBM throughout the crystal lattice, represented by the yellow in the figures. The dopant sites are represented by the different colours within the lattice, Ta_{Sn} in red, Sb_{Sn} in blue and F_O in green. It can be seen that there is little to no charge density around the Ta_Sn site while charge density is present around the Sb_{Sn} and F_O sites. This means that there are Sb and F states at the CBM for charge carrier to sit in while no such states exist for Ta. Once again this shows that the Ta states are energetically separate from the CBM, a strong indicator of a resonant dopant.

6.8 Defect Thermodynamics

As well as band structure, defect thermodynamics were calculated for Ta doped SnO_2. Figure 6.20 shows the defect formation energies for Ta, Sb and F species in SnO_2 as a function of Fermi level as presented in reference 218. The F and Sb defect formation energies have also been previously presented in references 56 and 219. The calculation were performed fro a temperature of 800 K and a pressure of 1 atm to simulate the growth conditions of the samples in this work.

This shows that the Ta_{Sn} defect is the most energetically favourable form for Ta to take in SnO_2 across the full range of Fermi energies. However a transition from the 1+ donor state to a 1- acceptor state can be seen for the Ta_{Sn} defect around 0.5 eV above the CBM. This means when the Fermi level reaches this point introducing more Ta can be expected to be detrimental to conductivity. Ta that is incorporated as an acceptor will no only reduce carrier concentration by removing free electrons from the conduction band but also can be expected to act as an ionised impurity and negatively impact mobility. This transition corresponds the a Fermi level about 4.1 eV above the VBM. This is in line with the highest Fermi level of 4.13 eV observed for TaTO experimentally as extracted in figure 6.11. It therefore seems unlikely that significantly higher carrier concentrations than the ones observed here are achievable. This transition does shift in energy dependent on growth conditions so slightly higher carrier concentrations may be achievable utilising different growth methods.

As shown in previous works F and Sb are similarly inhibited due to transition. In F this occurs similarly at 0.5 eV above the CBM when interstitial F becomes energetically preferential over F_O. This mechanism and its impact on FTO is discussed in length in reference 56. Sb_{Sn} transitions from the 1+ to 0 charge state around 0.2 eV above the CBM then from 0 to 1- around 0.45 eV above the CBM. Based on these limitations is seems likely that the carrier concentrations achieved in here are the literature are unlikely to imporved upon as the upper limits on Fermi level have already been achieved. Despite comparable limits on Fermi level for all three dopants higher carrier concentrations are seen in FTO and ATO than TaTO. This arises due to the lower effective mass found in TaTO as this changes the relationship between carrier concentration

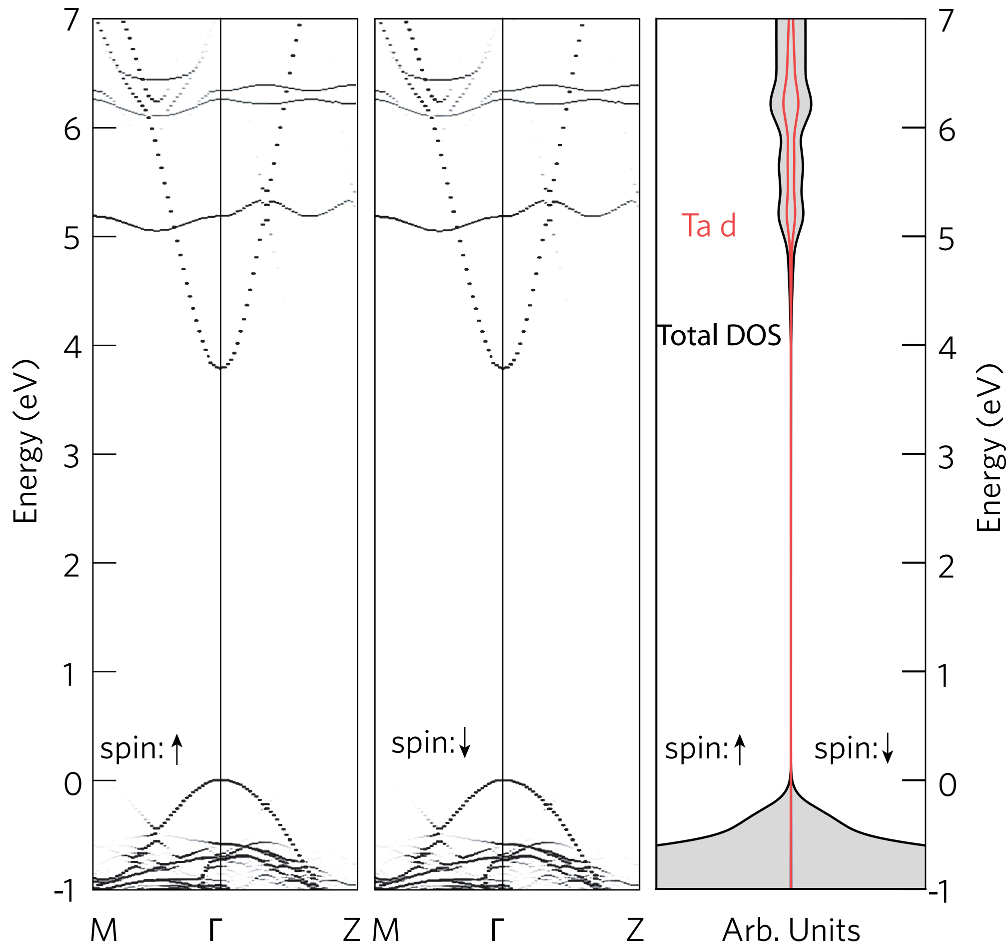

Figure 6.18: The calculated band structure for the Ta substitutional defect in SnO_2 in the +1 charge state. The badn structure is separated into spin-up and spin-down channels. The VBM has been set to 0 eV. Figure taken from reference 218

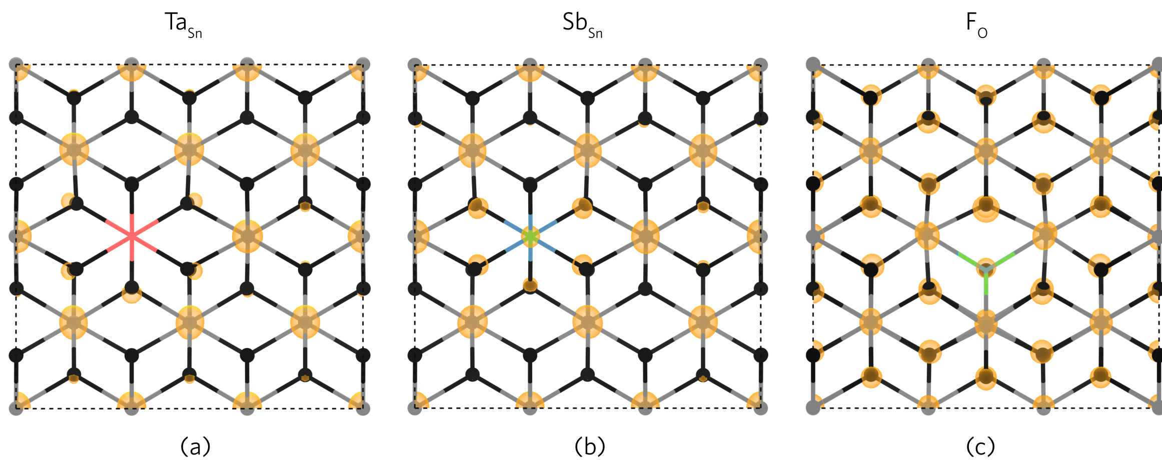

Figure 6.19: The calculated partial charge densities at the CBM for (a) Ta_{Sn}, (b) Sb_{Sn} and F_O.

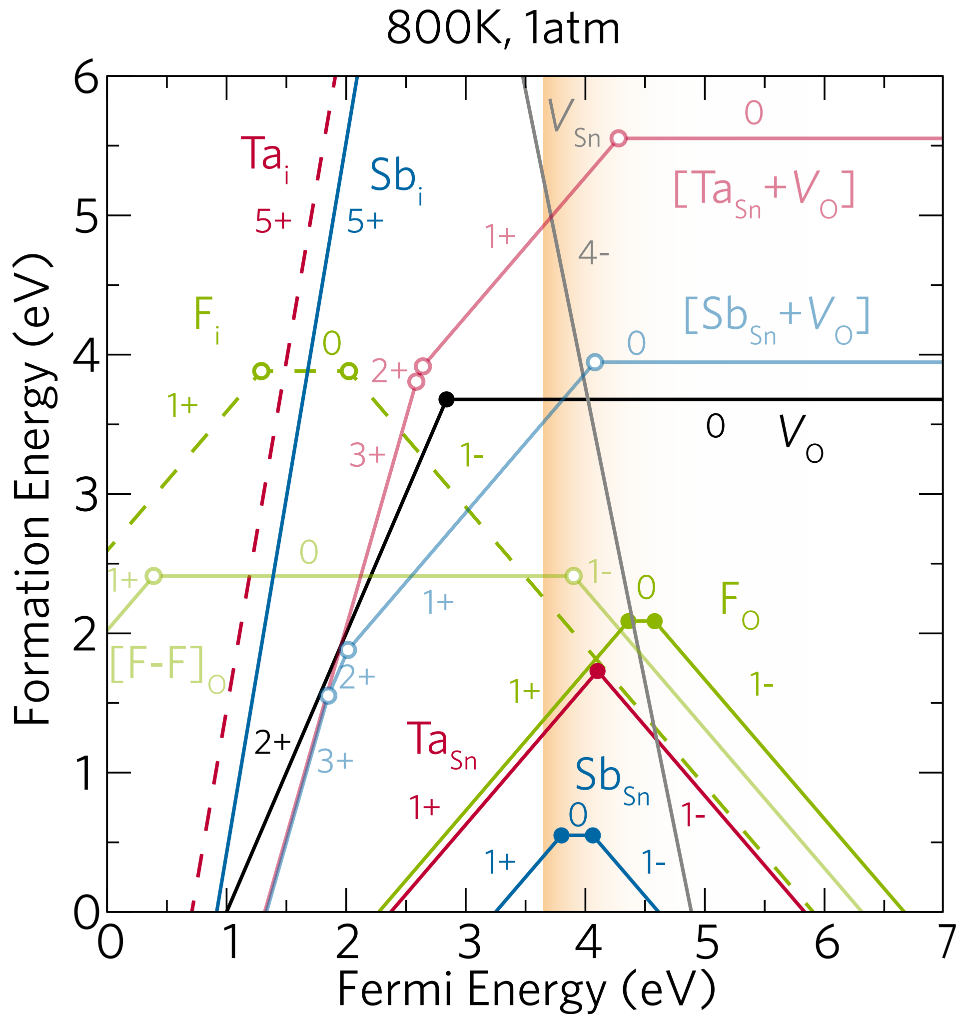

Figure 6.20: Defect formation energies of Ta (red), Sb (blue) and F (green) related species in SnO_2 as a function of Fermi energy.

and Fermi level so the Fermi level pinning point is reached for lower carrier concentrations. The difference in this relationship is shown in figure 6.15.

6.9 Conclusion

After identifying resonant doping as a mechanism for improving the carrier mobility and infra-red transparency In_2O_3 the next step was to investigate the possibility of improving the cheaper and more abundant SnO_2 using the same method. Transition metals stable in the correct oxidation state (V) are significantly fewer than those in the (IV) oxidation state required for doping In_2O_3. Of the three that exist, Nb and and V could be immediately discounted as candidates based on works in the literature which demonstrated that their d orbitals would not be resonant. With these two elements ruled out only Ta remains as a potential candidate.

Previous studies into Ta doping of SnO_2 have showed promising results with mobilities as high as 83 $cm^2V^{-1}s^{-1}$ that far surpass those seen with the traditional dopants, Sb and F. However, the highest mobilities appear to be the exception with many attempts to dope SnO_2 with Ta failing to show superior properties than FTO. However comparative studies comparing Ta and Sb doping deposited by the same method have generally shown Ta to give higher mobilites than the tradition analogue. For this work, samples of both TaTO and ATO were deposited by AACVD and TaTO displayed higher mobilities by around 50% across a wide range of carrier concentrations. TaTO displayed a peak mobility of 25.9 $cm^2V^{-1}s^{-1}$ while ATO displayed a peak mobility of 17.9 $cm^2V^{-1}s^{-1}$.

By measuring the VBM to Fermi level separation for samples with a range of carrier concentrations using HAXPES the carrier effective masses in the two systems were extracted. This revealed band edge effective masses of 0.23 m_0 and 0.29 m_0 for ATO and TaTO respectively. This is strongly indicative of Ta being a resonant dopant in SnO_2 similarly to Mo or Ce in In_2O_3. This was further supported by FTIR measurements of IR reflectvity which showed a difference in the position of the plasma edge for similar carrier concentrations which is indicative of a difference in effective mass. DFT calculations showed that the Ta d states lie well above the CBM reducing mixing of the donor states and thhe host states maintaining the shape of the systems conduction band. This allows for a lower effective mass and therefore higher mobilities.

The DFT calculations also revealed that substitutional Ta on a Sn site changed preferred charged state from 1+ to 1- for a Fermi level 4.1 eV above the CBM. This matches the highest Fermi level observed experimentally for TaTO suggesting that the highest carrier concentrations possible for TaTO have already been reached. ATO and FTO are similarly limited by dopant related defects pinning the Fermi level. This means while TaTO may surpass other SnO_2 based TCOs it will be unlikely that it, or doped SnO_2 generally, will ever be able to match the conductivities seen in In_2O_3 as it will never be able to reach the highest carrier concentration seen in that system.

XRD of the samples showed a difference in preferred orientation for ATO and TaTO. TaTO samples showed a preference towards the (200) orientation in comparison to the ATO samples. Similarly the best mobilities reported for TaTO in the literature are all reported for samples grown on seed layer that promote this same orientation. As SnO_2 is known to have anisotropic properties including effective mass it is possible that the (200) orientation is beneficial for conductivity and is key to reaching the highest possible mobilities.

Overall this paints a picture of SnO_2 being a more difficult system to optimise that In_2O_3 with more significant limitations, in particular with regards to carrier concentration. Despite this due to its cheaper and more abundant base elements it is still a necessary alternative for wide scale application and of the dopants Ta appears to be the best choice. If a scalable method to grow TaTO in the (200) orientation can be developed it could have the potential to replace FTO as the industry standard for such applications.

Chapter 7

Improved Infra-red Transparency and Impact for PV

7.1 Introduction

In the previous two chapters, resonant dopants, Ce and Ta, were identified and investigated in In_2O_3 and SnO_2. While these dopants improved on mobility, the limited carrier concentrations obtainable with them means that they fail to improve on the lowest resitivities obtainable with ITO. Primarily, the previous chapters focused on the impact on the electrical properties of the resonantly doped materials, but it is apparent that the choice of dopant also has significant impact on the optical properties of the material. One area where these dopants do consistently improve on the traditional dopants is in IR transparency when comparing samples displaying similar resistivities. The reason behind this is somewhat non-intuitive upon first examination of the relationships between carrier concentration, carrier effective mass and plasma frequency. The aim of this chapter is to better elucidate the origin of this improved IR transparency and the mechanisms behind it. This chapter also tries to further understanding of the link between resonant dopants and other optical properties such as absorption .

One of the main expected benefits of this improved IR transparency is for photovoltaic applications. Beyond understanding the origin of the improved IR transparency this chapter also aims to quantify the potential impact of these resonant dopants and better understand the potential impacts of choice of transparent electrode in PV devices.

7.2 Origin of Enhanced IR Transparency

7.2.1 Plasma Frequency, Effective Mass and Carrier Concentration

The onset if infra-red reflection in TCOs is determined by plasma frequency, ω_p, as free carriers prevent electric fields entering the material and for energies above ω_p the dialectic function is less than zero, $\epsilon < 0$. As a result all photons with an energy less than ω_p are reflected. The plasma frequency is determined by the carrier concentration and carrier effective mass of the material. The relationship between these properties is described by [24].

$$\omega_p = \sqrt{\frac{ne^2}{m^* \epsilon_\infty \epsilon_0}} \tag{7.1}$$

in which n is the free carrier concentration, e is the elementary charge, m^* is the carrier effective mass and ϵ_∞ and ϵ_0 the static dielectric constant and the permittivity of free space. m^* is specifically the density of states averaged effective mass for reasons discussed in section 3.5.1. The carrier mobility is also dependent on the carrier effective mass with the relationship described by

$$\mu = \frac{e\tau}{m^*} \tag{7.2}$$

where τ is the scattering time of the free carriers. Notably both are inversely related to effective mass. The origin of the improved mobilities seen in both ICO and TaTO was identified as lower carrier effective masses. As such if all other properties were the same as in the traditional TCOs this would be expected to also mean a higher plasma frequency based on equation 7.1. This is in fact what was observed when ATO and TaTO samples with comparable carrier concentrations were compared in figure 6.6. The improved IR transparency was observed when comparing samples of comparable resistivity. However, when combining equations 7.1 and 7.2, the expression for plasma frequency can be rewritten as

$$\omega_p = \sqrt{\frac{ne\mu}{\tau \epsilon_\infty \epsilon_0}} \tag{7.3}$$

Notably the expression for conductivity is $\sigma = ne\mu$ which is the same as the top of the fraction in equation 7.3. As such it should be expected that the plasma frequency should be proportional to the conductivity, $\omega_p \propto \sqrt{\sigma}$. However this is not what has been observed with the resonant dopants appearing to lower the plasma frequency compared to the traditional dopants at similar carrier concentrations.

7.2.2 Scattering Times

The only variable in any of the expression above that has not been considered is the scattering time τ. This is also dependent on many properties of the material including the carrier concentration, the doping density and the carrier effective mass. The scattering time can be accounted for by calculating the mobility using scattering models as discussed in section 3.7. Each of these impose an upper limit on mobility based on the mechanism. When multiple independent scattering mechanisms contribute to the scattering time of the carriers the mobility limits can be combined using Matthiessen's rule

$$\frac{1}{\mu_{tot}} = \sum_i \frac{1}{\mu_i} \tag{7.4}$$

where μ_i is the imposed mobility limit for each scattering mechanism. The different scattering mechanisms that contribute to this limit in TCOs are discussed in section 3.7.

Figure 7.1 shows the calculated upper mobility limits as a function of carrier concentration for a range of scattering mechanisms as well as the combined total limit as calculated using Matthiessen's rule.

In figure 7.1 the scattering mechanisms shown are ionised impurity scattering, IIS, grain boundary scattering, GBS, dislocation scattering, DS, acoustic deformation potential scattering, ADP, and longitudinal polar optical mode scattering, ADP. For these calculations, an effective mass of 0.22 m_0 to be representative of either IMO or ICO. For other variables in the model properties representative of In_2O_3 are used. For the static dielectric constant ϵ_s=8.9ϵ_0 was used and a high frequency dielectric constant ϵ_∞=4.8ϵ_0.

For calculating the limit associated with ionised impurity scattering, it has been assumed that every ionised impurity donates one electron so that the ionised impurity density, N_i, is equal the carrier concentration, n. This also means that the charge on the ionised impurity, Z, is 1.

For other the other scattering mechanisms, there are variables which are harder to ascertain, while values for them do exist in the literature for In_2O_3, they are not inherent to material they will vary dependent on growth conditions. In grain boundary scattering, such parameters are the trap density within the grains boundaries, Q_t and grain size, l. For these calculation the values used for these properties were Q_t=1×10^{-13} m^{-2} and l=20 nm. Trap density has previously been estimated by performing scattering calculations and fitting it to Hall effect data [120, 220]. The value used here was taken taken to fall roughly in the middle of the range of trap densities reported for doped In_2O_3 films.

For the phonon scattering, the longitudinal optical phonon energy, E_{LO}, was taken as 27.8 meV, the value reported for In_2O_3 in the literature [221, 222]. The acoustic phonon potential, E_c used was 4.3 eV also taken from the literature [180]. The density used was 7.12×10^{-3} kgm^{-3}, the widely reported density for In_2O_3. The speed of sound in In_2O_3 was taken as 6.4×10^{-3} ms^{-1} [180].

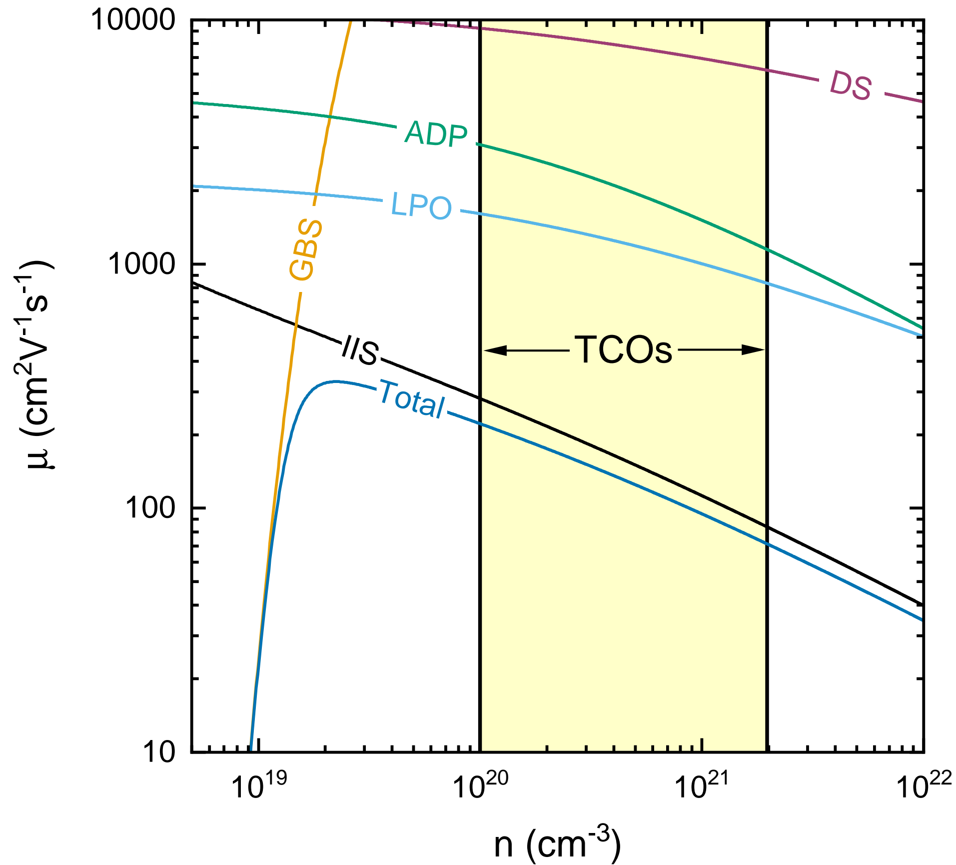

Figure 7.1: The combined scattering limited mobility for a carrier effective mass of 0.22 m_0 in In_2O_3 as a function of carrier concentration. Individual scattering limits are shown for dislocation scattering (DS), acoustic deformation potential scattering (ADP), longitudinal polar-optical mode scattering (LPO), grain boundary scattering(GBS) and ionised impurity scattering (IIS). The shaded region shows the range of carrier concentrations in which most high performance TCOs fall.

For the carrier concentration range within which most TCOs fall, shown by the shaded region in figure 7.1, ionised impurity scattering dominates with the lowest limit on mobility across the entire range. This is as expected as at high carrier concentrations, such as these, carriers can tunnel through grain boundaries. The exact onset where GBS stops being a significant scattering mechanism is mostly dependent on trap density. However the trap density would have to be orders of magnitude higher to push the onset into the shaded region. The value used in the calculations for figure 7.1 is representative of the values reported for TCOs and for GBS to be relevant in the shaded region Q_t would have to be much higher than any reported values. The two phonon scattering modes also contribute to a significantly lesser degree. The degree to which LPO contributes is dependent on the longitudinal phonon frequency, ω_{LO}. Resonant dopants in In_2O_3, Mo and Ce, readily achieve mobilities close to the limit calculated here making it therefore unlikely that LPO scattering contributes much more significantly than seen here. As scattering

mechanisms other than ionised impurity scattering have minimal or no contribution, the fact that a lot of the variables used in calculated in them have high uncertainty is unimportant, as any change in the values would not make them significant enough to significantly change the upper limit on mobility.

The calculations for scattering limited mobility have been repeated for an effective mass of 0.40 m_0 to represent Sn doping in In_2O_3 [75] and the results are shown in figure 7.2. Other than changing the effective mass, none of the other values were changed so the impact of different effective masses can be directly seen.

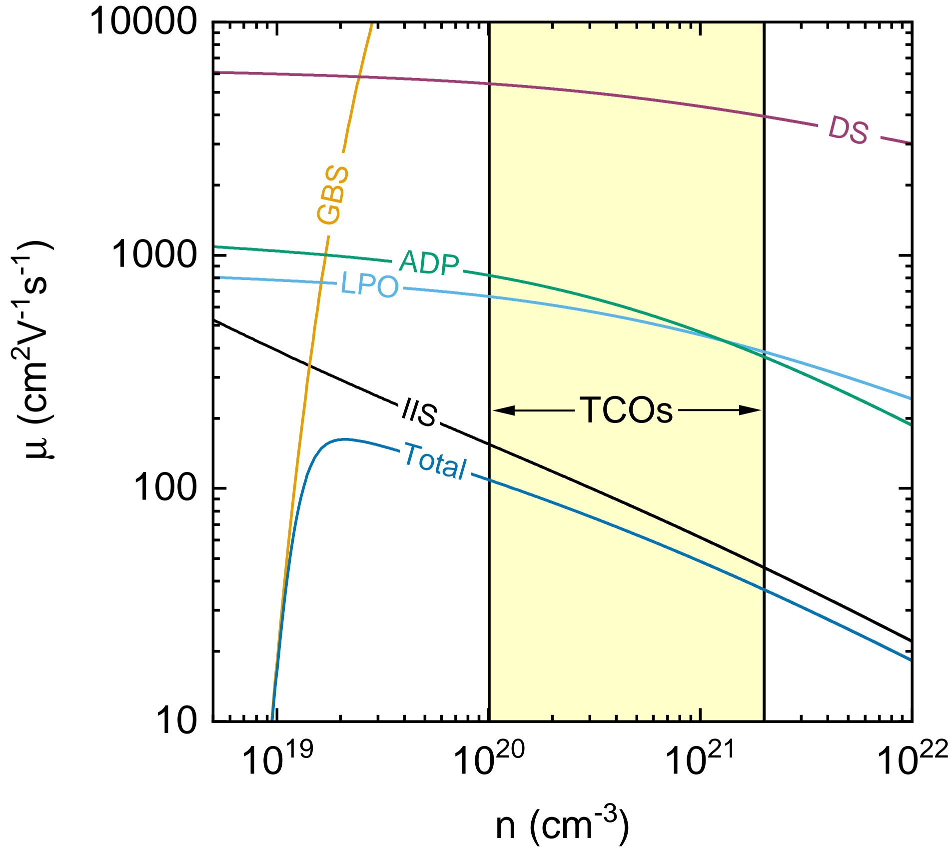

Figure 7.2: The combined scattering limited mobility for a carrier effective mass of 0.40 m_0 in In_2O_3 as a function of carrier concentration. Individual scattering limits are shown for dislocation scattering (DS), acoustic deformation potential scattering (ADP), longitudinal polar-optical mode scattering (LPO), grain boundary scattering (GBS) and ionised impurity scattering (IIS). The shaded region shows the range of carrier concentrations in which most high performance TCOs fall.

The lower effective mass lowers the limits imposed by ionised impurity scattering, both phonon scattering mechanisms and dislocation scattering. IIS is still greatest contributor to the mobility limit but overall in the shaded region the upper limit for mobility falls below 100 $cm^2V^{-1}s^{-1}$.

The upper limits calculated using these models are in reasonable good agreement with the results seen in the literature with resonant dopants Ce and Mo displaying mobilities close to the limit shown in figure 7.1 while Sn doping displays mobilities close to the line in figure 7.2.

7.2.3 Relating Scattering Limited Mobility to Plasma Frequency

As mobility has been calculated as a function of carrier concentration using the scattering models in the previous section, resistivity can also be calculated using ρ=1/(neμ) for each effective mass. Similarly the plasma frequency can be calculated as as function of carrier concentration for each effective mass using equation 7.1. Figure 7.3 shows plasma frequency plotted against resistivity calculated using the scattering limited mobility for the same carrier concentration.

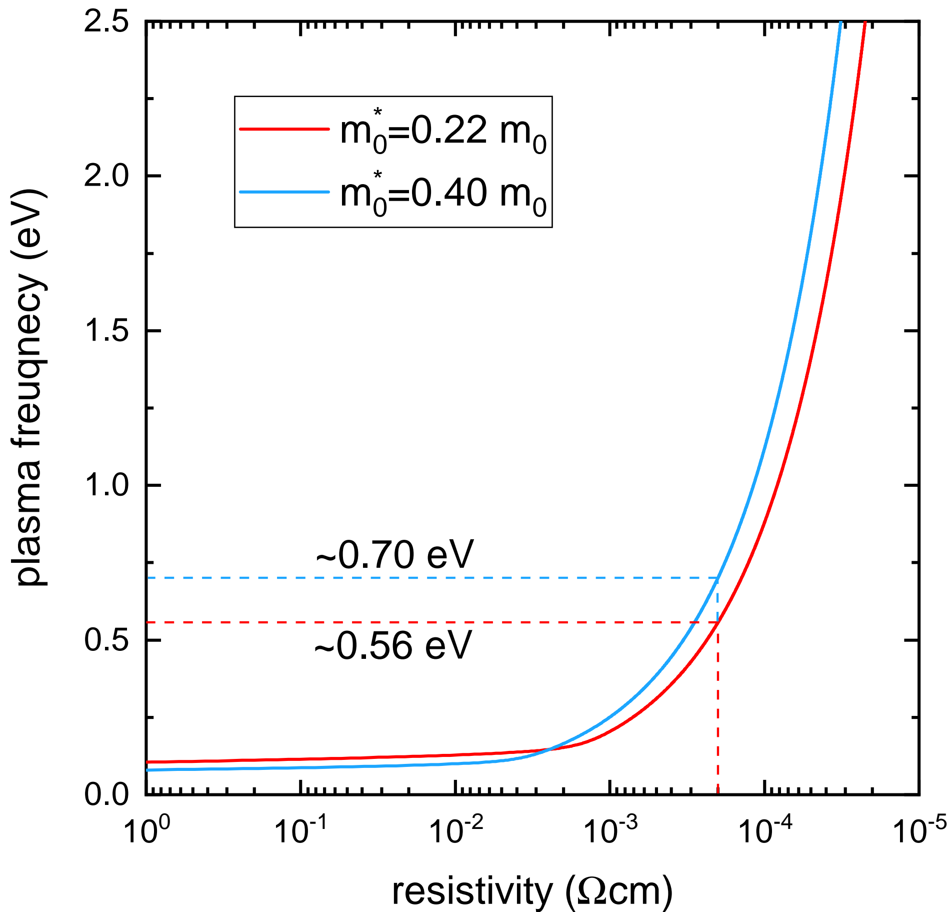

Figure 7.3: The plasma frequency calculated using the calculated combined scattering limited mobility against against resistivity calculated using the same mobility and carrier concentration. Calculations are for effective masses of 0.22 m_0 and 0.40 m_0. Dashed lines show the plasma frequency corresponding to a resistivity of 2×10^{-4} Ωcm

For the range of resistivities that optimal TCOs achieve (<1×10^{-3} Ωcm) the higher effective mass corresponds to a higher plasma frequency. The difference in plasma frequency increases

with decreasing resistivity. As an example, for a resistivity of 2×10^{-4} ωcm an effective mass of 0.22 m_0 corresponds to a plasma frequency of 0.56 eV while the higher effective mass of 0.40 m_0 corresponds to a plasma frequency of 0.70 eV. The difference in plasma frequency observed in these models is comparable to the difference in plasma onset seen experimentally for samples of resistivity in the region.

The result of this model generally agree with experimental results seen in the work in chapters 5 and 6 as well as the comparison of ITO and IMO in reference 75. Figure 7.4 shows the models over a smaller region of resistivities compared to experimental results for IMO, ITO and ICO.

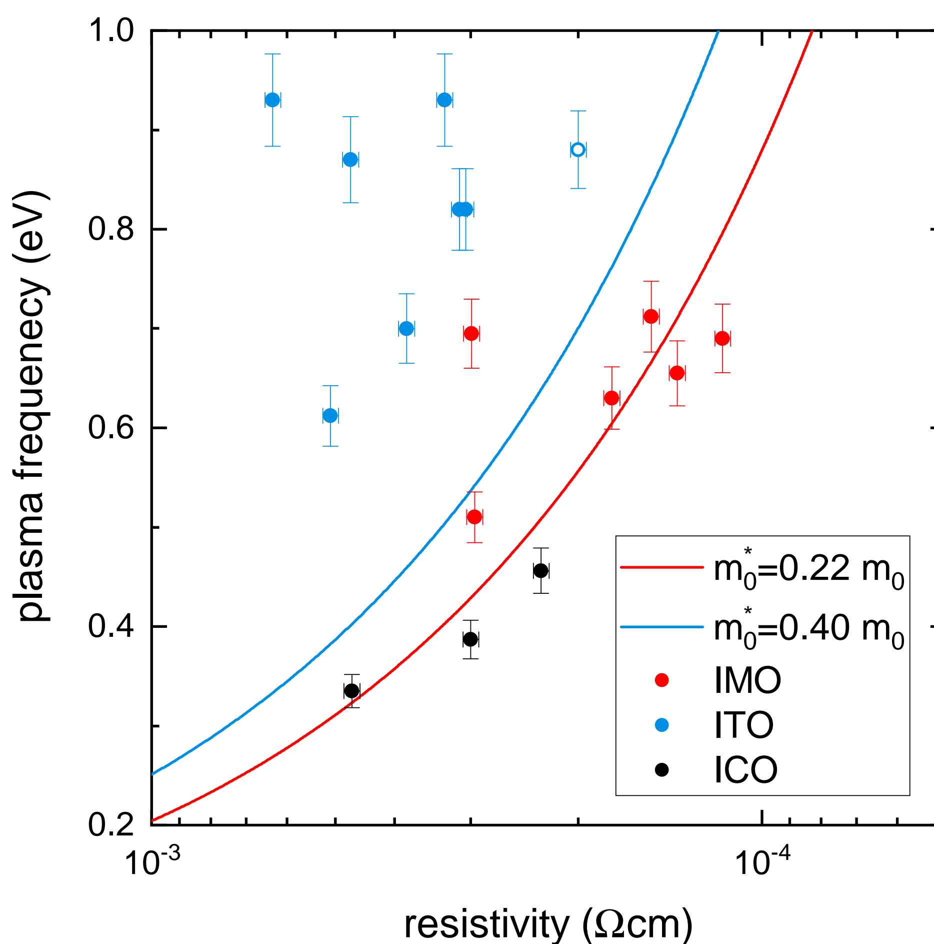

Figure 7.4: The plasma frequency calculated using the calculated combined scattering limited mobility against against resistivity calculated using the same mobility and carrier concentration. Calculations have been done for effective masses of 0.22 m_0 and 0.40 m_0. Dashed lines show the plasma frequency corresponding to a resistivity of 2×10^{-4} Ωcm

Despite the wide spread of results seen in figure 7.4, the general spread of the data points shows that ITO displays higher plasma frequencies for comparable resitivities. The discrepancy

from the models is unsurprising as a lot of assumptions were made with regards to film properties. Every property other than effective mass was kept constant throughout the models when in reality a lot of these properties will vary sample to sample and may even vary with dopant.

From the experimental data and the models shown here it is clear that the lower effective mass correlates with a lower plasma frequency allowing for the improved infra-red transparency seen experimentally.

7.3 Absorption

Absorption can also have an impact on the optical properties of a material. With high carrier concentrations seen in TCOs this can be expected to have a significant impact. In the transfer matrix method for modelling optical properties, described in section 3.4 and used throughout this thesis, all interactions between within the bulk, including absorption, are handled by the propagation matrices. this matrix is purely dependent on the phase change of the light described in equation 3.17. This expression is dependent on the thickness of the material and the imaginary part of the refractive index, $\bar{k}$. In the fitting processes and modelling done in the previous chapters, the two oscillator model for the dielectric function given in equation 3.7 and then $\bar{k}$ was calculated using equation 3.2. The two oscillator model includes terms accounting for the plasma oscillations and transverse optical phonon oscillations. Both of these contribute towards absorption but differentiating between the contributions of the two is challenging. Also, there are mechanisms for absorption which are not accounted for in this model, most importantly inter-band absorption which dominates at high frequencies. This was not important in fitting IR-reflectvity data as inter-band absorption would not occur at such low frequencies but when considering all potential differences in the optical properties of two materials this needs to be considered.

7.3.1 Free Carrier Absorption

In highly doped samples the absorption coefficient attributed to free carrier absorption is described by [223, 224]:

$$\alpha = \frac{\lambda^2 e^3 N_e}{4\pi^2 \epsilon_0 c^3 n m^{*2} \mu} \tag{7.5}$$

which arises from the Drude model. In this expression, λ is the wavelength of light, e is the elementary charge, N_e is the free carrier concentration, ϵ_0 is the permittivity of free space, c is the speed of light in a vacuum and n is the refractive index of the material at wavelength λ. As usual, m^* and μ are the free carrier effective mass and mobility respectively. However, in this case, as optical properties are being calculated, the optical effective mass and mobility should be used. The optical effective mass, also referred to as the density of states effective mass is described in section 3.5.1 along with how it is calculated. The optical mobility is the same as the

in-grain mobility as optical excitations are expected to deflect free carriers over a distance which is shorter than the grain size. In a lot of cases this can be expected to vary from the mobility as extracted from Hall effect measurements [225]. However, in the case of TCOs, grain boundaries have minimal effect on the mobility, as shown in figures 7.1 and 7.2. As such, it can be assumed that optical and transport mobilities will be roughly equal.

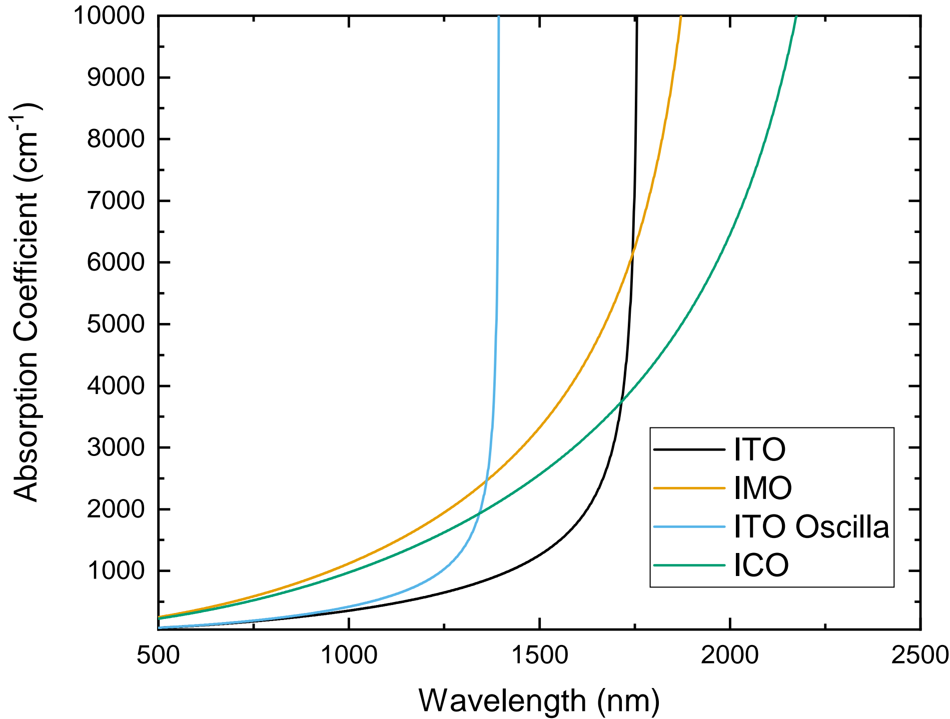

Figure 7.5: The free carrier absorption coefficient calculated using equation 7.3.1 for ICO, IMO and ITO thin films with resistivities around 2×10^{-4} Ωcm. The IMO and one of the ITO films are 1100 nm thick to represent films from reference 75 while the ICO and other ITO film (Oscilla) are 200 nm thick to represent films in chapter 6 of this thesis.

Figure 7.5 shows free carrier absorption coefficient as a function of wavelength for ICO, IMO and ITO samples with resistivities around 2×10^{-4} Ωcm.

These calculations show a clear difference in the behaviour of the carrier absorption between the ITO with a higher effective mass and the IMO and ICO with the lower effective masses. In these calculations, the real refractive index used was that which was calculated using the two oscillator model which means the expression is dependent on the plasma frequency of the material. The plasma frequencies of these films have been found experimentally and presented among those in figure 7.4. Specifically the plasma frequencies of these samples are ~0.70 eV for both the IMO and thick ITO and 0.52 and 0.88 eV for ICO and the Oscilla ITO respectively. The position of the onset of free carrier absorption correlates closely with the plasma frequency of the sample. 0.7 eV corresponds to a wavelength of 1770 nm, 0.52 eV corresponds to 2380 nm and 0.88

eV corresponds to 1410 nm. All these correspond closely to the onsets seen in figure 7.5.

The other obvious difference between the samples is how sharp the onset is. The ITO samples with a high effective mass have a much sharper onset for free carrier absorption than ICO and IMO which have a lower effective mass due to the resonant nature of the dopants. The combination of these two phenomena means that the absorption coefficients of the resonantly doped samples is higher than that of the non-resonantly doped samples in the visible range. However, the sharper onset seen in the tin doped samples means that the absorption coefficient in the infra-red is higher.

As the onset of free carrier absorption is dependent on plasma frequency, similarly to infra-red reflectivity, it can be expected that this absorption has little effect on the range over which the sample is transparent. Some amount of free carrier absorption appears to occur within the transparent range but this appears only to slightly lower the peak transmission.

7.4 Optical Modelling

Utilising the transfer matrix method described in section 3.4 and implementing interband absorption utilising the expressions described in section 3.5.7. Therefore it is possible to model a material, varying the effective mass while keeping other properties constant. This will show the potential impact of these resonant dopants if other properties of the system can be maintained. For this modelling In_2O_3 properties have been used.

7.4.1 Variable Dependencies

While it is acknowledged that it is unrealistic to assume that different dopants can be implemented without impacting other properties of the material there is value in doing this as there is a complicated interconnectivity between a lot of properties as many depend on the effective mass. For this modelling any property with a known dependence on effective mass will also be calculated. One example of such a property is plasma frequency, its complex relationship with effective mass was discussed above in section 7.2. Figure 7.6 shows a flow chart displaying the dependencies of properties on each other.

In this modelling the density of states and Fermi level are calculated using the alpha approximation described in section 3.5.4. The mobility is calculated using the scattering limited mobility as was done in section 7.2.2 but only ionised impurity scattering and phonon scattering have been used as other scattering mechanisms have minimal impact as shown in figure 7.1. The plasma frequency is calculated using this mobility which is then used in calculating the refractive index using the two oscillator model given in equation 3.7. The transfer matrix method is then used to calculate the optical properties as described in section 3.4. The interband absorption coefficient is then calculated using the Fermi level previously calculated and the transmission at frequencies close to above the band gap are calculated using 3.84 using the interband absorption coefficient

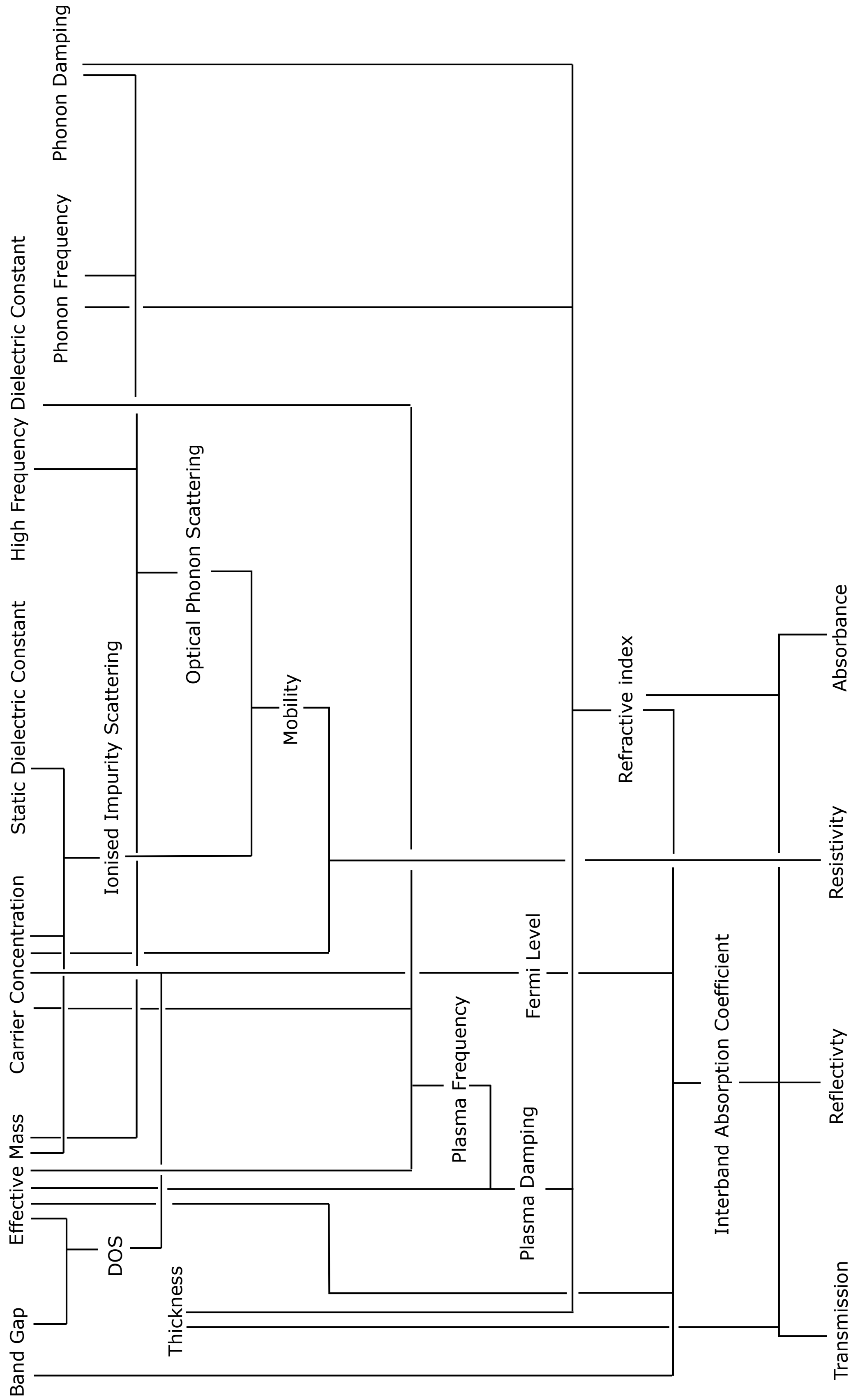

Figure 7.6: Flow chart showing the dependencies of properties used in optical modelling in this chapter.

as α. The transmission calculated using the transfer matrix method is then multiplied by this new transmission.

Figure 7.6 does not include temperature but many of the properties included are dependent on it. However, as temperature is a property of the environment and not the sample itself it can be assumed that it will be the same in all cases. In all modelling performed in this chapter the temperature is assumed to be room temperature, 300 K.

Another property not included in the flow chart is doping density which several properties such as ionised impurity scattering depend on. As in section 7.2.2, a one to one ratio of dopant defects to free carriers has been assumed so that doping density is equal to carrier concentration.

Phonon frequency and damping have no dependencies in the flow chart but they are dependent on the atomic masses within the lattices [226]. Introduction of dopant impurities will therefore impact the values of these properties. However, for this modelling the same values have been used throughout based on values reported for ITO. This decision was made as changing these properties would further complicate an already complicated model and based on fitting of reflectivity data for ITO, IMO and ICO the difference in these values were not significant enough to have a major impact on the outcome compared to differences in other properties.

7.4.2 Modelling Results

Figure 7.7 shows the modelled transmission, reflection and absorption spectra for In_2O_3 with effective masses of 0.22 m_0 and 0.40 m_0 to represent resonant and non-resonant dopants. A resistivity of 1×10^{-4} Ωcm was chosen by performing the scattering modelling and identifying the mobility and carrier concentration that corresponds closely to this. These properties were then used for the optical modelling. The static and high frequency dielectric constants used were 8.9 ϵ_0 and 4.1 ϵ_0, the values reported for In_2O_3 in the literature. The films modelled are 200 nm thick.

As expected, the primary difference between the two sets of spectra arises in the infra-red region. The onset for IR reflectivity occurs at longer wavelength for the lower effective mass. The plasma frequencies calculated in these models were 0.82 eV for $m_e^* = 0.22\ m_0$ and 1.02 eV for $m_e^* = 0.40\ m_0$. These plasma frequencies are higher energy than those seen experimentally in chapter 6. This is due to the resistivity of the modelled films being lower than the measured films. The carrier concentrations to reach these low resistivities in this model were 4.42×10^{20} cm^{-3} and 1.25×10^{21} cm^{-3} for the lower and higher effective mass respectively. These are higher than the experimentally reported carrier concentrations which leads to the higher plasma frequencies arising from the model.

Figure 7.7 (bottom) shows the same spectra on an energy scale rather than wavelength. This highlights differences at short wavelengths near the absorption edge due the inverse relationship between wavelength and energy. The scale used goes up to 5 eV, this corresponds to a wavelength of ~250 nm. This scale was chosen as the wavelength range approaching 0 nm would approach infinity on an energy scale and as such would make any usefully information difficult to discern.

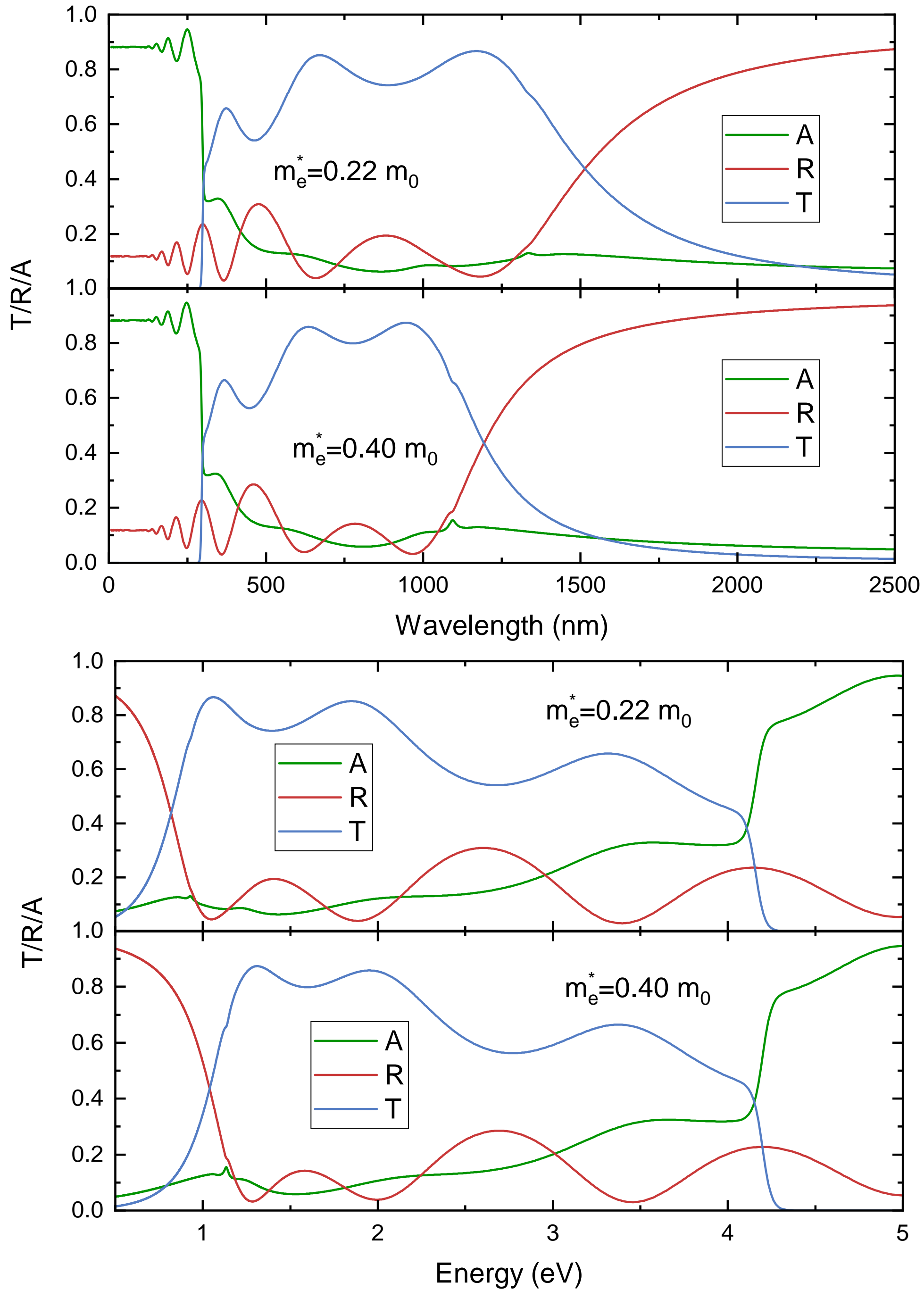

Figure 7.7: Transmission (T), reflectivty (R) and absorption (A) spectra for two hypothetical thin films with electron effective masses of 0.22 m_0 and 0.40 m_0. (Top) shows a wavelength scale and (bottom) shows a energy scale.

Even on this scale, no clear difference is apparent between the absorption edges in the two materials. In the model the optical gaps for the resonantly and non resonantly doped materials were 4.17 and 4.21 eV respectively, a difference of 0.04 eV which is negligible.

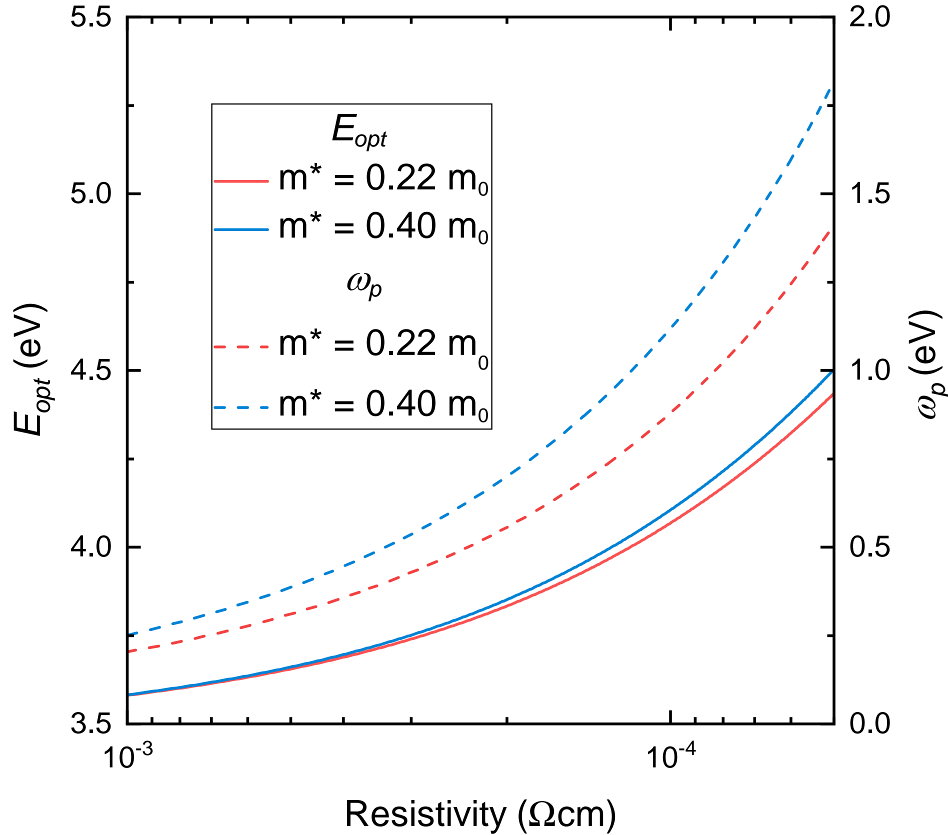

Figure 7.8: The optical gap and plasma frequency of modelled In_2O_3 with effective masses of 0.22 m_0 and 0.40 m_0 as a function of resistivity.

Figure 7.8 shows the modelled optical gap as a function of resistivity for the two effective masses. The difference between the two is minimal but increases at lower resistivities with the optical gap being slightly larger for the higher effective mass. The larger optical gaps for the lower effective mass arise as the lower mobilities mean higher carrier concentrations are required to reach such low resistivities. However, the difference is small as the dispersion of the conduction band changes with effective mass and therefore the Fermi level rises more quickly with carrier concentration for the lower effective mass as seen in sections 5.6.1 and 6.7.3 in previous chapters. As a result the optical gaps never have a difference greater than ~0.05 eV for the range of resistivities that have been previously reported in In_2O_3.

The range over which material is transparent is generally between the energy of the optical gap and the plasma frequency. Figure 7.8 also shows the plasma frequency for the two effective masses over the same range of resistivities (this has been previously shown in figure 7.4. The

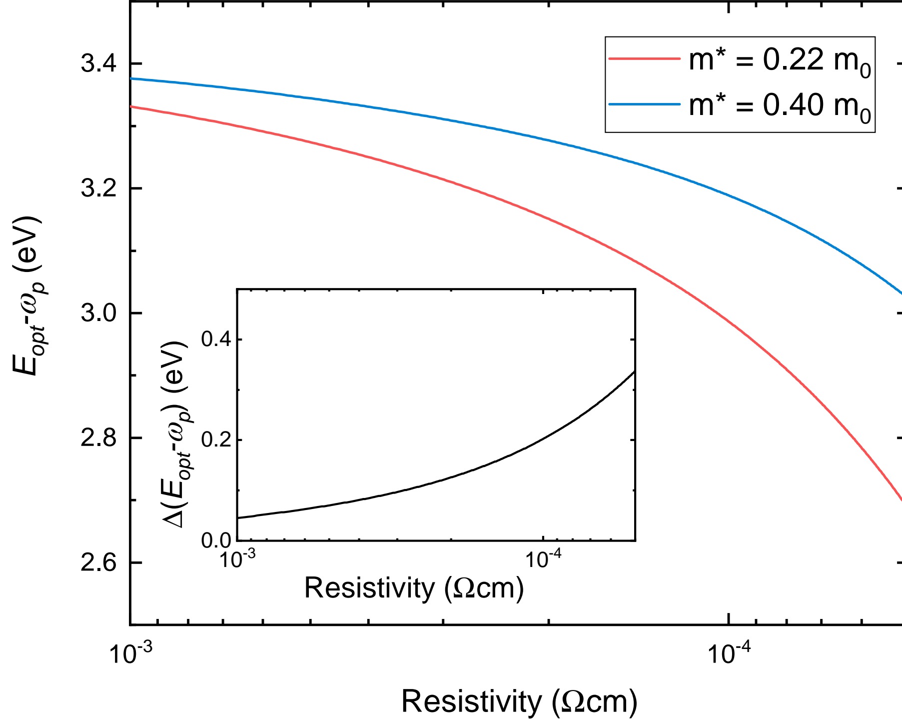

Figure 7.9: The separation of the absorption edge (optical gap) and plasma frequency as a function of resistivity for modelled In_2O_3 with electron effective masses of 0.22 m_0 and 0.40 m_0. This represents the range of energies over which the material will be transparent.

differences in plasma frequency are greater than the difference in optical gap for the full range. The energy range over which the modelled material is transparent for the two effective masses is plotted as a function resistivity in figure 7.9.

As the resistivity lowers, the difference in the size of energy range for which the material is transparent decreases. This is due to the difference in plasma frequency for the different effective masses increases at a higher rate than the difference in optical gap.

The higher effective mass has a lower transparency range for all resistivities. The rate at which this range reduces as resistivity increases is also faster for the higher effective mass. Based on this, resonant dopants should provide improved optical properties compared to traditional dopants when resistivities are comparable.

7.5 Comparing TCOs for Photovoltaics

The modelling performed in the previous section shows that resonant dopants can increase the size of the range over which the material is transparent compared to traditional dopants. An

increased range of transparency does not necessarily mean improved device efficiency.

As discussed in section 1.5.2, the solar spectrum does not emit equal energy across all wavelengths. In section 1.5.3 it was explained that photons with energy lower than the band gap of the photovoltaic absorber will not be absorbed, meaning transparency in this range poses no advantage. Also, not all energy will be absorbed from photons with energy greater than the band gap due to thermalisation. Thus, the relationship between transparency in TCOs and the impact on photovoltaic device efficiency in much more complicated.

In this section, the potential impact of transparent electrode choice on photovoltaic device efficiency is quantified accounting for these factors. This is then used to quantify the potential impact of utilising resonant dopants on devices, both for the experimental results shown in chapters 5 and 6 and the modelled materials shown earlier in this chapter.

7.5.1 Figures of Merit

To compare transparent conductors in a way that accounts for both electrical and optical properties several attempts have been made to define a 'figure of merit'. A figure of merit first proposed by Haacke in 1976 [227] is most commonly used for this purpose [156, 205, 228].

This figure of merit is defined as:

$$\phi_H = \frac{T^{10}}{R_\square} \tag{7.6}$$

where T is the transmission at a wavelength of 550 nm and $R_\square$ is the sheet resistance of the film. A wavelength of 550 nm is chosen because as it approximately corresponds to a photon energy of 2.25 eV, the energy of maximum flux in the solar spectrum. This wavelength is a reasonable gauge of how suitable the optical properties of the film are for the response of the human eye, which also peaks at 550 nm, and is therefore a good gauge of how suitable a TC is for devices such as touch screens. However, this is not representative of its optical suitability for a photovoltaic absorber.

Alternatively, sometimes the average transmission across the visible range is used in place of T. While this approach is more closely representative of the requirements for a transparent electrode in a photovoltaic device, several factors, such as the solar spectrum and thermalisation of photo-generated electrons, have not been considered.

Ref. 228 utilises the Haacke figure of merit for the purpose of comparing transparent electrodes for a specific organic photovoltaic device. To adjust this figure of merit for this purpose, the average T over a wavelength range of 450-600 nm is used. This range was chosen as it is the range of the absorption peak of the active layer in the device geometry used [229].

Another figure of merit that is some times used was proposed by Gordon in 1996 [230], and uses the ratio of the TCs conductivity, σ, and absorption coefficient, α. It is suggested that this can be calculated using the films sheet resistance, transmission, T, and reflectance, R.

$$\phi_G = \frac{\sigma}{\alpha} = -[R_\square \ln(T+R)]^{-1} \tag{7.7}$$

For this figure of merit the original paper only suggests using 'total visible transmission' and 'total visible reflectance'. In use, this has either been interpreted as the same definition as the transmission in the Haacke figure of merit or as the average transmission over the visible range. As with the Haacke figure of merit, neither of these approaches are truly representative of what is important for a solar absorber.

Recent work by Mendez-Gamboa et al. propose a new figure of merit specifically for the purpose of pairing a transparent conductor with a photovoltaic absorber [231]. This figure of merit is calculated by the ratio of the photo-generated current density, J_L, for a specific absorber band gap to the sheet resistance.

$$\phi_{PH} = \frac{J_L}{R_\square} \tag{7.8}$$

This approach to a figure of merit for photovoltaics has the advantage that J_L accounts for the solar spectrum and the band gap of the material. The expression suggested by Mendez-Gamboa for J_L is

$$J_L = e\int_{Eg}^{E_{TCO}} \Phi(E)T(E)dE \tag{7.9}$$

where e is the charge on an electron, E_g is the band gap of the absorber, E_{TCO} is the optical gap of the TCO, Φ is the incident photon flux density and T is the transmission of the TCO. This approach is ideal for comparing TCOs for photovoltaic applications. Despite this, this work by Mendez-Gamboa has garnered little attention. The following sections look to build upon this method, defining a method for quantifying the impact of a TCO on the efficiency of a photovoltaic device.

7.5.2 Defining Optical Suitability

To start, consider how suitable the optical properties of a TCO are for a photovoltaic absorber.

A photovoltaic absorber will absorb a certain about of power per unit area if the solar spectrum falls upon it. The maximum power a device utilising a specific absorber can generate from photons of energy E, $P_{max}(E)$, assuming no optical losses in other layer and no losses within the absorber due to recombination of other defects, under the AM1.5 spectrum is given by

$$P_{max}(E) = \frac{E_g}{E} P_{AM1.5}(E) \tag{7.10}$$

where E_g is the absorbers band gap and $P_{AM1.5}(E)$ is the power density of the AM1.5 spectrum at energy E. The origin of the AM1.5 spectrum and why it is used for calculating solar cell efficiency is described in section 1.5.2 and the spectrum is shown in figure 1.6. This expression holds true only for energies greater than E_g as photons with lower energies will not be absorbed.

With the addition of a transparent electrode, the power absorbed at an energy E is reduced by a factor of the transmission of the TCO at that energy, $T(E)$

$$P_{TCO}(E) = T(E)\frac{E_g}{E}P_{AM1.5}(E) \tag{7.11}$$

The total power absorbed from the AM1.5 spectrum without and with the transparent electrode present can be then calculated by integrating equations 7.10 and 7.11 respectively over all energies greater than the band gap. This gives the total power absorbed without the TCO as

$$P_{max} = \int_{E_g}^{\infty} \frac{E_g}{E}P_{AM1.5}(E)dE \tag{7.12}$$

and with the electrode:

$$P_{TCO} = \int_{E_g}^{\infty} T(E)\frac{E_g}{E}P_{AM1.5}(E)dE \tag{7.13}$$

The ratio of these two values, P_{TCO}/P_{max} quantifies the potential power loss due to optical losses in the TCO. Defining this ratio as the optical suitability, S_{opt}, for a TCO paired with a photovoltaic absorber

$$S_{opt} = \frac{\int_{Eg}^{\infty} T(E)\frac{E_g}{E}P_{AM1.5}(E)dE}{\int_{Eg}^{\infty} \frac{E_g}{E}P_{AM1.5}(E)dE} \tag{7.14}$$

7.5.3 Comparing Real Materials

To explore this method and compare resonant and non-resonant dopants in the context of photovoltaics, the Ce doped In_2O_3 sample and the ITO shown in figure 5.22 in chapter 5 will be compared. Initially, for this comparison an absorber with a band gap of E_g = 1.2 eV has been chosen. This was chosen to represent Sb_2Se_3, a novel absorber with a band gap around 1.2 eV [232].

Figure 7.10 shows the power absorption spectra for an absorber with a band gap of 1.2 eV without a transparent electrode and with ITO and ICO present. The absorber is assumed to have a 100% internal quantum efficiency at energies above its band gap, each photon contributes one photo-electron.

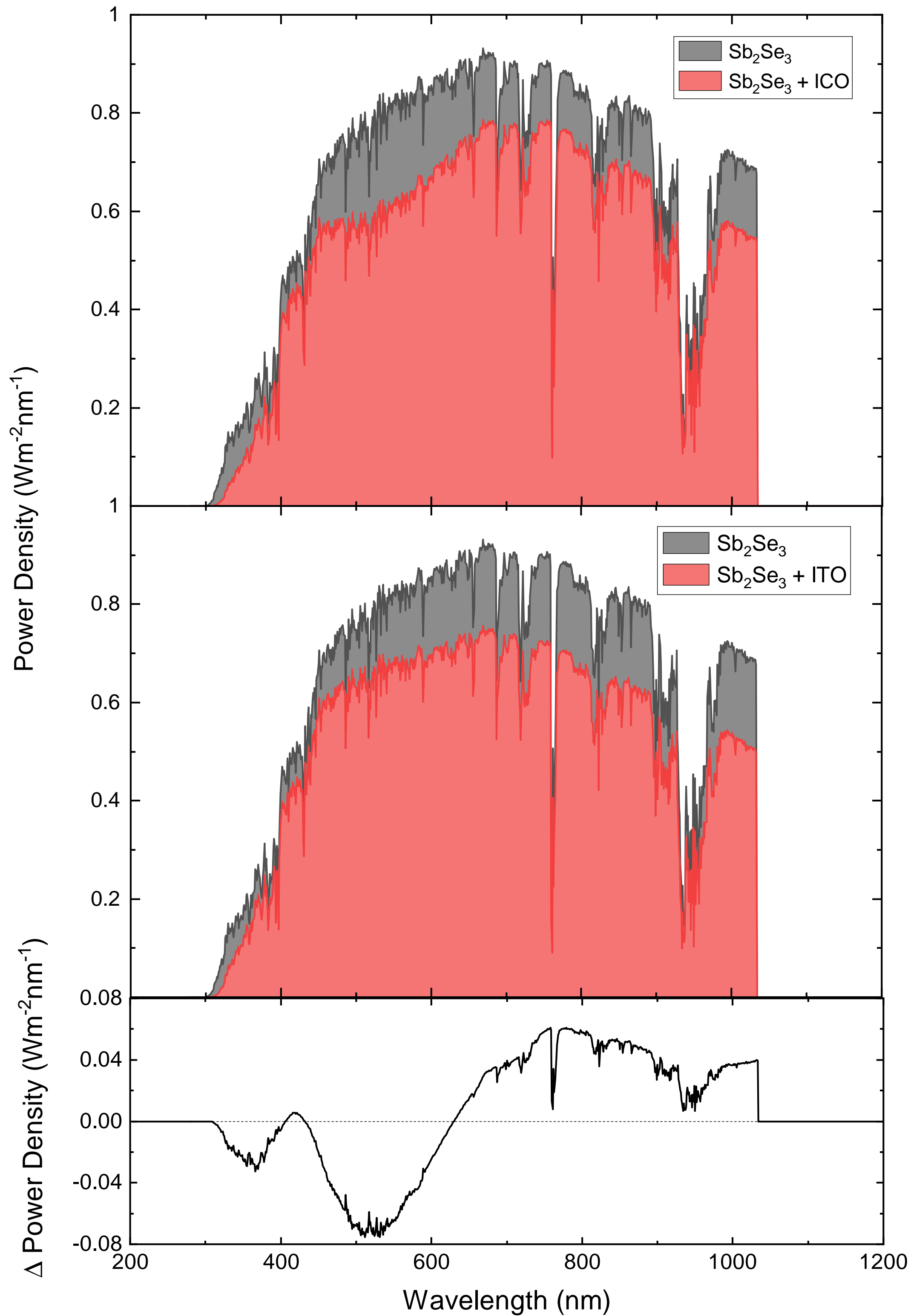

Figure 7.10: The theoretical power density for a solar absorber with a band gap of 1.2 eV with and without the impact transparent electrodes based on illumination under the AM1.5 spectrum. Top shows the impact of the ICO and ITO thin film shown in figure 5.22. The bottom shows the difference in power density as a function of wavelength (ICO-ITO).

Integrating under the data set gives the total theoretical power density for such a device. The device with ICO has a total power density of 389.9 Wm^{-2} while ITO has one of 384.6 Wm^{-2}. With no transparent electrode the power density limit for the material is 480.0 Wm^{-2}. Using these values the optical suitability, S_{opt} as defined in equation 7.14 is 0.812 for the ICO and 0.801 for the ITO. The difference in these values is small and would only correspond to small changes in device efficiency. For a device with around 10% efficiency this would only correspond to an difference in efficiency of 0.1%.

It is of note that as the AM1.5 spectrum has a total power density of ~1000 Wm^{-2} these values correspond to efficiencies greater that the Shockley-Queissar limit. This is the case because the Shockley-Queissar limit accounts for losses due to radiative recombination and impedance matching. Only accounting for spectral losses, as done here, the upper limit on efficiency is 48% which all values from these models fall below.

The bottom of figure 7.10 shows the difference in the power densities for using the ICO and using the ITO, the power density for ITO has been subtracted from that for ICO. Therefore a value greater than 1 corresponds to the ICO device having a greater power density at that wavelength and a value less than 1 corresponds to the ITO device having a greater power density. At longer wavelengths, greater than around 620 nm, the ICO device provides a higher power density. Below 620 nm ITO provides a greater power density except for a small region slightly above 400 nm.

The small region below 410 nm where ITO provides a higher power density than ICO arises due to differences in the optical gap of the two materials. The ICO sample has significantly lower carrier concentration than the ITO sample and as such a less full conduction band and therefore a small optical gap. In this case the impact of this is smaller than the impact of the improved IR transparency seen in the ICO.

At wavelengths greater than 1033 nm and less than 320 nm, the difference is 0 $Wm^{-2}nm^{-1}$. This is because wavelengths greater than 1033 nm corresponds to energies lower than 1.2 eV and as such no energy is absorbed by the absorber in this region. Similarly, wavelengths below 320 nm correspond to energies greater than 3.87 eV. This energy corresponds to the higher optical gap of the two TCOs and as such all photons with energy greater than it are absorbed by the TCO in both cases a no energy is absorbed by the absorber.

In the longer wavelength region, where ICO has the higher power density, this corresponds to the region of improved infra-red transparency due to its lower energy plasma frequency as seen in figure 5.22. The region where ITO provides the largest gains, between ~420 and 620 nm, corresponds to a region where the ITO is slightly more transparent than the ICO due to an interference fringe. In figure 5.22 the region of improved infra-red transparency is significantly larger than the region of improved transparency due to the interference fringe but the impact on the optical suitability is comparable. However, the difference in total power density that arises due to these features is comparable. The improved IR transparency has a less significant impact

that the transmission spectra would imply due two factors: most of the light in this region is of two low energy to be absorbed by an absorber with a band gap of 1.2 eV and the power density of the solar spectrum at these wavelengths is significantly lower as seen in figure 1.6. As such the improved IR transparency seen in ICO compared to ITO in figure 5.22 can be expected to only provide marginal improvements to a photovoltaic device with this band gap.

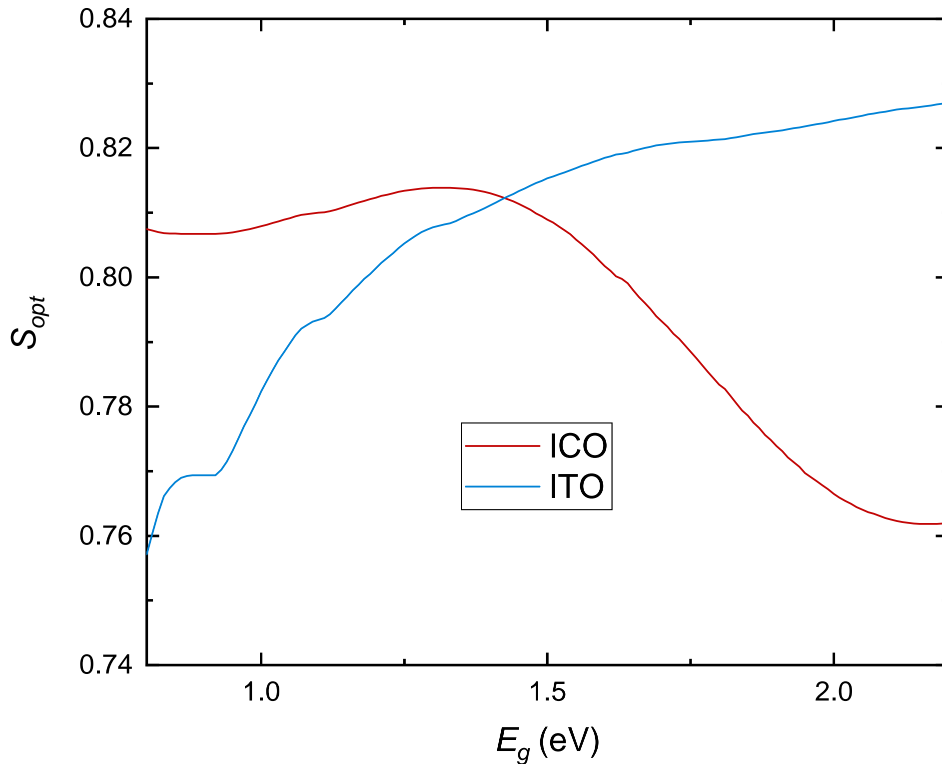

Figure 7.11: The optical suitability of the ICO and ITO thin films presented in figure 5.22 as a function of absorber band gap.

Sb_2S_3 also behaves as a photovoltaic absorber with a much wider band gap of around 1.8 eV [233]. Creating a mixture of the two compounds and varying the Se and S content ($Sb_2Se_xS_{3-x}$ it is possible to create a photovoltaic absorber with a band gap tuned to anywhere between 1.2 and 1.8 eV.

For the band gap of Sb_2S_3 the total power densities becomes 353.2 Wm^{-2} with no transparent contact and 276.7 Wm^{-2} and 290.1 Wm^{-2} for ICO and ITO contacts respectively. This corresponds to an S_{opt} of 0.783 for ICO and 0.821 for ITO.

With a wider band gap absorber, the improved infra-red transparency seen in ICO has no impact on the absorbed power density as no light within that region has enough energy to absorbed by the absorber layer. As such, difference in the total power density arises due to the differences in the interference fringes and the difference in optical gap.

Figure 7.11 shows the optical suitability for the two films as a function of absorber band gap.

As expected, ICO, the resonantly doped material, has a higher S_{opt} value for absorbers with smaller band gaps as those absorbers absorb more energy for the near infra-red region. As the band gap of the absorber increases, the more the optical suitability of the ITO sample improves as infra-red transparency becomes less important.

The point above which the ITO has more suitable optical properties than ICO is for band gaps of ~1.49 eV or higher. As show in figure 1.7, the ideal range for the band gap of a photovoltaic absorber is between 1.1 and 1.6 eV. Thus, the majority of widely used absorbers have band gaps falling within this range. However, the band gaps of some of the most commonly used absorbers, CdTe, CIGS and CZTS, fall very close to 1.5 eV [234–236]. As such, for this particular comparison the choice between ICO and ITO can be expected to make very little difference to efficiency of devices made with these absorbers. Absorbers with narrower band gaps, such as Sb_2Se_3 discussed earlier, could be expected to make marginal gains utilising ICO but, as previously stated, this increase would be limited to less than 1%.

7.5.4 Comparing Theoretical Materials

For the two materials compared in the previous section, the benefits of the improved infra-red transparency gained from a resonant dopant were inhibited by optical losses due to interference fringes which were present in the ICO but not the ITO. These differences arise due to differences in the film that are caused by differences in the deposition, such as roughness. This highlights that while the resonant dopants have potential benefits other differences in the film can easily have an as significant, or more significant, impact on the optical properties of the film and therefore any device it is incorporated into.

In section 7.4.2, the optical properties of two In_2O_3 thin films of comparable resistivity but different effective masses were modelled. These films were modelled to more directly compare the impact of the carrier effective mass in a material if other properties were kept constant. By comparing the optical suitability of these modelled films, the potential impact of resonant doping of TCOs for photovoltaic devices can be better quantified as the impact of other properties will be minimised. The transmission spectra of the films being compared in this section are displayed in figure 7.7.

Figure 7.12 shows the power absorption spectra for an absorber with 1.2 eV band gap, once again representing Sb_2Se_3, with and without the transparent electrode present for the two modelled films.

The total power density for the film with m^*=0.22 m_0 is 351.0 Wm^{-2} and 354.5 Wm^{-2} for the film with m^*=0.40 m_0 corresponding to S_{opt} values of 0.736 and 0.779 respectively. Unlike the case for the real films compared in the previous section, the non resonant dopant has more suitable optical properties for an absorber with a band gap of 1.2 eV.

The bottom of figure 7.12 shows the difference in power density for the two films as a function of wavelength. This shows that the higher effective mass provides greater power density at most

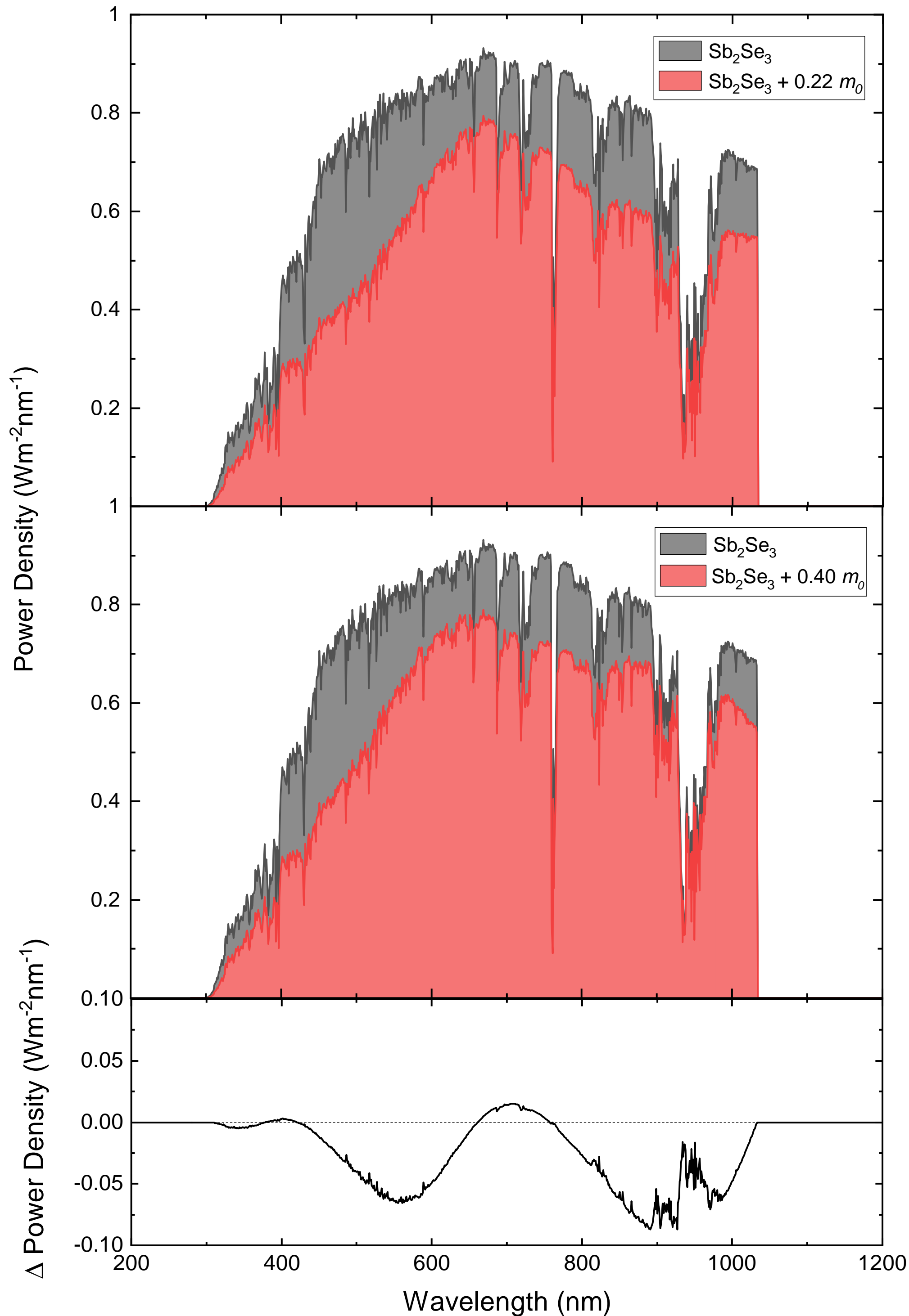

Figure 7.12: The theoretical power density for a solar absorber with a band gap of 1.2 eV with and without the impact transparent electrodes based on illumination under the AM1.5 spectrum. Top shows the impact of the In_2O_3 thin films with effective masses 0.22 m_0 and 0.40 m_0 shown in figure 7.7. The bottom shows the difference in power density as a function of wavelength (0.22 m_0 - 0.44 m_0).

wavelengths in the range absorbed by this absorber. This data displays an oscillation, similar to interference fringes seen in optical data. The position of the peaks and troughs also align with the positions of fringes in the modelled optical data presented in figure 7.7. In the case of these modelled films the region of improved IR transparency seen with the lower effective mass falls entirely outside the range absorbed by an absorber with this band gap.

The small difference seen below 400 nm arises due to the difference in the optical gaps rather than the interference fringes. As seen with the real films, the impact if the difference in optical gaps is negligible compared to the differences seen elsewhere.

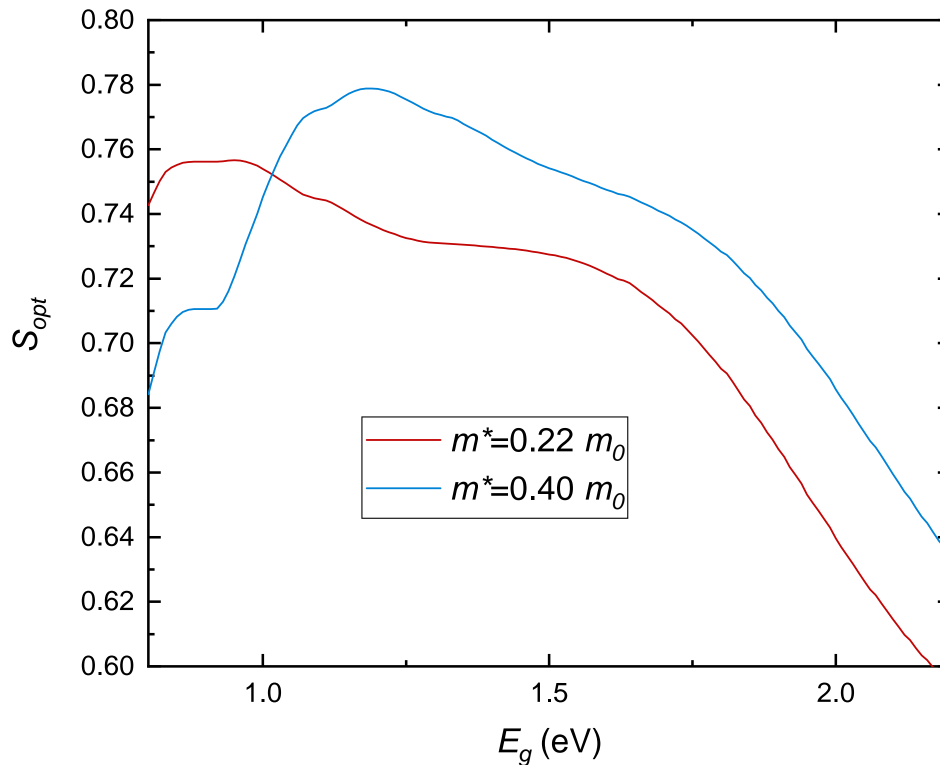

Figure 7.13: The optical suitability of the modelled In_2O_3 thin films with carrier effective masses of 0.22 m_0 and 0.40 m_0 as a function of absorber band gap. The optical spectra for these films are presented in figure 5.22.

Figure 7.13 shows the optical suitability of the two modelled films as a function of absorber band gap. For a band gap of 1.01 eV or higher the higher effective mass has more suitable optical properties. Below 1.01 eV the lower effective mass is more suitable. Based on this, it appears that only narrow band gap absorbers can be expected to benefit from the use of resonantly doped TCOs.

7.5.5 Discussion

In both the case of comparing real films and theoretical films with different effective masses the lower effective mass, and the resulting improved near infra-red transparency, was only of benefit for narrow band gap photovoltaic absorbers.

It is of note that the point below which the lower effective mass is beneficial for the modelled data is a band gap 1.01 eV. The plasma frequency of the higher effective mass material is 1.02 eV. This appears to indicate that when all other properties are comparable, the point at which the resonant doping becomes optically beneficial in a photovoltaic device is when the plasma frequency is greater than the absorber's band gap. Therefore a selection criteria when choosing a transparent electrode for photovoltaic applications should be that $E_g > \omega_p$ where E_g is the band gap of the material and ω_p is the plasma frequency of the transparent electrode. For a case where two materials that both meet this criteria, features such as interference fringes dictate which material has more suitable properties.

In section 2.4, several alternative, non oxide based, transparent conductors were discussed. Of these, the alternatives with the best electrical properties were ultra thin metal films, UTMFs, and strongly correlated metals. Both of these classes materials displayed low resitivities due to high carrier concentrations, $\sim 10^{-22}$ cm^{-3}. As such these both have very high plasma frequencies. The plasma frequencies reported in silver UTMFs varies significantly with thickness and other properties but are generally 3 eV or greater [237]. The reflection of certain wavelengths of light is generally prevented by the addition of other optically transparent films such as ZnO or ZnS. These allow for UTFMs to not be reflective at shorter wavelengths but generally they still start to reflect light beyond ~750 nm corresponding to energies less than ~1.65 eV. The band gaps of most photovoltaic absorbers are smaller than this and therefore significant optical losses can be expected due to infra-red reflectivity. Similarly, the plasma frequencies reported for optimised strongly correlated metals are around 1.75 eV [14]. Once again, higher than the band gap of most photovoltaic absorbers meaning that optical losses would be expected if utilised. While these materials have potential applications elsewhere, such as in low emissivity window coatings, it seems unlikely that they will have beneficial impacts on the photovoltaics field due to their high plasma frequencies.

In the comparison of the real thin films the band gap below which the ICO was more suitable was ~1.5 eV while the plasma frequency of the ITO film was measured to be 0.89 eV, significantly lower in energy. In this case, an interference fringe increasing the transparency of the ICO between 700 and 1000 nm (1.23 and 1.77 eV) keeps the properties of ICO preferable for band gaps above the ITO plasma frequency.

It is also of note that figure 7.4, which shows the plasma frequencies of several In_2O_3 thin films doped with Sn, Mo and Ce against resistivity, showed that the plasma frequencies measured in ITO thin films were significantly higher than the plasma frequencies obtained from the model at the same resistivity. This difference varies between ~0.3 and ~0.8 eV higher than the model.

Meanwhile, with the exception of one IMO sample, the measured plasma frequencies for the resonantly doped ICO and IMO samples were within 0.5 eV of the model. This indicates that the difference in plasma frequencies between the resonantly doped and the traditionally doped samples is even greater that the model predicts. This likely arises due to the mobilities being lower than those predicted by the scattering model so higher carrier concentrations are needed to reached theses resistivities and therefore the plasma frequency is higher. The lower mobilities could arise due to the scattering modelling underestimating the contribution of one or more scattering mechanism. The likely candidate is phonon scattering as ionised impurity scattering is linked closely to carrier concentration and other scattering mechanisms have been shown to have minimal impact. Phonon properties, particularly lifetime, have been found to be impacted by dopants in other systems [238, 239]. Meanwhile in the scattering modelling presented here, the properties of the phonons have be assumed to be independent of doping density, this is a likely origin of this discrepancy between model and experimental results. Whichever scattering mechanism is underestimated, this also means that higher carrier concentrations are required to reach the same resistivity and therefore the impact of ionised impurity scattering is further increased. If this is unavoidable, the difference in plasma frequencies for the resonantly doped and non-resonantly doped samples may be greater than predicted and the impact these materials could have on photovoltaic devices could be even greater than previously predicted.

Another consideration is how sharp the onset of the plasma reflectivity is. In the modelled materials this onset is significantly sharper than that seen in the experimental data for ITO. In the modelled material with an effective mass of 0.40 m_0 the onset begins at around λ=1000 nm and has reach transmission less than ~0.1 by λ=1500 nm. In the real ITO film the onset begins similarly at around λ=1000 nm but transmission is still significantly above 0.1 for the entirety of the measured range in figure 5.22 up to λ=2500 nm. The broader onset arises due to differences in the plasmon damping, γ_p, and the broadening causes the onset of plasma reflectivity to shift. This shows that, while the minimum band gap that the non-resonant dopant can be preferable for is decided by its plasma frequency, the resonantly doped sample can still have preferable properties for larger band gaps.

In 2019 Aydin et al. reported an improvement in device efficiency from 23.3% to 26.2% in silicon-perovskite tandem solar cells when utilising Zr doped In_2O_3 in place of Sn doped In_2O_3 [240]. They reported that the higher device efficiency arose due to improved infra-red transparency in the Zr doped material compared to the Sn doped. The mobilities reported for the Zr doped material was also higher than that in the Sn doped material. This, along side the fact the Zr is a transition metal dopant supports Zr being a resonant dopant in In_2O_3 and demonstrates the improvements in photovoltaic device efficiency that could be gained through utilising such materials.

In tandem solar cells, multiple p-n junctions are utilised, in this particular case, two. The top utilises a perovskite absorber layer with a wide band gap to capture high frequency blue

light while the bottom utilises narrow band gap silicon to capture the lower frequency light. Such devices are significantly more expensive than single junction solar cells but are utilised in low surface area applications such as on satellites and in concentrator solar cells. As in tandem solar cells a lower band gap absorber is utilised, the infra red region of light is of greater importance to the gains from using a resonantly doped TCO can be expected to be more significant. In some tandems absorbers with band gaps as small at 0.65 eV, such as Ge, are utilised. In these cases, the improved IR transparency can be expected to have a significant impact[241].

7.6 Conclusion

In the previous chapters resonant dopants were identified for both In_2O_3 and SnO_2 and the mechanism behind the improved mobilities observed in these materials was explained. Another property observed in the resonantly doped material was improved infra-red transparency compared to the traditionally doped material at comparable resistivities. This improved IR transparency was initially unintuitive based on the relationships between carrier concentration, mobility and plasma frequency. It seemed that the plasma frequency, which dictates the frequency at which the material is reflective, should be the same for similar resistivities, independent of whether the conductivity arose due to higher mobilities or higher carrier concentrations.

Free carrier scattering modelling showed that ionised impurity scattering was the dominant scattering mechanism for the carrier concentration range in which most TCOs operate with phonon scattering having a minor contribution. This scattering modelling showed that for comparable resistivities higher plasma frequencies could be expected for systems with higher electron effective masses. Comparing the trends for plasma frequency as a function of resistivity to experimental data showed good agreement between the model using an effective mass of 0.22 m_0 and the experimental data from resonant samples. However the model underestimated the plasma frequency for an effective mass of 0.40 m_0 compared to experimental data from ITO samples. This discrepancy between model and experimental data is likely due to the model underestimating the contribution of a scattering mechanism such a phonon scattering. This does mean that the range of improved transparency gained from resonantly doping a material is larger than this model suggests.

Combining the scattering modelling with models for inter-band absorption and optical modelling utilising the transfer matrix method, optical spectra for different effective masses were modelled while keeping all other properties constant. This showed that a difference in effective mass primarily effected infra-red transparency, as seen in experimental data, with the lower effective mass corresponding to a greater range of infra-red transparency. A small difference in optical gap was seen, with a higher effective mass corresponding to a larger optical gap, however this difference was significantly smaller than the one seen with infra-red transparency.

A new quantity, labelled optical suitability, S_{opt}, was defined with the purpose of comparing

transparent conductors for use as transparent electrodes for photovoltaic absorbers with a specific band gap. This quantity accounted for the solar spectrum and thermalisation of excessively energetic photo-generated carriers, two factors that significantly impact the upper limit on photovoltaic device efficiency and are often disregarded when comparing transparent conductors with commonly used figures of merit.

When comparing real films of Ce doped In_2O_3 and Sn doped In_2O_3 it was found that the resonantly doped ICO was more suitable for narrower band gaps below 1.5 eV while the non-resonantly doped ITO sample was more suitable for larger band gaps. The shift to the ITO being more suitable occurs when the band gap is too large for infra-red light in the range that ICO is transparent to be absorbed, at which point differences in interference fringes has the greatest impact on the optical suitability.

Performing a similar comparison for the modelled films of different effective mass but same resistivity, the lower effective mass material was found to be more suitable for band gaps below the plasma frequency of the higher effective mass film. Based on this, a selection rule for transparent electrodes was suggested of $\omega_p < E_g$ where ω_p is the plasma frequency of the transparent electrode and E_g is the band gap of the photovoltaic absorber. The experimental data supports the range over which the resonant doping is beneficial being larger than the model suggests due to higher plasma frequencies than the model predicts and also other differences in film properties.

This selection criteria also rules out several novel, non-oxide, transparent conductors for photovoltaic applications including ultra-thin metal films and highly correlated metals as these materials achieve their low resistivities though very high carrier concentrations and therefore have much higher plasma frequencies.

The models and experimental data suggest that utilisation of resonantly doped TCOs could have a significant impact on photovoltaic device performance in particular for devices with narrow band gaps. One example of this has already been seen in the literature where utilisation of Zr doped In_2O_3 has improved the absolute efficiency of silicon/perovskite tandems by around 3%. Zr has already been identified as a potential resonant dopant in In_2O_3 due to it being a transition metal in the correct oxidation state and the high mobilities previously reported for Zr doped In_2O_3. This example in combination with the results presented in this chapter indicate that further investigation in to utilising resonantly doped TCOs in photovoltaic devices is warranted and they may have the potential to lead to significant improvements in device efficiency in cases where narrower band gap absorbers are used.

Chapter 8

Summary and Future Work

8.1 Summary

This thesis has been focused on the phenomena of resonant dopants in transparent conductive oxides and the potential impact they could have for photovoltaic devices through a combination of experimental techniques and modelling looking at the band structure of these materials and how they correspond to optical and electrical properties.

Traditionally TCOs are based on ZnO, In_2O_3 and SnO_2 doped with elements from the *p* block of the periodic table. The chosen dopants have to be in the correct oxidation state, one greater than the element they are replacing. Traditional logic suggested that the element one to the right on the periodic table of the replaced element would therefore be the best choice of dopant as it will be in the correct oxidation state and similar in size, reducing lattice strain. Due to the elemental makeup of the materials TCOs are based on, this results in the dopants of choice being in the *p* block.

However, recent reports of transition metal dopants in TCOs have resulted in significant improvements in free carrier mobility in comparison to the traditional dopants. While high mobilities have been observed with a broad range of transition metal dopants, only Mo doped In_2O_3 had previously been investigated to the point of understanding the mechanism behind the improved mobilities. Two possible explanations for the improved mobility have been presented. First in 2015 a phenomena described as 'remote screening' was suggested [168]. This suggested that as the donating *d* orbitals were well above the CBM, conduction band electrons did not travel through the Mo states and as such were not scattered by them. In 2019 Swallow et al. suggested a that the donor states being higher in the conduction band reduced mixing of the host states and the donor states resulting in a lower effective mass [75].

It was noted that a group of elements often neglected in the search for optimal dopants was the f-block elements, also called the lanthanides and actinides. All actinides could be immediately ruled out being either radioactive or not existing naturally within the Earth's crust. For cation doping in In_2O_3 an element stable in the 4+ oxidation state is required and as such only one candidate was found among the lanthanides, cerium. The only stable oxidation state of the other lanthanides is 3+ due to lanthanide contractions preventing the removal of further electrons. Ce has a half full f orbital in the 4+ oxidation state allowing for its stability in this state.

Some work had been previously performed investigating Ce doping of In_2O_3. This work had shown Ce doped In_2O_3, ICO, to display high mobilities of greater than 100 $cm^2V^{-1}s^{-1}$ but carrier concentrations appeared to be limitted to 2×10^{20} cm^{-3} or lower. In Chapter 5, the behaviour of Ce as a dopant in In_2O_3 was investigated through a combination of experimental techniques and DFT calculations.

Three ICO thin films with different doping concentrations, deposited by rapid plasma deposition, were investigated. Trends in the Fermi level position and plasma frequency as a function of carrier concentration showed the films to have a band-edge carrier effective mass of $0.23m_0$. In comparison Sn doped In_2O_3 has been reported to display carrier effective masses of around $0.40m_0$ and $0.22m_0$ in Mo doped In_2O_3. DFT calculations of the band structure of ICO found that the donating f-states sit 1.5 eV above the CBM. Combined, these experimental and theoretical results suggest that Ce behaves in a similar way to Mo in In_2O_3 with the difference being that donating orbitals are f-states rather than d-states. The f-states are well above the CBM, and are of such different shapes to the host p-states that dominate the conduction band, so mixing between the dopant states and host conduction band is minimal. As such, the shape of the host conduction band is maintained allowing for a low effective mass and higher mobilities. Dopants that display this behaviour have been dubbed 'resonant dopants'. [75, 218, 242]

HAXPES spectra observing the Ce 3d states showed that Ce was present in both the 3+ and the 4 + oxidation state. The percentage of the Ce in the 3+ oxidation state increased with increased Ce content. Defect formation energy calculations for the system showed that substitutional Ce on an In site showed a transition from donor to neutral defect for Fermi levels around 0.1 eV above the CBM. This transition represents the preferred oxidation state of the substitutional Ce changing from 4+ to 3+. This suggests that at high doping densities Ce incorporates as a neutral substitutional defect rather than a dopant. This is likely the reason that the carrier concentration reported in ICO seem to be limited to around 2×10^{20} cm^{-3}. As a result, while Ce doped In_2O_3 displays high mobilities, it is unable to achieve resistivities lower than those displayed in the best ITO thin films.

One area in which ICO is superior to ITO thin films is in infra-red transparency, meaning that despite not improving on the electrical properties it may still have applications in some areas such as photovoltaics.

Even with these resonant dopants, the main issue presented by In_2O_3-based TCOs is the

scarcity and cost of In which changing the dopant had no impact on. Therefore, the next logical step was to try and identify a resonant dopant in a non In_2O_3-based TCO. Chapter 6 aimed to do this for SnO_2 as F doped SnO_2, FTO, is the current standard choice of TCO for wide area application where ITO would be too expensive.

Based on the observation made in In_2O_3 systems, the candidates for resonant dopants are transition metals or lanthanides in the correct oxidation state. For SnO_2, the correct oxidation state for cation doping is 5+. No lanthanides are stable in this oxidation state and only 4 transition metals are. Of these 4, three could be immediately eliminated as candidates. Db is radioactive while previous work into V and Nb doping of SnO_2 showed that the dopant states sat within the bandgap and are therefore definitely not resonant. This meant that the only remaining candidate was Ta.

Previous work into Ta doped SnO_2, TaTO, has shown mixed results. Some films have displayed mobilities up to 83 $cm^2V^{-1}s^{-1}$ with carrier concentrations > but other reported mobilities often fail to surpass those observed in FTO [200]. Comparisons between TaTO and Sb doped SnO_2, ATO, the traditional cation doped SnO_2 system, have shown higher mobilities.

Chapter 6 compared 5 TaTO and 5 ATO films deposited by aerosol assisted chemical vapour deposition with varied carrier concentrations. The Ta doped films displayed mobilities around 50% higher than those displayed by the Sb doped films at similar carrier concentrations. Fermi level positions extracted from HAXPES measurements plotted as a function of carrier concentration revealed the TaTO films to have a carrier effective mass of 0.23 m_0 and that the ATO films have one of $0.29 m_0$. This difference supports Ta being a resonant dopant in SnO_2.

DFT calculated band structures further supported this as it shows that the Ta d states sit 2.47 eV above the CBM while similar calculation for Sb doped SnO_2 showed the dopant states mixing with the CBM. Defect formation energy calculations showed a transition from the dopant state to an acceptor state for a Fermi energy about 0.5 eV above the CBM. The carrier concentrations observed in TaTO films, those presented here and in the literature, rarely exceed 4×10^{20} cm^{-3}. These observations combined suggest that this transition is pinning the Fermi level due to self compensation by the substitutional Ta.

As Sb and F have already been observed to be similarly limited by self compensation mechanisms it seems likely that SnO_2 will fail to reach carrier concentrations comparable to those seen in ITO and some other In_2O_3-based TCOs. While dopants in In_2O_3 also have transitions into neutral or acceptor charge states these generally occur for much higher Fermi energies. This is likely due to the wider band-gap of SnO_2 meaning that the CBM is at a higher energy rather than the pinning points being at lower energy. In this regard the forbidden transition from the VBM to CBM observed in In_2O_3 is beneficial as it allows for transparency while keeping the CBM energetically lower compared to the pinning points. Based on this, the high carrier concentration observed in ITO may never be achieved in SnO_2-based TCOs. As such, improving the mobility by optimising Ta doping is the best route to improving their conductivity.

Significant optimisation is still required however as the the majority of TaTO films reported here and in the literature have mobilities of 30 $cm^2V^{-1}s^{-1}$ or lower, much lower than the reported peak mobility of 83 $cm^2V^{-1}s^{-1}$ for carrier concentrations >1×10.

As previously stated, despite at best matching the electrical properties of traditionally doped TCOs, one area where these resonantly TCOs have been shown to be consistently superior is infra-red transparency. This is attributed to the films having lower plasma frequencies at comparable resistivities. However, initial consideration of the relationships between band-edge effective mass, mobility, carrier concentration and plasma frequency make it seem unintuitive for this to be the case. In chapter 7 scattering modelling was performed to calculate the scattering dependent mobility limit for different band-edge effective masses. Using these calculated mobilities it was shown that higher plasma frequencies are expected for higher effective masses at comparable resistivities, in good agreement with experimental observations.

With the improved infra-red transparency explained, an attempt to quantify the potential benefits was made. Utilising the transfer matrix method, films with consistent properties other than having different effective masses were modelled. These similarly showed that the main difference that arises from differences in effective masses is infra-red transparency.

One of the main applications where infra-red transparency is of importance is photovoltaics as absorbers tend to utilise the near infra-red region of light to some degree. To quantify the potential impact of resonantly doped TCOs a new parameter dubbed 'optical suitability' was defined. This assigns a value to a pairing of transparent electrode and photovoltaic absorber. It accounts for the bandgap of the absorber, the solar spectrum and the transmission spectrum of the TCO.

This newly defined quantity found that the improved IR transparency meant that the resonantly doped TCOs were beneficial for narrow bandgap solar absorbers but in the case of wider bandgap materials minor features in the transmission spectra, such as interference fringes, had a greater impact. Based on the modelled transmission spectra, a selection criterion for transparent electrodes was suggested, that the plasma frequency was of lower energy than the absorbers bandgap. In cases where this criterion is not fulfilled, the optical losses in the near infra-red can be expected to have a negative impact on the device efficiency. One are where this could be expected to be of importance is tandem solar cells where multiple absorbers are utilised. The band gaps of the narrow bandgap absorbers utilised in such devices fall consistently below the plasma frequencies of traditionally doped TCOs. Zr doped In_2O_3, a likely resonantly doped system, has already been shown to have significantly improved the efficiency of silicon perovskite tandem solar cells.

8.2 Future Work

While an understanding of how resonant dopants behave and what their potential benefits are has been developed, there are several avenues which further work on the subject could follow.

In In_2O_3 there are many potential transition metal dopants which are likely resonant. Hf, Zr, Ti and W all have been use to doped In_2O_3 and material doped with these elements have displayed mobilities >80 $cm^2V^{-1}s^{-1}$ with carrier concentrations >1×10^{20} cm^{-3}. Based on these high mobilities, in combination with their position in the periodic table, it seems likely that these dopants are resonant. However, experimental work is required to confirm this. Similar experiments to those used to obtain the effective masses of IMO, ICO or TaTO could be used, measuring the Fermi level position or plasma frequency as a function of carrier concentration and fitting the data with a model. Zr doped In_2O_3, IZrO, is of particular interest as it has displayed the highest mobilities of any In_2O_3-based TCO other than IMO and has already been used to improve the efficiency of some photovoltaic devices.

It appears that potential dopants in SnO_2 have now been exhausted and while Ta doping has shown great promise further work is required to optimise its fabrication to consistently achieve its best optoelectric properties. One observation made in chapter 6 was that there appeared to be a trend between mobility and the orientation of SnO_2. Films with a greater preference towards the (100) orientation seemed to display higher mobilities. This was observed for films both investigated in this work and reports in the literature with the highest mobility films having an almost purely (100) orientation. An investigation into the impact of orientation on the carrier mobility in TaTO would be the logical first step in optimisation of the material and quantifying the impact of the resonant nature of dopant in comparison to the impact of orientation. SnO_2 has an anisotropic crystal structure so orientation having an impact seems likely.

Of the three commonly used host materials for TCOs, ZnO has not been investigated in this thesis. An attempt to a resonat dopant in ZnO has yet to be made. For cation doping of ZnO an element in the 3+ oxidation state is required. A wide range of transition metals are stable in this oxidation state including Sc, Y, Cr, Fe, Ru, Co, Rh, Ir and Au. While attempts to dope ZnO with many of these elements have been made they have generally been for non TCO applications such as LEDs or gas sensors. [243–247] An exception to this is Sc doped ZnO, attempts to use this material as a transparent conductor has been made but mobilities reported have been lower than those achieved by doping with Al or Ga. [248] Further investigation into these elements as potential resonant dopants in ZnO is needed, with such a wide range of candidates, a theoretical screening is likely the best approach to begin with to exclude those where the donor state lies close to or below the conduction band similarly to V or Nb in SnO_2. This would also identify those which would not incorporate in the correct oxidation state as several, such as Fe or Co, are also stable in other oxidation states. Another avenue to consider is lanthenide doping of ZnO as all the lanthanides are stable in the 3+ oxidation state, mostly exclusively. Similar to the transition metals what work that has been performed into lanthenide doping of ZnO has been for purposes

other than transparent conductors such as photocatalysts. With such a broad range of potential resonant dopants in ZnO with minimal research investigating them, there is clearly a lot of potential for further improvements on AZO or GZO if significant work is performed looking into them.

Finally, the area in which the improved infra-red transparency achieved with resonant dopants has the greatest potential impact is photovoltaics. Integrating these materials into actual photovoltaic devices and experimentally showing the impact would be the next step in demonstrating this. Considerations other than the transmission spectra are required for transparent electrodes, such as band alignment, so confirming that the resonant dopants have no other impacts that could negatively impact device efficiency is necessary. The resonantly doped In_2O_3-based TCOs would be the best candidates for such an investigation as Ta doped SnO_2 requires further optimisation and significant work is required to identify a resonant dopant in ZnO.

Currently it is clear that resonant doping is a route to creating TCOs with higher carrier mobilities and improved infra-red transparency and that these could have a positive impact on photovoltaic device efficiency. However, there is plenty of work to still be performed in optimising these materials, identifying other potential resonant dopants and to incorporate them into photovoltaic devices.

BIBLIOGRAPHY

[1] B. A. D. Williamson, T. J. Featherstone, S. S. Sathasivam, J. E. N. Swallow, H. Shiel, L. A. H. Jones, M. J. Smiles, A. Regoutz, T. Lee, X. Xia, C. Blackman, P. K. Thakur, C. J. Carmalt, I. P. Parkin, T. D. Veal, and D. O. Scanlon.
Resonant Ta doping for enhanced mobility in transparent conducting SnO_2.
Chemistry of Materials, 32(5):1964–1973, 2020.

[2] T. J. Featherstone, J. Willis, J. E. N. Swallow, B. A. D. Williams, L. A. H. Jones, T. Lee, P. K. Thakur, G. W. Watson, T. Koida, D. O. Scanlon, and T. D. Veal.
Resonant Ce doping for high-mobility In_2O_3-based conductors with enhanced near-infrared transparency.
Submitted to Advanced Functional Materials.

[3] T. J. Featherstone, J. E. N. Swallow, and T. D. Veal.
Mechanism of enhanced infra-red transparency in resonantly doped TCOs.
In Preparation.

[4] A. Stadler.
Transparent conducting oxides—an up-to-date overview.
Materials, 5(4):661–683, 2012.

[5] S. C. Dixon, D. O. Scanlon, C. J. Carmalt, and I. P. Parkin.
n-type doped transparent conducting binary oxides: an overview.
J. Mater. Chem. C, 4:6946–6961, 2016.

[6] H. Hosono.
Recent progress in transparent oxide semiconductors: Materials and device application.
Thin Solid Films, 515(15):6000 – 6014, 2007.
Proceedings of Sympodium O on Thin Film Chalcogenide Photovoltaic Materials, EMRS 2006 Conference.

[7] K. Bädeker.
über die elektrische leitfhigkeit und die thermoelektrische kraft einiger schwermetallverbindungen.
Annalen der Physik, 327(4):749–766, 1907.

[8] M. Grundmann.
Karl Bädeker (1877–1914) and the discovery of transparent conductive materials.
physica status solidi (a), 212(7):1409–1426, 2015.

[9] P. H. Jefferson, S. A. Hatfield, T. D. Veal, P. D. C. King, C. F. McConville, J. Zúñiga–Pérez, and V. Muñoz–Sanjosé.
Bandgap and effective mass of epitaxial cadmium oxide.
Applied Physics Letters, 92(2):022101, 2008.

[10] D. S. Ginley.
Handbook of Transparent Conductors.
Springer US, 2010.

[11] M. M. Aliyu, S. Hossain, J. Husna, N. Dhar, M. Q. Huda, K. Sopian, and N. Amin.
High quality indium tin oxide (ITO) film growth by controlling pressure in RF magnetron sputtering.
In *2012 38th IEEE Photovoltaic Specialists Conference*, pages 002009–002013, June 2012.

[12] T. Minami.
New n-type transparent conducting oxides.
MRS Bulletin, 25(8):38–44, 2000.

[13] L. Lian, X. Xi, D. Dong, and G. He.
Highly conductive silver nanowire transparent electrode by selective welding for organic light emitting diode.
Organic Electronics, 60:9 – 15, 2018.

[14] J. L. Stoner, P. A. E. Murgatroyd, M. O'Sullivan, M. S. Dyer, T. D. Manning, J. B. Claridge, M. J. Rosseinsky, and J. Alaria.
Chemical control of correlated metals as transparent conductors.
Advanced Functional Materials, 29(11):1808609, 2019.

[15] S. A. Holgate.
Understanding Solid State Physics.
CRC Press, 2009.

[16] C. Kittel.
Introduction to Solid State Physics.
Wiley, 8th edition, 2004.

[17] P. Hofmann.
Solid State Physics : An Introduction, pages 132–155.
John Wiley & Sons, Incorporated, 2nd edition, 2015.

[18] S. S. Li.
Semiconductor Physical Electronics, pages 183–211.
Springer US, Boston, MA, 1993.

[19] P. Y. Yu and M. Cardona.
Fundementals of Semiconductors.
Springer, 1976.

[20] D. K. Schroder.
Semiconductor material and device characterization, pages 1–59.
IEEE Press, 3rd edition, 2006.

[21] T. S. Moss.
The interpretation of the properties of indium antimonide.
Proceedings of the Physical Society. Section B, 67(10):775–782, oct 1954.

[22] E. Burstein.
Anomalous optical absorption limit in InSb.
Phys. Rev., 93:632–633, Feb 1954.

[23] A. Luque and S. Hegedue.
Handbook of Photovoltaic Science and Engineering.
John Wiley & Sons, 2nd edition, 1972.

[24] F. Wooten.
Optical Properties of Solids.
Imperial College Press, 1st edition, 1972.

[25] J. Nelson.
The Physics of Solar Cells.
Imperial College Press, 2003.

[26] Solar spectral irradiance: Air mass 1.5.
https://rredc.nrel.gov/solar//spectra/am1.5/.
Accessed: 09/10/2019.

[27] ASTM G173−03(2012).
Standard Tables for Reference Solar Spectral Irradiances: Direct Normal and Hemispherical on 37° Tilted Surface.
ASTM International, West Conshohocken PA, 2012.

[28] W. Shockley and H. J. Queisser.
Detailed balance limit of efficiency of p-n junction solar cells.
Journal of Applied Physics, 32(3):510–519, 1961.

[29] S. Rühle.
Tabulated values of the Shockley–Queisser limit for single junction solar cells.
Solar Energy, 130:139 – 147, 2016.

[30] J. Britt and C. Ferekides.
Thin-film CdS/CdTe solar cell with 15.8% efficiency.
Applied Physics Letters, 62(22):2851–2852, 1993.

[31] M. Gloeckler and J.R. Sites.
Efficiency limitations for wide-band-gap chalcopyrite solar cells.
Thin Solid Films, 480-481:241 – 245, 2005.
EMRS 2004.

[32] D. Huang and C. Persson.
Band gap change induced by defect complexes in Cu_2ZnSnS_4.
Thin Solid Films, 535:265 – 269, 2013.

[33] M. Birkett, W. M. Linhart, J. Stoner, L. J. Phillips, K. Durose, J. Alaria, J. D. Major, R. Kudrawiec, and T. D. Veal.
Band gap temperature-dependence of close-space sublimation grown Sb_2Se_3 by photo-reflectance.
APL Materials, 6(8):084901, 2018.

[34] T. G. Allen, J. Bullock, X. Yang, A. Javey, and S. De Wolf.
Passivating contacts for crystalline silicon solar cells.
Nature Energy, 4.

[35] S. Braun, G. Hahn, R. Nissler, C. Pönisch, and D. Habermann.
The multi-busbar design: An overview.
Energy Procedia, 43:86 – 92, 2013.
Proceedings of the Fourth Workshop on Metallization for Crystalline Silicon Solar Cells.

[36] O. Lang, C. Pettenkofer, J. F. Sánchez Royo, A. Segura, A. Klein, and W. Jaegermann.
Thin film growth and band lineup of In_2O_3 on the layered semiconductor InSe.
Journal of Applied Physics, 86(10):5687–5691, 11 1999.

[37] K. T. Butler, J. Buckeridge, C. Richard A. Catlow, and A. Walsh.
Crystal electron binding energy and surface work function control of tin dioxide.
Phys. Rev. B, 89:115320, Mar 2014.

[38] A. M. Ganose and D. O. Scanlon.
Band gap and work function tailoring of sno2 for improved transparent conducting ability in photovoltaics.

J. Mater. Chem. C, 4:1467–1475, 2016.

[39] M. Leszczyński, E. Litwin-Staszewska, and T. Suski.
Lattice constant of doped semiconductor.
Acta Physica Polonica A, 88(5):837–840, 1995.

[40] K. Persson.
Materials data on In_2O_3 (sg:206) by materials project, 11 2014.
(https://materialsproject.org/materials/mp-22598/) Accessed 21/10/2019.

[41] K. Persson.
Materials data on SnO_2 (sg:136) by materials project, 7 2014.
(https://materialsproject.org/materials/mp-856/) Accessed 21/10/2019.

[42] K. Persson.
Materials data on ZnO (sg:186) by materials project, 11 2014.
(https://materialsproject.org/materials/mp-2133/) Accessed 21/10/2019.

[43] K. H. L. Zhang, D.J. Payne, R. G. Palgrave, V. K. Lazarov, W. Chen, A. T. S. Wee, C. F. McConville, P. D. C. King, T. D. Veal, G. Panaccione, P. Lacovig, and R. G. Egdell.
Surface structure and electronic properties of In_2O_3(111) single-crystal thin films grown on y-stabilized ZrO_2(111).
Chemistry of Materials, 21(19):4353–4355, 2009.

[44] A. Gurlo, P. Kroll, and R. Riedel.
Metastability of corundum-type In_2O_3.
Chemistry – A European Journal, 14(11):3306–3310, 2008.

[45] M. Marezio.
Refinement of the crystal structure of In_2O_3 at two wavelengths.
Acta Crystallographica, 20(6):723–728, Jun 1966.

[46] Y. Shigesato, Y. Hayashi, and T. Haranoh.
Doping mechanisms of tin-doped indium oxide films.
Applied Physics Letters, 61(1):73–75, 1992.

[47] M. Thirumoorthi and J. T. J. Prakash.
Structure, optical and electrical properties of indium tin oxide ultra thin films prepared by jet nebulizer spray pyrolysis technique.
Journal of Asian Ceramic Societies, 4(1):124 – 132, 2016.

[48] A. Walsh, J. L. F. Da Silva, S.i Wei, C. Körber, A. Klein, L. F. J. Piper, A. DeMasi, K. E. Smith, G. Panaccione, P. Torelli, D. J. Payne, A. Bourlange, and R. G. Egdell.

Nature of the band gap of In_2O_3 revealed by first-principles calculations and x-ray spectroscopy.
Phys. Rev. Lett., 100:167402, Apr 2008.

[49] P. D. C. King, T. D. Veal, F. Fuchs, Ch. Y. Wang, D. J. Payne, A. Bourlange, H. Zhang, G. R. Bell, V. Cimalla, O. Ambacher, R. G. Egdell, F. Bechstedt, and C. F. McConville.
Band gap, electronic structure, and surface electron accumulation of cubic and rhombohedral in_2o_3.
Phys. Rev. B, 79:205211, May 2009.

[50] T. Maruyama and K. Fukui.
Fluorine-doped indium oxide thin films prepared by chemical vapor deposition.
Japanese Journal of Applied Physics, 29(Part 2, No. 9):L1705–L1707, sep 1990.

[51] G.G. Untila, T.N. Kost, and A.B. Chebotareva.
Fluorine- and tin-doped indium oxide films grown by ultrasonic spray pyrolysis: Characterization and application in bifacial silicon concentrator solar cells.
Solar Energy, 159:173 – 185, 2018.

[52] T. Maruyama and T. Nakai.
Fluorine-doped indium oxide thin films prepared by chemical vapor deposition.
Journal of Applied Physics, 71(6):2915–2917, 1992.

[53] P. A Cox.
The Elements: Their Origin, Abundance, and Distribution.
Oxford University Press, 1989.

[54] D. Ginley.
8 - hybrid multifunctional transparent conductors.
In *Advanced Micro- and Nanomaterials for Photovoltaics*, pages 175 – 194. Elsevier, 2019.

[55] Z. M. Jarzebski and J. P. Marton.
Physical properties of SnO_2 materials 1. preparation and defect structure.
Journal of The Eletrocehemical Sociert, 123(7):199c–205c, 1976.

[56] J. E. N. Swallow, B. A. D. Williamson, T. J. Whittles, M. Birkett, T. J. Featherstone, N. Peng, A. Abbott, M. Farnworth, K. J. Cheetham, P. Warren, D. O. Scanlon, V. R. Dhanak, and T. D. Veal.
Self-compensation in transparent conducting F-doped SnO_2.
Advanced Functional Materials, page 1701900, 2018.

[57] M. E. White, O. Bierwagen, M. Y. Tsai, and J. S. Speck.

Electron transport properties of antimony doped SnO_2 single crystalline thin films grown by plasma-assisted molecular beam epitaxy.
Journal of Applied Physics, 106(9):093704, 2009.

[58] C. D. Canestrar, M. M. Oliveira, R. Valaski, M.V.S. da Silva, D.G.F. David, I. Pepe, A. F. da Silva, L.S. Roman, and C. Persson.
Strong inter-conduction-band absorption in heavily fluorine doped tin oxide.
Applied Surface Science, 255(5, Part 1):1874 – 1879, 2008.

[59] M. Fantini and I. Torriani.
The compositional and structural properties of sprayed SnO_2:F thin films.
Thin Solid Films, 138(2):255 – 265, 1986.

[60] E. Elangovan and K. Ramamurthi.
A study on low cost-high conducting fluorine and antimony-doped tin oxide thin films.
Applied Surface Science, 249(1):183 – 196, 2005.

[61] F. J. Berry and B. J. Laundy.
Antimony-121 mössbauer study of the effects of calcination on the structure of tin–antimony oxides.
J. Chem. Soc., Dalton Trans., (6):1442–1444, 1981.

[62] C. Terrier, J.P. Chatelon, J.A. Roger, R. Berjoan, and C. Dubois.
Analysis of antimony doping in tin oxide thin films obtained by the sol-gel method.
Journal of Sol-Gel Science and Technology, 10(1):75–81, 1997.

[63] B. Gržeta, E. Tkalčec, C. Goebbert, M. Takeda, M. Takahashi, K Nomura, and M Jakšić.
Structural studies of nanocrystalline SnO_2 doped with antimony: XRD and mössbauer spectroscopy.
Journal of Physics and Chemistry of Solids, 63(5):765–772, 2002.

[64] F. Montilla, E. Morallon, A. De Battisti, S. Barison, S. Daolio, and J.L. Vazquez.
Preparation and characterization of antimony-doped tin dioxide electrodes. 3. XPS and SIMS characterization.
J. Phys. Chem. B, 108:15976–15981, 2004.

[65] C. Chen, F. Wang, S. Chang, and C. Yang.
Using oxygen plasma pretreatment to enhance the properties of F-doped ZnO films prepared on polyimide substrates.
Materials, 11(9):1501, Aug 2018.

[66] Y. Ammaih, B. Hartiti, A. Ridah, A. Lfakir, B. Marí Soucase, and P. Thevenin.

Effect of F-doping on structural, electrical, and optical properties of ZnO thin films for optoelectronic application.
In *2016 International Renewable and Sustainable Energy Conference (IRSEC)*, pages 208–211, Nov 2016.

[67] K. Ellmer.
Resistivity of polycrystalline zinc oxide films: current status and physical limit.
Journal of Physics D: Applied Physics, 34(21):3097–3108, oct 2001.

[68] C. Moditswe, C. M. Muiva, and A. Juma.
Highly conductive and transparent ga-doped zno thin films deposited by chemical spray pyrolysis.
Optik, 127(20):8317 – 8325, 2016.

[69] J. Nomoto, M. Konagai, K. Okada, T. Ito, T. Miyata, and T. Minami.
Comparative study of resistivity characteristics between transparent conducting AZO and GZO thin films for use at high temperatures.
Thin Solid Films, 518(11):2937 – 2940, 2010.

[70] Jiazhen Sheng, TaeHyun Hong, Hyun-Mo Lee, KyoungRok Kim, Masato Sasase, Junghwan Kim, Hideo Hosono, and Jin-Seong Park.
Amorphous IGZO TFT with high mobility of ~70 cm^2/(v s) via vertical dimension control using peald.
ACS Applied Materials & Interfaces, 11(43):40300–40309, 2019.
PMID: 31584254.

[71] Kenji Nomura, Hiromichi Ohta, Akihiro Takagi, Toshio Kamiya, Masahiro Hirano, and Hideo Hosono.
Room-temperature fabrication of transparent flexible thin-film transistors using amorphous oxide semiconductors.
Nature, 432(7016):488–492, Nov 2004.

[72] Antoine Kahn.
Fermi level, work function and vacuum level.
Mater. Horiz., 3:7–10, 2016.

[73] P. D. C. King, R. L. Lichti, Y. G. Celebi, J. M. Gil, R. C. Vilão, H. V. Alberto, J. Piroto Duarte, D. J. Payne, R. G. Egdell, I. McKenzie, C. F. McConville, S. F. J. Cox, and T. D. Veal.
Shallow donor state of hydrogen in in_2o_3 and sno_2: Implications for conductivity in transparent conducting oxides.
Phys. Rev. B, 80:081201, Aug 2009.

[74] Barbara Falabretti and John Robertson.
Electronic structures and doping of sno2, cualo2, and cuino2.
Journal of Applied Physics, 102(12):123703, 2007.

[75] Jack E. N. Swallow, Benjamin A. D. Williamson, Sanjayan Sathasivam, Max Birkett, Thomas J. Featherstone, Philip A. E. Murgatroyd, Holly J. Edwards, Zachary W. Lebens-Higgins, David A. Duncan, Mark Farnworth, Paul Warren, Nianhua Peng, Tien-Lin Lee, Louis F. J. Piper, Anna Regoutz, Claire J. Carmalt, Ivan P. Parkin, Vin R. Dhanak, David O. Scanlon, and Tim D. Veal.
Resonant doping for high mobility transparent conductors: the case of Mo-doped In_2O_3.
Mater. Horiz., 7:236–243, 2020.

[76] W Shan, K M Yu, W Walukiewicz, J Wu, J W Ager, and E E Haller.
Band anticrossing in dilute nitrides.
Journal of Physics: Condensed Matter, 16(31):S3355–S3372, jul 2004.

[77] Y. G. Bi, Y. F. Liu, X. L. Zhang, D. Yin, W. Q. Wang, J. Feng, and H. B. Sun.
Ultrathin metal films as the transparent electrode in ITO-free organic optoelectronic devices.
Advanced Optical Materials, 7(6):1800778, 2019.

[78] C. Guillén and J. Herrero.
TCO/metal/TCO structures for energy and flexible electronics.
Thin Solid Films, 520(1):1 – 17, 2011.

[79] J. Yun.
Ultrathin metal films for transparent electrodes of flexible optoelectronic devices.
Advanced Functional Materials, 27(18):1606641, 2017.

[80] G. Ding and C. Clavero.
Silver-based low-emissivity coating technology for energy- saving window applications.
In Nikolay N. Nikitenkov, editor, *Modern Technologies for Creating the Thin-film Systems and Coatings*, chapter 20. IntechOpen, Rijeka, 2017.

[81] S. Zhu, S. Yuan, and G. C. A. M. Janssen.
Optical transmittance of multilayer graphene.
Europhysics Letters, 108(1):17007, sep 2014.

[82] A. K. Geim and K. S. Novoselov.
The rise of graphene.
Nature Materials, 6(3):183–191, 2007.

[83] J.-H. Chen, C. Jang, S. Xiao, M. Ishigami, and M. S. Fuhrer.
Intrinsic and extrinsic performance limits of graphene devices on SiO_2.
Nature Nanotechnology, 3(4):206–209, 2008.

[84] J. Wang, S. Deng, Z. Liu, and Z. Liu.
The rare two-dimensional materials with Dirac cones.
National Science Review, 2(1):22–39, 01 2015.

[85] I. Khrapach, F. Withers, T. H. Bointon, D. K. Polyushkin, W. L. Barnes, S. Russo, and M. F. Craciun.
Novel highly conductive and transparent graphene-based conductors.
Advanced Materials, 24(21):2844–2849, 2012.

[86] G. Eda, G. Fanchini, and M. Chhowalla.
Large-area ultrathin films of reduced graphene oxide as a transparent and flexible electronic material.
Nature Nanotechnology, 3(5):270–274, 2008.

[87] R. S. Datta, N. Syed, A. Zavabeti, M. Jannat, A.and Mohiuddin, M. Rokunuzzaman, B. Yue Zhang, M. A. Rahman, P. Atkin, K. A. Messalea, M. B. Ghasemian, E. D. Gaspera, S. Bhattacharyya, M. S. Fuhrer, S. P. Russo, C. F. McConville, D. Esrafilzadeh, K. Kalantar-Zadeh, and T. Daeneke.
Flexible two-dimensional indium tin oxide fabricated using a liquid metal printing technique.
Nature Electronics, 3(1):51–58, Jan 2020.

[88] S. Iijima and T. Ichihashi.
Single-shell carbon nanotubes of 1-nm diameter.
Nature, 363(6430):603–605, 1993.

[89] S. Iijima.
Helical microtubules of graphitic carbon.
Nature, 354(6348):56–58, 1991.

[90] S. Jiang, P. Hou, M. L. Chen, B. W. Wang, D. M. Sun, D. M. Tang, Q. Jin, Q. X. Guo, D. D. Zhang, J. H. Du, K. P. Tai, J. Tan, E. I. Kauppinen, C. Liu, and H. M. Cheng.
Ultrahigh-performance transparent conductive films of carbon-welded isolated single-wall carbon nanotubes.
Science Advances, 4(5):eaap9264, 2018.

[91] L. Zhang, Y. Zhou, L. Guo, W. Zhao, A. Barnes, H. Zhang, C. Eaton, Y. Zheng, M. Brahlek, H. F. Haneef, N. J. Podraza, M. H. W. Chan, V. Gopalan, K. M. Rabe, and R. Engel-Herbert.

Correlated metals as transparent conductors.
Nature Materials, 15(2):204–210, Feb 2016.

[92] M. Imada, A. Fujimori, and Y. Tokura.
Metal-insulator transitions.
Rev. Mod. Phys., 70:1039–1263, Oct 1998.

[93] E. Fortunato, P. Barquinha, and R. Martins.
Oxide semiconductor thin-film transistors: A review of recent advances.
Advanced Materials, 24(22):2945–2986, 2012.

[94] D. O. Scanlon and G. W. Watson.
On the possibility of p-type SnO_2.
J. Mater. Chem., 22:25236–25245, 2012.

[95] B. A. D. Williamson, J. Buckeridge, S. Brown, J.and Ansbro, R. G. Palgrave, and D. O. Scanlon.
Engineering valence band dispersion for high mobility p-type semiconductors.
Chemistry of Materials, 29(6):2402–2413, 2017.

[96] K. H. L. Zhang, K. Xi, M. G. Blamire, and R. G. Egdell.
P-type transparent conducting oxides.
Journal of Physics: Condensed Matter, 28(38):383002, jul 2016.

[97] N. Zhang, J. Sun, and H. Gong.
Transparent p-type semiconductors: Copper-based oxides and oxychalcogenides.
Coatings, 9(2):9020137, 2019.

[98] A. N. Fioretti and M. Morales-Masis.
Bridging the p-type transparent conductive materials gap: synthesis approaches for disperse valence band materials.
Journal of Photonics for Energy, 10(4):1 – 17, 2020.

[99] M. Wang, H. Wei, Y. Wu, C. Yang, P. Han, F. Juan, Y. Chen, F. Xu, and B. Cao.
Highly transparent and conductive γ-CuI films grown by simply dipping copper films into iodine solution.
Physica B: Condensed Matter, 573:45 – 48, 2019.

[100] M. Cota-Leal, D. Cabrera-German, M. Sotelo-Lerma, M. Martínez-Gil, and J.A. García-Valenzuela.
Highly-transparent and conductive CuI films obtained by a redirected low-cost and electroless two-step route: Chemical solution deposition of CuS_2 and subsequent iodination.
Materials Science in Semiconductor Processing, 95:59 – 67, 2019.

[101] C. Yang, M. Kneiß, M. Lorenz, and M. Grundmann.
Room-temperature synthesized copper iodide thin film as degenerate p-type transparent conductor with a boosted figure of merit.
Proceedings of the National Academy of Sciences, 113(46):12929–12933, 2016.

[102] M. Grundmann, F. Schein, M. Lorenz, T. Böntgen, J. Lenzner, and H. von Wenckstern.
Cuprous iodide – a p-type transparent semiconductor: history and novel applications.
physica status solidi (a), 210(9):1671–1703, 2013.

[103] X. Dai, H. Lei, C. Chen, Y. Guo, and G. Fang.
A simple synthesis of transparent and highly conducting p-type $Cu_xAl_{1-x}S_y$ nanocomposite thin films as the hole transporting layer for organic solar cells.
RSC Adv., 8:16887–16896, 2018.

[104] S. K. Maurya, Y. Liu, X. Xu, R. Woods-Robinson, C. Das, J. W. Ager, and K. R. Balasubramaniam.
High figure-of-merit p-type transparent conductor, Cu alloyed ZnS via radio frequency magnetron sputtering.
Journal of Physics D: Applied Physics, 50(50):505107, nov 2017.

[105] A. Kasic, M. Schubert, S. Einfeldt, D. Hommel, and T. E. Tiwald.
Free-carrier and phonon properties of n- and p-type hexagonal gan films measured by infrared ellipsometry.
Phys. Rev. B, 62:7365–7377, Sep 2000.

[106] K. H. Rieder, M. Ishigame, and L. Genzel.
Infrared absorption by coupled surface-phonon-surface-plasmon modes in microcrystals of CdO.
Phys. Rev. B, 6:3804–3810, Nov 1972.

[107] Charalambos C. Katsidis and Dimitrios I. Siapkas.
General transfer-matrix method for optical multilayer systems with coherent, partially coherent, and incoherent interference.
Appl. Opt., 41(19):3978–3987, Jul 2002.

[108] M. Born and E. Wolf.
Principles of Optics.
Cambridge University Press, 1975.

[109] Jun Hyuk Park, Dong Yeong Kim, E. Fred Schubert, Jaehee Cho, and Jong Kyu Kim.
Fundamental limitations of wide-bandgap semiconductors for light-emitting diodes.
ACS Energy Letters, 3(3):655–662, 2018.

[110] B. K. Ridley.
Quantum Processes in Semiconductor.
Oxford University Press, 5th edition, 2013.

[111] N. W. Ashcroft and N. D. Mermin.
Solid State Physics.
Holt, Rinehart and Winston, 1976.

[112] C. Hamaguchi.
Basic Semiconductor Physics.
Springer-Verlag Berlin Heidelberg, 2010.

[113] E. O. Kane.
Band structure of indium antimonide.
Journal of Physics and Chemistry of Solids, 1(4):249 – 261, 1957.

[114] M.W. Prairie and R.M. Kolbas.
A general derivation of the density of states function for quantum wells and superlattices.
Superlattices and Microstructures, 7(4):269 – 277, 1990.

[115] J. Singleton.
Band Theory and Electronic Properties of Solids.
Oxford University Press, 2001.

[116] Mattis Fondell, T. Jesper Jacobsson, Mats Boman, and Tomas Edvinsson.
Optical quantum confinement in low dimensional hematite.
J. Mater. Chem. A, 2:3352–3363, 2014.

[117] T Edvinsson.
Optical quantum confinement and photocatalytic properties in two-, one- and zero-dimensional nanostructures.
R. Soc. open sci., 5:180387, 2018.

[118] E. Stern, R. Wagner, F. J. Sigworth, R. Breaker, T. M. Fahmy, and M. A. Reed.
Importance of the debye screening length on nanowire field effect transistor sensors.
Nano Letters, 7(11):3405–3409, 2007.
PMID: 17914853.

[119] K. F. Berggren and B. E. Sernelius.
Band-gap narrowing in heavily doped many-valley semiconductors.
Phys. Rev. B, 24:1971–1986, Aug 1981.

[120] K. Ellmer and R. Mientus.

Carrier transport in polycrystalline transparent conductive oxides: A comparative study of zinc oxide and indium oxide.
Thin Solid Films, 516(14):4620 – 4627, 2008.
6th International Conference on Coatings on Glass and Plastics (ICCG6)- Advanced Coatings for Large-Area or High-Volume Products-.

[121] D. C. Look, H. Lu, W. J. Schaff, J. Jasinski, and Z. Liliental-Weber.
Donor and acceptor concentrations in degenerate InN.
Applied Physics Letters, 80(2):258–260, 2002.

[122] S. Wang, S. Hui, K. Peng, T. P. Bailey, X. Zhou, X. Tang, and C. Uher.
Grain boundary scattering effects on mobilities in p-type polycrystalline SnSe.
J. Mater. Chem. C, 5:10191–10200, 2017.

[123] M. Born and K. Huang.
Dynamical Theory of Crystal Latices.
Oxford University Press, 1988.

[124] C. G. Fonstad and R. H. Rediker.
Electrical properties of high-quality stannic oxide crystals.
Journal of Applied Physics, 42(7):2911–2918, 1971.

[125] F. E. Low and D. Pines.
Mobility of slow electrons in polar crystals.
Phys. Rev., 98:414–418, Apr 1955.

[126] D. L. Dexter and F. Seitz.
Effects of dislocations on mobilities in semiconductors.
Phys. Rev., 86:964–965, Jun 1952.

[127] R. M. Martin.
Electronic Structure: Basic Theory and Practical Methods.
Cambridge University Press, 2004.

[128] D. P. Chong.
Recent Advances in Density Fucntional Methods.
World Scientific, 1995.

[129] P. J. Hasnip, K. Refson, M. I. J. Probert, J. R. Yates, S. J. Clark, and C. J. Pickard.
Density functional theory in the solid state.
Philosophical Transactions of the Royal Society A: Mathematical, Physical and Engineering Sciences, 372(2011):20130270, 2014.

[130] W. Kohn and L. J. Sham.
Self-consistent equations including exchange and correlation effects.
Phys. Rev., 140:A1133–A1138, Nov 1965.

[131] J. P. Perdew, K. Burke, and M. Ernzerhof.
Generalized gradient approximation made simple.
Phys. Rev. Lett., 77:3865–3868, Oct 1996.

[132] M. Marsman, J. Paier, A. Stroppa, and G. Kresse.
Hybrid functionals applied to extended systems.
Journal of Physics: Condensed Matter, 20(6):064201, jan 2008.

[133] L. J. van de Pauw.
A method of measuring specific resistivity and Hall effect of lamellae of arbitrary shape.
Phillips Technical Report, 20:220–224, 1958.

[134] J. Tauc.
Optical properties and electronic structure of amorphous Ge and Si.
Materials Research Bulletin, 3(1):37 – 46, 1968.

[135] E. A. Davis and N. F. Mott.
Conduction in non-crystalline systems V. conductivity, optical absorption and photoconductivity in amorphous semiconductors.
The Philosophical Magazine: A Journal of Theoretical Experimental and Applied Physics, 22(179):0903–0922, 1970.

[136] B D. Viezbicke, S. Patel, B. E. Davis, and D. P. Birnie III.
Evaluation of the Tauc method for optical absorption edge determination: ZnO thin films as a model system.
physica status solidi (b), 252(8):1700–1710, 2015.

[137] Y. Shvyd'ko.
High-Resolution X-Ray Monochromators, pages 215–286.
Springer Berlin Heidelberg, Berlin, Heidelberg, 2004.

[138] J. C. Fuggle and J. E. Inglesfield.
Unoccupied electronic states.
Springer-Verlag Berlin Heidelberg, 1st edition, 1992.

[139] C. S. Fadley.
Hard X-ray Photoemission: An Overview and Future Perspective, pages 1–34.
Springer International Publishing, Cham, 2016.

[140] S. Hofmann.
Qualitative Analysis (Principle and Spectral Interpretation), pages 43–76.
Springer Berlin Heidelberg, Berlin, Heidelberg, 2013.

[141] J. F. Moulder, W. F. Stickle, P. E. Sobel, and K. D. Bombden.
Handbook of X-ray Photoelectron Spectroscopy.
Perkin-Elmer Corporation, 1992.

[142] H. A. Bethe and E. W. Salpeter.
Quantum mechanics of one and two electron atoms.
Springer-Verlag Berlin Heidelberg, 1957.

[143] J.J. Yeh and I. Lindau.
Atomic subshell photoionization cross sections and asymmetry parameters: $1 \leqslant Z \leqslant 103$.
Atomic Data and Nuclear Data Tables, 32(1):1 – 155, 1985.

[144] J Scofield.
Theoretical photoionization cross sections from 1 to 1500 keV.
LAWRENCE LIVERMORE LABORATORY, 1973.

[145] M.B. Trzhaskocskaya, V.I. Nefedov, and V.G. Yarzhemsk.
Photoelectron angular distribution parameters for elements Z=1 to Z=54 in the photoelectron energy range 100–5000 eV.
Atomic Data and Nuclear Data Tables, 77(1):97 – 159, 2001.

[146] M.B. Trzhaskocskaya, V.I. Nefedov, and V.G. Yarzhemsky.
Photoelectron angular distribution parameters for elements Z=55 to Z=100 in the photoelectron energy range 100–5000 eV.
Atomic Data and Nuclear Data Tables, 82(2):257 – 311, 2002.

[147] M.B. Trzhaskovskaya, V.K. Nikulin, V.I. Nefedov, and V.G. Yarzhemsky.
Non-dipole second order parameters of the photoelectron angular distribution for elements Z=1–100 in the photoelectron energy range 1–10keV.
Atomic Data and Nuclear Data Tables, 92(2):245 – 304, 2006.

[148] R. T. Haasch.
X-Ray Photoelectron Spectroscopy (XPS) and Auger Electron Spectroscopy (AES), pages 93–132.
Springer New York, New York, NY, 2014.

[149] H.C. Aspinall.
Chemistry of the f-Block Elements, pages 10–20.
Advanced chemistry texts. Gordon and Breach Science Publishers, 2001.

[150] R. D. Shannon.
Revised effective ionic radii and systematic studies of interatomic distances in halides and chalcogenides.
Acta Crystallographica Section A, 32(5):751–767, 1976.

[151] S. Parthiban, E. Elangovan, K. Ramamurthi, R. Martins, and E. Fortunato.
Investigations on high visible to near infrared transparent and high mobility Mo doped In_2O_3 thin films prepared by spray pyrolysis technique.
Solar Energy Materials and Solar Cells, 94(3):406 – 412, 2010.

[152] Y. Meng, X. Yang, H. Chen, J. Shen, Y. Jiang, Z. Zhang, and Z. Hua.
A new transparent conductive thin film In_2O_3:Mo.
Thin Solid Films, 394(1):218 – 222, 2001.

[153] Y. Meng, X. Yang, H. Chen, J. Shen, Y. Jiang, Z. Zhang, and Z. Hua.
Molybdenum-doped indium oxide transparent conductive thin films.
Journal of Vacuum Science & Technology A, 20(1):288–290, 2002.

[154] R. Bel Hadj Tahar, T. Ban, Y. Ohya, and Y. Takahashi.
Tin doped indium oxide thin films: Electrical properties.
Journal of Applied Physics, 83(5):2631–2645, 1998.

[155] Mamoru M.
Electrical properties of vacuum-deposited indium oxide and indium tin oxide films.
Thin Solid Films, 70(1):91 – 100, 1980.

[156] H. Kim, C. M. Gilmore, A. Piqué, J. S. Horwitz, H. Mattoussi, H. Murata, Z. H. Kafafi, and D. B. Chrisey.
Electrical, optical, and structural properties of indium–tin–oxide thin films for organic light-emitting devices.
Journal of Applied Physics, 86(11):6451–6461, 1999.

[157] Y. Shigesato and D. C. Paine.
Study of the effect of sn doping on the electronic transport properties of thin film indium oxide.
Applied Physics Letters, 62(11):1268–1270, 1993.

[158] Y. Shigesato, D. C. Paine, and T. E. Haynes.
Study of the effect of ion implantation on the electrical and microstructural properties of tin-doped indium oxide thin films.
Journal of Applied Physics, 73(8):3805–3811, 1993.

[159] M. Morales-Masis, E. Rucavando, R. Monnard, L. Barraud, J. Holocsky, M. Desoeisse, M. Boccard, and C. Ballif.
Highly conductive and boradband transparent Zr-doped In_2O_3as front electrode for solar cell.
IEEE journal of photovolatics, 8(5):1202–1207, 2018.

[160] C. Manoharan, M. Jothibas, S. Johnson Jeyakumar, and S. Dhanapandian.
Structural, optical and electrical properties of Zr-doped In_2O_3 thin films.
Spectrochimica Acta Part A: Molecular and Biomolecular Spectroscopy, 145:47 – 53, 2015.

[161] M. F. A. M. van Hest, M. S. Dabney, J. D. Perkins, D. S. Ginley, and M. P. Taylor.
Titanium-doped indium oxide: A high-mobility transparent conductor.
Applied Physics Letters, 87(3):032111, 2005.

[162] Y. Abe and N. Ishiyama.
Titanium-doped indium oxide films prepared by d.c. magnetron sputtering using ceramic target.
Journal of Materials Science, 41(22):7580–7584, Nov 2006.

[163] Y. Abe and N. Ishiyama.
Polycrystalline films of tungsten-doped indium oxide prepared by d.c. magnetron sputtering.
Materials Letters, 61(2):566 – 569, 2007.

[164] X. Li, Q. Zhang, W. Miao, L. Huang, and Z. Zhang.
Transparent conductive oxide thin films of tungsten-doped indium oxide.
Thin Solid Films, 515(4):2471 – 2474, 2006.

[165] T. Koida, Y. Ueno, and H. Shibata.
In_2O_3-based transparent conducting oxide films with high electron mobility fabricated at low process temperatures.
physica status solidi (a), 215(7):1700506, 2018.

[166] E. Kobayashi, Y. Watabe, and T. Yamamoto.
High-mobility transparent conductive thin films of cerium-doped hydrogenated indium oxide.
Applied Physics Express, 8(1):015505, dec 2014.

[167] Shi-Yao Sun, Jow-Lay Huang, and Ding-Fwu Lii.
Properties of indium molybdenum oxide films fabricated via high-density plasma evaporation at room temperature.
Journal of Materials Research, 20(1):247–255, 2005.

[168] D. S. Bhachu, D. O. Scanlon, G. Sankar, T. D. Veal, R. G. Egdell, G. Cibin, A. J. Dent, C. E. Knapp, C. J. Carmalt, and I. P. Parkin.
Origin of high mobility in molybdenum-doped indium oxide.
Chemistry of Materials, 27(8):2788–2796, 2015.

[169] J. C. C. Fan and J. B. Goodenough.
X-ray photoemission spectroscopy studies of Sn-doped indium-oxide films.
Journal of Applied Physics, 48(8):3524–3531, 1977.

[170] T. Szörényi, L.D. Laude, I. Bertóti, Z. Kántor, and Zs. Geretovszky.
Excimer laser processing of indium-tin-oxide films: An optical investigation.
Journal of Applied Physics, 78(10):6211–6219, 1995.

[171] H. Yamaura, T. Jinkawa, J. Tamaki, K. Moriya, N. Miura, and N. Yamazoe.
Indium oxide-based gas sensor for selective detection of CO.
Sensors and Actuators B: Chemical, 36(1):325 – 332, 1996.
Proceedings of the Sixth International Meeting on Chemical Sensors.

[172] M. Faur, M. Faur, D. T. Jayne, M. Goradia, and C. Goradia.
XPS investigation of anodic oxides grown on p-type InP.
Surface and Interface Analysis, 15(11):641–650, 1990.

[173] J. M. Baker, R. W. Johnson, and R. A. Pollak.
Surface analysis of rf plasma oxidized In and PbInAu films using ESCA.
Journal of Vacuum Science and Technology, 16(5):1534–1541, 1979.

[174] Joel C. Schuurman, Alexandra R. McNeill, Rodrigo F. Martinez-Gazoni, Jonty I. Scott, Roger J. Reeves, Martin W. Allen, and Alison J. Downard.
The effect of covalently bonded aryl layers on the band bending and electron density of SnO_2 surfaces probed by synchrotron x-ray photoelectron spectroscopy.
Phys. Chem. Chem. Phys., 21:17913–17922, 2019.

[175] E. Bêche, P. Charvin, D. Perarnau, S. Abanades, and G. Flamant.
Ce 3d XPS investigation of cerium oxides and mixed cerium oxide ($Ce_xTi_yO_z$).
Surface and Interface Analysis, 40(3-4):264–267, 2008.

[176] L. Truffault, M. Ta, T. Devers, K. Konstantinov, V. Harel, C. Simmonard, C. Andreazza, I. P. Nevirkovets, A. Pineau, O. Veron, and J. Blondeau.
Application of nanostructured Ca doped CeO_2 for ultraviolet filtration.
Materials Research Bulletin, 45(5):527 – 535, 2010.

[177] H. Ohno, A. Iwase, D. Matsumura, Y. Nishihata, J. Mizuki, N. Ishikawa, Y. Baba, N. Hirao, T. Sonoda, and M. Kinoshita.

Study on effects of swift heavy ion irradiation in cerium dioxide using synchrotron radiation X-ray absorption spectroscopy.
Nuclear Instruments and Methods in Physics Research Section B: Beam Interactions with Materials and Atoms, 266(12):3013 – 3017, 2008.
Radiation Effects in Insulators.

[178] V. Scherer, C. Janowitz, A. Krapf, H. Dwelk, D. Braun, and R. Manzke.
Transport and angular resolved photoemission measurements of the electronic properties of In_2O_3 bulk single crystals.
Applied Physics Letters, 100(21):212108, 2012.

[179] K. H. L. Zhang, R. G. Egdell, F. Offi, S. Iacobucci, L. Petaccia, S. Gorovikov, and P. D. C. King.
Microscopic origin of electron accumulation in In_2O_3.
Phys. Rev. Lett., 110:056803, 2013.

[180] N. Preissler, O. Bierwagen, Ashok T. Ramu, and J. S. Speck.
Electrical transport, electrothermal transport, and effective electron mass in single-crystalline In_2O_3 films.
Phys. Rev. B, 88:085305, Aug 2013.

[181] I. Hamberg and C. G. Granqvist.
Evaporated Sn-doped In_2O_3 films: Basic optical properties and applications to energy-efficient windows.
Journal of Applied Physics, 60(11):R123–R160, 1986.

[182] R. Clanget.
Ionized impurity scattering in degenerate In_2O_3.
Applied physics, 2(5):247–256, 1973.

[183] A. Walsh, J. L. F. Da Silva, and S-H. Wei.
Origins of band-gap renormalization in degenerately doped semiconductors.
Phys. Rev. B, 78:075211, Aug 2008.

[184] C. Janowitz, V. Scherer, M. Mohamed, A. Krapf, H. Dwelk, R. Manzke, Z. Galazka, R. Uecker, K. Irmscher, R. Fornari, M. Michling, D. Schmeißer, J. R. Weber, J. B. Varley, and C. G. Van de Walle.
Experimental electronic structure of In_2O_3 and Ga_2O_3.
New Journal of Physics, 13(8):085014, aug 2011.

[185] Péter Ágoston, Christoph Körber, Andreas Klein, Martti J. Puska, Risto M. Nieminen, and Karsten Albe.

Limits for n-type doping in In_2O_3 and SnO_2: A theoretical approach by first-principles calculations using hybrid-functional methodology.
Journal of Applied Physics, 108(5):053511, 2010.

[186] J. E. N Swallow, B. A. D. Williamson, S. Sathasivam, M. Birkett, T. J. Featherstone, P. A. E. Murgatroyd, H. J. Edwards, Z. W. Lebens-Higgins, D. A. Duncan, M. Farnworth, P. Warren, N. Peng, T. L. Lee, L. F. J. Piper, A. Regoutz, C. J. Carmalt, I. P. Parkin, V. R. Dhanak, D. O. Scanlon, and T. D. Veal.
Resonant doping for high mobility transparent conductors: the case of Mo-doped In_2O_3 (Supplementary Information).
Materials Horizons, 2019.
In Press.

[187] H. Cotal, C. Fetzer, J. Boisvert, G. Kinsey, R. King, P. Hebert, H. Yoon, and N. Karam.
III–V multijunction solar cells for concentrating photovoltaics.
Energy Environ. Sci., 2:174–192, 2009.

[188] A. E. Taverner, C. Rayden, S. Warren, A. Gulino, P. A. Cox, and R. G. Egdell.
Comparison of the energies of vanadium donor levels in doped SnO_2 and TiO_2.
Phys. Rev. B, 51:6833–6837, Mar 1995.

[189] Y. J. Seo, G. W. Kim, C. H. Sung, M.S. Anwar, C. G. Lee, and B. H. Koo.
Characterization of transparent and conductive electrodes of Nb-doped SnO_2 thin film by pulsed laser deposition.
Current Applied Physics, 11(3, Supplement):S310 – S313, 2011.
Joint International Conference on the 7th Asian Meeting on Ferroelectricity (AMF-7) and the 7th Asian Meeting on Electroceramics.

[190] V. Gokulakrishnan, S. Parthiban, K. Jeganathan, and K. Ramamurthi.
Investigations on the structural, optical and electrical properties of Nb-doped SnO_2 thin films.
Journal of Materials Science, 46(16):5553–5558, 2011.

[191] A. Y. Suzuki, K. Nose, A. Ueno, M. Kamiko, and Y. Mitsuda.
High transparency and electrical conductivity of SnO_2:Nb thin films formed through (001)-oriented SnO:Nb on glass substrate.
Applied Physics Express, 5(1):011103, jan 2012.

[192] S. Nakao, N. Yamada, T. Hitosugi, Y. Hirose, T. Shimada, and T. Hasegawa.
High mobility exceeding $80\,cm^2\,v^{-1}\,s^{-1}$ in polycrystalline Ta-Doped SnO_2 thin films on glass using anatase TiO_2 seed layers.
Applied Physics Express, 3(3):031102, feb 2010.

[193] S. W. Lee, Y. Kim, and H. Chen.
Electrical properties of Ta-doped SnO_2 thin films prepared by the metal–organic chemical-vapor deposition method.
Applied Physics Letters, 78(3):350–352, jan 2001.

[194] Y. Kim, S. W. Lee, and H. Chen.
Microstructural evolution and electrical property of Ta-doped SnO_2 films grown on Al_2O_3 (0001) by metalorganic chemical vapor deposition.
Thin Solid Films, 405(1-2):256–262, feb 2002.

[195] S.W. Lee, A. Daga, Z.K. Xu, and Haydn Chen.
Characterization of MOCVD grown optical coatings of Sc_2O_3 and Ta-doped SnO_2.
Materials Science and Engineering: B, 99(1-3):134–137, may 2003.

[196] S. Nakao, N. Yamada, T. Hitosugi, Y. Hirose, T. Shimada, and T. Hasegawa.
Fabrication of highly conductive Ta-doped SnO_2 polycrystalline films on glass using seed-layer technique by pulse laser deposition.
Thin Solid Films, 518(11):3093–3096, mar 2010.

[197] H. Toyosaki, M. Kawasaki, and Y. Tokura.
Electrical properties of Ta-doped SnO_2 thin films epitaxially grown on TiO_2 substrate.
Applied Physics Letters, 93(13):132109, sep 2008.

[198] G. Turgut.
Effect of Ta doping on the characteristic features of spray-coated SnO_2.
Thin Solid Films, 594:56–66, nov 2015.

[199] Y. Muto, S. Nakatomi, N. Oka, Y. Iwabuchi, H. Kotsubo, and Y. Shigesato.
High-rate deposition of Ta-doped SnO_2 films by reactive magnetron sputtering using a Sn–Ta metal-sintered target.
Thin Solid Films, 520(10):3746–3750, mar 2012.

[200] N. M. Nguyen, M. Q. Luu, M. H. Nguyen, D. T. Nguyen, V. D. Bui, T. T. Truong, V. T. Pham, and T. Nguyen-Tran.
Synthesis of tantalum-doped tin oxide thin films by magnetron sputtering for photovoltaic applications.
Journal of Electronic Materials, 46(6):3667–3673, jan 2017.

[201] M. Weidner, J. Jia, Y. Shigesato, and A. Klein.
Comparative study of sputter-deposited SnO_2 films doped with antimony or tantalum.
physica status solidi (b), 253(5):923–928, jan 2016.

[202] M. Weidner, J. Brötz, and A. Klein.
Sputter-deposited polycrystalline tantalum-doped SnO_2 layers.
Thin Solid Films, 555:173–178, mar 2014.

[203] N. Yamada, S. Nakao, T. Hitosugi, and T. Hasegawa.
Sputter deposition of high-mobility $Sn_{1-x}Ta_xO_2$ films on anatase-TiO_2-coated glass.
Japanese Journal of Applied Physics, 49(10):108002, 2010.

[204] S. D. Ponja, B. A. D. Williamson, S. Sathasivam, D. O. Scanlon, I. P. Parkin, and C. J. Carmalt.
Enhanced electrical properties of antimony doped tin oxide thin films deposited via aerosol assisted chemical vapour deposition.
J. Mater. Chem. C, 6:7257–7266, 2018.

[205] B. Thangaraju.
Structural and electrical studies on highly conducting spray deposited fluorine and antimony doped SnO_2 thin films from $SnCl_2$ precursor.
Thin Solid Films, 402(1-2):71–78, jan 2002.

[206] B. Bissig, T. Jäger, L. Ding, A. N. Tiwari, and Y. E. Romanyuk.
Limits of carrier mobility in Sb-doped SnO_2 conducting films deposited by reactive sputtering.
APL Materials, 3(6):062802, 2015.

[207] S. Jäger, B. Szyszka, J. Szczyrbowski, and G. Bräuer.
Comparison of transparent conductive oxide thin films prepared by a.c. and d.c. reactive magnetron sputtering.
Surface and Coatings Technology, 98(1):1304 – 1314, 1998.

[208] G. Turgut, E. F. Keskenler, S. Aydın, E. Sönmez, S. Doğan, B. Düzgün, and M. Ertuğrul.
Effect of Nb doping on structural, electrical and optical properties of spray deposited SnO_2 thin films.
Superlattices and Microstructures, 56:107–116, apr 2013.

[209] K. J. Button, C. G. Fonstad, and W. Dreybrodt.
Determination of the electron masses in stannic oxide by submillimeter cyclotron resonance.
Physical Review B, 4(12):4539–4542, dec 1971.

[210] M. Feneberg, C. Lidig, K. Lange, M. E. White, M. Y. Tsai, J. S. Speck, O. Bierwagen, and R. Goldhahn.
Anisotropy of the electron effective mass in rutile SnO_2 determined by infrared ellipsometry.
physica status solidi (a), 211(1):82–86, 2014.

[211] M. Batzill, K. Katsiev, J. M. Burst, U. Diebold, A. M. Chaka, and B. Delley.
Gas-phase-dependent properties of SnO_2 (110), (100), and (101) single-crystal surfaces: Structure, composition, and electronic properties.
Phys. Rev. B, 72:165414, Oct 2005.

[212] S. K. Vasheghani Farahani, T. D. Veal, J. J. Mudd, D. O. Scanlon, G. W. Watson, O. Bierwagen, M. E. White, J. S. Speck, and C. F. McConville.
Valence-band density of states and surface electron accumulation in epitaxial SnO_2 films.
Phys. Rev. B, 90:155413, Oct 2014.

[213] D.J. Payne, G. Paolicelli, F. Offi, G. Panaccione, P. Lacovig, G. Beamson, A. Fondacaro, G. Monaco, G. Vanko, and R.G. Egdell.
A study of core and valence levels in β-PbO_2 by hard X-ray photoemission.
Journal of Electron Spectroscopy and Related Phenomena, 169(1):26 – 34, 2009.

[214] C. Körber, V. Krishnakumar, A. Klein, G. Panaccione, P. Torelli, A. Walsh, J. L. F. Da Silva, S.-H. Wei, R. G. Egdell, and D. J. Payne.
Electronic structure of In_2O_3 and Sn-doped In_2O_3 by hard x-ray photoemission spectroscopy.
Phys. Rev. B, 81:165207, Apr 2010.

[215] J. J. Mudd, Tien-Lin Lee, V. Muñoz Sanjosé, J. Zúñiga Pérez, D. J. Payne, R. G. Egdell, and C. F. McConville.
Valence-band orbital character of CdO: A synchrotron-radiation photoelectron spectroscopy and density functional theory study.
Phys. Rev. B, 89:165305, Apr 2014.

[216] J. B. Mann, T. L. Meek, and L. C. Allen.
Configuration Energies of the Main Group Elements.
Journal of the American Chemical Society, 122(12):2780–2783, 2000.

[217] J. B. Mann, T. L. Meek, E. T. Knight, J. F. Capitani, and L. C. Allen.
Configuration energies of the d-block elements.
Journal of the American Chemical Society, 122(21):5132–5137, 2000.

[218] B. A. D. Williamson, T. J. Featherstone, S. S. Sathasivam, J. E. N. Swallow, H. Shiel, L. A. H. Jones, M. J. Smiles, A. Regoutz, T. Lee, X. Xia, C. Blackman, P. K. Thakur, C. J. Carmalt, I. P. Parkin, T. D. Veal, and D. O. Scanlon.
Resonant Ta doping for enhanced mobility in transparent conducting SnO_2.
Chemistry of Materials, 32(5):1964–1973, 2020.

[219] S. D. Ponja, B. A. D. Williamson, S. Sathasivam, D.O. Scanlon, I. P. Parkin, and C. J. Carmalt.

Enhanced electrical properties of antimony doped tin oxide thin films deposited via aerosol assisted chemical vapour deposition.
J. Mater. Chem. C, 6:7257–7266, 2018.

[220] J. Szczyrbowski, K. Schmalzbauer, and H. Hoffmann.
Optical properties of In_2O_3-SnO_2 films in the transparent and plasma reflection region.
Thin Solid Films, 137(2):169 – 183, 1986.

[221] H. Sobotta, H. Neumann, G. Kühn, and V. Riede.
Infrared lattice vibrations of In_2O_3.
Crystal Research and Technology, 25(1):61–64, 1990.

[222] A. Schleife, M.D. Neumann, N. Esser, Z. Galazka, A. Gottwald, J. Nixdorf, R. Goldhahn, and M. Feneberg.
Optical properties of In_2O_3 from experiment and first-principles theory: influence of lattice screening.
New Journal of Physics, 20(5):053016, may 2018.

[223] K.L. Chopra, S. Major, and D.K. Pandya.
Transparent conductors—a status review.
Thin Solid Films, 102(1):1 – 46, 1983.

[224] C. Tsai.
Interband and intraband absorption coefficients of silicon: Theoretical frameworks and formulations.
IEEE Journal of Selected Topics in Quantum Electronics, 26(2):1–10, 2020.

[225] Hiroyuki Fujiwara and Michio Kondo.
Effects of carrier concentration on the dielectric function of ZnO:Ga and In_2O_3:Sn studied by spectroscopic ellipsometry: Analysis of free-carrier and band-edge absorption.
Phys. Rev. B, 71:075109, Feb 2005.

[226] O. Manasreh.
Introduction to Nanomaterials and Devices.
John Wiley & Sons, 1st edition, 2012.

[227] G. Haacke.
New figure of merit for transparent conductors.
Journal of Applied Physics, 47(9):4086–4089, 1976.

[228] Z. Zhao and T.L. Alford.
The optimal TiO_2/Ag/TiO_2 electrode for organic solar cell application with high device-specific haacke figure of merit.

Solar Energy Materials and Solar Cells, 157:599 – 603, 2016.

[229] Y. Jang, J. Seo, J. Seok, J. Lee, and K. Kim.
Roughening conjugated polymer surface for enhancing the charge collection efficiency of sequentially deposited polymer/fullerene photovoltaics.
Polymers, 7(8):1497–1509, 2015.

[230] R. G. Gordon.
Criteria for choosing transparent conductors.
MRS Bulletin, 25(8):52–57, 2000.

[231] J.A. Mendez-Gamboa, R. Castro-Rodriguez, I.V. Perez-Quintana, R.A. Medina-Esquivel, and A. Martel-Arbelo.
A figure of merit to evaluate transparent conductor oxides for solar cells using photonic flux density.
Thin Solid Films, 599:14 – 18, 2016.

[232] T. D. C. Hobson, L. J. Phillips, O. S. Hutter, H. Shiel, J. E. N. Swallow, C. N. Savory, P. K. Nayak, S. Mariotti, B. Das, L. Bowen, L. A. H. Jones, T. J. Featherstone, M. J. Smiles, M. A. Farnworth, G. Zoppi, P. K. Thakur, T. Lee, H. J. Snaith, C. Leighton, D. O. Scanlon, V. R. Dhanak, K. Durose, T. D. Veal, and J. D. Major.
Isotype heterojunction solar cells using n-type Sb_2Se_3 thin films.
Chemistry of Materials, 32(6):2621–2630, 2020.

[233] R. Kondrotas, Chao Chen, and Jiang Tang.
Sb_2S_3 solar cells.
Joule, 2(5):857–878, May 2018.

[234] A. M. Ali, K.S. Rahman, L. M. Ali, M. Akhtaruzzaman, K. Sopian, S. Radiman, and N. Amin.
A computational study on the energy bandgap engineering in performance enhancement of cdte thin film solar cells.
Results in Physics, 7:1066 – 1072, 2017.

[235] A. Belghachi and N. Limam.
Effect of the absorber layer band-gap on CIGS solar cell.
Chinese Journal of Physics, 55(4):1127 – 1134, 2017.

[236] C. Malerba, F. Biccari, C. L.eonor Azanza Ricardo, M. Valentini, R.Chierchia, M. Müller, A. Santoni, E. Esposito, P. Mangiapane, P. Scardi, and A. Mittiga.
CZTS stoichiometry effects on the band gap energy.
Journal of Alloys and Compounds, 582:528 – 534, 2014.

[237] Pei Zhao, Weitao Su, Reng Wang, Xiaofeng Xu, and Fengshan Zhang.
Properties of thin silver films with different thickness.
Physica E: Low-dimensional Systems and Nanostructures, 41(3):387 – 390, 2009.

[238] K. Ishioka, K. Kato, N. Ohashi, H. Haneda, M. Kitajima, and H. Petek.
The effect of n- and p-type doping on coherent phonons in GaN.
Journal of Physics: Condensed Matter, 25(20):205404, apr 2013.

[239] I. Williamson, S. Li, A. Correa Hernandez, M. Lawson, Y. Chen, and L. Li.
Structural, electrical, phonon, and optical properties of Ti- and V-doped two-dimensional MoS_2.
Chemical Physics Letters, 674:157 – 163, 2017.

[240] E. Aydin, M. De Bastiani, X. Yang, F. Sajjad, M.and Aljamaan, Y. Smirnov, M. N. Hedhili, W. Liu, T. G. Allen, L. Xu, E. Van Kerschaver, M. Morales-Masis, U. Schwingenschlögl, and S. De Wolf.
Zr-doped indium oxide (IZRO) transparent electrodes for perovskite-based tandem solar cells.
Advanced Functional Materials, 29(25):1901741, 2019.

[241] I. Rey-Stolle, Y. Lee, I. García, L. Cifuentes, K. M. Yu, C. Algora, and W. Walukiewicz.
On the use of transparent conductive oxides in high concentrator iii-v multijunction solar cells.
In *2017 IEEE 44th Photovoltaic Specialist Conference (PVSC)*, pages 1204–1209, 2017.

[242] T. J. Featherstone, J. Willis, J. E. N. Swallow, B. A. D. Williams, L. A. H. Jones, T. Lee, P. K. Thakur, G. W. Watson, T. Koida, D. O. Scanlon, and T. D. Veal.
Resonant Ce doping for high-mobility In_2O_3-based conductors with enhanced near-infrared transparency.
Submitted to Advanced Functional Materials.

[243] Amjid Iqbal, Arshad Mahmood, Taj Muhammad Khan, and Ejaz Ahmed.
Structural and optical properties of cr doped zno crystalline thin films deposited by reactive electron beam evaporation technique.
Progress in Natural Science: Materials International, 23(1):64 – 69, 2013.

[244] T. Srinivasulu, K. Saritha, and K.T. Ramakrishna Reddy.
Synthesis and characterization of Fe-doped ZnO thin films deposited by chemical spray pyrolysis.
Modern Electronic Materials, 3(2):76 – 85, 2017.

[245] Fatma Sarf, Irmak Karaduman Er, Emin Yakar, and Selim Acar.

The role of rare-earth metal (Y, Ru and Cs)-doped ZnO thin films in NH.
Journal of Materials Science: Materials in Electronics, 31:10084–10095, 2020.

[246] Milan Gacic, Gerhard Jakob, Christian Herbort, Hermann Adrian, Thomas Tietze, Sebastian Brück, and Eberhard Goering.
Magnetism of Co-doped ZnO thin films.
Phys. Rev. B, 75:205206, May 2007.

[247] Jiaqiang Xu, Yu'an Shun, Qingyi Pan, and Jianhua Qin.
Sensing characteristics of double layer film of ZnO.
Sensors and Actuators B: Chemical, 66(1):161 – 163, 2000.

[248] Sebastian C. Dixon, Sanjayan Sathasivam, Benjamin A. D. Williamson, David O. Scanlon, Claire J. Carmalt, and Ivan P. Parkin.
Transparent conducting n-type ZnO:Sc – synthesis, optoelectronic properties and theoretical insight.
J. Mater. Chem. C, 5:7585–7597, 2017.